THE HONG KONG
POLYTECHNIC UNIVERSITY
香港理工大學
Pao Yue-kong Library
包玉剛圖書館

Copyright Undertaking

This thesis is protected by copyright, with all rights reserved.

By reading and using the thesis, the reader understands and agrees to the following terms:

1. The reader will abide by the rules and legal ordinances governing copyright regarding the use of the thesis.
2. The reader will use the thesis for the purpose of research or private study only and not for distribution or further reproduction or any other purpose.
3. The reader agrees to indemnify and hold the University harmless from and against any loss, damage, cost, liability or expenses arising from copyright infringement or unauthorized usage.

IMPORTANT

If you have reasons to believe that any materials in this thesis are deemed not suitable to be distributed in this form, or a copyright owner having difficulty with the material being included in our database, please contact lbsys@polyu.edu.hk providing details. The Library will look into your claim and consider taking remedial action upon receipt of the written requests.

Pao Yue-kong Library, The Hong Kong Polytechnic University, Hung Hom, Kowloon, Hong Kong

http://www.lib.polyu.edu.hk

This thesis in electronic version is provided to the Library by the author. In the case where its contents is different from the printed version, the printed version shall prevail.

NOVEL NANOSTRUCTURE ENGINEERING VIA SELF-ASSEMBLY OF AMPHIPHILIC HOLLOW PARTICLES

LEE CHENG HAO

Ph.D

The Hong Kong Polytechnic University

2011

The Hong Kong Polytechnic University

Department of Applied Biology and Chemical Technology

Novel Nanostructure Engineering via Self-Assembly of Amphiphilic Hollow Particles

Lee Cheng Hao

A thesis submitted in partial fulfillment of the requirements for
the degree of Doctor of Philosophy

October 2010

CERTIFICATE OF ORIGINALITY

I hereby declare that this thesis is my own work and that, to the best of my knowledge and belief, it reproduces no material previously published or written, nor material that has been accepted for the award of any other degree or diploma, except where due acknowledgement has been made in the text.

Lee Cheng Hao

(October 2010)

Abstract

The research work described in this thesis aims to the preparation of novel nanostructured materials starting from an inexpensive building block, amphiphilic hollow particles. These particles are composed of polyethyleneimine-*g*-poly(methyl methacrylate) (PEI-*g*-PMMA) copolymer which is derived from its corresponding PMMA/PEI core-shell particle. A wide range of interesting nanostructured materials such as nanotubes, nanofibers, urchin-like, snowflake-like hierarchical structures have been constructed by simply manipulating assembling conditions such as co-solvent composition, temperature and solution pH.

Assembling mechanism for the formation of nanotubes from hollow particles of PEI-*g*-PMMA was first investigated at either 15 or 17°C with fluid shear in a mixture of dichloromethane (DCM) and water. Effects of stirring rate and DCM to water volume ratio on the hollow particle assembly were systematically examined. Surface properties and morphology of the hollow particles as well as the resulting assemblies in both DCM and water were characterized by X-ray photoelectron spectroscopy and transmission electron microscopy. Results from these studies suggest four key features of this assembly process: 1) Morphology of the amphiphilic hollow particle is inversable in organic solvent and water. 2) The assembly process can only occur with appropriate fluid shear and DCM/water ratio. 3) The hollow particles can undergo deformation to ellipsoidal shape with fluid shear at 350 rpm in an appropriate DCM/water (e.g. 3:7 v/v) mixture. 4) The elongated hollow particles are able to assemble into linear aggregates via tip-to-tip connection, followed by coalescence and fusion to generate hollow nanotubes with diameters less than 150 nm. The lengths of the nanotubes can be extended to micron-scale, and they can be easily aligned via a simple dip-

coating method. This simple and inexpensive assembly process using amphiphilic hollow particle as a building block is dramatically different from the well-known self-assembly of block copolymers into different nanostructures under equilibrium conditions.

Assembling temperature has shown profound effect on the morphology of the hollow particles and resulting assemblies. Varying solution temperatures from 15 to 45°C lead to the formation of different sizes of hollow particles ranging from 28 to 225 nm in diameter, respectively. The resultant hollow particles could be further converted into snowflake-shape under a rapid temperature quenching process. In the case of preformed nanotubes, increasing solution temperature can enhance the hydrophobic interaction between PMMA graft chains inside the nanotube, resulting in the transformation of nanotube to nanofiber with diameter ranging from 17 to 137 nm**.**

Various novel hierarchical microstructures can also be fabricated using preformed nanotubes as building block through pH tuning. The formation of three-dimensional hierarchical structures in aqueous solution over a pH range from 5 to 13 are captured by field-emission scanning electron microscopy (FE-SEM), transmission electron microscopy (TEM) and atomic force microscopy (AFM). The hierarchical structures display distinct assembly profiles across three pH regimes. At low pH (pH =3.0), nanotube building blocks appear in random orientation and distribution. There is almost no hierarchical assembly under this condition. At pH between 6 and 8, the nanotube building blocks transform into straw-sheaflike bundle and fractal-like structures. At pH 9 which is close to isoelectric point of the nanotubular charge density as determined with a *zeta*-potential measurement, nanotubes align into parallel bundles and pack into highly packed columnar structures. When solution pH is above 10, the bundles (in straw-sheaf morphology) with loosely agglomerated fantail-shaped morphology are further assembled into plate-like morphology with interwoven networks.

The in-depth understanding gained through this study can guide the design and manipulation of self-assembly of various amphiphilic hollow particles, thus generating diverse and intriguing nanostructured materials.

Publications

1. Kin Man Ho, Wei Ying Li, Cheng Hao Lee, Chun Ho Yam, Robert G. Gilbert, Pei Li "Mechanistic study of the formation of amphiphilic core-shell particles by grafting methyl methacrylate from polyethylenimine through emulsion polymerization". *Polymer* , **2010**, 51, 3512-3519.

2. Cheng Hao Lee, Kin Man Ho, Harris F. W., Stephen Z. D. Cheng, Pei Li "Formation of nanostructured materials using inexpensive hollow particles of amphiphilic graft copolymers as building blocks: 1. insight into the mechanism of nanotube formation". *Soft Matter*, **2009**, *5*, 4914-4921.

3. Cheng Hao Lee, Pei Li "Formation of intriguing hierarchical structures from preformed amphiphilic copolymer nanotubes" (Manuscript in preparation)

4. Cheng Hao Lee, Pei Li "Study of temperature-induced morphological change of hollow particles of amphiphilic graft copolymers" (Manuscript in preparation)

Conferences and Symposia

1. Cheng Hao Lee, Pei Li. "Formation of Nanostructured Materials Using Inexpensive Hollow Particles of Amphiphilic Graft Copolymers as Building Blocks: Insight into the Mechanism of Nanotube Formation", *Abstract of Papers*, The 3rd Asian Symposium on Emulsion Polymerization and Functional Polymeric Microspheres, Jeju, South Korea, Sept. 20-23, 2009. (**won the Best Poster Award of the Conference)**

2. Cheng Hao Lee, Pei Li. "Formation of Hieraachical Superstructures via Self-assembly of Amphiphilic Hollow Nanoparticles at Different Solution pH" *Abstract Papers*, The 16th Symposium on Chemistry Postgraduate Research in Hong Kong, Hong Kong Baptist University, April 18, 2009

3. Cheng Hao Lee, Pei Li. "Formation of Multiple Nanostructured Materials via Shear-Induced Self-Assembly of Amphiphilic Hollow Nanoparticles" *Abstract Papers*, The 15th Symposium on Chemistry Postgraduate Research in Hong Kong, The University of Hong Kong, April 26, 2008.

4. Cheng Hao Lee, Pei Li. "Formation of Multiple Nanostructures and Their Transformations via Self-Assembly of Amphiphilic Hollow Nanoparticles" *Abstract Papers*, The 14th Symposium on Chemistry Postgraduate Research in Hong Kong, The Chinese University of Hong Kong, April 26, 2007.

ACKNOWLEDGEMENTS

Foremost, with a deep sense of gratitude, I wish to express my sincere thanks to my advisor, Prof. Pauline Pei Li, for her immense help in planning and valuable advice. She led me into a fascinating scientific world of nanotechnology and gave me a space that allowed me to devote myself to research without interference. Her insights and suggestions throughout the course of my PhD work are greatly acknowledged. Without her continuous support and encouragement, I would never have been able to accomplish this work. The many improvements in my knowledge about polymer science and in my writing and presentation skills can be attributed to her guidance.

I would also like to thank Prof. Daniel Ou-Yang, Prof. Mi Yongli for serving on my examination committee and providing me with valuable comments that have greatly enhanced the quality of my dissertation.

I am grateful to all of my group colleagues who have enriched my graduate experiences: Dr. Edmond Kin Man Ho, Dr. Phenix Aihua Wu, Miss Hetti Mimi, Dr. Hon Pui Yau, Mr. Chun Ho Yam, Miss Vera Mou, Mr. Max Wong, Miss. Sandra Siu and Mr. Noel Peter Tan. I would like to thank them for their many insightful discussions of my research project and the organization of various recreational activities that have brought my lab life lots of joy.

During my PhD study, I would like to thank Mr. Tsz kin Cheung, Ms. Yan Zhang and Mr. Nick Ho at Materials Characterization and Preparation Facility (MCPF), The Hong Kong University of Science and Technology for valuable advices in my TEM and XPS characterizations, Mr. C. S. Lo from Department of Applied Physics for support in my FE-

SEM characterizations and Mr. Jeremy Man Nin Yeung at Materials Research Centre, The Hong Kong Polytechnic University for assistance in AFM experiments in fluid mode.

During my PhD research period, I gratefully acknowledged the Research Committee of The Hong Kong Polytechnic University and Research Grant Council of HKSAR (PolyU 5016/09P) for the financial support of this project and for a grant supporting my conference presentation in the Third Asian Symposium on Emulsion Polymerization and Functional Polymeric Microspheres held in Jeju Island, South Korea in September, 2009.

Finally, I would like to express my deepest appreciation to my parents, wife and son. Without their unconditional love, support, and sacrifice, I could not come this far and finished my Ph.D. study. To them, I am forever indebted.

TABLE OF CONTENTS

Chapter 1 Introduction

Chapter 2 Fundamentals and Methods of Chemical and Physical Characterization Techniques

Chapter 3 Fabrication and characterization of core shell and hollow particles

Chapter 4 Effect of Solvent Composition in Morphological Changes

Chapter 5 Effect of Reaction Temperature on Structural Transitions of Hollow Particles and Nanotubes

Chapter 6 Effect of pH on the Formation of Hierarchical Structures

Chapter 7 Concluding Remarks and Future Studies

LIST OF FIGURES

Chapter 1

Chapter 2

Chapter 3

Chapter 4

Chapter 5

Chapter 6

LIST OF TABLES

LIST OF SCHEMES

LIST OF ABBREVIATIONS

PEI	poly(ethylenimine)
PMMA	poly(methyl methacrylate)
DCM	Dichloromethane
$CDCl_3$	Deuterated chloroform
PTA	Phosphotungstic acid
FT-IR	Fourier Transform Infrared
^{1}H NMR	proton nuclear magnetic resonance
SEM	scanning electron microscope
TEM	transmission electron microscope
AFM	atomic force microscope
XPS	x-ray photoelectron spectroscopy
GPC	gel permeation chromatography
PEI-*g*-PMMA	poly(ethylenimine)-*graft*-poly(methyl methacrylate)
B_1	Larmor frequency
TMS	Tetramethylsilane
K	Kelvin
keV	kilo electron volt
kV	kilovolt
µA	micro-ampere
mL	milliliter
µL	microliter
nm	nanometer

$V(r)$	Lennard-Jones potential
σ	hard sphere radius
mM	millimole
ppm	parts per million

LIST OF SYMBOLS NOMENCLATURE

Symbol	**Definition**
Mn	Number-average molecular weight
Mw	Weight-average molecular weight
wt. %	Weight percent
h	hour
v/v	Volume ratio
$\mathbf{n}$	Normal vector
$\boldsymbol{t}$	Non-azimuthal tangent
θ_c	Contact angle
γ	Surface tension
L_p	Planar length
L_c	Curved length
A_E	Excess surface area
Λ	Aspect ratio
ΔG_m^0	Standard Gibbs free energy change
ΔH_m^0	Standard enthalpy change
ΔS_m^0	Standard entropy change
ΔS_{HI}	Entropy change of hydrophobic interaction
R	gas law constant
X_{CMC}	critical micelle concentration
D_h	Hydrodynamic diameter
χ_{ps}	Polymer-solvent interaction parameter
V_s	Molar volume of solvent
δ_P	Solubility parameter of polymer
δ_S	Solubility parameter of solvent
ϕ	Volume percentage of solvent
Φ	Volume fraction
$\Delta\mu_P^o$	Partition coefficient of polymer

H	Heat of enthalpy
χ_{ps}	polymer-solvent interaction parameter
ζ	zeta potential
ε	dielectric constant
$f(ka)$	Henry’s function
η	viscosity
E_b	Binding energy
E_k	Kinetic energy
Φ_A	work function
h	Planck’s constant
ν	X-ray frequency
Cp	Heat capacity at constant pressure

Chapter 1 Introduction

1.1 Self-assembly of amphiphilic molecules

Self-assembly has become a very effective and promising approach to prepare a wide range of nanoscale materials. It can be defined as the spontaneous and reversible organization of molecular units into ordered structures by non-covalent interactions. In general, materials can be regarded as two states: the dispersed and the condensed state. The transition from a dispersed state to a condensed state is a universal phenomenon and is the beginning stage of the self-assembly. The self-assembling process relies on a sequence of spontaneous recognition, growth, and termination steps to form the final equilibrium supramolecular entity through forces such as metal ion coordination, hydrogen bonds, electrostatic interactions, and Van der Waals attraction.

Amphiphilic molecules contain both hydrophilic and hydrophobic segments which play a critical role in a wide range of self-assembly phenomena. The unique properties of these molecules rely on their intermolecular interactions such as hydrophobic and hydrophilic interactions between the moieties, and electrostatic interaction between the charged groups. The final equilibrium supramolecular structures are determined by the thermodynamics of self-assembly conditions such as pH, temperature, solvent composition etc. and both inter-and intra-aggregate forces.

When considering self-assembly of a targeted structure from the spontaneous organization of building blocks with dimensions that are beyond the sub-nanometer scale of most molecules or macromolecules, there are five fundamental principles which should be taken into account: (i) Building blocks, length, shape, surface structure; (ii) Attractive and repulsive interactions between building blocks; (iii) Reversible association-dissociation and/or adaptable motion of building blocks in assembly, lowest energy structure; (iv) Building block interactions with solvents, interfaces, templates; and (v) Building block dynamics, mass transport and agitation.

A challenge for perfecting structures via this kind of self-assembly chemistry is to find ways to synthesize (bottom-up) or fabricate (top-down) building blocks that not only have the right composition, but also have the same size and shape. However, no matter which way the building blocks are made, they are never truly monodisperse unless they happen to be single atoms, molecules or clusters. Thus the polydispersity of the building blocks in their size and shape manifest in the achievable degree of structural perfection of the assembly. Equally demanding is to control external environment of the building blocks, which ultimately determines the geometry and distance at which building blocks come to equilibrium in a self-assembled system. In fact, building blocks that are not too strongly bound in the assembly are able to adjust themselves to form an ordered structure. Those building blocks in the assembly which interact too strongly are more difficult to adjust their relative positions, thus resulting in less ordered metastable structure.

1.2 Self-assembly of block copolymer

Amphiphilic copolymers are comprised of chemically distinct polymers connected by a covalent bond. When they are dissolved in a selective solvent, like a good solvent for one of the segments and a poor solvent for the other, the copolymer molecules can undergo self-assembly to form a variety of morphologies, such as spherical, rod-like, interconnected rods, lamella, vesicles and large compound micelles (LCM) as shown Figure 1.1. The grey part corresponds to the hydrophobic core and individual black lines correspond to the hydrophilic chains. It is well known that molecular architecture of the block copolymers is an important parameter in designing nanostructured materials with desired properties.[1-7] Thus, with increased understanding of the mechanisms that govern supramolecular assemblies, in both synthetic and natural materials,[8-13] a variety of nanostructured materials have been developed for diverse applications such as drug delivery capsules,[14-18] micellar nanoreactors containing metallic nanoclusters,[19-24] electrophoretic separation media,[25-27] templates for biomineralization,[28,29] polymer electrolyte membranes for use in fuel cells,[30] micropatterning in soft lithography[31] and other functional materials.[32]

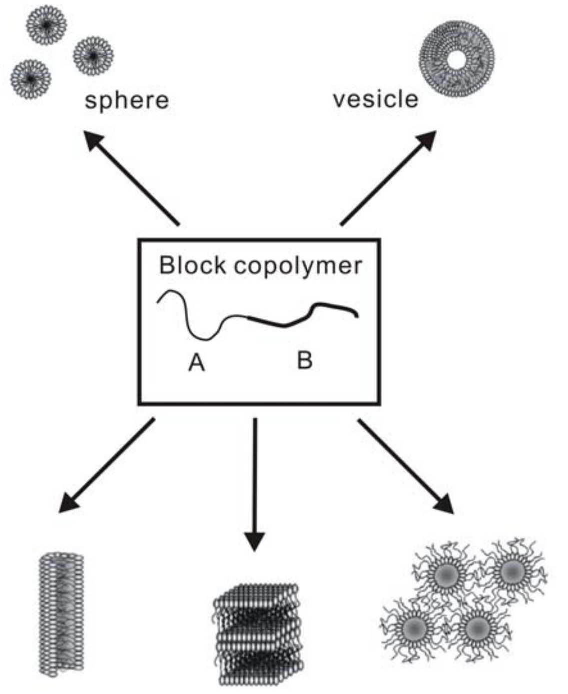

Figure 1.1 Multiple morphologies obtained from block copolymers: (a) spherical, (b) vesicles, and (c) inverse micelles, (d) lamellar structures, and (e) cylindrical or tubular micelles.

The first study towards the aggregates formed by amphiphilic block copolymers were performed by Discher *et al*.[33,34] using polyethylethene-*block*-poly(ethylene glycol)

(PEE_{37}-*b*-PEO_{40}) copolymers. Upon dispersion the block copolymer in an aqueous solution by hydration and subsequent preparative vitrification, worm-like and spherical micelles were found coexisting with small (D < 200 nm) vesicles (Figure 1.2).

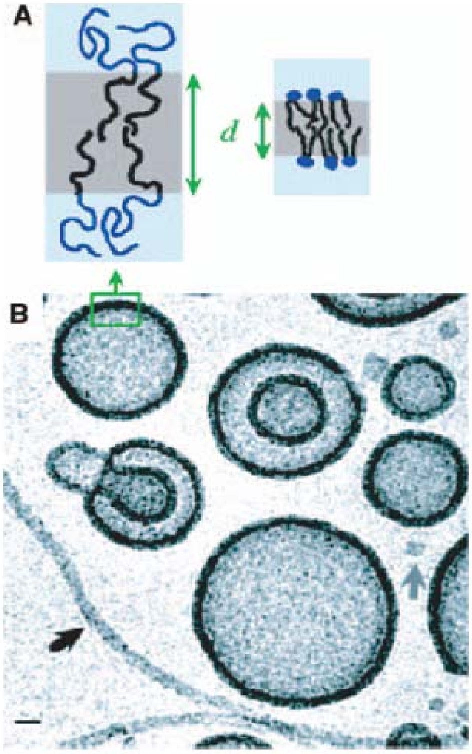

Figure 1.2 (A) Schematic representation of the bilayer membrane formed by PEE_{37}-b-$PEO_{40,}$ and comparing it with phospholipid bilayer.(B) Dispersion of PEE_{37}-b-PEO_{40} in water, showing vesicles, rod like micelles (black arrow) and spherical micelles (grey arrow).[33,34]

In fact, amphiphilic block copolymers can self-assemble to form one layer, while another series of molecules can form another layer, thus they can from bilayers which can be in the form of huge sheets and lamellae. These lamella can close to form hollow structures; vesicles. The closure of the lamella is governed by the interaction of rim energy and bending energy.[33] Figure 1.3 shows the multiple morphologies of assembled polystyrene-*b*-poly(acrylic acid) observed by transmission electron microscopy. These morphologies include spheres, rod, vesicles and large compound micelles.[35]

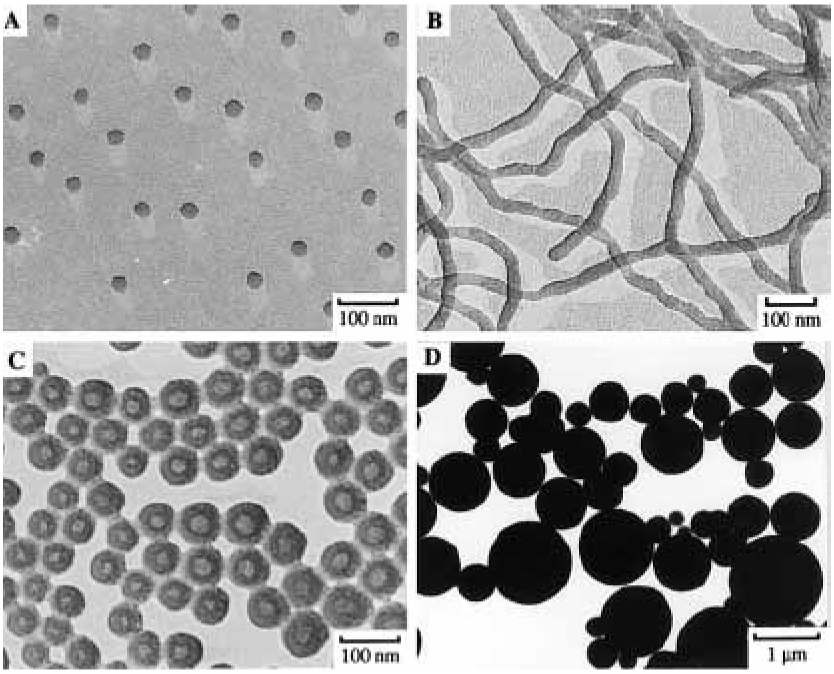

Figure 1.3 Transmission electron microscopy images of multiple morphologies assembled from polystyrene-*b*-poly(acrylic acid): (A) spheres; (B) rod; (C) vesicles; (D) large compound micelles.[35]

Other intriguing morphologies have also been obtained from various types of diblock copolymers. Figure 1.4a shows helical morphology assembled from polystyrene-*b*-poly(isocyanopeptide)[36], while Figure 1.4b exhibits pearl necklace morphology obtained from polystrene-*b*-poly(dimethylsiloxane) PS_{193k}-*b*-$PDMS_{39k}$.[36]

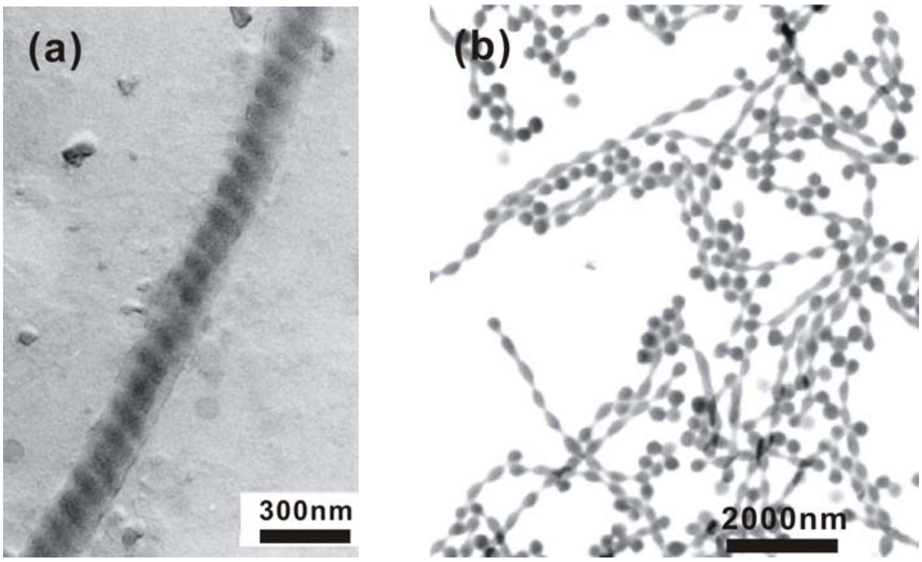

Figure 1.4 Bright-field TEM images of (a) Helical morphology for PS_{40}-b-$PIAA_{10}$ and (b) pearl necklace morphology for $PS_{(193k)}$-b-$PDMS_{(39k)}$ diblock copolymer.[36]

Comparing to the assembled morphologies using diblock copolymers, triblock copolymers possess additional complexity, resulting from three polymer-polymer Flory-Huggins interaction parameters χ (instead of one in diblock copolymers), and other effects such as conditions for solution-state assembly and block copolymer architecture. Wooley and coworkers reported a unique toroidal (ring-like) morphology, originating from triblock copolymers comprised of acrylic acid, methyl acrylate, and styrene chain segments.[37] The ability to form toroids was dependent upon various parameters, including the presence of divalent counter ions and the use of a controlled mixture of solvent. However, the kinetics and thermodynamics for toroid assembly, the compositional and structural requirements for assembling block copolymers, and the morphological stabilities are still required further studies.[38]

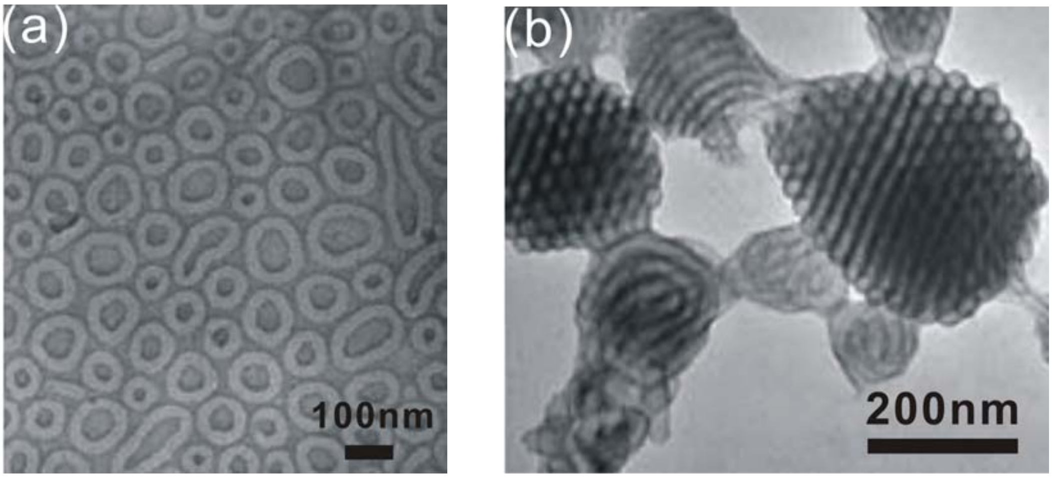

Figure 1.5 (a) Negatively-stained cryo-TEM image of PAA_{99}-b-PMA_{73}-b-PS_{66} micelles in toroidal morphology. (b) Cryo-TEM image of close-packed cylinder bundle morphology.[37]

1.3 Self-assembly of graft copolymer

When changing from simple block copolymers to graft copolymers in self-assembly, the morphological behaviors are considerably altered because the graft copolymers possess additional complexity due to their complicated and confined structures.[39-42] Thus they may provide additional prospect on the control of morphologies, allowing the design of new nanomaterials. However, synthetic difficulties have limited the scope of studies on the self-assembly behavior of graft copolymers. Generally, there are three synthetic strategies to prepare graft copolymers including grafting-through,[43-45] grafting-onto[46] and grafting-from[47]. For the grafting-from strategy, the pendant initiation groups on the polymer backbone can initiate the polymerization of the corresponding monomer to form side chains. Recently, well-defined graft copolymers with hydrophobic backbone and hydrophilic side chains have been synthesized by a combination of atom transfer radical polymerization (ATRP) and grafting-from techniques,[47,48] and their self-assembly behaviors were preliminarily investigated.[49,50] For instance, Zhang *et al.*[49] developed the synthetic route for amphiphilic graft copolymers of with poly(acrylic acid)-*g*-poly(n-butylacrylate) (PAA-*g*-PnBA) as shown in Scheme 1.

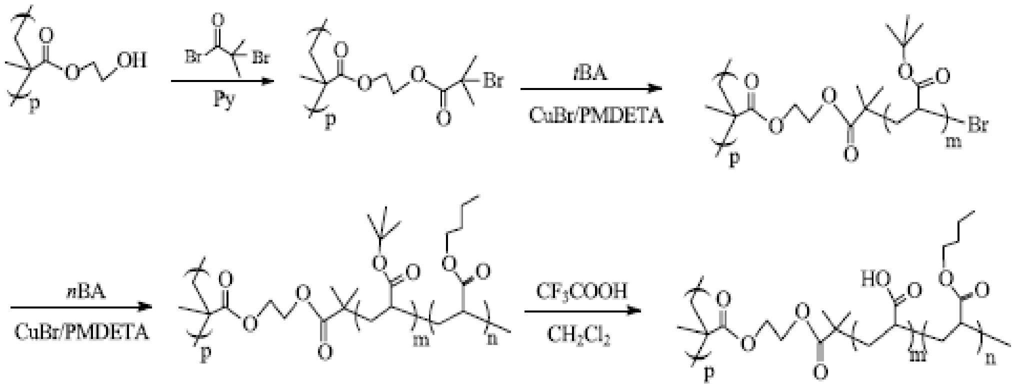

Scheme 1.1 Synthetic route for the preparation of amphiphilic PAA-*g*-PnBAcopolymer.[49]

Figure 1.6 shows AFM images of the amphiphilic brush as $[(AA)_{37}$-*g*-$(nBA)_{76}]_{1500}$ with regular cylindrical shape in the mixture of $CH_3OH/CHCl_3$ (v/v = 1:1). In the height image, the corona is invisible, probably because the height of the PnBA shell is too small to be detectable. However, in the phase image, the corona is very clear, making it possible to obtain size information about the core and the shell directly from the AFM height and phase images, respectively. The average diameter of the core of cylinders is measured to be about 25 nm and the diameter of whole cylinder (core and shell) is about 65 nm.

Recently, researchers describe the synthesis and characterization of amphiphilic graft copolymers with hydrophilic poly(acrylic acid) (PAA) backbone and hydrophobic poly(methyl methacrylate) (PMMA) side chains by ATRP using grafting-from techniques (Scheme 2).[51] This kind of amphiphilic graft copolymer can form only vesicle micelles in aqueous media as shown from TEM image in Figure 1.7.

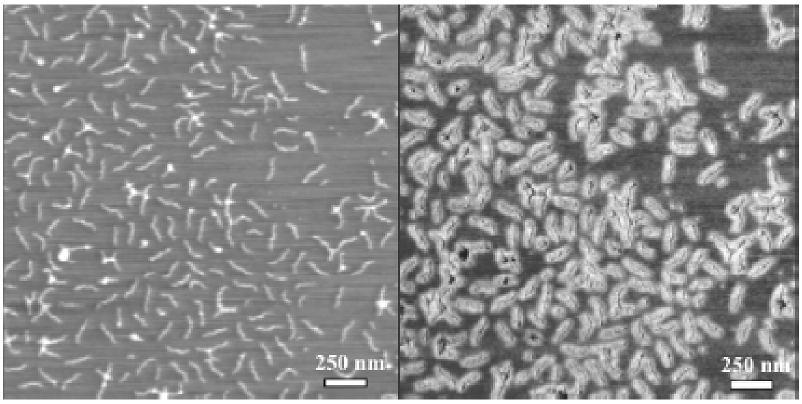

Figure 1.6 AFM Tapping Mode images of the brush, $[(AA)_{37}\text{-g-}(nBA)_{76}]_{1500}$ dip coated from dilute $CH_3OH/CHCl_3$ (4/1) solution mixture on mica: (left) height image (z-range: 6 nm) and (right) phase image (range: 40°).[49]

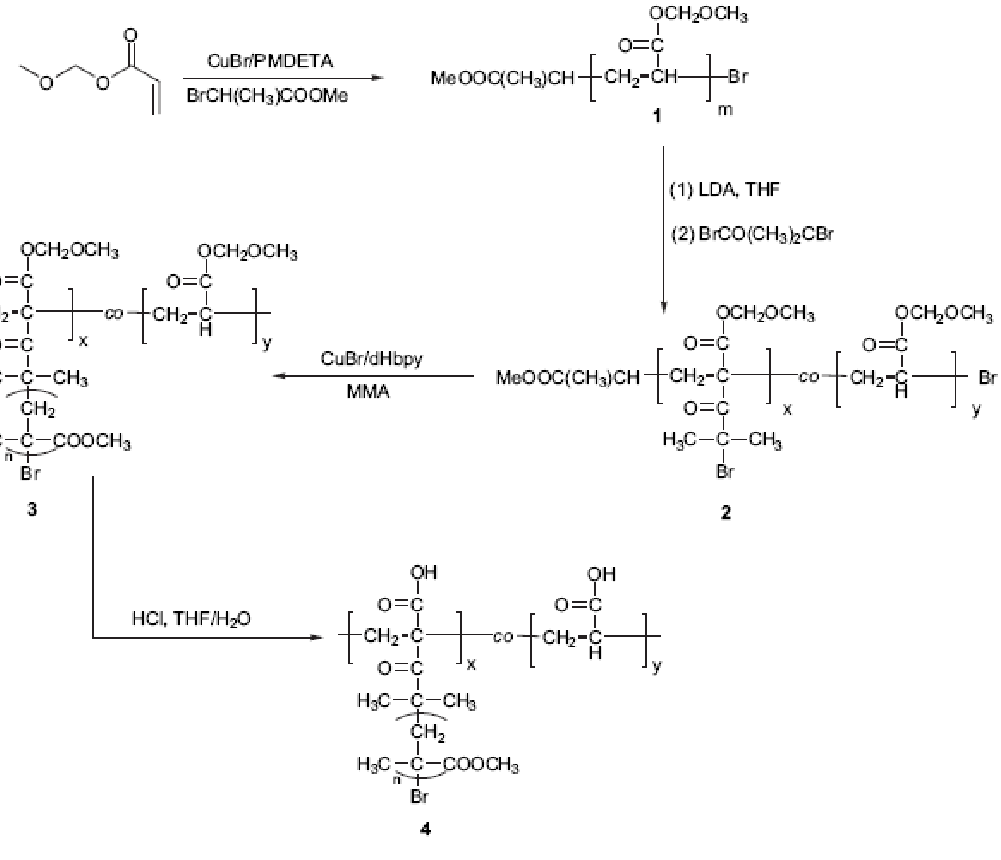

Scheme 1.2 Synthesis of PAA-*g*-PMMA amphiphilic graft copolymer.[51]

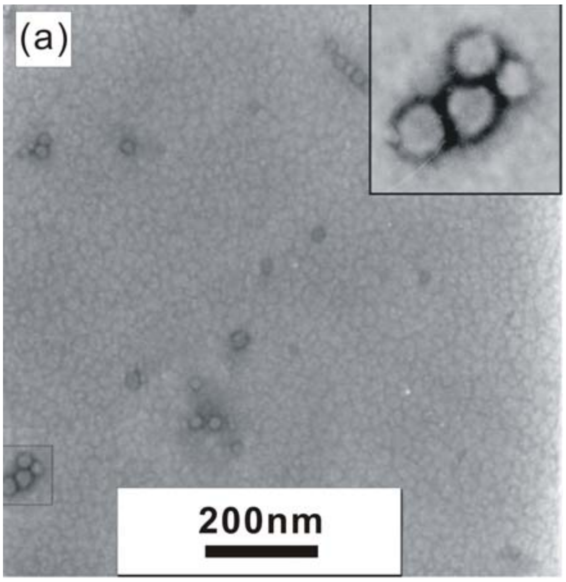

Figure 1.7 Bright-field TEM images of PAA-g-PMMA amphiphilic graft copolymer in vesicle morphology.[51]

Conventional comb- or brush-shaped graft copolymers, which have long backbones and short graft segments, are difficult to assemble into different morphologies because of their tendency to form spherical micelles. Recently, a new type of amphiphilic graft copolymer that contains a short hydrophilic backbone (oligomer of chitosan) and long hydrophobic side chains poly(ε-caprolactone) (Figure 1.8) have been self-assembled into not only classical micelles such as spheres, rods, and vesicles, but also self-organized into a new "petal-like" morphology.[52] (Figure 1.9) Another amphiphilic T-shaped graft copolymer consisting of a rigid backbone and a flexible side chain has been reported using Brownian dynamics simulation. In particular, this work focuses on how the conformational restriction of the graft copolymers both backbone rigidity and chain topology affects the packing geometry of wire-like micellar structure in a solvent selective for the flexible side chain.[53] Double-bond-based amphiphilic graft copolymer consisting of hydrophobic polyallene backbone and hydrophilic poly(ethylene glycol) side chains in tetrahydrofuran (THF)/water mixture was also investigated. Scheme 3 shows the synthetic route to this copolymer. Polyallene backbone is first prepared via living coordination polymerization of 6-methyl-1,2-heptadien-4-ol (MHDO) initiated by [(η3-allyl)NiOCOCF$_3$]$_2$.[54] The amphiphilic graft copolymer (PMHDO-*g*-PEG) with relative narrow molecular weight distribution (Mw/Mn = 1.22) was synthesized by the coupling reaction between the pendant hydroxyls of the backbone and acyl chloride end group of poly (ethylene glycol) via the grafting-onto approach. Multiple morphologies could be well tuned by adjusting water content.[54] Figure 1.11 illustrates some interesting morphologies, such as formation of chiral helical nanostructures through aggregation of an achiral copolymer under appropriate conditions.

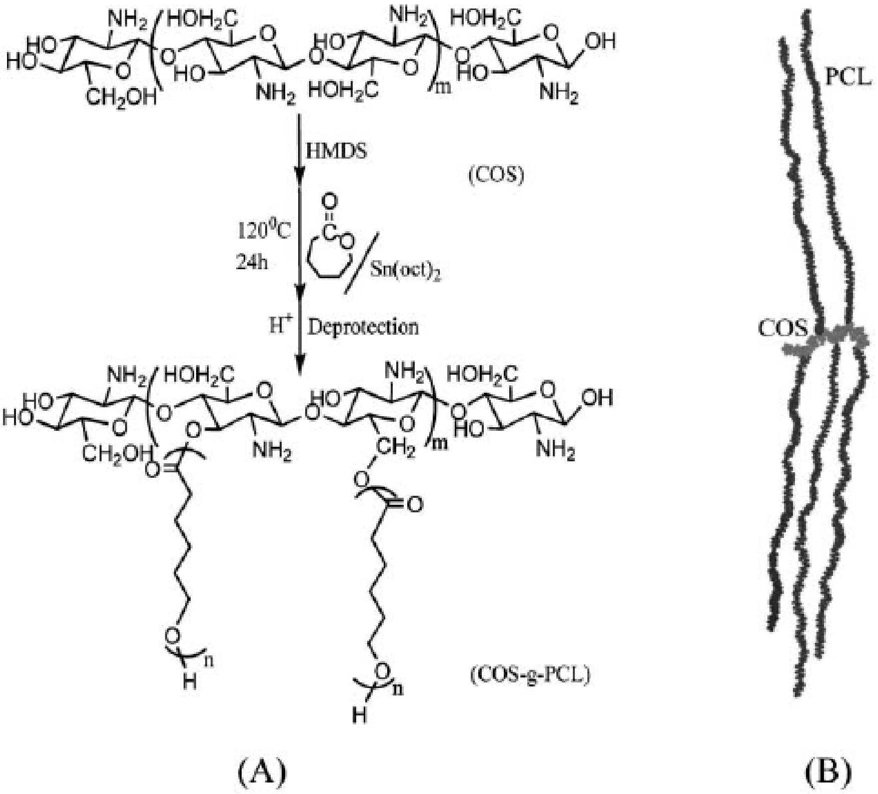

Figure 1.8 (A) Synthetic route of amphiphilic graft copolymer COS-g-PCL; (B) schematic illustration of graft copolymer COS-g-PCL containing long PCL branches.[52]

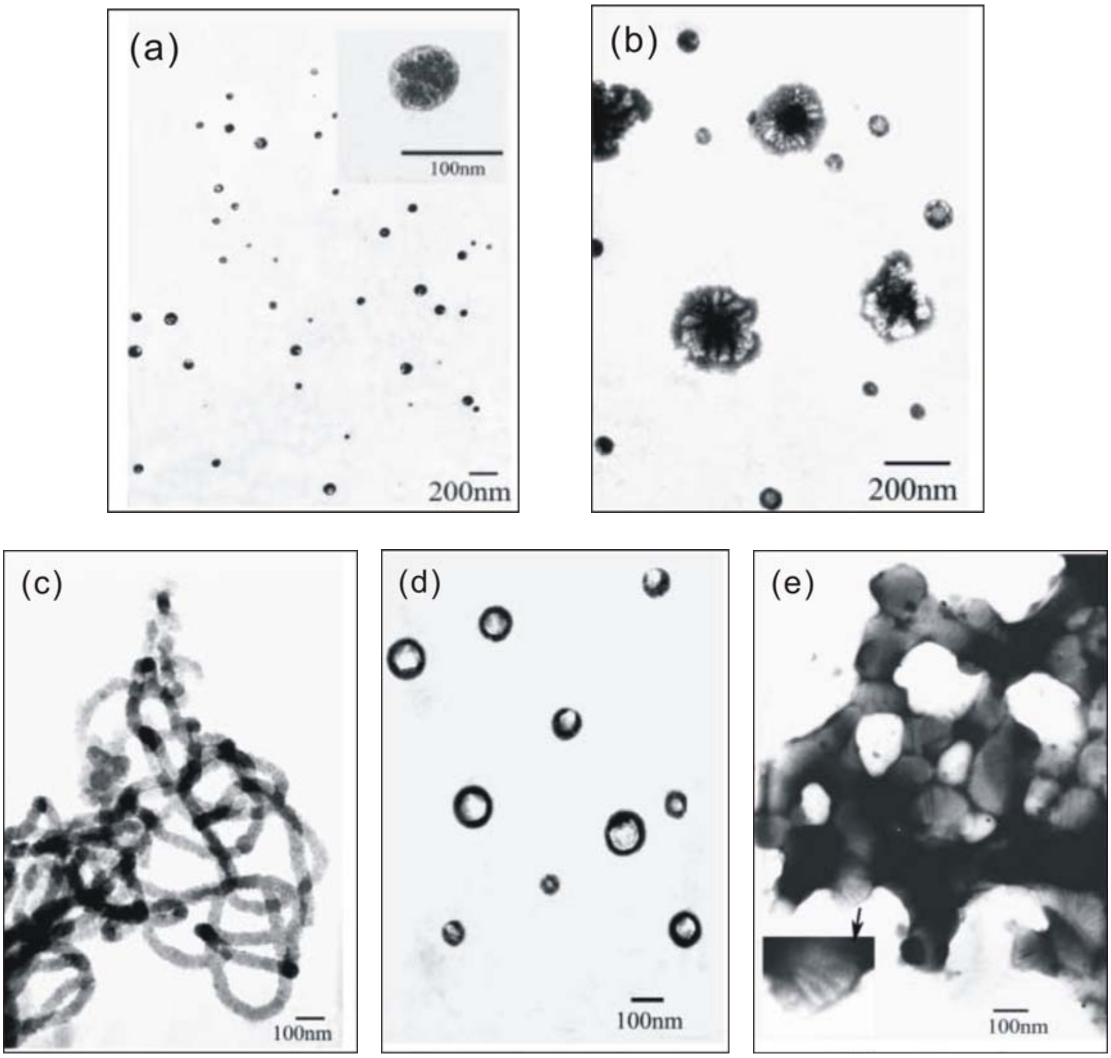

Figure 1.9 Transmission electron micrographs of multiple morphologies for amphiphilic graft copolymer chitooligosaccharides-*g*-polycaprolactones. (a) sphere; (b) petal-like and normal sphere; (c) threadlike rod; (d) vesicle and (e) network [52]

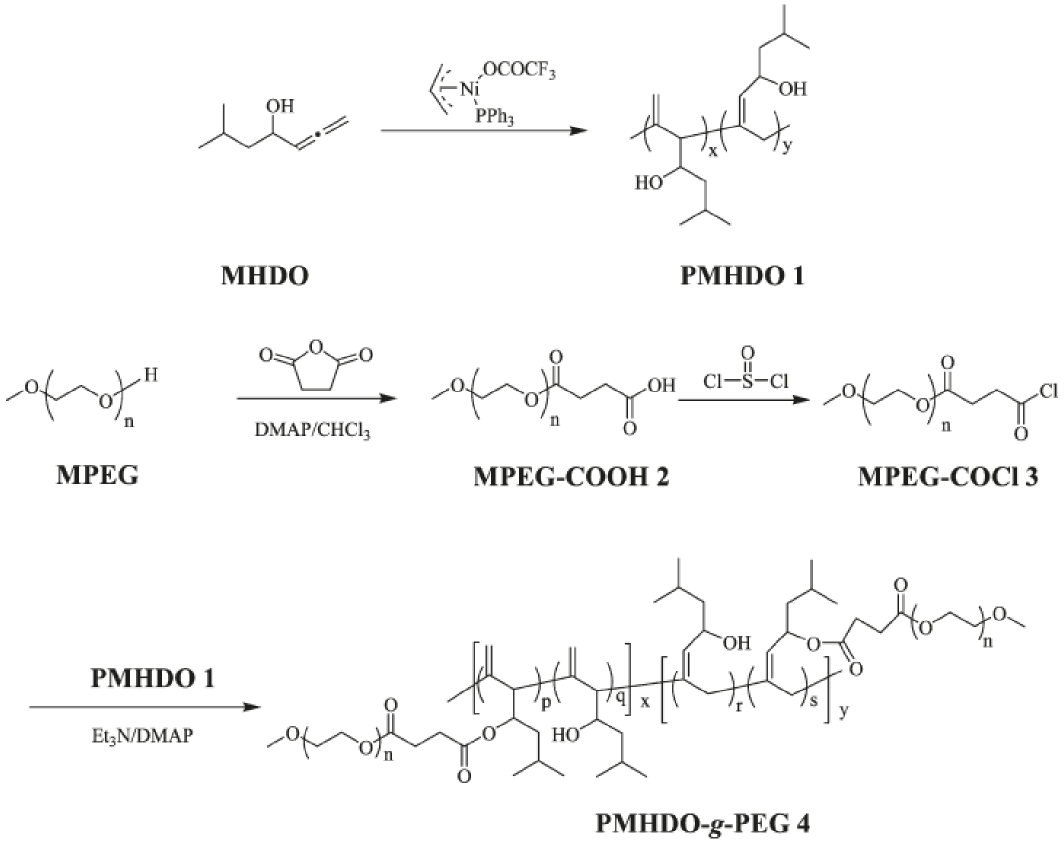

Scheme 1.3 Synthesis of polyallene-based amphiphilic graft copolymer.[54]

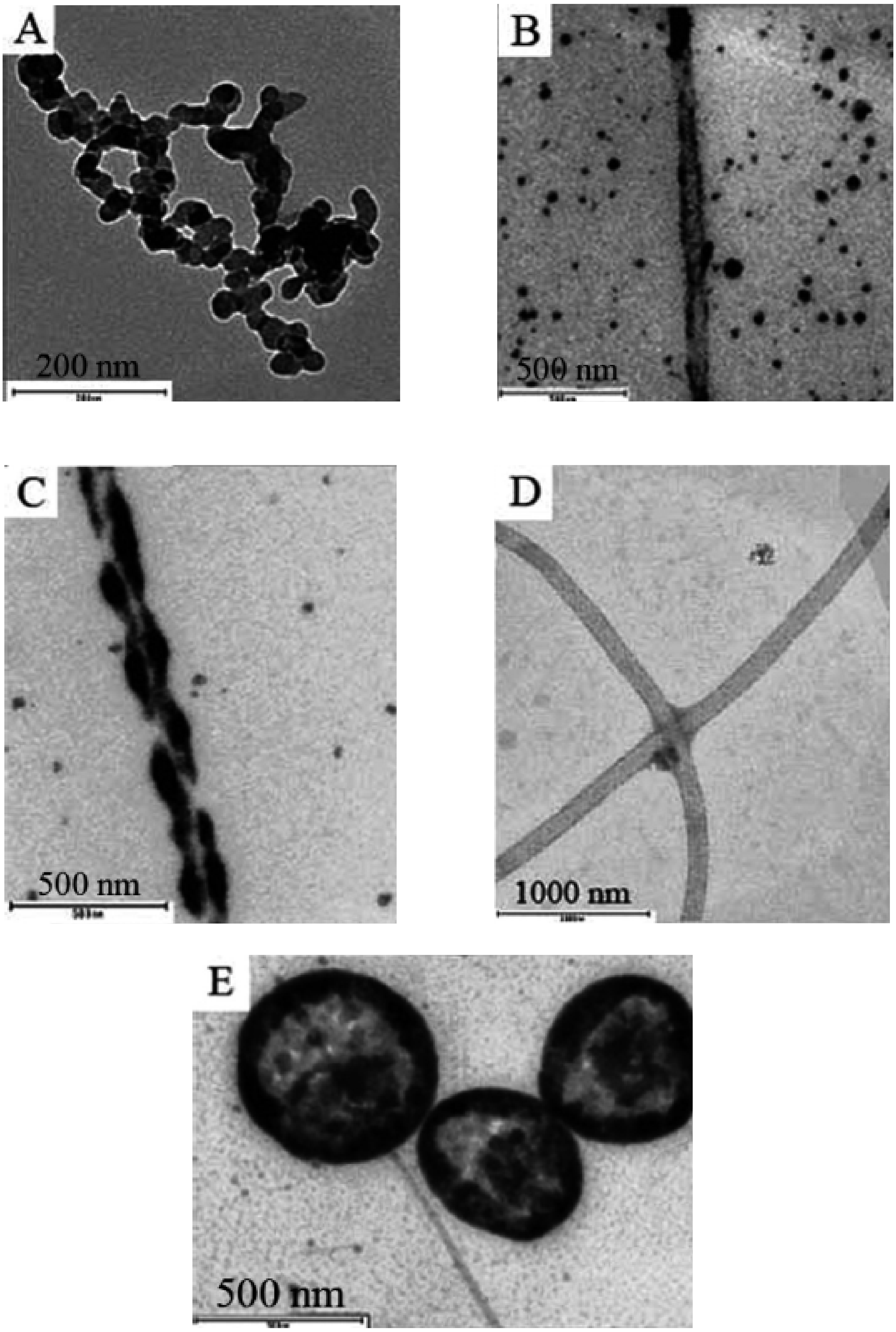

Figure 1.10 Bright-field transmission electron micrographs of multiple morphologies for amphiphilic graft copolymer PMHDO_{45}-*g*-PEG_{125} with a water content of (A) 14, (B) 25, (C) 33, (D) 48 and (E) 63 wt. % in THF/water mixture.[54]

Other recent work on the synthesis of well-defined amphiphilic graft copolymer is poly(acrylic acid)-*g*-poly(propylene oxide) (PAA-*g*-PPO) copolymer (Figure 1.11). Different micellar morphologies have been created with varying the graft hydrophobic PPO segment.[55] (Figure 1.12)

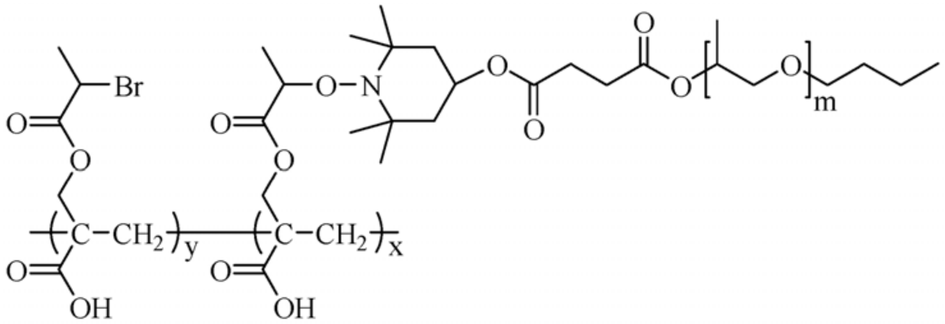

Figure 1.11 Chemical structure of amphiphilic PAA-g-PPO copolymer.[55]

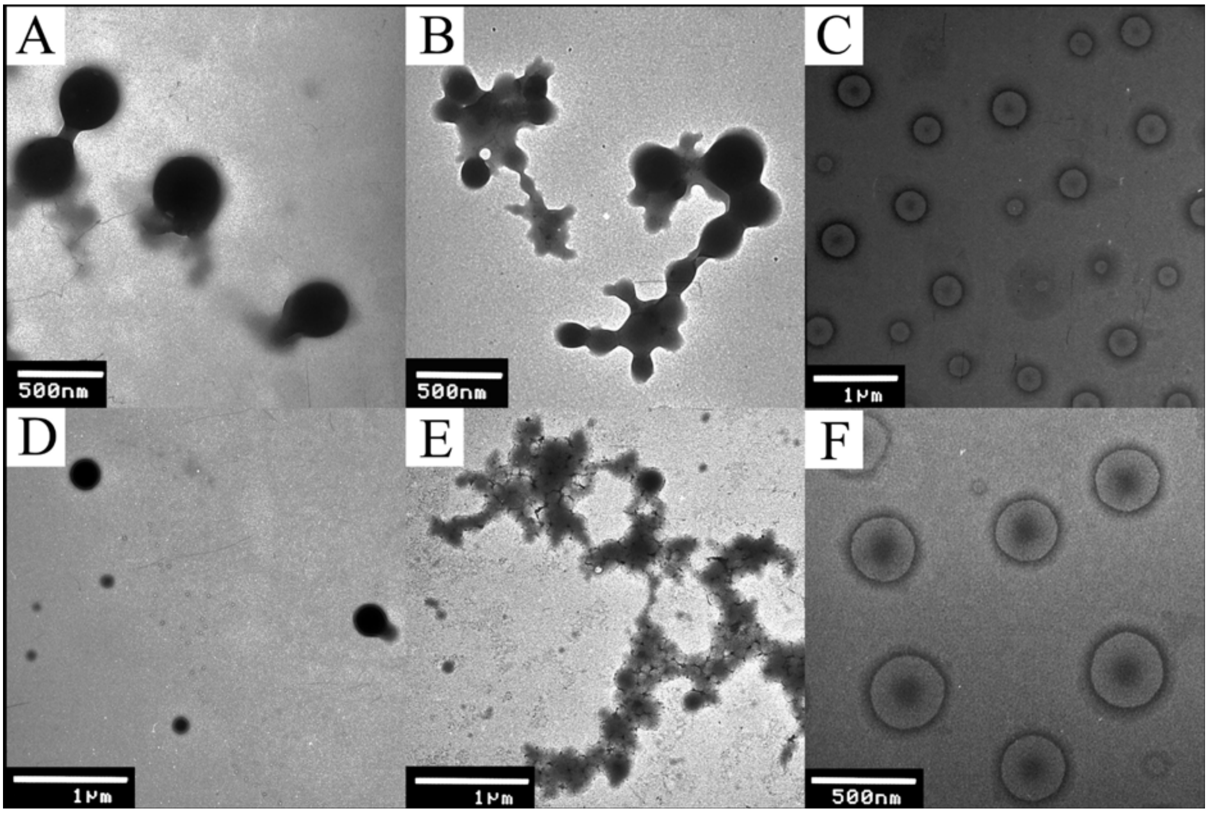

Figure 1.12 TEM images of multiple morphologies formed by PAA-g-PPO with grafting percentage of (A) 19.5 %, (B) 33.7 %; (C) 56.6%, (D) 22.9 %; (E) 42.0 % and (F) 65.4 % in pure water.[55]

Besides amphiphilic graft copolymers, cyclic copolymer brushes that contain poly(chloroethyl vinyl ether) backbones and randomly distributed polystyrene and polyisoprene side chains have been assembled into supramolecular tubes up to 700 nm long when treated in solvents that selectively interact with the polyisoprene branches.[56] (Figure 1.13)

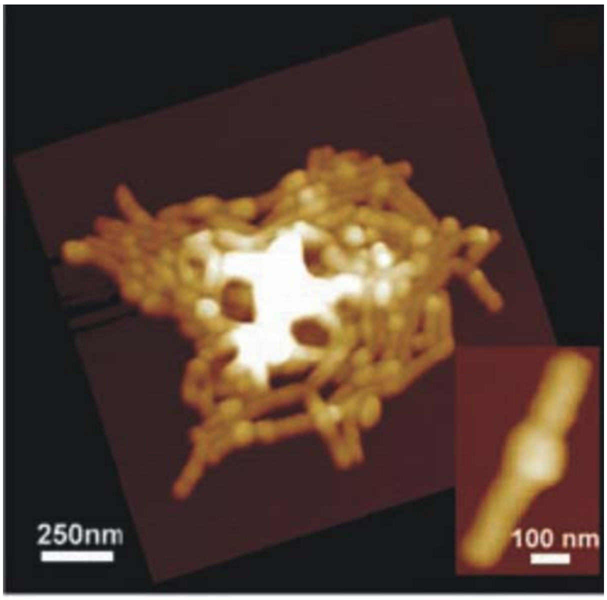

Figure 1.13 AFM topographic image (tapping mode) of nanotubular aggregates and isolated tube (diameter, 100 nm; length, 700 nm).[56]

1.4 Self assembly of nanotubes from amphiphilic copolymer

One-dimensional (1D) polymer nanostructures with hollow interiors have become a focus of many research efforts inspired by the functions of similar assemblies in biological systems.[57-59] Thus, much efforts have been devoted to fabricate various polymer nanotubes from the viewpoint of both fundamental research and practical applications in micro- and nanoelectronics, selective ion transport, biosensor applications, chemical catalysis, nanocomposite etc.[60-62] Strategies for fabricating polymer nanotubes can be divided into two approaches: template-assisted and template-free synthesis. Most polymer nanotubes are produced by template-assisted synthesis using porous membranes, nanofibers, surfactants, and cyclodextrin. Template synthesis using porous alumina and track etched polycarbonate membranes is a well-established approach for fabricating polymer nanotubes. The elegance of this approach lies in its ability to produce a wide range of polymer nanotubes, yet depending on few physical and chemical parameters.[63] Precise control on these parameters is required for tailoring the shape, size, and properties of final products. In the case of thermoplastic or soluble polymers, nanotubes can be prepared via wetting of porous membranes.[64,65] When a polymer melt or solution is placed on a porous membrane, it invades the porous membrane and wet rapidly the pore walls due to the high surface energy of the membrane, finally giving rise to tubular nanostructures. The thickness of wetting layer is mainly determined by the polymer-template interaction. Moreover, conducting polymer nanotubes have been extensively synthesized by chemical[66,67] and electrochemical[68-70] polymerization using porous membranes. Polyelectrolytes could be deposited within the cylindrical pores of templates to obtain nanotubes.[71,72] Vapor deposition-mediated template synthesis has also been proven to be an effective approach for obtaining nanotubes with controlled wall thicknesses on the scale of a few nanometers.[73-77] Several kinds of polymer nanotubes consisting of poly(pyrrole) (PPy), carboxylated PPy, and poly(aniline) (PAN) have been successfully fabricated and applied to carbon precursors, fluorescence resonance energy transfer (FRET) platforms, catalyst supports, signal transducers, molecular probes, and DNA carriers. Another well-established route to nanotubes is the so-called “tubes by fiber templates” approach. Soluble or degradable nanofibers are coated with polymer thin layers, and then selectively removed the template nanofibers, generating hollow nanotubes. As expected, the size and shape of the nanotubes strongly depended on the nanorod template. In many cases, electrospun nanofibers have been utilized as template nanofibers. A particular example is the preparation of poly(p-xylylene) (PPX) nanotubes through chemical vapor deposition of PPX onto electrospun poly(lactic acid) (PLA) nanofibers, followed by subsequent pyrolysis of the PLA nanofibers.[78] Using this approach, PPX nanotubes with inner diameters of less than 10 nm and outer diameters of ca. 50 nm could be obtained.

Recently, cylindrical micelles have turned out to be excellent soft templates for 1D nanostructure. The geometry of micelles depends on the molecular structure of surfactants such as the area of head-group, length and volume of tail-group, and kinds of counterion and solvent. From the viewpoint of external macroscopic variables, the thermodynamic conditions, such as temperature, pressure, and concentration of surfactant and additives, are also critical to the self-assembly and growth of micelles. For example, there have been a series of studies on the fabrication of conducting polymer nanotubes by cylindrical micelle templating. Sodium bis(2-ethylhexyl) sulfosuccinate (AOT) has been employed in order to generate reverse (water-in-oil) cylindrical micelles in an apolar solvent.[79-84] When an appropriate amount of ferric chloride was added into the AOT solution, spherical AOT micelles were transformed into cylindrical micelles. This transformation can be explained by the fact that the incorporation of metal salt into AOT emulsion strongly affects the micelle aggregation number as well as the second CMC. Importantly, iron cations (oxidizing agent) are concentrated in the anionic head-group of AOT due to electrostatic interactions. Therefore, when pyrrole or EDOT monomers were introduced into the AOT cylindrical micelle phase, they were chemically polymerized by iron cations along the surface of the cylindrical micelles. Thus, 1D nanostructures of poly(pyrrole) (PPy) and poly(3,4-ethylenedioxythiophene) P(EDOT) can be successfully fabricated, and the simple synthetic procedure offers a great possibility to produce 1D nanostructures in large quantities[85] as illustrated in Figure 1.14. It is also possible to control the size and shape of those nanostructures by changing synthetic variables such as the amounts of surfactant and oxidizing agent, kind of solvent, and polymerization temperature. This facile and effective approach might be expanded to allow the fabrication of various kinds of nanotubes.[85]

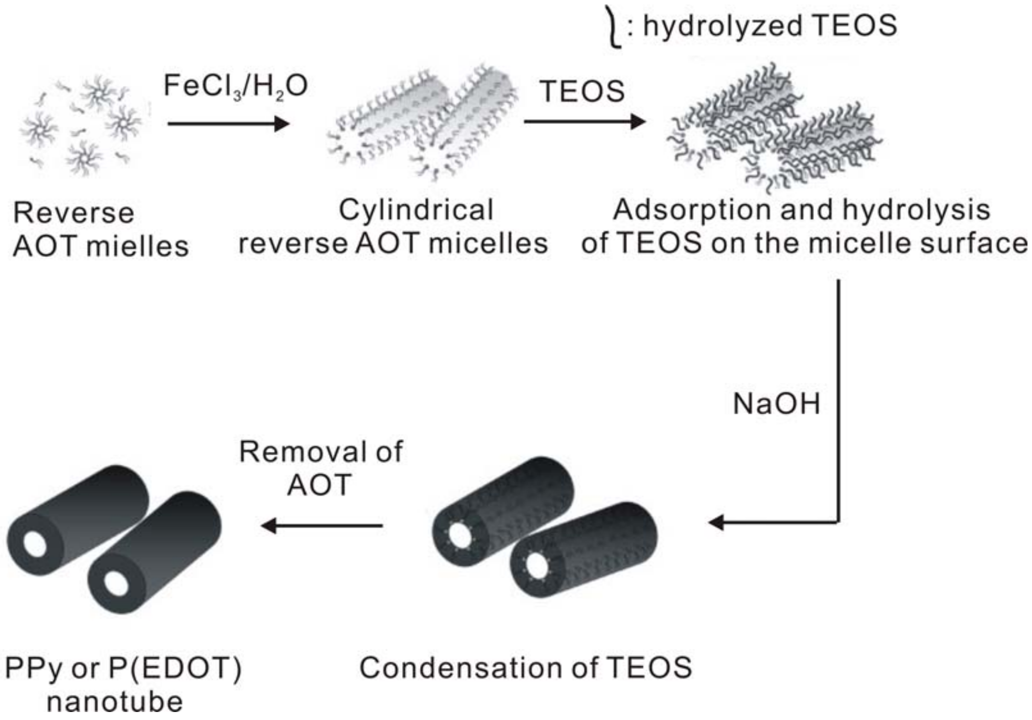

Figure 1.14 Schematic representation of the fabrication of PPy or P(EDOT) nanotubes using reverse-microemulsion sol-gel (RMSG) approach.[85]

It has been demonstrated that block copolymer self-assembly is an effective technique to generate nanotubes. The approach comprises design and synthesis of block copolymers, self-assembly of block copolymers, the interlocking of the self-assembled nanostructures, and the selective removal of the core domain. Winnik and coworkers synthesized well-defined poly(ferrocenyldimethylsilane-*b*-dimethylsiloxane) (PFS-*b*-PDMS) copolymer by living anionic ring-opening polymerization as shown in Scheme 4. The copolymer could self-assemble into tubular nanostructures in non-solvents for PFS as illustrated in TEM micrographs (Figure 1.15).[86] The PFS blocks aggregate and crystallize to make a shell with a cavity in the middle of the tube, while the PDMS blocks form the corona. The wall-thickness of the nanotubes is 7 nm and the inner diameter is approx. 8 nm, depending on kind of solvents.

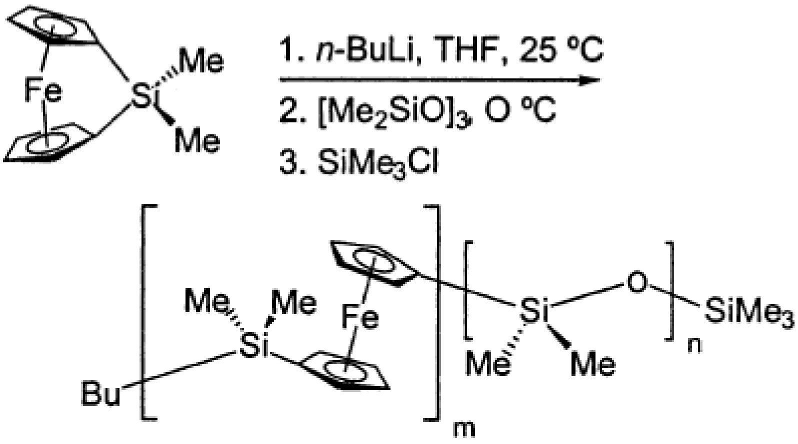

Scheme 1.4 Synthesis of PFS-*b*-PDMS copolymer by living anionic ring-opening polymerization which involves (1) the initiation of the strained silicon bridged ferrocenophane with *n*-butyllithium and the subsequent addition of hexamethyltrisiloxane. The polymerization reaction was terminated with chlorotrimethylsilane.[86]

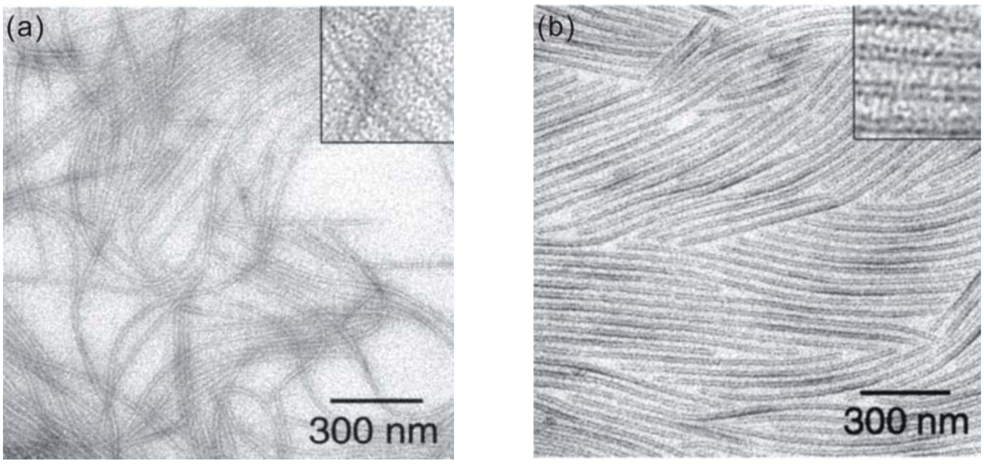

Figure 1.15 TEM micrographs of PFS-*b*-PDMS$_{480}$ assemblies prepared in (a) *n*-hexane and (b) *n*-decane at 61 °C and cooled to room temperature. The inset shows a section of the image at enhanced magnification.[86]

Liu et al. described the fabrication of nanotubes using a triblock copolymer, poly(isoprene-*b*-2-cinnamoylethylmethacrylate-*b*-tert-butylacrylate) (PI-*b*-PCEMA-*b*-PBA) (Figure 1.16).[87] This block copolymer self-assembled to cylindrical micelles with a PBA corona, a PCEMA shell and a PI core in methanol. The PCEMA shell is photocrosslinked, then ozonolysis decomposes the PI core. The PtBA corona chains rendered solvent dispersibility to the nanotubes (Figure 1.17). Tubular nanostructures were obtained after photo-crosslinking of PCEMA and degradation of PI. A series of similar works have been reported by the same group.[88-90]

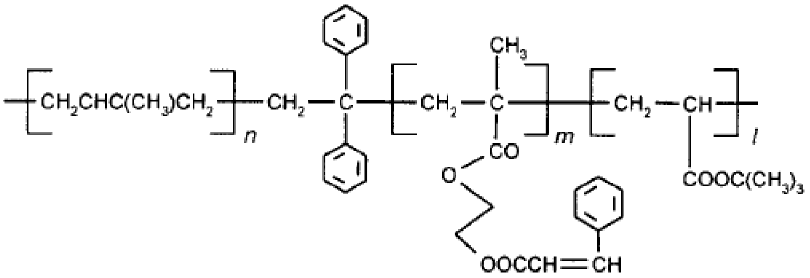

Figure 1.16 Chemical structure of triblock copolymer poly(isoprene-b-2-cinnamoylethylmethacrylate-b-tert-butylacrylate) (PI-*b*-PCEMA-*b*-PBA).[87]

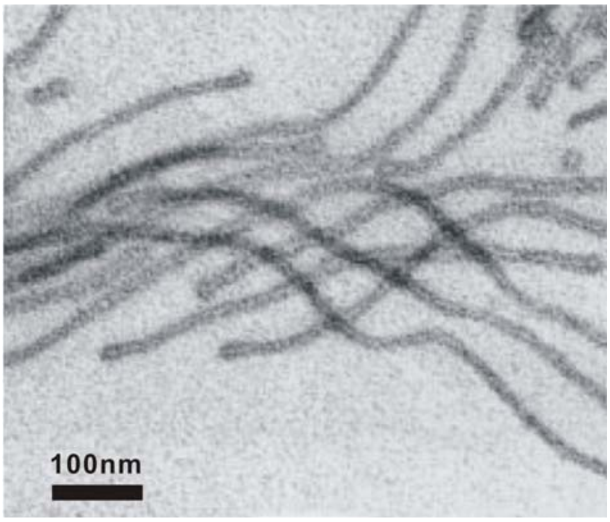

Figure 1.17 TEM image of nanotubes of poly(2-cinnamoylethyl methacrylate) (PCEMA) shell with poly(tert-butyl acrylate) (PtBA) corona.[87-90]

Another method explored by Liu's group for structure control and the use of these structures as templates to support catalytically active metal nanoparticles has been reported.[91] They focused on triblock copolymers such as poly(*t*-butyl acrylate-*b*-cinnamoylethyl methacrylate-*b*-glycerol methacrylate) (e.g. $PtBA_{107}$-*b*-$PCEMA_{193}$-*b*-$PGMA_{115}$). (Figure 1.18)

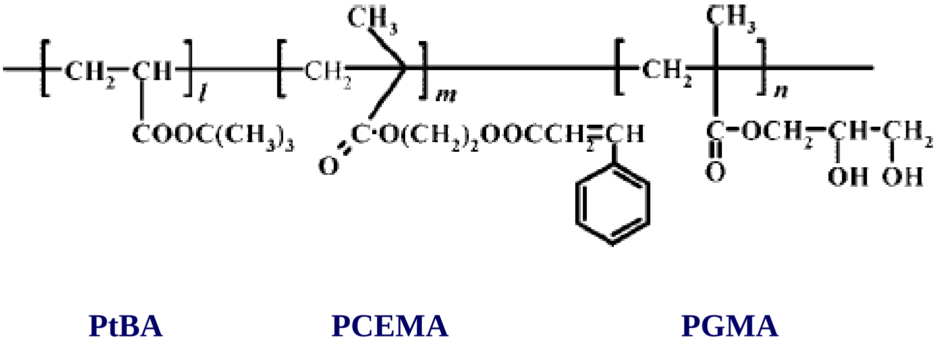

Figure 1.18 Chemical structure of triblock copolymer poly(t-butyl acrylate-*b*-cinnamoylethyl methacrylate-*b*-glycerol methacrylate).[91]

The triblock copolymer contains hydrophilic PGMA and hydrophobic PtBA. The two terminal blocks are highly incompatible. The micelle-like aggregates (MAs) were prepared in pyridine/methanol (Py/MeOH) with different MeOH volume fraction (f_{MeOH}). Here Py was a mutual solvent for all of the three blocks of the copolymer and MeOH was selective toward PtBA and PGMA. As the fraction of methanol (f_{MeOH}) increased from 80 to 90 %, the morphology of the micelle-like aggregates changed from spheres to tubular structures as illustrated in Figure 1.19a and 1.19b.

Much of their research was designed to take advantage of the photodimerization of cinnamate ester groups. Photoirradiation of cylindrical micelles containing PCEMA as an insoluble block crosslinks the core, providing robust filamentous structures for further transformation.[92,93]

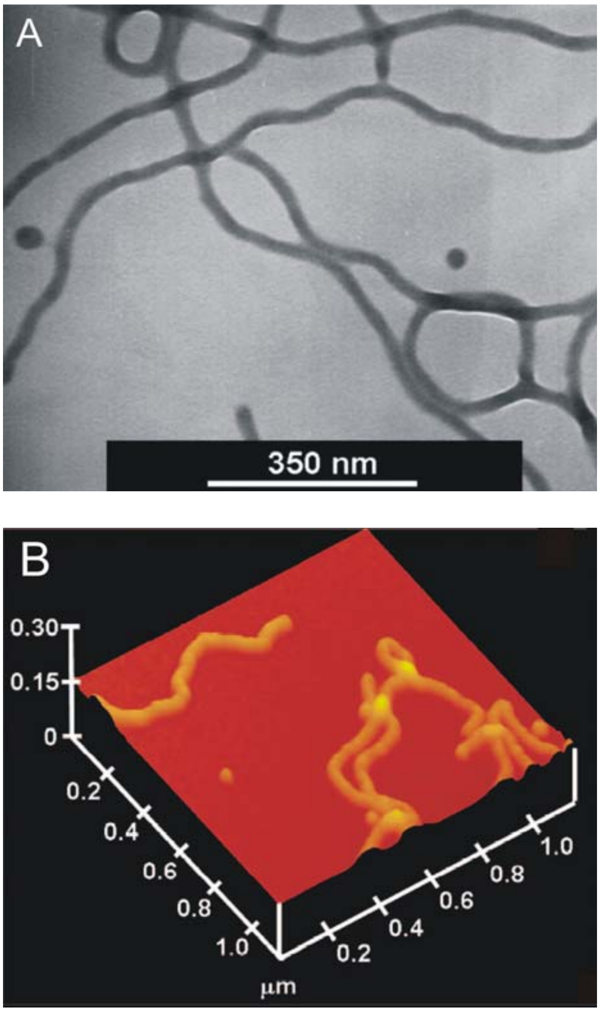

Figure 1.19 (a) TEM images of nanotubes aspirated from pyridine/methanol at methanol volume fractions 90 % The nanotube sample was stained by OsO_4 vapor. (b) 3D AFM topographic image profile of PtBA$_{107}$–PCEMA$_{193}$–PGMA$_{115}$ nanotubes.[91]

A simple self-assembly approach to obtain polymer nanotubes has also been reported by Wan and co-workers through in-situ doping polymerization method.[94-96] Typically, polyaniline (PANI) nanotubes were synthesized using ammonium persulfate (APS) in the presence of β-naphthalene sulfonic acid (NSA) as a dopant.[94] It was found that the NSA played a "template-like" role in creating the tubular nanostructures. (Figure 1.20) The size, morphology, and electrical properties of the resulting nanostructures were strongly dependent upon the kind of dopant and the reaction conditions. Similar works related to the formation of polymer nanotubes by self-assembly approach have also been achieved on the basis of crystallization of oligomers[97] and aggregation of methyl orange.[98, 99]

Figure 1.20 TEM image of self-assembled polyaniline nanotubes.[94]

Beside above mentioned examples, other synthetic efforts to fabricate polymeric nanotubes include self-assembly of smaller building blocks such as cyclic peptides, dendrons, or organic macrocycles.[100-104] In these approaches, hydrogen-bonding, π-stacking, and other interactions between small structural units lead to their organization into tubular stacks of uncontrolled lengths. Another methods of fabricating nanotubes are based on helical polymer precursors[105-107] and on cylindrical nanostructures obtained by block copolymer self-assembly.[87,88,108] These methods have been used to prepare a variety of fascinating tubular structures that continue to enrich our understanding of supramolecular organization and provide inspiration for future research in the field. However, the deficiency in length control often results in the formation of uncontrollable size, wide distribution of tubular diameter or polydisperse tubular assemblies, thus unavoidably limits the scope and potential application of polymeric nanotubes. Thus development of new building blocks, which allow us to construct new nanostructured materials via simple, robust and inexpensive approaches are highly desirable.

1.5 Self-assembly of nanofibers from amphiphilic copolymer

Amphiphilic copolymers that self-assemble in solution to form long fiber-like structures (>1 mm) with uniform diameter and widths ranged from few to tens of nanometers are referred to as wormlike micelles, fiber-like micelles, filamentous micelles or, if the micelles are relatively rigid, as rod-like micelles. This research area is part of a broader and growing interest in nanofiber formation in solution via the self-assembly of molecular building blocks. For example, some surfactants in water can form worm-like micelles that are in rapid equilibrium with their amphiphilic components.[109,110] These structures are useful rheology modifiers in applications such as enhanced oil recovery. In the surfactant case, they are referred to as 'living' micelles because they constantly break and reform, particularly when subjected to shear force.[111] In contrast, micelles prepared from the self-assembly of amphiphilic copolymers with a higher molar mass generally possess much higher stability, which can be advantageous for many applications. In the biomedical field, there is much interest in the formation of protein nanofibers from soluble protein precursors.[112] For instance, actin fibers are important for cell motion and amyloid fibers are associated with disease process.

Filamentous amphiphilic copolymer micelles are also of interest because of their growing potential applications, some well on the way to being realized. For example, filamentous block copolymer micelles have been used for drug delivery *in vitro*[110] and *in vivo*.[113] Other fiber-like block copolymer structures have shown promise as impact modifiers to reduce brittleness and suppress crack propagation in epoxy resins.[114] Filamentous nanotubes obtained through block copolymer self-assembly have been used as templates for the deposition of metal nanoparticles,[115,116] creating fascinating structures with a regular linear array of metal nanoparticles that could have important applications as catalysts. Fiber-like micelles in which the core polymer contains an Fe atom have been positioned on GaAs wafers using a lift-off process and have been converted to nanoscale ceramic features.[117]

Most synthetic polymers are amorphous, with random coil dimensions in the bulk state and swollen coil dimensions in a good solvent. Thus, most amphiphilic block copolymers can be thought of as coil–coil block copolymers. Interest in fiber-like structures for this class of polymers has been given a major boost by a report published by Bates group about giant wormlike micelles of polybutadiene–poly(ethylene oxide) (PB–PEO) diblock copolymer formed in water.[118] This polymer, PB_{45}–PEO_{55} formed fiber-like structures with a width of 7 nm and lengths >1 mm (Figure 1.21).

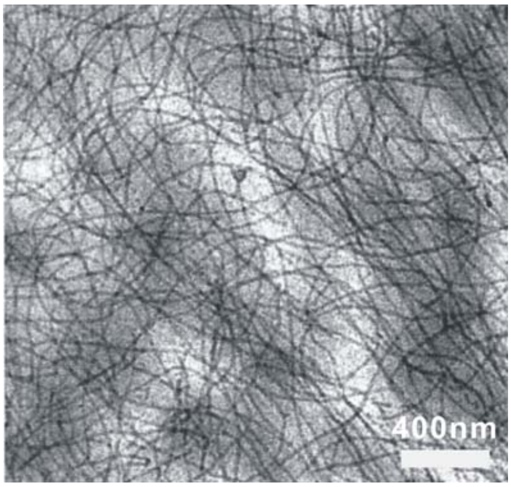

Figure 1.21 Cryo-TEM image of PB_{45}–PEO_{55} diblock copolymer formed nanofiber-like structures.[118]

Over the past several years, a considerable amount of work on potential biomedical applications of poly(acrylic acid)-(1,4)-polybutadiene (PAA_{45}-PBD_{107}) filamentous micelles in aqueous media has been published by Discher's group. They draw analogies to the shapes of filamentous viruses and argue that such long thin flexible structures will pass more easily through blood capillaries than spherical block copolymer micelles.[113] To characterize their self-assembled structures, they introduced video fluorescence microscopy to visualize individual micelles in which a highly fluorescent hydrophobic dye was dissolved.[119] (Figure 1.22)

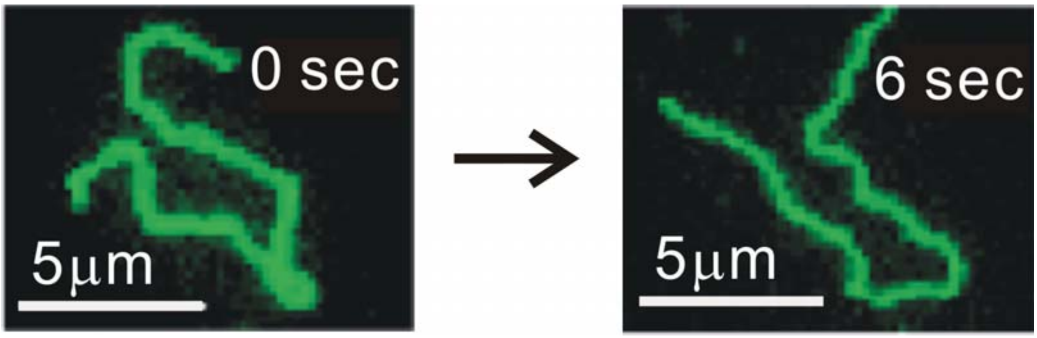

Figure 1.22 Dynamic snapshots from video of fluorescence microscopy (0-6 secs) of an amphiphilic PAA_{45}-PBD_{107} nanofiber , demonstrating flexibility of this fiber-like aggregate.[119]

Amphiphilic rod–coil block copolymer refers to a polymer in which one block has a rigid and elongated shape. This rigidity can be the result of π-conjugation along the backbone, or of secondary structure, as for helical polypeptide derivatives. The self-assembly of rod–coil block copolymers in the bulk state and in solution are well described in a recent review by Olsen and Segalman.[120] In amphiphilic copolymer thin films, various block copolymers with a rigid π-conjugated oligomer or polymer block form a microphase-separated morphology consisting of long thin fibers that are thought to arise from π-stacking of the conjugated block.

In contrast, there are very few examples of long, uniform fiber-like morphology formed by these rod-coil copolymers in solution. The typical example of such micelles is that of oligophenylenevinylene attached either to polyethylene oxide (OPV–PEO)[121] (Figure 1.23) or to poly(propylene oxide) (OPV–PPO).[122] The function of the two n-hexyl substituents on an alternating backbone of phenylene groups is to lower the melting temperature of the rigid block and enhance its solubility in organic solvents. Even so, the diblock copolymer with 45 EO units in the PEO block has limited solubility in tetrahydrofuran (THF) and rapidly self-assemble with the addition of small amounts of water in a THF solution of the polymer. Long nanofibers, with a uniform diameter on the order of 8 nm, an elliptical cross-section and lengths well over 1 mm can be generated as shown from the TEM image in Figure 1.24

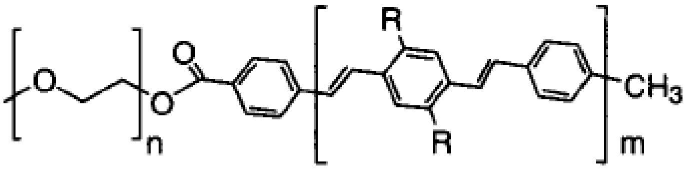

PEO OPV

where R= -C_6H_{13} n = 45 m = 6

Figure 1.23 Chemical structure of amphiphilic diblock copolymer oligophenylenevinylene-b-polyethylene oxide (OPV$_6$-PEO$_{45}$).[121]

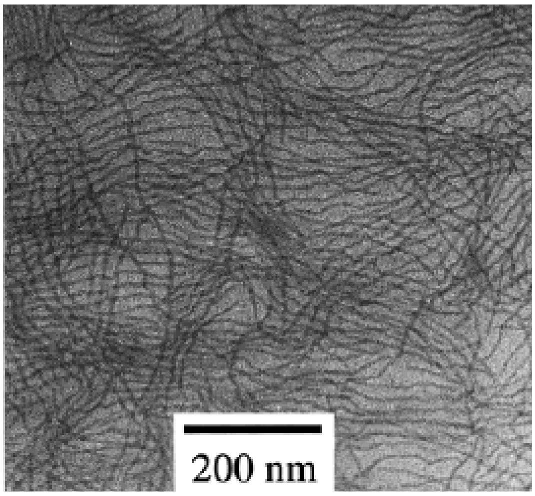

Figure 1.24 TEM image of OPV_6-PEO_{45} nanofiber in THF-water mixture.[121]

Small changes in the structure of the rod block, however, can complicate the self-assembly process. For example, an OPV–PEO block copolymer with different pendant substituents attached to the OPV block, under seemingly similar self-assembly conditions, formed elongated structures that were at most a few hundred nanometers in length.[123]

Several impressive descriptions of nanofiber formation using amphiphilic copolymer have been recently reported by Pochan and Wooley research groups. Many of these experiments involve the use of poly(acrylic acid)-poly(methyl acrylate)-polystyrene (PAA–*b*-PMA–*b*-PS) triblock copolymers, often in the presence of various concentrations of diamines.[124] (Figure 1.25) The PS block is hydrophobic. The PAA block is hydrophilic, particularly when complexed with diamines, and the PMMA block is a spacer of intermediate polarity. This combination offers many degrees of freedom with which to explore a complex self-assembly landscape. For example, when PAA_{94}–PMA_{103}–PS_{44} in THF was treated with 2,2’-(ethylenedioxy)diethylamine (EDDA, one amine per carboxylic acid group), followed by the addition of water, cylindrical fibers formed with the unique nanostructures as shown in Figure 1.26.

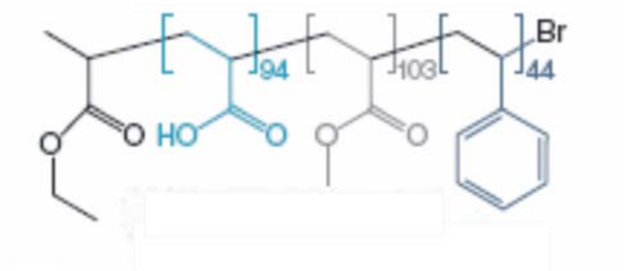

PAA_{94}-*b*-PMA_{103}-*b*-PS_{44}

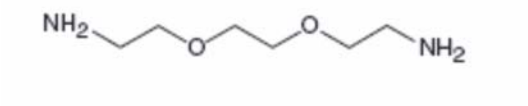

2,2'-(ethylenedioxy)diethylamine

Figure 1.25 Chemical structure of triblock copolymer PAA_{94}-b-PMA_{103}-b-PS_{44} and 2,2'-(ethylenedioxy)diethylamine.[124]

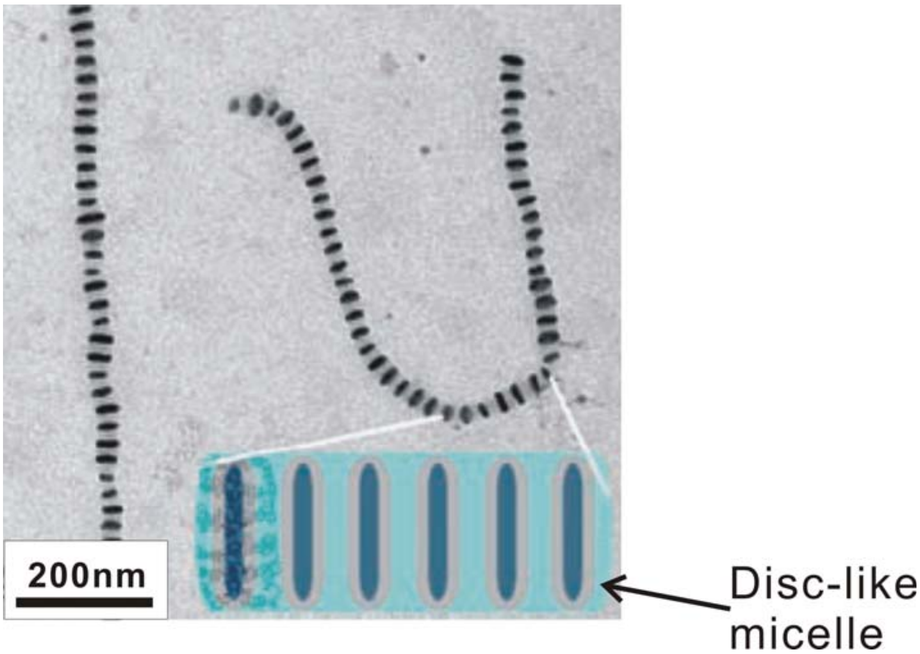

Figure 1.26 TEM image of one-dimensional assembled nanofiber structures of PAA_{94}-*b*-PMA_{103}-*b*-PS_{44} at 67% THF/water solution in the presence of 2,2'- (ethylenedioxy)diethylamine (EDDA).[124]

The periodic stripes perpendicular to the cylinder axes indicate alternating layers of hydrophilic PAA–EDDA complex and hydrophobic PMA–PS domains.[124,125] This unusual structure can be thought of being formed from face-to-face assembly of disk-like building blocks (insert of Figure 1.26). Alternatively, with triethylenetetramine in combination with PAA_{94}–PMA_{103}–PS_{88} at a much higher ratio of amine to acid group (15:1) at the same water content, single-stranded or double-stranded helical nanofibers with extremely regular superstructures were obtained (Figure 1.27).[126]

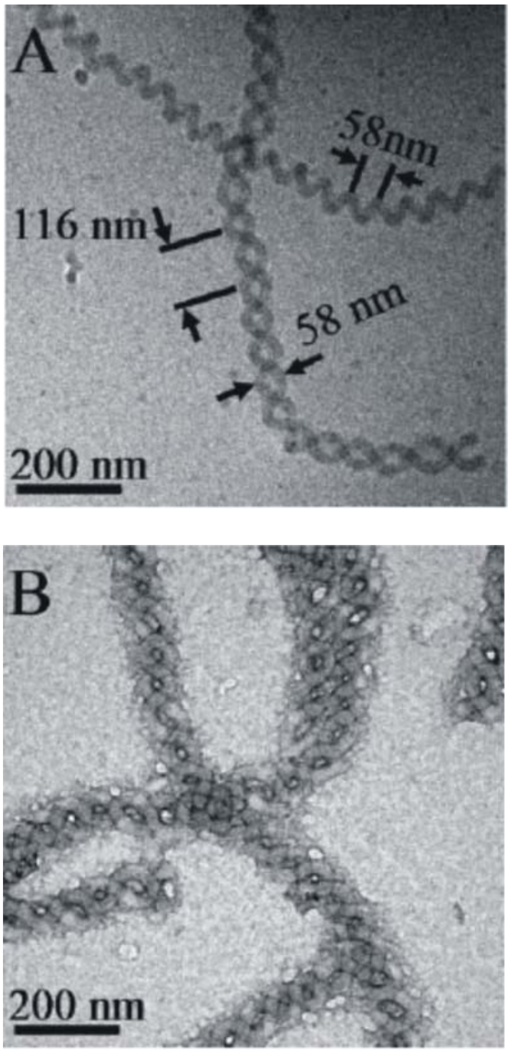

Figure 1.27 (A) Cryogenic TEM image of double-stranded and single-stranded helices. (B) Conventional TEM image nanofibers in double-stranded helices.[126]

1.6 Formation of hierarchical structures by self-assembly of amphiphilic copolymer

Hierarchical characteristics of material are ubiquitous in nature.[127-132] Materials having hierarchical structures are widely found in collagen, abalone nacre, and dendrons. The construction of materials presenting complex hierarchical structures such as those observed in natural materials are of great interest because of their promising applications in smart coatings, biosensors, and fuel cells.[133] Thus the self-assembly of soft matter is considered to be an effective approach for constructing microstructure with hierarchical order.[134-139]

Amphiphilic copolymers composed of two or more chemically different species constitute an important class of soft materials capable of self-assembling into hierarchical microstructures.[140-154] ten Brinke and co-workers reported a hierarchically ordered structure which were self-assembled from the comb-shaped supramolecules. [146-152] As indicated from molecular structure in Figure 1.28a, PS-*b*-P4VP (poly(styrene)-*block*-poly(4-vinylpyridine)) fully complexed with nonadecylphenol, we were able to resolve these mutually perpendicular lamellar structures as indicated from TEM image. (Figure 1.28b) [146,151]

The structures are comprised of two different kinds of periodicity: the large-length-scale period corresponds to the length of different blocks in the polymeric backbone, and the small-length-scale period is determined by the length of the bound low-molecular-weight compound within the comb blocks. Furthermore, the hierarchical structures with double periodicity have also been observed in linear multiblock copolymers composed of one or two end blocks that are significantly longer than the other blocks.[155-160]

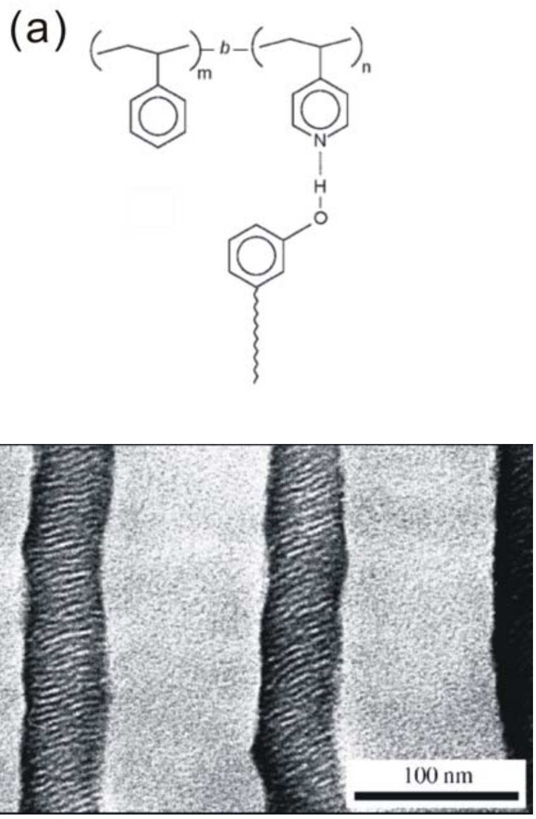

Figure 1.28 (a) Chemical structure of diblock-copolymer/amphiphile complexes poly(styrene)-*b*-poly(4-vinylpyridine) (PS-b-P4VP). One pentadecylphenol (PDP) molecule is hydrogen bonded with each pyridine group, with the molecular weights of the PS block 238,000 g mol^{-1} and the P4VP block of 49,500 g mol^{-1}.[146,151] (b)TEM images of lamellar-within-lamellar structure of poly(styrene)-*b*-poly(4-vinylpyridine) PS-b-P4VP The large-length scale periodicity of the alternating PS (light grey) and P4VP(NDP) (dark grey) lamellae equals L_b~100 nm.[151]

An amphiphilic block copolymer may self-assemble into micellar structures with shapes ranging from spheres to cylinders, vesicles, nanotubes and toroidal morphologies, etc.[161-163] Further assembly of these structures or the hierarchical assembly of amphiphilic copolymers may lead to functional "superstructures". For instance, assembly of micellar structures into 2-D superlattices on substrate surfaces has been applied as lithographic[164] or electrochemical masks[165] for production of inorganic nanoparticle arrays with potential applications as memory devices in nanoelectronics. Although hierarchical assembly allows molecular order and structural control at two or three dimensional scales,[138,166] solution based assembly process is scarcely explored.[167,168] Liu and his coworkers introduced the hierarchical interfacial assembly of amphiphilic triblock copolymer (Figure 1.29) into superstructures with different surface morphologies.[169] Figure 1.29a and 1.30a shows the building blocks of cylindrical morphology in straight, branched or looped pattern and the spherical micellar aggregates coexisted with some short cylinders. The TEM diameters of the cylindrical micellar and spherical micellar aggregates are 20.4 ± 0.8 nm and 21.9 ± 1.7 nm, respectively.

TEM images (Figure 1.30 and 1.31) show the superaggregates formed in 5 min after addition of MeOH into the cylindrical micelles (CMs) and spherical micelle (SMs) solutions at 52 ± 2 °C and 22 ± 2 °C, respectively. The original individual CMs and SMs have assembled in some cases into bowl-shaped superaggregates (marked by arrows in Figures 1.30b and 1.31b). While the 2-D projections of many particles in Figure 1.31b are still circular, the average diameter of the circles increases from 21.9 ± 1.7 nm in Figure 1.31a to 36.0 ± 6.1 nm in Figure 1.30b, suggesting the flattening or fusion of the SMs. The fusion of the CMs is evident in Figure 1.30b, where no individual cylinders but cylinder ladders and networks are seen. The CMs probably also flattened because the TEM width in Figure 1.30b is 33.9 ± 5.6 nm rather than 20.4 ± 0.8 nm as in Figure 1.30a. The assembled cross-linked CMs had a width of 27.0 ± 2.6 nm rather than 20.4 ± 0.8 nm. Figure 1.30c and 1.30d show TEM images of the spherical superaggregates (SSAs) formed at 52 ± 2 °C from CMs 3 days after MeOH addition and Figure 1.31c shows TEM images of SSAs of SMs 2 days after MeOH addition at 22 ± 2

°C. These structures were unchanged up to the longest observation time of 7 days. At 52 ± 2 °C, the SSAs were ribbon cages, while they were flower-like at 22 ± 2 °C in which some SMs had fused into ribbons surrounding deformed "balls", resulting in a "ball in socket" surface morphology. These hierarchical structures are hundreds of nanometers in size or larger, are formed via micellar-like structures adsorption and fusion on surfaces of droplets.[169]

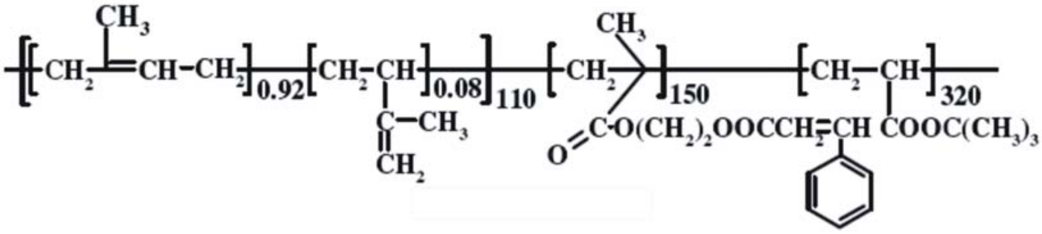

Figure 1.29 Chemical structure of triblock copolymer (polyisoprene-*block*-poly(2-cinnamoyloxyethyl methacrylate)-*block*-poly(*tert*-butyl acrylate) or PI-*b*-PCEMA-*b*-PtBA.[169]

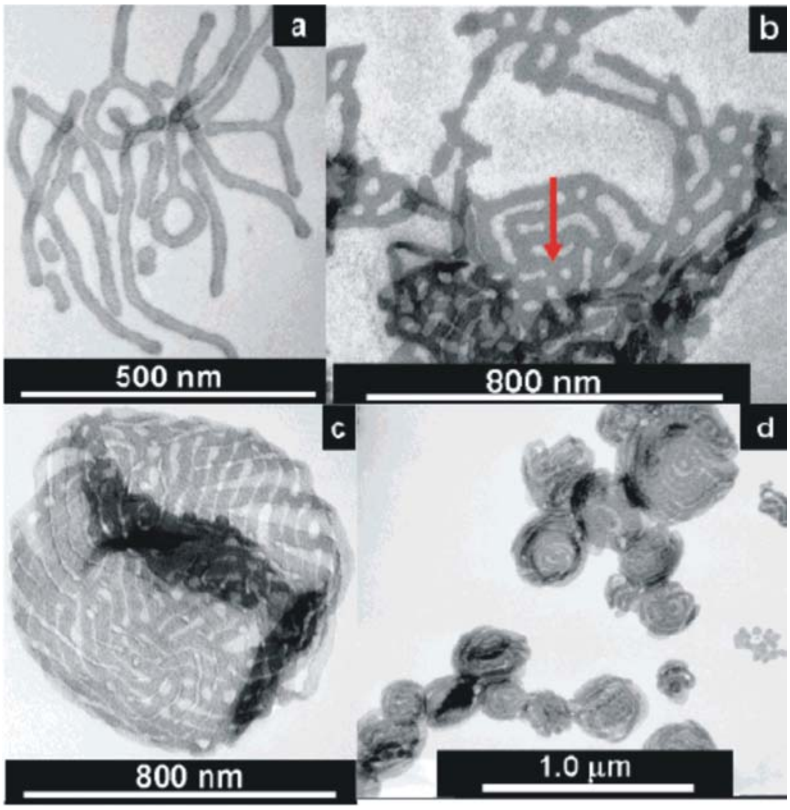

Figure 1.30 Bright-field TEM images of (a) fiber-like micellar structures; (b) micellar aggregates after 5 min.; (c) and (d) hierarchical structures formed after 3 days.[169]

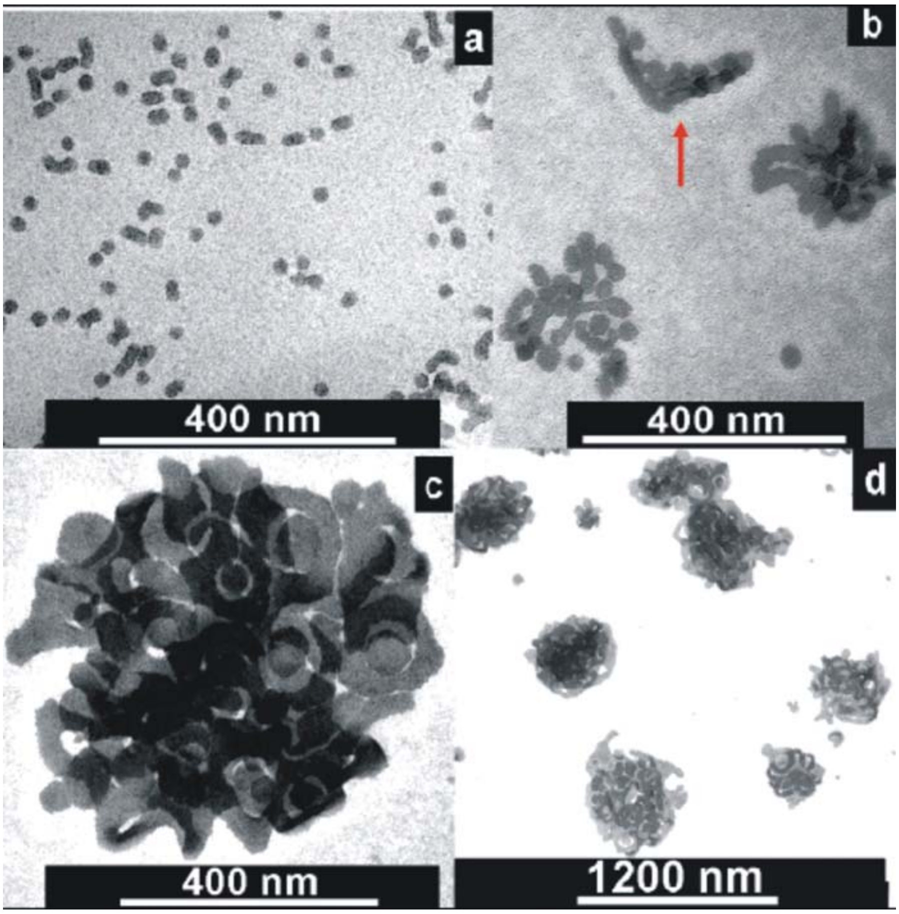

Figure 1.31 TEM images of (a) spherical-like micellar structures; (b) micellar aggregates after 5 min.; (c) and (d) hierarchical structures formed after 2 days.[169]

1.7 Amphiphilic core-shell nanoparticles

Over the last decade, there have been considerable efforts to fabricate core-shell nanoparticles with electrical, optical, magnetic, and catalytic functions.[170,171] Owing to their advantageous characteristics over single-component nanoparticles, extensive investigations have been made into the state-of-the-art applications of core-shell nanoparticles.[172-174] Compared with nanocomposites or copolymer nanoparticles, core-shell nanoparticles have beneficial properties originating from the well-defined compartments of two distinct polymer phases as illustrated in Figure 1.32.

They are also of interest from a fundamental and academic point of view, especially in the area of colloid and interface science.

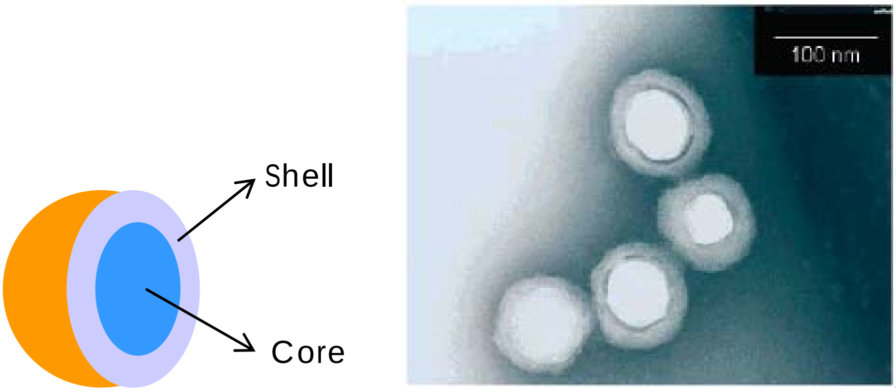

Figure 1.32 Illustration of typical core-shell nanoparticles and TEM image of PEI/PMMA core-shell nanoparticles.[195]

The amphiphilic core-shell particles can be prepared according to four general approaches: (1) stepwise deposition of polyelectrolytes onto charged particle surfaces;[175-178] (2) self-assembly of amphiphilic block copolymers by covalent cross-linking of the shells to form shell-cross-linked "knedle" (SCK) micelles;[179-184] (3) graft copolymerization of hydrophilic monomers onto reactive seeded particles;[185-189] (4) free radical copolymerization of hydrophilic macromonomers with hydrophobic monomers.[190-194] (5) Emulsion polymerization in the presence of block or comb-like copolymer containing controlled free-radical moiety.[195] Despite the success of these approaches, there are still some drawbacks, such as time consuming sequential polyelectrolyte deposition cycles and purification steps, tedious multiple-step syntheses, and the use of hydrophilic monomers, resulting in low surface incorporation and the formation of a large amount of water soluble homopolymers. In addition, most of these methods can only be carried out under very dilute conditions, which are not commercially viable. Recently, Li *et al.* describe a novel and efficient method to prepare well-defined amphiphilic core-shell nanospheres in the absence of surfactant via the direct graft copolymerization of vinyl monomers from water-soluble polymers containing amino groups.[196] Scheme 1.5 illustrates the synthetic approach which involves reactions between alkyl hydroperoxides and the amino groups of the water soluble polymer in water in the presence of dispersed hydrophobic monomer. Amphiphilic graft copolymers and hydrophobic homopolymers are generated concurrently to form highly monodispersed particles with amphiphilic core-shell nanostructures.

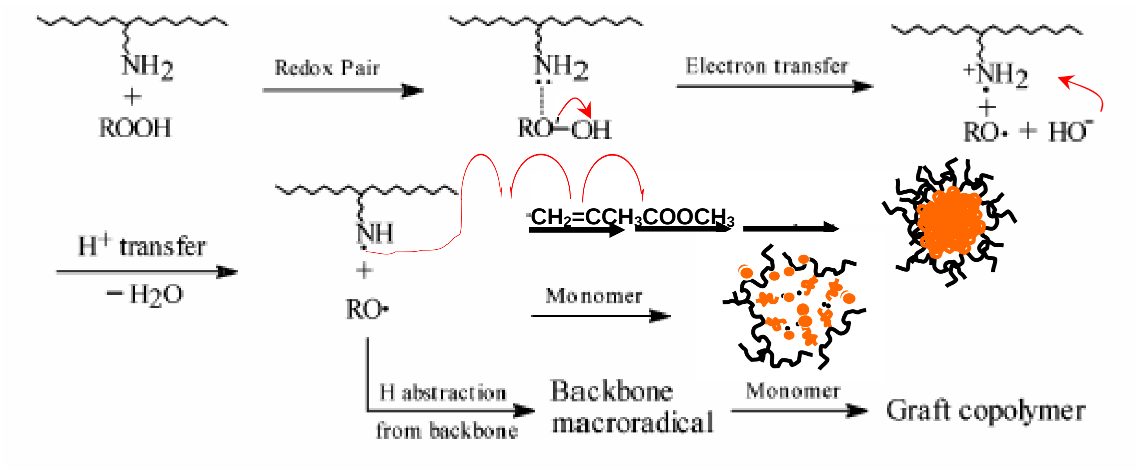

Scheme 1.5 Mechanism for the Graft Copolymerization of MMA from Water-Soluble Polymers Containing Amino Groups (Polyethyleneimine).[196]

1.8 Amphiphilic hollow particles

Hollow particles have attracted great interest due to their potential applications as sensors, catalyst carriers, nanoreactors, and delivery vessels;[197-201] broader applications can be envisioned if hollow nanostructures could be prepared with tailored composition and morphology. The various hollow particles and their self-assembled structures employed by nature, such as lipid vesicles and gated ionic channels, clearly demonstrate the potentials of such controls. Synthetic hollow particles have been realized only in a few systems. Vesicles and nanotubes were prepared by self-assembly of amphiphiles such as block copolymers[202] and lipid-like small molecules.[203-205] However, these nanostructures are largely dictated by the chemical nature of the constituent amphiphilic molecules and cannot be readily tailored. Alternative class of hollow particle is derived from core-shell nanoparticles (NPs), through removing the core component such as inorganic or metallic core.[206-210] The size and shape of the resulting hollow particles can be readily controlled by the choice of the initial core.[211,212] However, the overall shells are generally isotropic and lack of flexibility. In order to fabricate hollow particle with anisotropic nature for self-assembly, both core and shell materials should be maintained in integrity. Thus, the exploitation of a benign treatment method for the removal of the core is indispensable for fabricating stable and flexible hollow particles for further self-assembled process.

1.9 Our previous work on the self-assembly of amphiphilic hollow particles

Despite significant progress in the pursuit of strategies for self-assembly of copolymers, a diversity of new types of polymer building blocks which allow for the rational design of desired materials is still very much needed, especially those copolymers which are easy to synthesize, are inexpensive and can be produced on a large scale. We have previously reported the use of inexpensive amphiphilic hollow particles as a building block to generate various supramolecular assemblies via the controlled aggregation and coalescence of the hollow particles in a dichloromethane-water mixture.[213] The hollow particles, that consist of hydrophilic backbone with hydrophobic grafts, were prepared by extracting out a portion of the core from poly(methyl methacrylate)-poly(ethyleneimine) (PMMA-PEI) core-shell nanoparticles.

The preliminary discovery of nanotubes such as linear and worm-like nanotubes as shown in Figure 1.33 prompted us to carry out an in-depth investigation of various experimental conditions that influence nanotubular formation. The PMMA homopolymer inside the PMMA/PEI particles is first removed through solvent extraction. The resulting PEI-*g*-PMMA hollow particles are then treated under appropriate conditions in a water/DCM mixture, fiber and rod-like structures that were microns in length can be produced in high yield. The diameters of the nanotubes are ranged from 60 to 100 nm, and their wall thickness is approximately 10 nm (Figure 1.33a and 1.33b). In this case, the diameter of the nanotube is approximately 50 nm, while it is microns in length.

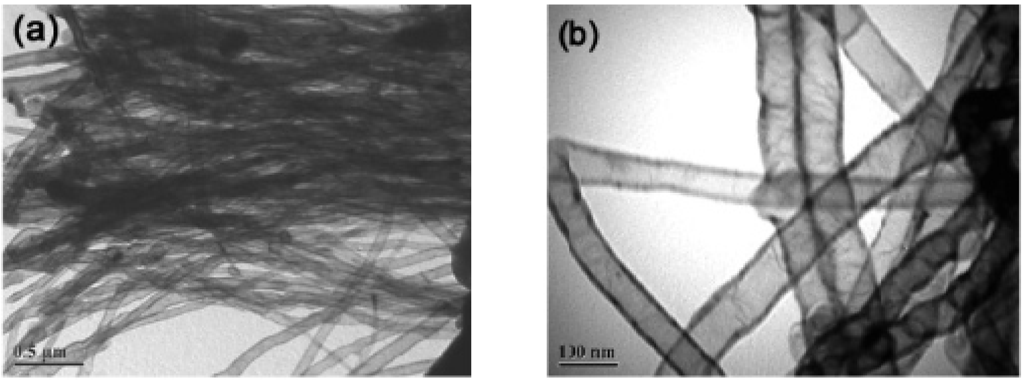

Figure 1.33 TEM images of nanotubes fabricated from PEI-*g*-PMMA hollow particles.[213]

1.10 Thesis overview

The remainder of this thesis consists of five additional chapters. Chapter 2 presents the general concepts of instrumental techniques used in this thesis. The techniques reviewed include Fourier transform infrared spectroscopy (FTIR), field-emission scanning electron microscopy (FE-SEM), transmission electron microscopy (TEM), atomic force microscopy (AFM), x-ray photoelectron spectroscopy (XPS), zeta-sizer and UV-vis spectrophotometer for turbidity measurement. Chapter 3 demonstrates the nanotubes were produced by stirring induced elongation and curvature-dependent assembly of elongated copolymer hollow particles in solution of dichloromethane-water mixture. Chapter 3 also shows that the anisotropic nature of hollow particles is crucial in controlling the orientation and alignment of elongated hollow particles. Chapter 4 extends the work presented in Chapter 3 to investigate the effect of solvent composition (DCM/water volume ratio) in the morphological transition from spheres to long nanotubes. Chapter 5 investigates the temperature effect on the particle size and morphology. Transmission electron microscopic results reveal a temperature-dependent transition from loosely packed to highly packed hollow particles in terms of size (diameter). The hydrophobic interaction between PMMA grafts in the particle cavity region is significantly enhanced as temperature in the solution increased. In chapter 6, we use preformed nanotubes as building blocks to study the effect of solution pH on the morphologies of the assembled hierarchical structures. Finally, Chapter 7 discusses possible future research work we may have using these facile approaches to fabricate other novel supramolecular structures.

References

1. Halperin, A.; Tirrell, M.; Lodge, T. P. *Adv. Polym. Sci.* **1992**, *100*, 31.

2. Prochazka, K.; Martin, T. J.; Munk, P.; Webber, S. E. *Macromolecules* **1996**, *29*, 6518.

3. Stupp, S. I.; LeBonheur, V.; Walker, K.; Li, L. S.; Huggins, K. E.; Keser, M.; Amstutz, A. *Science* **1997**, *276*, 384.

4. Shen, H.; Eisenberg, A. *Macromolecules* **2000**, *33*, 2561.

5. Discher, D. E.; Eisenberg, A. *Science* **2002**, *297*, 967.

6. Yan, X.; Liu, G.; Li, Z. *J. Am. Chem. Soc.* **2004**, *126*, 10059.

7. Jain, S.; Bates, F. S. *Science* **2003**, *300*, 460.

8. Cornelissen, J. J. L. M.; Fischer, M.; Sommerdijk, N. A. J. M.; Nolte, R. J. M. *Science* **1998**, *280*, 1427.

9. Lodge, T. P.; Hillmyer, M. A.; Zhou, Z.; Talmon, Y. *Macromolecules* **2004**, *37*, 6680.

10. Bates, F. S. *Science* **1991**, *251*, 898.

11. Bellomo, E. G.; Wyrsta, M. D.; Pakstis, L.; Pochan, D. J.; Deming, T. J. *Nat. Mater.* **2004**, *3*, 244.

12. Thordarson, P.; Coumans, R. G. E.; Elemans, J. A. A. W.; Thomassen, P. J.; Visser, J.; Rowan, A. E.; Nolte, R. J. M. *Angew. Chem., Int. Ed.* **2004**, *43*, 4755.

13. Vriezema, D. M.; Kros, A.; de Gelder, R.; Cornelissen, J. J. L. M.; Rowan, A. E.; Nolte, R. J. M. *Macromolecules* **2004**, *37*, 4736.

14. Ahmed, F.; Discher, D. E. *J. Controlled Release* **2004**, *96*, 37.

15. Pan, D.; Turner, J. L.; Wooley, K. L. *Chem. Commun.* **2003**, *19*, 2400.

16. Rösler, A.; Vandermeulen, G. W. M.; Klok, H.-A. *Adv. Drug Delivery Rev.* **2001**, *53*, 95.

17. Torchilin, V. P. *J. Controlled Release* **2001**, *73*, 137.

18. Adams, M. L.; Lavasanifar, A.; Kwon, G. S. *J. Pharm. Sci.* **2003**, *92*, 1343.

19. Seregina, M. V.; Bronstein, L. M.; Platonova, O. A.; Chernyshov, D. M.; Valetsky, P. M.; Hartmann, J.; Wenz, E.; Antonietti, M. *Chem. Mater.* **1997**, *9*, 923.

20. Bronstein, L. M.; Chernyshov, D. M.; Valetsky, P. M. *Langmuir* **1999**, *15*, 83.

21. Bronstein, L. M.; Sidorov, S. N.; Valetsky, P. M.; Hartmann, J.; Cölfen, H.; Antonietti, M. **1999**, *15*, 6256.

22. Antonietti, M.; Wenz, E.; Bronstein, L. M.; Seregina, M. V. *Adv. Mater.* **1995,** *7*, 1000.

23. Persigehl, P.; Jordan, R.; Nuyken, O. *Macromolecules* **2000**, *33*, 6977.

24. Nuyken, O.; Weberskirch, R.; Bortenschlager, M.; Schönfelder, D. *Macromol. Symp.* **2004**, *215*, 215.

25. Svensson, M.; Joabsson, F.; Linse, P.; Tjerneld, F. *J. Chromatogr. A* **1997**, *761*, 91.

26. Tani, H.; Matsuda, A.; Kamidate, T.; Watanabe, H. *Anal. Sci.* **1997**, *13*, 925.

27. Svensson, M.; Berggren, K.; Veide, A.; Tjerneld, F. *J. Chromatogr. A* **1999**, *839*, 71.

28. Hartgerink, J. D.; Beniash, E.; Stupp, S. I. *Science* **2001**, *294*, 1684.

29. Li, M.; Cölfen, H.; Mann, S. *J. Mater. Chem.* **2004**, *14*, 2269.

30. Won, J.; Park, H. H.; Kim, Y. J.; Choi, S. W.; Ha, H. Y.; Oh, I. H.; Kim, H. S.; Kang, K. S.; Ihn, K. J. *Macromolecules* **2003**, *36*, 3228.

31. Deng, T.; Ha, Y. H.; Cheng, J. Y.; Ross, C. A.; Thomas, E. L. *Langmuir* **2002**, *18*, 6719.

32. Li, L.; Beniash, E.; Zubarev, E. R.; Xiang, W.; Rabatic, B. M.; Zhang, G.; Stupp, S. I. *Nat. Mater.* **2003**, *2*, 689.

33. Discher, B. M.; Won, Y. Y.; Ege, D. S.; Lee, J. C. M.; Bates, F. S.; Discher, D. E.; Hammer, D. A. *Science* **1999**, *284***,** 1143.

34. Discher, B. M.; Bermudez, H.; Hammer, D. A.; Discher, D. E.; Won, Y. Y.; Bates, F. S. *J. Phys. Chem. B.* **2002**, *106*, 2848.

35. Yu, G.; Eisenberg, A. *Macromolecules* **1998**, *31*, 5546.

36. Zhou, Z.; Li, Z.; Ren, Y.; Hillmyer, M. A.; Lodge, T. P. *J. Am. Chem. Soc.* **2003**, *125*, 10182.

37. Pochan, D. J.; Chen, Z.; Cui, H.; Hales, K.; Qi, K.; Wooley, K. L. *Science* **2004**, *306*, 94.

38. Jain, S.; Bates, F. S. *Macromolecules* **2004**, *37*, 1511.

39. Tuzar, Z.; Kratochvil, P. In *Surface and Colloid Science*, Plenum Press: New York. **1993**; Vol. 15, pp 1-83.

40. Riess, G. *Prog. Polym. Sci.* **2003**, 28, 1107–1170.

41. Cai, Y. L.; Tang, Y. Q.; Armes, S. P. *Macromolecules* **2004**, *37*, 9728–9737.

42. Forster, S.; Plantenberg, T. *Angew. Chem., Int. Ed.* **2002**, *41*, 688–714.

43. Yamada, K.; Miyazaki, M.; Minoda, M. *Macromolecules* **1999**, *32*, 290.

44. Zhang, D.; Macias, C.; Ortiz, C. *Macromolecules* **2005**, *38*, 2530.

45. Hong, S.C.; Jia, S.;Teodorescu,M.;Kowalewski, T.;Matyjaszewski, K.; Gottfried, A. C.; Brookhart, M. *J. Polym. Sci., Polym. Chem*. **2002**, *40*, 2736.

46. Deffieux, A.; Schappacher, M. *Macromolecules* **1999**, *32*, 1797.

47. Matyjaszewski, K.; Xia, J. *Chem. Rev.* **2001**, *101*, 2921.

48. Wang, J; Matyjaszewski, K. *J. Am. Chem. Soc.* **1995**, *117*, 5614.

49. Zhang, M; Breiner, T; Mori, H; Müller, A.H. E. *Polymer* **2003**, *44*, 1449.

50. Cheng, G; Boker, A; Zhang, M; Krausch, G; Müller, A.H.E. *Macromolecules* **2001**, *34*, 6883.

51. Peng, D.; Zhang, X.H.; Feng, C.; Lu, G.L.; Zhang, S.; Huang, X.Y. *Polymer* **2007,** *48*, 5250.

52. Wang, C.; Li, G.; Guo, R. *Chem. Commun.*, **2005,** 3591.

53. Kim, K. H.; Huh, J.; Jo, W. H. *Macromolecules*, **2004**, *37*, 676.

54. Zhang, X.; Shen, Z.; Feng, C.; Yang, D.; Li, Y.; Hu, J.; Lu, G.; Huang, X. *Macromolecules* **2009**, *42*, 4249.

55. Li, Y.; Zhang, Y.; Yang, D.; Li, Y.; Hu, J.; Feng, C.; Zhai, S.; Lu, G.; Huang, X. *Macromolecules* **2010**, *43*, 262.

56. Schappacher, M.; Deffieux, A. *Science* **2008**, *319*, 1512.

57. Bong, D. T.; Clark, T. D.; Granja, J. R.; Ghadiri, M. R. *Angew. Chem. Int. Ed.* **2001**, *40*, 988.

58. Block, M. A. B.; Hecht, S. *Angew. Chem. Int. Ed.* **2005**, *44*, 6986.

59. Block, M. A. B.; Kaiser, C.; Khan, A.; Hecht, S. Discrete organic nanotubes based on a combination of covalent and non-covalent approaches. In *Functional Molecular Nanostructures*; Springer-Verlag Berlin: Berlin, **2005**; Vol. 245, pp 89-150.

60. Sapp, S. A.; Mitchell, D. T.; Martin, C. R. Chem. Mater. **1999**, *11*, 1183.

61. Lahav, M.; Weiss, E. A.; Xu, Q; Whitesides, G. M. *Nano Lett.* **2006**, *6*, 2166.

62. Park, S.; Lim, J. H.; Chung, S. W.; Mirkin, C. *Science* **2004**, *303*, 348.

63. Martin, C. R. *Chem. Mater.* **1996**, *8*, 1739.

64. Steinhart, M.; Wehrspohn, R. B.; Gösele, U.; Wendorff, J. H. *Angew. Chem. Int. Ed*. **2004**, *43*, 1334.

65. Steinhart, M.; Wendorff, J. H.; Greiner, A.; Wehrspohn, R. B.; Nielsch, K.; Schilling, J.; Choi, J.; Gösele, U. *Science* **2002**, *296*, 1997.

66. Menon, V. P.; Lei, J. ; Martin, C. R. *Chem. Mater.* **1996**, *8*, 2382.

67. Han, M. G.; Foulger, S. H. *Chem. Commun.*, **2005**, 3092.

68. Xiao, R.; Cho, S. I.; Liu, R.; Lee, S. B. *J. Am. Chem. Soc.* **2007**, *129*, 4483.

69. Fu, M.; Zhu,Y.; Tan, R.; Shi, G. *Adv. Mater.* **2001**, *13*, 1874.

70. Demoustier-Champagne, S.; Stavaux, P. Y. *Chem. Mater.* **1999**, *11*, 829.

71. Liang, Z.; Susha, A. S.; Yu, A.; Caruso, F. *Adv. Mater.* **2003**, *15*, 1849.

72. Ai, S.; Lu,G.; He, Q.; Li, J. *J. Am. Chem. Soc.* **2003**, *125*, 11140.

73. Ko, S.; Jang, J. *Biomacromolecules* **2007**, *8*, 182.

74. Lee, K. J.; Oh, J. H.; Kim, Y.; Jang, J. *Chem. Mater.* **2006**, *18*, 5002.

75. Ko, S.; Jang, J. *Angew. Chem. Int. Ed.* **2006**, *118*, 7726.

76. Jang, J.; Ko, S.; Kim, Y. *Adv. Funct. Mater.* **2006**, *16*, 754.

77. Jang, J.; Oh, J. H. *Chem. Commun.* **2004**, 882.

78. Hou, H.; Jun, Z.; Reuning, A.; Schaper, A.; Wendorff, J. H.; Greiner, A. *Macromolecules* **2002**, *35*, 2429.

79. Jang, J.; Yoon, H. *Langmuir* **2005**, *21*, 11484.

80. Jang, J.; Yoon, H. *Chem. Commun.* **2003**, 720.

81. Yoon, H.; Chang, M.; Jang, J. *J. Phys. Chem. B* **2006**, *110*, 14074.

82. Jang, J.; Yoon, H. *Adv. Mater.* **2003**, *15*, 2088.

83. Yoon, H.; Chang, M.; Jang, J. *Adv. Funct. Mater.* **2007**, *17*, 431.

84. Yoon, H.; Hong, J. Y.; Jang, J. *Small* **2007**, *3*, 1774.

85. Jang, J.; Yoon, H. *Adv. Mater.* **2004**, *16*, 799.

86. Raez, J.; Manners, I.; Winnik, M. A. *J. Am. Chem. Soc.* **2002**, *124*, 10381.

87. Stewart, S.; G. Liu, G. *Angew. Chem. Int. Ed.* **2000**, *39*, 340.

88. Yan, X.; Liu, G.; Li, Z. *J. Am. Chem. Soc.* **2004**, *126*, 10059.

89. Li , Z.; Liu, G. *Langmuir* **2003**, *19*, 10480.

90. Yan, X.; Liu, F.; Li, Z.; Liu, G. *Macromolecules* **2001**, *34*, 9112.

91. Njikang, G.; Han, D.; Wang, J.; Liu, G. *Macromolecules* **2008**, *41*, 9727.

92. Stewart, S.; Liu, G. *Angew. Chem., Int. Ed.* **2000**, *39*, 340.

93. Yan, X. H.; Liu, G.; Li, Z. *J. Am. Chem. Soc.* **2004**, *126*, 10059.

94. Wei, Z.; Zhang, Z.; Wan, M. *Langmuir* **2002**, *18*, 917.

95. Zhang, Z.; Wei, Z.; Wan, M. *Macromolecules* **2002**, *35*, 5937.

96. Huang, K.; Wan, M. *Chem. Mater.* **2002**, *14*, 3486.

97. Stejskal, J.; Sapurina, I.; Trchová, M.; Konyushenko, E. N.; Holler, P. *Polymer* **2006**, *47*, 8253.

98. Yang, X.; Dai, T.; Zhu, Z.; Lu, Y. *Polymer* **2007**, *48*, 4021.

99. Yang, X.; Zhu, Z.; Dai, T.; Lu, Y. *Macromol. Rapid Commun.* **2005**, *26*, 1736.

100. Ghadiri, M. R. *Biopolymers* **2003**, *71*, 284.

101. Percec, V.; Dulcey, A. E.; Balagurusamy, V. S. K.; Miura, Y.; Smidrkal, J.; Peterca, M.; Nummelin, S.; Edlund, U.; Hudson, S. D.; Heiney, P. A.; Hu, D. A.; Magonov, S. N.; Vinogradov, S. A. *Nature (London)* **2004**, *430*, 764.

102. Percec, V.; Dulcey, A. E.; Peterca, M.; Ilies, M.; Nummelin, S.; Sienkowska, M. J.; Heiney, P. A. *Proc. Natl. Acad. Sci. U.S.A.* **2006**, *103*, 2518.

103. Zhao, D. H.; Moore, J. S. *Chem. Commun.* **2003**, 807.

104. He, L.; An, Y.; Yuan, L. H.; Feng, W.; Li, M. F.; Zhang, D. C.; Yamato, K.; Zheng, C.; Zeng, X. C.; Gong, B. *Proc. Natl. Acad. Sci. U.S.A.* **2006**, *103*, 10850.

105. Ray, C. R.; Moore, J. S. Supramolecular organization of foldable phenylene ethynylene oligomers. In *Poly(Arylene Ethynylene)S: from Synthesis to Application*; Springer-Verlag Berlin: Berlin, **2005**; Vol. 177, pp 91-149.

106. Hecht, S.; Khan, A. *Angew. Chem., Int. Ed.* **2003**, *42*, 6021–6024.

107. Gong, B. *Chem.- Eur. J.* **2001**, *7*, 4336–4342.

108. Ho, R. M.; Chen, C. K.; Chiang, Y. W.; Ko, B. T.; Lin, C. C. *Adv. Mater.* **2006**, *18*, 2355.

109. Lee, C.C.; Grenier, C.; Meijer, E. W.; Schenning, A. *Chem. Soc. Rev.* **2009**, *38*, 671.

110. Dalhaimer, P.; Engler, A. J.; Parthasarathy, R.; Discher, D. E. *Biomacromolecules* **2004**, *5*, 1714.

111. Dreiss, C. A. *Soft Matter* **2007**, *3*, 956.

112. Dobson, C. M. *Nature* **2003**, *426*, 884.

113. Geng, Y.; Dalhaimer, P.; Cai, S.; Tsai, R.; Tewari, M.; Minko, T.; Discher, D. E. *Nat. Nanotechnol.* **2007**, *2*, 249.

114. Dean, J. M.; Verghese, N. E.; Pham, H. Q.; Bates, F. S. *Macromolecules* **2003**, *36*, 9267.

115. Yan, X. H.; Liu, G.; Haeussler, M.; Tang, B. Z. *Chem. Mater.* **2005**, *17*, 6053.

116. Wang, H.; Wang, X. S.; Winnik, M. A.; Manners, I. *J. Am. Chem. Soc.* **2008**, *130*, 12921.

117. Cao, L.; Massey, J. A.; Winnik, M. A.; Manners, I.; Riethmüller, S.; Banhart, F.; Spatz, J. P.; Möller, M. *Adv. Funct. Mater.* **2003**, *13*, 271.

118. Won, Y. Y.; Davis, H. T.; Bates, F. S. *Science* **1999***, 283*, 960.

119. Geng, Y.; Ahmed, F.; Bhasin, N.; Discher, D. E. *J. Phys. Chem. B* **2005,** *109,* 3772.

120. Olsen, B. D.; Segalman, R. A. *Mater. Sci. Eng. R* **2008**, *62*, 37.

121. Wang, H.B.; Wang, H. H.; Urban, V. S.; Littrell, K. C.; Thiyagarajan, P.; Yu, L. *J. Am. Chem. Soc.* **2000**, *122*, 6855.

122. Wang, H.B.; You, W.; Jiang, P.; Yu, L.; Wang, H. H. *Chem. Eur. J.* **2004**, *10*, 986.

123. Mori, T.; Watanabe,T.; Minagawa,K.; Tanaka, M. *J. Polym. Sci. A Polym. Chem*. **2005**, *43*, 1569.

124. Cui, H. G.; Chen, Z.Y.; Zhong, S.; Wooley, K.L.; Pochan, D. J. *Science* **2007,** *317*, 647.

125. Li, Z. B.; Chen, Z. Y.; Cui, H. G.; Hales, K.; Wooley, K. L.; Pochan, D. J. *Langmuir* **2007**, *23*, 4689.

126. Zhong, S.; Cui, H. G.; Chen, Z. Y.; Woooley, K. L.; Pochan, D. J. *Soft Matter* **2008**, *4*, 90.

127. Sanchez, C.; Arribart, H.; Guille, M. M. G. *Nat. Mater.* **2005**, *4*, 277.

128. Lakes, R. *Nature* **1993**, *361*, 511.

129. Heuer, A. H.; Fink, D. J.; Laraia, V. J.; Arias, J. L.; Calvert, P. D.; Kendall, K.; Messing, G. L.; Blackwell, J.; Rieke, P. C.; Thompson, D. H.; Wheeler, A. P.; Veis, A.; Caplan, A. I. *Science* **1992**, *255*, 1098.

130. Tang, Z.; Kotov, N. A.; Magonov, S.; Ozturk, B. *Nat. Mater.* **2003**, *2*, 413.

131. Zeng, X.; Ungar, G.; Liu, Y.; Percec, V.; Dulcey, A. E.; Hobbs, J. K. *Nature* **2004**, *428*, 157.

132. Vaia, R.; Baur, J. *Science* **2008**, *319*, 420.

133. Sanchez, C.; Boissiere, C.; Grosso, D.; Laberty, C.; Nicole, L. *Chem. Mater.* **2008**, *20*, 682.

134. Ma, X.; Xia, Y.; Chen, E.-Q.; Mi, Y.; Wang, X.; Shi, A.-C. *Langmuir* **2004**, *20*, 9520.

135. Xu, W.; Lin, H.; Lu, S.; Xi, J.; Wang, Y. *Langmuir* **2008**, *24*, 10895.

136. Sel, O.; Kuang, D.-B.; Thommes, M.; Smarsly, B. *Langmuir* **2006**, *22*, 2311.

137. Zhao, Y.; Li, M.; Lu, Q.; Shi, Z. *Langmuir* **2008**, *24*, 12651.

138. Muthukumar, M.; Ober, C. K.; Thomas, E. L. *Science* **1997**, *277*, 1225.

139. Tenneti, K. K.; Chen, X. F.; Li, C. Y.; Tu, Y.; Wan, X.; Zhou, Q.-F.; Sics, I.; Hsiao, B. S. *J. Am. Chem. Soc.* **2005**, *127*, 15481.

140. Matsushita, Y. *Macromolecules* **2007**, *40,* 771.

141. Tyler, C. A.; Qin, J.; Bates, F. S.; Morse, D. C. *Macromolecules* **2007**, *40*, 4654.

142. Guo, Z.; Zhang, G.; Qiu, F.; Zhang, H.; Yang, Y.; Shi, A.-C. *Phys. Rev. Lett.* **2008**, *101*, 028301.

143. Ye, X.; Shi, T.; Lu, Z.; Zhang, C.; Sun, Z.; An, L. *Macromolecules* **2005**, *38*, 8853.

144. Huang, C. I.; Lin, Y. H. *Macromol. Rapid Commum*. **2007**, *28*, 1634.

145. Hanski, S.; Houbenov, N.; Ruokolainen, J.; Chondronicola, D.; Iatrou, H.; Hadjichristidis, N.; Ikkala, O. *Biomacromolecules* **2006**, *7*, 3379.

146. Ikkala, O.; ten Brinke, G. *Science* **2002**, *295*, 2407.

147. Ruokolainen, J.; Makinen, R.; Torkkeli, M.; Makela, T.; Serimaa, R.; ten Brinke, G.; Ikkala, O. *Science* **1998**, *280*, 557.

148. Valkama, S.; Kosonen, H.; Ruokolainen, J.; Haatainen, T.; Torkkeli, M.; Serimaa, R.; ten Brinke, G.; Ikkala, O. *Nat. Mater.* **2004**, *3,* 872.

149. Ruokolainen, J.; ten Brinke, G.; Ikkala, O. *Adv. Mater.* **1999**, *11*, 777.

150. Ruotsalainen,T.; Turku, J.;Heikkila,P.;Ruokolainen, J.;Nykanen,A.; Laitinen, T.; Torkkeli, M.; Serimaa, R.; ten Brinke, G.; Harlin, A; Ikkala, O. *Adv.Mater.* **2005**, *17*, 1048.

151. Ikkala, O.; ten Brinke, G. *Chem. Commum.* **2004**, 2131.

152. Valkama, S.; Ruotsalainen, T.; Nykanen, A.; Laiho, A.; Kosonen, H.; ten Brinke, G.; Ikkala, O.; Ruokolainen, J. *Macromolecules* **2006**, *39*, 9327.

153. Chen, H.-L.; Lu, J.-S.; Yu, C.-H.; Yeh, C.-L.; Jeng, U.-S.; Chen, W.-C. *Macromolecules* **2007**, *40*, 3271.

154. Matsushita, Y. *Polym. J.* **2008**, *40*, 177.

155. Masuda, J.; Takano, A.; Nagata, Y.; Noro, A.; Matsushita, Y. *Phys. Rev. Lett.* **2006**, *97*, 098301.

156. Nagata,Y.; Masuda, J.; Noro, A.; Cho, D.; Takano, A.; Matsushita, Y. *Macromolecules* **2005**, *38*, 10220.

157. Masuda, J.; Takano, A.; Suzuki, J.; Nagata, Y.; Noro, A.; Hayashida, K.; Matsushita, Y. *Macromolecules* **2007**, *40*, 4023.

158. Nap, R.; Sushko, N.; Erukhimovich, I. Y.; ten Brinke, G. *Macromolecules* **2006**, *39*, 6765.

159. Subbotin, A.; Klymko, T.; ten Brinke, G. *Macromolecules* **2007**, *40*, 2915.

160. Klymko, T.; Subbotin, A.; ten Brinke, G. *J. Chem. Phys.* **2008**, *129*, 114902.

161. Ding, J. F.; Liu, G. J.; Yang, M. L. *Polymer* **1997**, *38*, 5497.

162. Li, Z. B.; Kesselman, E.; Talmon, Y.; Hillmyer, M. A.; Lodge, T. P. *Science* **2004**, *306*, 98.

163. Rodriguez-Hernandez, J.; Lecommandoux, S. *J. Am. Chem. Soc.* **2005**, *127*, 2026.

164. Park, M.; Harrison, C.; Chaikin, P. M.; Register, R. A.; Adamson, D. H. *Science* **1997**, *276*, 1401.

165. Aizawa, M.; Buriak, J. M. *J. Am. Chem. Soc.* **2006**, *128*, 5877.

166. Ozin, G. A.; Arsenault, A. C., *Nanochemistry: A Chemical Approach to Nanomaterials*; RSC Publishing: Cambridge, **2005**.

167. Ding, J. F.; Liu, G. J. *Macromolecules* **1999**, *32*, 8413.

168. Yan, X. H.; Liu, G. J.; Hu, J. W.; Willson, C. G. *Macromolecules* **2006**, *39*, 1906.

169. Hu, J. W.; Liu, G. J.; Nijkang, G. *J. Am. Chem. Soc.* **2008**, *130*, 3236.

170. Khan, M. A.; Armes, S. P. *Adv. Mater.* **2000**, *12*, 671.

171. Caruso, F. *Adv. Mater.* **2001**, *13*, 11.

172. Crooks, R. M.; M. Zhao, M.; Sun, L.; Chechik, V.; Yeung, L. K. *Acc. Chem. Res.* **2001**, *34*, 181.

173. Zhong, C. J.; Maye, M. M. *Adv. Mater.* **2001**, *13*, 1507.

174. Kim, K.; Kim, J. H.; Kim, S.; Chung, H.; Choi, K.; Kwon, I. C.; Park, J. H.; Kim, Y. S. ; Park, R. W.; Kim, I. S.; S. Y. Jeong, S. Y. *Macromol. Res.* **2005**, *13*, 167.

175. Radtchenko, I. L.; Sukhorukov, G. B.; Leporatti, S.; Khomutov, G. B.; Donath, E.; Möhwald, H. *J Colloid Interface Sci*. **2000**, *230*, 272.

176. Caruso, F.; Molhwald, H. *J Am Chem Soc* **1999**, *121*, 6039.

177. Sukhorukov, G. B.; Donath, E.; Lichtenfeld, H.; Knippel, E.; Knippel, M.; Budde, A.; Möhwald, H. *Colloids Surf. A: Physicochem. Eng. Aspects* **1998**, *137*, 253.

178. Sukhorukov, G. B.; Donath, E.; Davis, S.; Lichtenfeld, H.; Caruso, F.; Popov, V. I.; Möhwald, H. *Polym. Adv. Technol.* **1998**, *9*, 759.

179. Zhang, Q.; Remsen, E. E.; Wooley, K. L. *J. Am. Chem. Soc.* **2000**, *122*, 3642.

180. Bütün, V.; Wang, X. S.; De Paz Báňez, M. V.; Robinson, K. L.; Billingham, N. C.; Armes, S. P.; Tuzar, Z. *Macromolecules* **2000**, *33*, 1.

181. Huang, H.; Remsen, E. E.; Kowalewski, T.; Wooley, K. L. *J. Am. Chem. Soc.* **1999**, *121*, 3805.

182. Thurmond, K. B.; Kowalewski, T.; Wooley, K. L. *J. Am. Chem. Soc.* **1997**, *119*, 6656.

183. Huang, H.; Kowalewski, T.; Remsen, E. E.; Gertzmann, R.; Wooley, K. L. *J. Am. Chem. Soc.* **1997**, *119*, 11653.

184. Thurmond, K. B. ; Kowalewski, T.; Wooley, K. L. *J. Am. Chem. Soc.* **1996**, *118*, 7239.

185. Yun, Y.; Li, H.; Ruckenstein, E. *J. Colloid Interface Sci.* **2001**, *238*, 414.

186. Matsuoka, H.; Fujimoto, K.; Kawaguchi, H. *Polym. J.* **1999**, *31*, 1139.

187. Hritcu, D.; Muller, W.; Brooks, D. E. *Macromolecules* **1999**, *32*, 565.

188. Guo, X.; Weiss, A.; Ballauff, M. *Macromolecules* **1999**, 32, 6043.

189. Saito, R.; Ni, X.; Ichimura, A.; Ishizu, K. *J. Appl. Polym. Sci.* **1998**, *69*, 211.

190. Serizawa, T.; Takehara, S.; Akashi, M. *Macromolecules* **2000**, *33*, 1759.

191. Soula, O.; Guyot, A.; Williams, N.; Grade, J.; Blease, T. *J. Polym. Sci., Part A: Polym. Chem.* **1999**, *37*, 4205.

192. Roy, S.; Favresse, P.; Laschewsky, A.; De La Cal, J. C.; Asua, J. M. *Macromolecules* **1999**, *32*, 5967.

193. Búcsi, A.; Forcada, J.; Gibanel, S.; Héroguez, V.; Fontanille, M.; Gnanou, Y. *Macromolecules* **1998**, *31*, 2087.

194. Chen, M.; Kishida, A.; Akashi,M. *J. Polym. Sci., Part A: Polym. Chem.* **1996**, *34*, 2213.

195. Ho, K. M.; Li, W. Y.;Wong, C. H.; Li, P. *Colloid Polym. Sci.* DOI 10.1007/s00396-010 2276-9

196. Li, P.; Zhu, J.; Sunintaboon, P.; Harris, F. W. *Langmuir* **2002,** *18,* 8641.

197. Geest, B. G. D.; Sanders, N. N.; Sukhorukov, G. B.; Demeester, J.; Smedt, S. C. D. *Chem. Soc. Rev.* **2007**, *36*, 636.

198. Shchukin, D. G.; Sukhorukov, G. B. *Adv. Mater.* **2004**, *16*, 671.

199. Peer, D.; Karp, J. M.; Hong, S.; Farokhzad, O. C.; Margalit, R.; Langer, R.. *Nat. Nano* **2007**, *2*, 751.

200. Mann, S. *Angew. Chem. Int. Ed.* **2008**, *47*, 5306.

201. Christensen, S. M.; Stamou, D. *Soft Matter* **2007**, *3*, 828.

202. Discher, D. E.; Eisenberg, A. Polymer Vesicles. *Science* **2002**, *297*, 967.

203. Zhou, Y.; Shimizu, T. *Chem. Mater.* **2008**, *20*, 625.

204. Shimizu, T.; Masuda, M.; Minamikawa, H. *Chem. Rev.* **2005**, *105*, 1401.

205. Zhao, H.; Chen, J. F.; Zhao, Y.; Jiang, L.; Sun, J.-W.; Yun, J. *Adv. Mater.* **2008**, *20*, 3682.

206. Daniel, M. C.; Astruc, D. *Chem. Rev.* **2004**, *104*, 293.

207. Fan, H. J.; Gösele, U.; Zacharias, M. *Small* **2007**, *3*, 1660.

208. Caruso, F.; Caruso, R. A.; Mohwald, H. *Science* **1998**, *282*, 1111.

209. Xing, S.; Tan, L. H.; Yang, M.; Pan, M.; Lv, Y.; Tang, Q.; Yang, Y.; Chen, H. *J. Mater. Chem.* **2009**, *19*, 3286.

210. Xing, S.; Tan, L. H.; Chen, T.; Yang, Y.; Chen, H. *Chem. Commun.* **2009**, *13*, 1653.

211. Cheng, D. M.; Xia, H. B.; Chan, H. S. O. *Nanotechnology* **2006**, *17*, 1661.

212. Obare, S. O.; Jana, N. R.; Murphy, C. J. *Nano Lett.* **2001**, *1*, 601.

213. Sunintaboon, P.; Ho, K. M.; Li, P.; Cheng, S. Z. D.; Harris, F. W. *J. Am. Chem. Soc.*, **2006**, *128*, 2168.

Chapter 2

Fundamentals and Methods of Chemical and Physical Characterization Techniques

2.1 Molecular Characterization

2.1.1 Fourier Transform Infrared (FT-IR) Spectroscopy

Fourier transform-infrared spectroscopy (FTIR) is a very useful analytical technique for identifying chemicals that are either organic or inorganic species. This technique is used to measure the infrared intensity versus the infrared light wavelength (wavenumber) absorbed by the materials of interest. These infrared absorption bands can identify different chemical bonding environments based on the vibrational characteristics associated with specific bonds upon infrared irradiation. When an infrared light interacts with the matter, chemical bonds will stretch, contract, and bend. As a result, a specific chemical functional group absorbs infrared radiation in a specific wavenumber range. For example, the C=O stretch of the carbonyl group appears at around 1700 cm^{-1} in a variety of molecules. Therefore, the correlation of the band wavenumber position with the chemical structure is used to identify a functional group and probe chemical changes within a sample.

In this study, FTIR measurements were performed on a Perkin Elmer spectrometer equipped with an MCT detector at room temperature. Samples were mixed with appropriate amounts of KBr and compressed them into a disk form. All spectra were recorded for 500 scans at a resolution of 2 cm^{-1}. A spectrum from a pure KBr disk was used for background correction.

2.1.2 Nuclear Magnetic Resonance (NMR) Spectroscopy

A drawing of a superconducting magnet used in modern high-field NMR spectrometers is presented in Figure 2.1. The magnet is bathed in liquid helium to maintain its superconductivity, thereby alleviating the exorbitant electrical power operating requirements of electromagnets producing these same high magnetic fields. The radio frequency coil provides the radiofrequency (rf) energy appropriate to excite the nuclei in the sample to resonance.

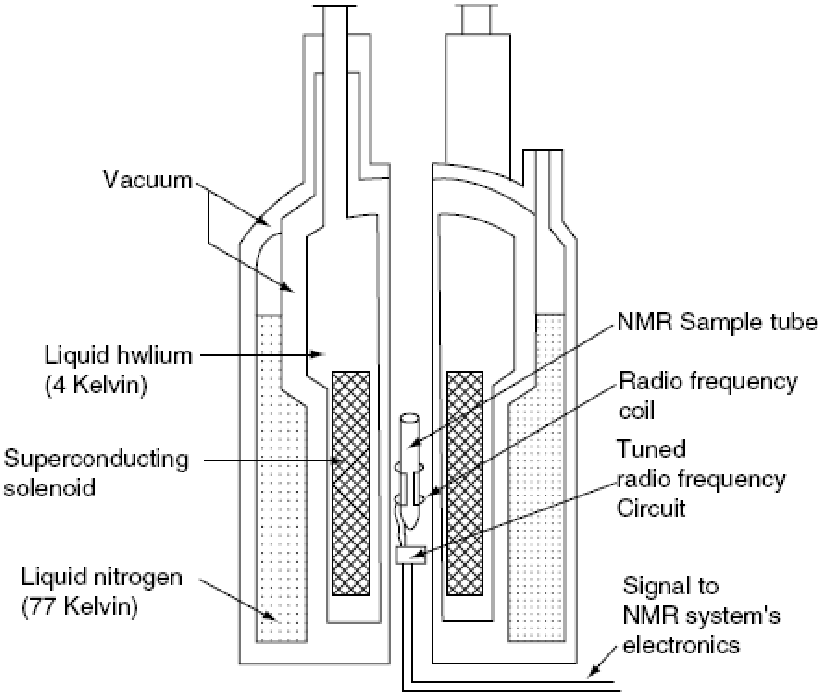

Figure 2.1 Cross-section of a superconducting NMR assembly. Magnet assembly has a B_0 and B_1 lie along the horizontal and vertical directions, respectively.[1]

The degeneracy of the nuclear magnetic spin energy levels is removed by the static magnetic field B_0. Application of the rotating magnetic, or electromagnetic, field B_1 excites transitions between these energy levels. When the frequency of the B_1 field (radio frequency, or rf, in MHz) is equal to the Larmor frequency of the observed nucleus, the resonance condition occurs, i.e., when

$$B_1 = v_0 = \gamma(B_o/\pi) \text{....................Eq. (2.1)}$$

Most samples will have nuclei with multiple Larmor frequencies, because most molecules have more than a single magnetically equivalent group (CH, CH_2, CH_3, for example), leading to several resonance frequencies or chemical shifts. The method used to excite the nuclei and achieve resonance must clearly be capable of covering all of the Larmor frequencies in the sample. This is achieved in the Fourier transform (FT) method by simultaneously exciting all the Larmor frequencies by application of a pulse (short burst) of rf signal (B_1) at or near all v_0s, which results in the equalization of the populations of the nuclear spin energy levels. Equilibrium spin populations are reestablished in a free induction decay (FID) process following the rf pulse.

All ^{1}H-NMR measurements were performed and recorded on a Bruker DPX400 NMR Spectrometer (400 MHz) in $CDCl_3$. Tetramethylsilane(TMS) in (^{1}H NMR) was used as internal standards.

2.2 Morphological observation by imaging techniques

2.2.1 Field Emission Scanning Electron Microscopy (FE-SEM)

Scanning electron microscopy (SEM) is a technique for imaging the surface of materials at nanometer length resolutions. Resolution is determined by the wavelength of an electron (λ), expressed by the de Broglie equation:

$$\lambda = \frac{h}{mv} \quad \text{…………………………….. (Eq. 2.2)}$$

where λ is the wavelength, h is Planck's constant, m is the mass of an electron, and ν is the velocity of an electron. The scanning electron microscope functions by emitting electrons from a field emission gun. The field emission gun requires extremely high vacuum condition (10^{-7} Pa) and generates the brightest high electron density beam and narrowest probe size. It produces high resolution images at low accelerating voltage (below 5 keV), thus does not cause thermal damage on thermally unstable specimens like polymers.

The ejected electrons are focused by condenser lenses to a very small focal spot and then scanned across the sample surface with scanning coils as illustrated in Figure 2.1. Interaction of the incident electron beam with the sample is limited to a tear shaped volume with nanometer to micron depth from the surface of the sample. Samples are imaged by detecting secondary electrons emitted from the sample surface with a photomultiplier device.

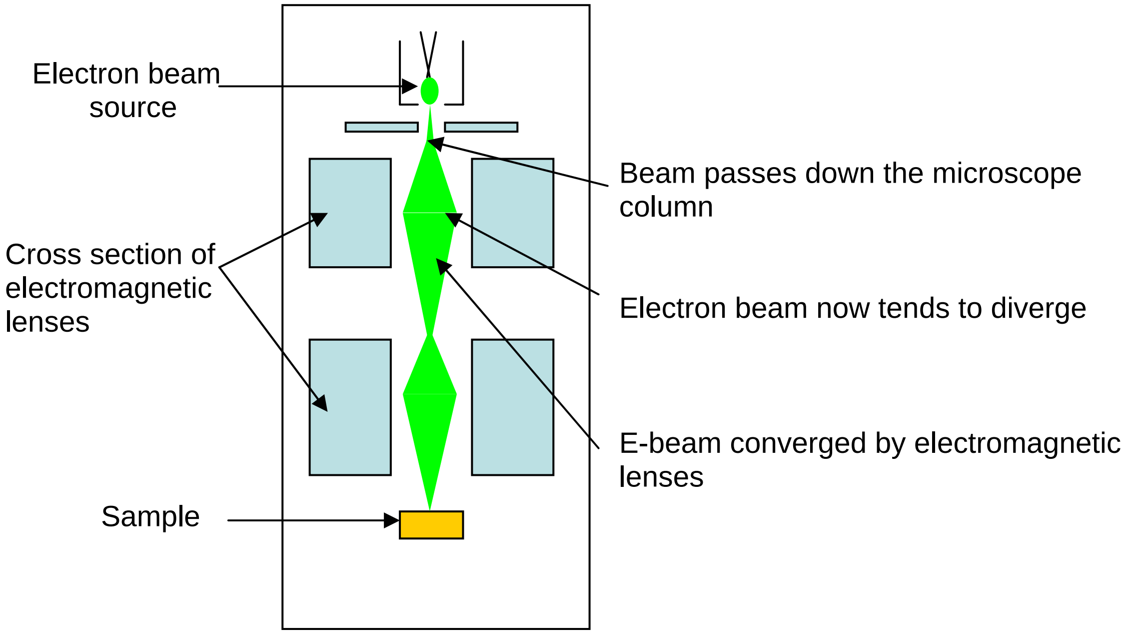

Figure 2.2 Schematic diagram of SEM setup

2.2.2 Transmission Electron Microscopy (TEM)

The working principle of TEM is based on electron scattering. In the characterization, a thin solid sample is placed in a high-vacuum chamber and illuminated by a fine-controlled high energy electron beam generated by an electron gun. As demonstrated in Figure 2.3, the interaction between the emitted electrons and the atomic electrons of the sample makes some of the emitted electrons scatter while others transmit through the sample. The intensities of scattering and transmission are strongly affected by the electron density of sample atoms. For example, gold atoms have higher electron density resulting in more scattering and less transmission, while carbon atoms allow more electrons to pass through. The difference in transmission intensity from various parts of a sample appears on the final negative image film as a difference in a gray-scale contrast.

In TEM characterization of copolymer structure, sufficient differences in electron density between copolymer layers and the supporting matrix should be the major criteria. However, the small difference in electron density between copolymers and ambient matrix makes it difficult to image them with high contrast. This problem can be solved by using phase contrast techniques or heavy-metal staining. The contrast can be further enhanced by choosing the appropriate supporting film materials, which have low electron density. For this reason, poly(vinylformal) (formvar) or cellulose acetate butyrate (CAB) is normally used as the supporting film material for TEM investigation.

In this work, TEM images of particles and assembled nanostructures were obtained from a JEOL 100 CX II TEM equipped with a multiscan CCD camera (1024 × 1024 pixels) and operated at 100 kV. The images were scanned into electronic file format and processed with Image J software to extract information such as particle surface, internal structures of core shell nanoparticles and particle size distributions.

Samples for TEM observation were prepared according to the following procedure: Sample solutions (5 μL) were dropped onto graphite-coated copper grids (400 mesh, Electron Microscopy Science) and air-dried. For some experiments, further positive-staining has been applied after drying the samples completely. This staining was done by dropping 2 μL of phosphotungstic acid ranging from 0.5 to 2 % (w/w) in deionized H_2O on the dried samples ranging from 30 sec. to 3 min. All images were obtained at an accelerating voltage of 100kV and emission current of 50 μA.

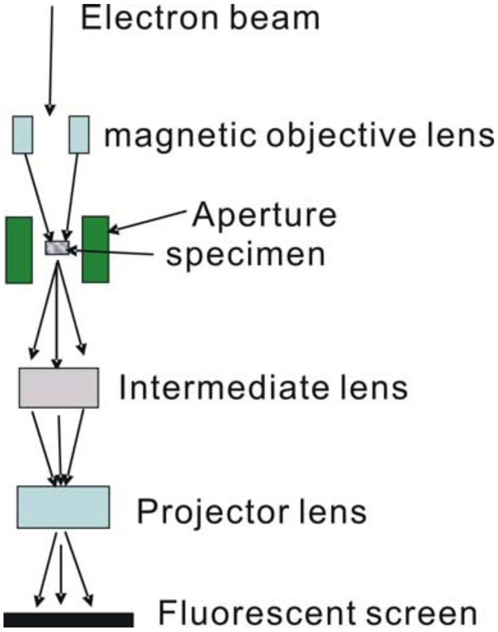

Figure 2.3 Schematic diagram of Transmission Electron Microscope

2.2.3 Atomic Force Microscopy (AFM)

The atomic force microscopy (AFM) is a versatile technique to investigate non-conductive materials such as polymers and biological samples. It is a technique in scanning probe microscopy (SPM) category, which includes scanning tunneling microscopy (STM), scanning near-field optical microscopy (SNOM) and magnetic force microscopy (MFM), etc. Contrary to so called far field characterization techniques such as optical microscopy and scanning electron microscopy (SEM), the SPM belongs to near field techniques due to the nanoscale interactions of probe apex and sample surface. The resolution of optical microscopy and SEM is usually of the order of half a wavelength of the photons and electrons. However, the resolution of SPM is determined by the geometrical shape of the probe apex at the atomic scale, thus atomic resolution can be achieved. The surface structures, the local electronic/magnetic properties of sample surface and the absorption of molecules can be analyzed with SPM. Hence, the SPM provides not only the topography and local properties of sample surface, but also enables the manipulation of single atoms and molecules on the sample surface. Among different SPM techniques, AFM is the most commonly used method to investigate copolymer nanostructures due to its high resolution and versatility.

The AFM technique basically determines the van der Waals force between the sample and the probing tip at individual locations over the imaging area. The potential between two hard spheres is given as the Lennard-Jones potential in the form of Eq 2.3, where ε is the well depth and σ is the hard sphere radius.[2]

$$V(r) = 4\varepsilon\left[\left(\frac{\sigma}{r}\right)^{12} - \left(\frac{\sigma}{r}\right)^{6}\right] \qquad \text{…………….(Eq 2.3)}$$

The first term $(\sigma/r)^{12}$ describes the repulsive force and the second term $(\sigma/r)^{6}$ describes the attractive force. As shown in Figure 2.4, when the probing tip approaches to the sample until on the Lennard-Jones potential, it experiences an attractive force, which bends the tip downward. The extent of bending is dependent upon the distance between the tip and the sample surface. Since the tip does not touch the surface, imaging in this region is called non-contact or tapping mode AFM. By contrast, the probing tip is bent up by a repulsive force when the tip and the sample surface are extremely close. AFM imaging carried on this region is called contact mode AFM. Tapping mode AFM has been mainly used in our sample characterizations because it allows imaging soft materials, such as biomolecules or polymers without causing sample damage.

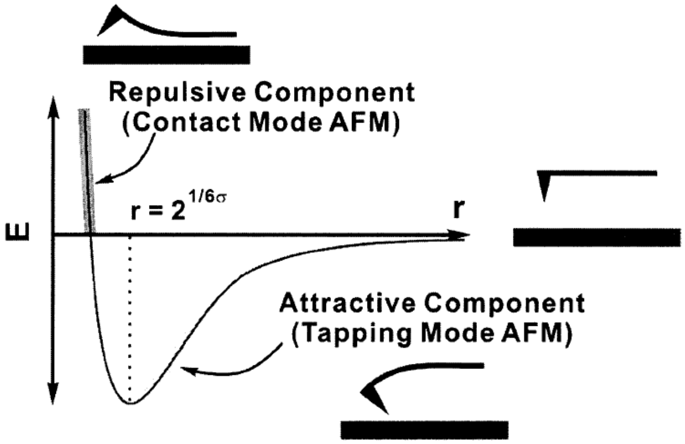

Figure 2.4 Schematic model of the interaction between the sample and the probe tip as a function of the sample-tip distance, based on the Lennard-Jones potential. As the probe tip and the sample approach one another until r = $2^{1/6}$, the interaction is predominantly attractive (Tapping mode). When the probe tip and the sample are extremely close to each other, the interaction is predominantly repulsive (Contact mode)

Figure 2.5 shows the AFM set-up. The subtle movements of the imaging tip are monitored by laser/photodiode detector, and the topological profiles of the sample in the area are obtained by a computer-assisted feedback and piezo-scanner system, which allows the probing tip to move over the sample surface within a certain range of distance. In tapping mode AFM, the cantilever tip is oscillated close to its resonance frequency (hundreds of kHz) and positioned above the surface and the tip taps the surface for a very small fraction of its oscillation cycle. This extremely short contact can reduce the lateral forces applied to the sample surface and minimize the damage to the surface of soft materials. When the cantilever tip scans across the surface and the amplitude is kept constant, the feedback signals collected by the photodetector can provide the image of surface topography.[2] On the other hand, phase imaging has received more attention simply because the phase of the oscillating cantilever is sensitive to the tip-surface interaction. Thus sample properties, for example, softness and viscoelasticity can be investigated from phase image.

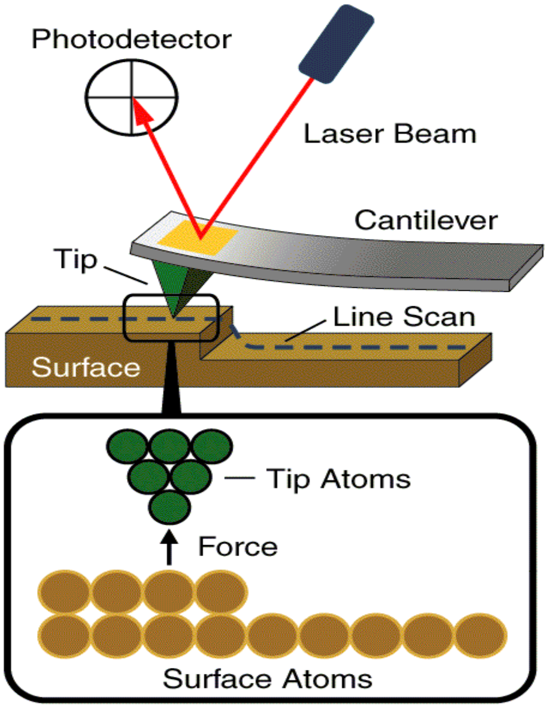

Figure 2.5 Schematic diagram of AFM set up

The greatest advantage of AFM over other imaging techniques is its extremely good resolution in variety of media, including vacuum, air, and even liquid.[3] AFM can provide topographical information with lateral resolution of ~ 1nm and height resolution of less than 1Å.[4] The practical resolution of AFM, however, is significantly affected by sample vibration and the sharpness of the imaging tip.

Accurate structural information can be obtained by AFM imaging of nanoparticles and self–assembled nanostructures if they are deposited on an atomically flat surface. This can be easily obtained from silicon wafers or freshly cleaved mica substrates. In this study, AFM samples were prepared by depositing nanomaterials onto freshly cleaved mica (AFM Mica Disks, Ted Pella, Inc. Redding, CA). AFM images were obtained on a Nanoscope IV system (Digital Instruments, Santa Barbara, CA) with a vertical scanner (J-type) in air. During *in-situ* AFM in fluid mode, the sample in the solution was confined in a liquid cell as shown in Figure 2.6. Extra caution should be taken to avoid contact the cantilever tip on the liquid cell. Stability is extremely important for aqueous scanning. Particularly, the air bubbles trap must be avoided in filling solution into the liquid cell. The tip should be wet by water droplet before being brought into the liquid cell. Flow through liquid cell enabled us to monitor the real morphology of the structure in solution state.

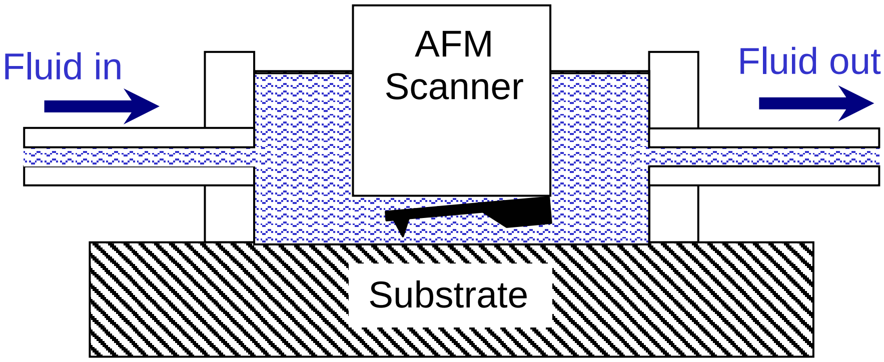

Figure 2.6 Schematic diagram of AFM imaging in fluid

2.3 Turbidity measurements

Turbidity was measured by a Hewlett Packard HP 8453 Photo-diode array UV-Visible Spectrophotometer with UV-Visible Chem Station software. The measurements were carried out at a wavelength of 700 nm where the absorption of the aggregates was minimized. The sample vials were sealed with Teflon tape and placed in a temperature cell in which the temperature was controlled by a temperature controller. Deionized water was used as the reference for all the measurements.

2.4 Zeta-potential measurements

The development of a net charge at the particle surface affects the distribution of ions in the surrounding interfacial region as shown in Figure 2.7, resulting in an increased concentration of counter ions (ions of opposite charge to that of the particle) close to the surface. Thus an electrical double layer exists around each particle. The liquid layer surrounding the particle exists as two parts; an inner region, called the Stern layer, where the ions are strongly bound and an outer, diffuse region where they are less firmly attached. Within the diffuse layer, there is a notional boundary inside which the ions and particles form a stable entity. When a particle moves (e.g. due to gravity), ions within the boundary move with it, but any ions beyond the boundary do not travel with the particle. This boundary is called the surface of hydrodynamic shear or slipping plane. The potential that exists at this boundary is known as the Zeta potential.

The magnitude of the zeta potential gives an indication of the potential stability of the colloidal system. A colloidal system is when one of the three states of matter: gas, liquid and solid, are finely dispersed in one of the others. In the case of solid particles dispersing in a liquid, if all the particles in suspension have a large negative or positive zeta potential, then they will tend to repel each other and there is no tendency to flocculate. However, if the particles have low zeta potential values, then there is little force to prevent the particles coming together and flocculating. The general dividing line between stable and unstable suspensions is taken at either +30mV or -30mV. Particles with zeta potentials more positive than +30mV or more negative than -30mV are normally considered stable.

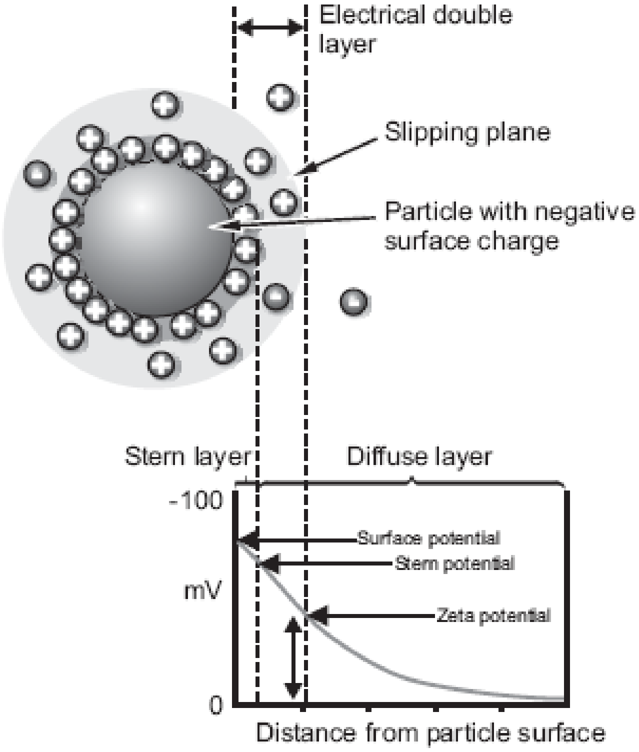

Figure 2.7 Schematic diagram of the distribution of ions in the surrounding interfacial region versus the distance from particle surface.

The most important factor that affects zeta potential is pH. A zeta potential value on its own without a quoted pH is a virtually meaningless number. Imagine a particle in suspension with a negative zeta potential, if more alkali is added to this suspension, then the particles will tend to acquire a more negative charge. If acid is then added to this suspension, a point will be reached where the negative charge is neutralised. Any further addition of acid can cause a build up of positive charge. Therefore a zeta potential versus pH curve will be positive at low pH and lower or negative at high pH. Therefore, the point where the plot passes through zero zeta potential is called the isoelectric point. This value is very important from a practical consideration because it is the point where the colloidal system is least stable.

In this research, electrophoretic mobility measurements were performed using Malvern Zetasizer 3000 HSA (Malvern, UK) with a 30 mW solid-state laser operated at a laser wavelength of 635 nm. All measurements of electrophoresis mobility (EPM) were performed at room temperature (~25°C). The zeta-potential (ζ) of the particles was calculated from the electrophoretic mobility (U_E) values using Henry equation

$$U_E = \frac{2\varepsilon\zeta f(ka)}{3\eta} \quad \text{……………………………Eq. (2.4)}$$

where ε: dielectric constant
ζ: Zeta potential
f(ka): Henry's function
η: viscosity

Two values are generally used as approximations for the *f(ka)* determination which is either 1.5 or 1.0.

Electrophoretic determination of zeta potential is most commonly made in aqueous media and moderate electrolyte concentration. *f(ka)* in this case is 1.5, and is referred to as the Smoluchowski approximation. Therefore calculation of zeta potential from the mobility is straightforward for systems that fit the Smoluchowski model, i.e. particle size larger than 200 nm diameterdispersed in electrolytes containing more than 10^{-3} M salt solution. For particles in low dielectric constant media *f(ka)* becomes 1.0.

Effective hydrodynamic diameters (D_{eff}) of the particles were obtained by a photon correlation spectroscopy in a thermostatic cell at a scattering angle of 90^o. Software provided by manufacturer was used to calculate D_{eff} values. All solutions were prepared using 1 mM NaCl aqueous solution as suspension fluid to about 1000 ppm. The particle suspension was then thoroughly dispersed with an ultrasonic vibrator for 5 minutes, prior to injecting it into a cleaned sample cell of Zetasizer with a syringe.

2.5 X-ray photoelectron Spectroscopy

X-ray photoelectron spectroscopy (XPS) is also called ESCA (Electron Spectroscopy for Chemical Analysis) which is a powerful and convenient surface (2 to 10 nm) quantitative technique. This technique, based on the photoemission of electrons induced by soft X-rays, allows multiple-element detection and provides chemical bonding and state information simultaneously with quantitative information.[5-9]

Figure 2.8 presents the working mechanism of XPS based on the photoelectric effect. Mg Kα X-rays (1253.6 eV) or Al Kα X-rays (1486.6 eV) is normally used in the measurements. When soft X-ray photon of energy $h\nu$ hits an atomic orbital electron, the photons transfer its total energy to the electron. Given that the photon energy is greater than the binding energy E_b of the orbital electron in the atom, the electron is then ejected from the atom with a kinetic energy E_k, approximately equal to the difference between the photon energy $h\nu$ and the sum of binding energy E_b and work function of the analyzer (Φ_A). Therefore, the fundamental energy equation for XPS is:

$$E_b \cong h\nu - E_k - \Phi_A \qquad \text{.............................(2.3)}$$

Here h is Planck's constant and ν is the X-ray frequency. Energies are usually expressed in electron volts (eV). Measuring the kinetic energy allows us to calculate the binding energy, which is used to identify the chemical information of atom.

Probabilities of interaction of the electrons with matter far exceed those of the photons, so while the path length of the photons is of the order of micrometers, the electrons is of the order of tens of Angstroms. Thus, while ionization occurs to a depth of a few micrometers, only those electrons that originate within tens of Angstroms below the solid surface can leave the surface without energy loss. It is these electrons which produce the peaks in the spectra and are most useful.[6]

Using XPS technique to identify all elements, except H and He, are possible. From photoemission spectra, qualitative (chemical state) and quantitative (surface concentration) information can be obtained. The identification of chemical states depends primarily upon the accurate determination of line energies. To determine line energies accurately, the voltage scale of the instrument must be precisely calibrated, a line with a narrow sweep range must be recorded with good statistics, and accurate correction must be made for static charge if the sample is an insulator.

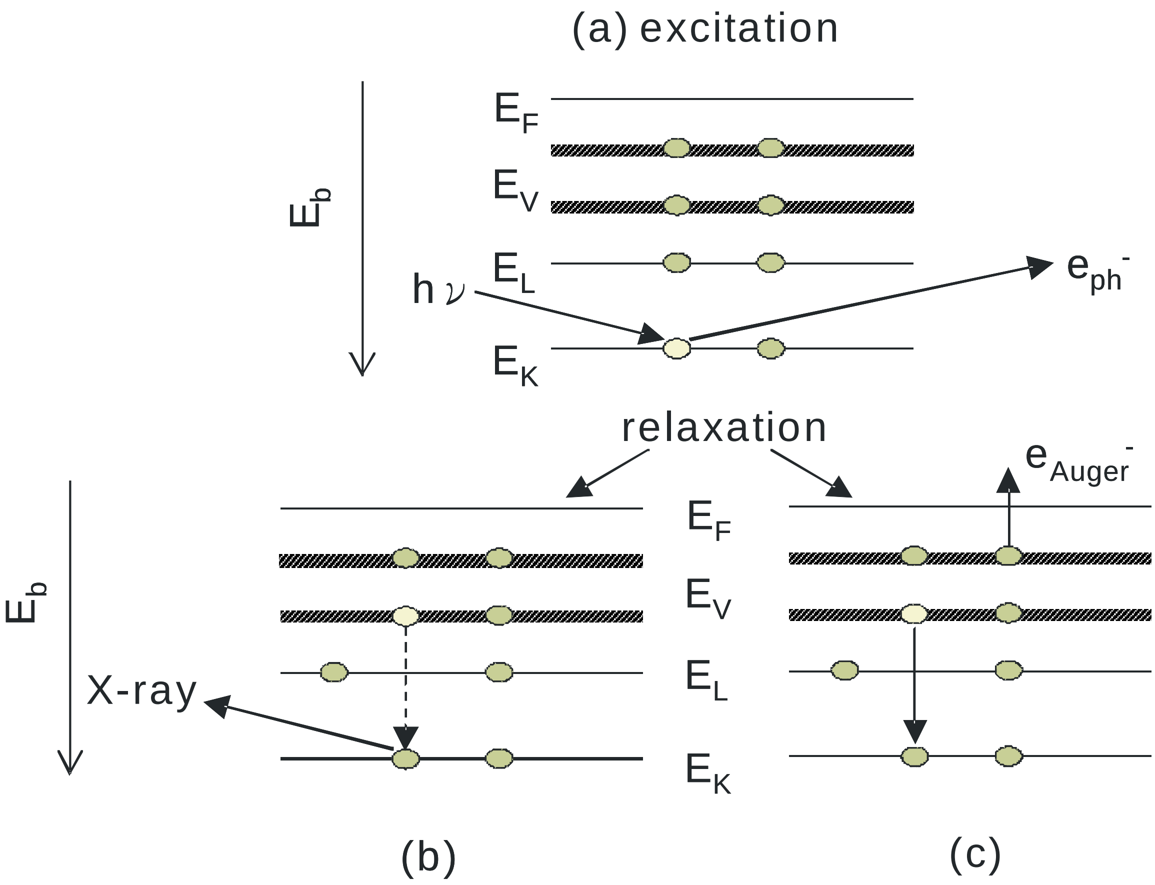

Figure 2.8 Working principle of XPS based on photoelectric effect

To determine the relative concentrations of the various constituents, methods for quantifying the XPS measurement utilizing peak area sensitivity factors and peak height sensitivity factors are both available, with the former one being more accurate. A general expression for determination of the atom fraction of any component in a sample, C_x, can be written as follows:

$$C_x = \frac{I_x / S_x}{\sum_i I_i / S_i} \quad \text{……………………………………………………(Eq. 2.4)}$$

where S is atomic sensitivity factor based on the calculated cross-section[7] (σ) corrected for the kinetic energy dependence of the spectrometer detection efficiency and an average value for the dependence of inelastic mean free path on kinetic energy, I is the measured peak area.[8]

References

1. F. A. Bovey, F. A.; Jelinski, L. W. *Nuclear Magnetic Resonance*, *Encyclopedia of Polymer Science, vol. 10*, Wiley, New York, **1987**, 254.
2. Atkins, P. W. *Physical Chemistry*, 7th ed., W. H. Freeman, New York, **2002**.
3. Hansma, H. G.; Pietrasanta, L. *Curr. Opin. Chem. Biol.* **1998**, *2*, 579.
4. Binning, G.; Quate, C. F. *Phys. Rev. Lett.* **1986**, *56*, 930.
5. Watts, J. C.; Wolstenholme, J. *An Introduction to Surface Analysis by XPS and AES*, John Wiley & Sons Ltd., England, **2003**.
6. Briggs, D.; Seah, M. P. *Practical Surface Analysis: Auger and X-Ray Photoelectron Spectroscopy (Practical Surface Analysis)*, John Wiley & Sons Ltd, 2nd edition, **1996**.
7. Vickerman, J. C. (Editor), *Surface Analysis ─ The Principal Techniques*, John Wiley & Sons Ltd, **1997**.
8. Walls, J. M. (Editor), *Methods of Surface Analysis: Techniques and Applications*, Cambridge University Press, **1990**.

Chapter 3

Fabrication and characterization of core-shell and hollow particles

3.1 Synthesis of PMMA/PEI core-shell particles

3.1.1 Materials

Branched PEI (50 wt. % aqueous solution, $<M_w>$ ~ 750,000 g/mol) was purchased from Aldrich and used as-received. Methyl methacrylate (MMA, Aldrich) was purified by being washed three times with 10% w/w sodium hydroxide solution [MMA to NaOH (v/v) = 10 : 1], followed by repeated washing with deionized water [MMA to water (v/v)= 5 : 1] until the pH of the water layer dropped to 7. It was further purified by vacuum distillation prior to use. *tert*-Butyl hydroperoxide (TBHP, 70% w/w solution in water) was obtained from Acros and used as-received. Dichloromethane (DCM) was obtained from Lab-Scan. Freshly deionized was used as the dispersion medium.

3.1.2 Synthesis and purification of PMMA/PEI core-shell particles

The PEI/PMMA core-shell particles were prepared according to the following procedure: branched poly(ethylenimine) (PEI) (2.0 g, 50 wt. % aqueous solution) was diluted with deionized water (45 mL) and mixed with the purified methyl methacrylate (MMA) (4.0 g) in a water-jacketed flask equipped with a thermometer, a condenser, a magnetic stirrer, and a nitrogen inlet. The stirred mixture was purged with nitrogen for 30 min., followed by the addition of TBHP solution (0.625 mL, $1.0\text{x}10^{-2}$ M). The mixture was stirred at 80°C for 2 hrs under nitrogen atmosphere. The MMA conversion was usually greater than 90 % as determined gravimetrically.

The prepared PMMA/PEI latex particles were purified by multiple cycles of centrifugation, decantation and rewetting. The purified particle dispersion was then dried with freeze-dryer (TFD 5505, Ilshin Lab. Co. Ltd.) at -48°C and chamber pressure of 5 mTorr. The dried product was extracted with chloroform for 48 hrs using a Soxhlet extractor. The insoluble portion of PEI-*g*-PMMA copolymer remained in the thimble, while the PMMA homopolymer was dissolved in the chloroform. The grafting percentage is calculated as percentage of weight ratio of the grafted PMMA to the weight of PEI charged. The grafting efficiency is calculated as weight ratio of the grafted PMMA to the total polymerized MMA.

3.1.3 Characterization of the PMMA/PEI core-shell particles

Infrared spectra were recorded on a Nicolet 750 FT-IR spectrophotometer using KBr disks. Proton and carbon magnetic resonance spectral determinations were made on a Bruker Advance DPX 400 or a Varian Gemini 200. Gel permeation chromatography (GPC) was performed on a Waters Associate GPC system. Tetrahydrofuran was used as the eluent at a flow rate of 1.0 mL/min. The GPC system was calibrated with polystyrene standard samples. Particle size and distribution were measured on a Coulter LS230 particle size analyzer. The $\zeta-$potential was measured with a Brookhaven Zeta Plus Analyzer with 1mM NaCl aqueous solution as the suspension fluid. Transmission electron microscopy (TEM) photographs were obtained using a JEM 100 CX transmission microscope at an accelerating voltage of 100 kV. The sample was prepared by wetting either a Formvar-coated or a carbon-coated grid with a small drop of the dilute latex solution (5mL, 500 ppm). Upon drying, it was stained with a small drop of 2% phosphotungstic acid (PTA) for 10 min and dried at room temperature before analysis.

3.1.4 Properties of the core-shell particles

The average particle diameter of the PEI/PMMA core-shell particles was found to be 148 nm based on statistical counts of 100 particles from FE-SEM micrograph as shown in Figure 3.1a. The SEM image also indicates that the particles are quite uniform. Figure 3.1b shows the nanostructure of the particles which was observed by a transmission electron micrograph under high magnification (60,000 X). Well-defined core-shell particle morphology is reveled where darker phase is the PEI and the lighter phase is the PMMA. The phase contrast was attributed to the selective staining of the PEI chains by a phosphotungstic acid (PTA) solution which is known to be a good staining agent for amino group.

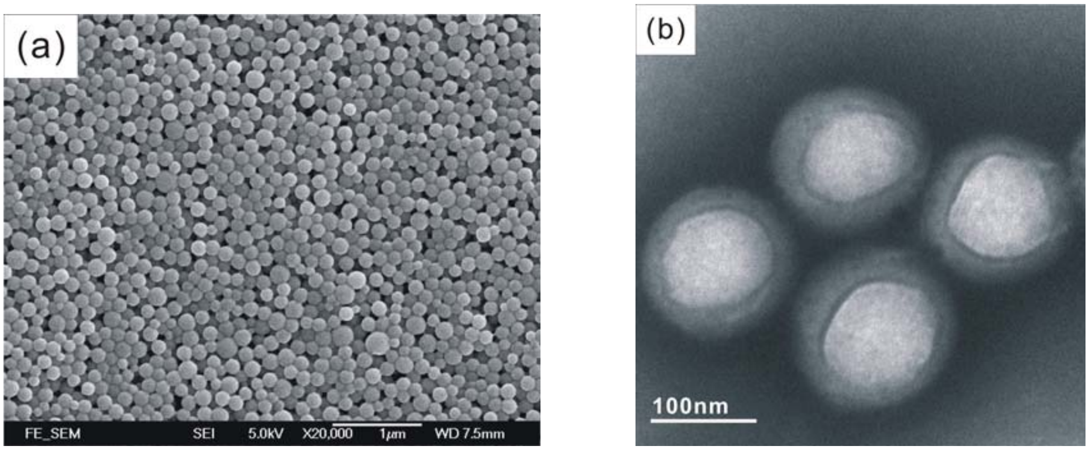

Figure 3.1 (a) FE-SEM and (b) TEM micrographs of PEI/PMMA core-shell nanoparticles.

3.2 Fabrication of PEI-*g*-PMMA hollow particles via core extraction of PMMA homopolymer

3.2.1 Fabrication of PEI-*g*-PMMA hollow particles from PMMA/PEI core-shell particles

Freeze-dried PMMA/PEI particles (0.1 g) was first mixed with 8 mL of dichloromethane (DCM) in a jacketed flask. The suspension was gently stirred at 150 rpm at 25^{o}C for 3 hrs in order to extract the PMMA homopolymer from the cores. Viscosity of the solution increased considerably due to the dissolution of the PMMA homopolymer. Water was then added dropwise at a rate of 1 drop per second, and the heterogeneous mixture was stirred at a rate of 150 rpm for 3 hrs. The aqueous phase was then isolated, diluted with water and stored at room temperature for characterization.

3.2.2 Identification of chemical structure of the extracted polymer and hollow particles by Fourier Transform Infra-Red Spectroscopy

The PMMA homopolymer in the core and PEI-*g*-PMMA copolymer were isolated with chloroform using a Soxhlet extractor for 48 h and their chemical structures were identified by FTIR spectroscopy. Figure 3.2a shows a spectrum of the extracted homopolymer. A very strong absorption peaks at 1730 cm^{-1} is observed which is due to stretching vibration of C=O. Other characteristic peaks including medium absorption peak at 1486 cm^{-1}, due to stretching vibration of -CH$_2$-; medium absorption peaks at 1241 and 1270 cm^{-1}, due to stretching vibrations of C-O bond ; strong absorption peaks at 1193 and 1149 cm^{-1}, due to stretching vibrations of C-O-C bond; medium absorption peak at 988 cm^{-1}, due to rotation of -CH$_3$ bond; two weak absorption peaks at 839 and 749 cm^{-1}, corresponding to rotation of -CH$_2$- and -CH$_3$

bonds. Figure 3.2b shows FTIR spectrum of the PEI-*g*-PMMA hollow particles. A strong absorption peaks at 1730 cm^{-1} (stretching vibration of C=O) and 3400 cm^{-1} (stretching vibration of N–H), corresponding to carbonyl groups of PMMA and amino groups of PEI, respectively.

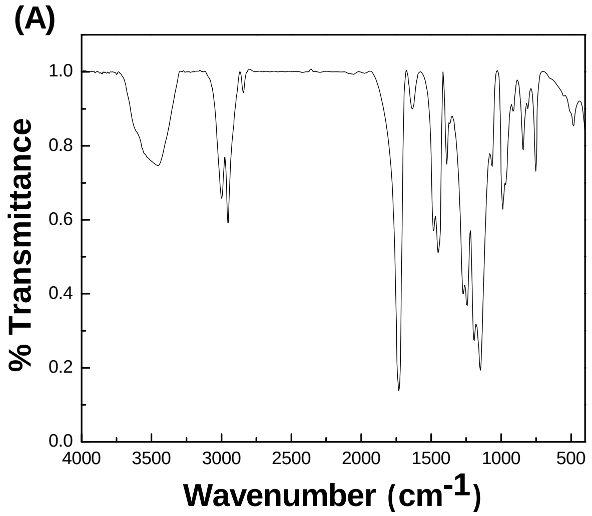

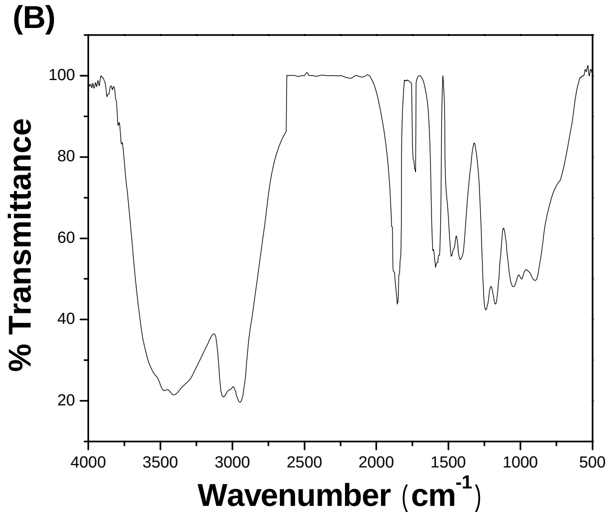

Figure 3.2 FTIR spectra of (A) extracted PMMA homopolymer, and (B) PEI-*g*-PMMA hollow particles

3.2.3 Identification of extracted homopolymer by nuclear magnetic spectroscopy

Figure 3.3 shows ^{1}H-NMR spectrum of the extracted PMMA homopolymer in $CDCl_3$. The peaks at δ=4.8 ppm attribute to methoxy carbon (-OCH_3), thus suggesting chemical structure of PMMA.

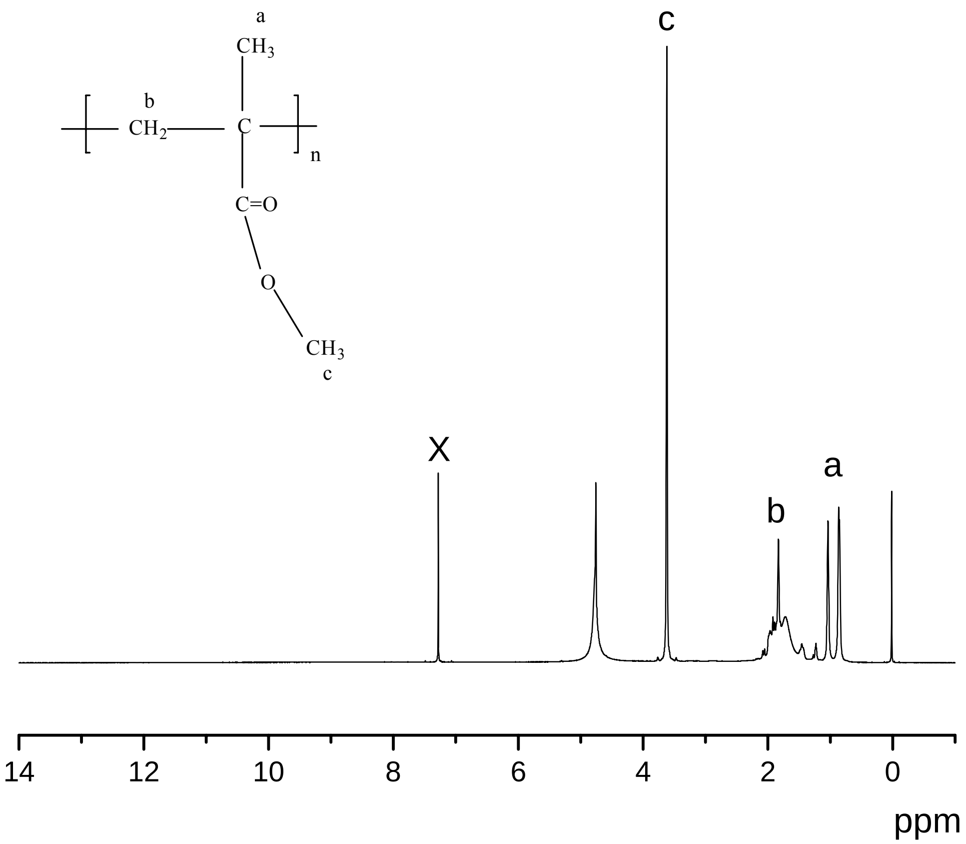

Figure 3.3 ^{1}H-NMR spectrum of the extracted PMMA homopolymer in $CDCl_3$ solvent

3.3 Characterization of hollow particle surface property using X-ray photoelectron spectroscopy (XPS)

3.3.1 Rationale of this study

Amphiphilic copolymers are copolymers consisting of both hydrophilic and hydrophobic segments. Many amphiphilic copolymers have been reported to undergo surface rearrangements upon exposure to different environments such as solvent-dependent switching.[1-13,14,15] When a hollow particle is formed in water, the low-surface-energy hydrophobic segment will preferentially migrate to the inner cavity, thereby minimizing the total free energy of the system. Upon exposure to dichloromethane, a surface reorganization can occur, which dramatically change in the surface chemical structure of the hollow particle as depicted in Figure 3.4 The thermodynamic driving force for the preferential segregation of the high-surface-energy hydrophilic phase to the polymer-water interface is to minimize the interfacial free energy and the total free energy of the system. The polarity of water provides a high interfacial free energy which is the driving force for the migration of the hydrophilic PEI segment to water medium, thereby minimizing the interfacial free energy. Upon exposure to hydrophobic environment, the PMMA grafts surface is driven by the low interfacial free energy provided by organic solvent (dichloromethane) and can reorganize back to the surface to various degrees and at different rates of rearrangement depending on the composition, structure, morphology and etc.[6-7, 10-13]

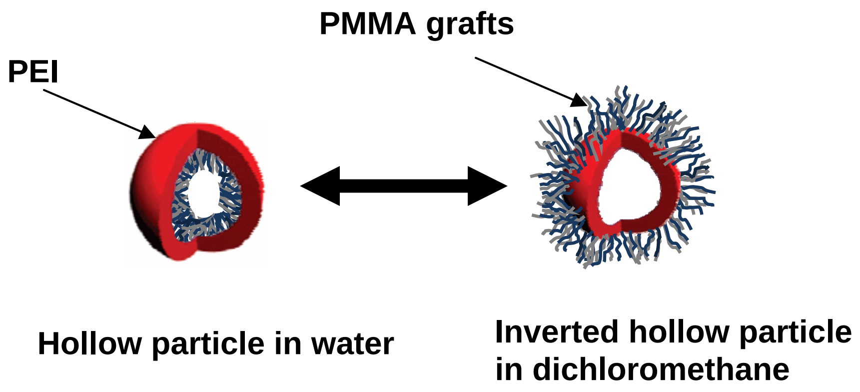

Figure 3.4 Schematic representation of switching hollow particle surfaces in water and dichloromethane.

Therefore, understanding the surface composition and morphology of hollow particles in both water and organic solvent medium is important since this will help understand the surface structures of these copolymers hollow particles and their interactions with solvent phases, thus improving polymer design for potential applications.

3.3.2 Materials and Methods

Freeze-dried PEI-*g*-PMMA hollow particles were examined by the X-ray photoelectron spectroscopy (XPS) analyses. The samples were prepared by coating the copolymer film on a flat mica substrate through dip coating of the sample from either DCM or aqueous solution, followed by drying the sample overnight in a vacuum oven at room temperature. XPS measurements were performed using a PHI 5600 (Physical Electronics) multi-detection system equipped with a monochromatic AlK_α X-ray source (1486.6 eV). The X-ray spot size was 400 × 400 μm. The pass energy of exciting radiation was set at 187 and 45 eV for survey and narrow scans, respectively. Charge compensation was achieved with a combination of electron and argon ion flood guns. The energy and emission current of the electrons were 4 eV and 0.35 mA, respectively. The partial pressure for the argon ion flood gun was maintained at a vacuum level of 2×10^{-8} mbar. These conditions of charge compensation resulted in a perfect uniform static charge distribution. Argon-ion sputtering was made by a PHI Versa Probe ion gun at an incidence angle of 45° for removal of physiosorbed adsorbates. The beam energy and ion current were set at 600 eV and 4 μA, respectively. The spot size was confined at 800 x 800 μm. The sputtering was performed at the substrate temperature of 300 K for 15 minutes in each cycle. Data acquisition and processing were achieved with the PC-based Avantage software (version 1.85). Spectral calibration was determined by setting the main C1s component at 285.0 eV. The surface composition was determined using the manufacturer's sensitivity factors. Spectra were obtained in a digital form. Curve fitting of the spectra was accomplished using a nonlinear least-squares method, and a Gaussian function was assumed for the curve-fitting process.

Hollow particles treated in dichloromethane and water, respectively were performed on a TEM (JEOL-2010) with an accelerating voltage of 120 kV. In order to observe the particle morphology under TEM which reflects the original morphological sizes and geometries as in the solution, a small amount of solution was "quenched" in excess water (≥ 100 times) to quickly vitrify the PMMA graft into its glassy state and then, a drop from the quenched solution was placed on a carbon-coated grid (400 mesh). After 5 min, the excess solution was blotted away with filter paper and further stained with 2 wt. % phosphotungstic acid (PTA) solution for 10 minutes. The grids were then dried at room temperature and atmospheric pressure for 24 hrs before examination in the TEM. Since the PMMA grafts were in their glassy state, the “quenched” morphologies were observed in TEM.

3.3.3. Results and discussion

In order to understand the surface reorganization behavior of the hollow particles in organic (DCM) and aqueous environments, the surface properties of the hollow particles were examined with XPS spectra. From the survey scan of XPS spectrum of hollow particles treated with dichloromethane as shown in Figure 3.5a, strong C1s and O1s peaks are observed, but there is no peak that are attributed to N1s. However, strong C1s, O1s, and N1s peaks of the hollow particles in water are clearly displayed as shown in Figure 3.5b.

To elaborate the chemical bonding information of the shell structure, individual peak-fitting and deconvolution of each elemental peak were investigated. Figure 3.6 shows the high-resolution C1s spectra of hollow particles in DCM. There is no N1s peak. Peak-fitting and deconvolution of the high resolution C1s peak reveal that there are four binding energy peaks at 285.0, 285.6, 286.7 and 289.02 eV, which are characteristic binding energies of aliphatic carbon atoms (C-C/C-H), carbon atoms that are adjacent to carbonyl groups (C-COO), C-O, and carbonyl carbon atoms (O-C=O), respectively. Furthermore, peak-fitting and deconvolution of the O1s peak indicate the presence of ester groups. The atomic ratio of carbon to oxygen atoms is 2.58, which is very close to the calculated ratio of carbon to oxygen atom in the PMMA molecule (C/O ratio = 2.5). These results indicate that the surface layer of the dispersed hollow particles in DCM is the PMMA grafts. This implies that the hollow particle morphology undergoes an inversion in DCM environment. Thus, the hydrophilic PEI tends to be buried at the inner core. Such reorganization of PEI-g-PMMA hollow particle morphology can explain the formation of stable latex dispersion in organic solvent.

For the surface reorganization behavior of hollow particles in aqueous solution, XPS spectra as shown in Figure 3.7 exhibit strong C1s, O1s, and N1s peaks. Peak-fitting and deconvolution of the N1s peak reveal two binding energy peaks at 400 and 401.23 eV, which are typical values for neutral amine and cationic nitrogen species, respectively. These results indicate that the PEI chains are localized on the outer shell layer when the hollow particles are dispersed in water. Thus, the particles again undergo inversion where the hydrophobic PMMA shells exchange positions with the hydrophilic cores. The XPS spectrum also shows an O1s peak at a binding energy of 529.5 eV. This binding energy peak is different from the oxygen-containing functional group. To verify the molecular structure of O1s peak, the sample was treated by argon ion sputtering. The intensity of this O1s peak was subsequently reduced, while the envelope profile of the high resolution C1s and N1s peaks were not affected. The reduction of O1s peak was due to the removal of physisorbed oxygen at the polymer surface.[16] Furthermore, the typical carbonyl carbon atom peak at 532 eV was not discernible in the C1s deconvolution profiles. These results suggest that O1s peak is attributed to the presence of physisorbed oxygen molecules on the particle surface, not attributed from the PMMA polymer.

XPS is a powerful quantitative tool for polymer surface analysis. A special sample handling technique is needed to analyze hydrated polymer surfaces treated with water or organic solvent. Since XPS is operated under an ultra high vacuum environment (UHV) and the UHV environment requires that the analysis of hydrated or wet surfaces is performed in the frozen state. In addition, for polymeric particle samples that may undergo a surface reorganization based on the solvent environment, the hydrated sample must be frozen to below the glass transition temperature (Tg) of the mobile constituent to stabilize or preserve the hydrated surface composition. If the temperature is above the Tg of the mobile polymer constituent under UHV, the hydrated polymer surface may reorganize towards the surface composition of the dehydrated structure. Therefore, the first step of the special sample preparation technique is to freeze the sample to below Tg of the polymer. After the wet sample is frozen and introduced into the vacuum system, the protective ice layer has to be sublimated as completely as possible to expose the real polymer surface for subsequent XPS analysis. Therefore, sublimation of surface water or ice in vacuum (and below Tg) is the second step of the special sample preparation technique. This special technique is called a freeze-drying technique,[17] or more generally, so-called cryogenic sample handling technique.

When freezing-dried treatment is used to slow polymer chain motion and to allow samples to be examined in vacuum, several concerns must be addressed. Freezing process may induce artifacts, and contamination may condense on the sample surface. Artifacts due to the formation and growth of ice or solvent crystals as a result of freezing and thawing are well described in the electron microscopy literature.[18-19] The exact sample preparation protocol becomes increasingly important as the solvent content and the thickness of the sample are increased. It is known that the occurrence of artifacts can be strongly reduced by rapid freezing and by subliming at low temperatures.[19-20] Freezing-induced artifacts such as voids and cracks are often observed in electron microscopy. Voids, if present, are not likely to have a significant effect on XPS since a relatively larger surface area of packed hollow particles is sampled. Likewise, unless there are large numbers of cracks due to damaged hollow particles which expose the core of the copolymer particle, the majority of the XPS signal should arise from the surface region.[21]

Surface contamination is a major consideration in XPS analysis. The buildup of surface contamination can occur during freeze pump process for sample handling without appropriate care in sample preparation. Surface contamination is a very common problem for freeze-dried samples in XPS analysis and was reported in several papers.[21-24]

The buildup of surface contamination can occur during the solvent treatment process and the freeze dried process for sample handling without appropriate care in sample preparation. During handling of solvent-treated PEI-*g*-PMMA hollow particles in wet state at low freeze-drying temperatures (-50^{o}C), the buildup of surface contamination is not significant because PEI-*g*-PMMA hollow particle is a highly packed solid material and will not absorb water into the grafted PMMA matrix in which water repelled from the PMMA core would be sublimated completely. Test results indicated that the contaminant signal intensity at the solvent-treated surface is extremely low (after sublimation of freeze contaminant in solvent crystal) enough to enable the examination of the surface composition of solvent-treated PEI-*g*-PMMA hollow particles.

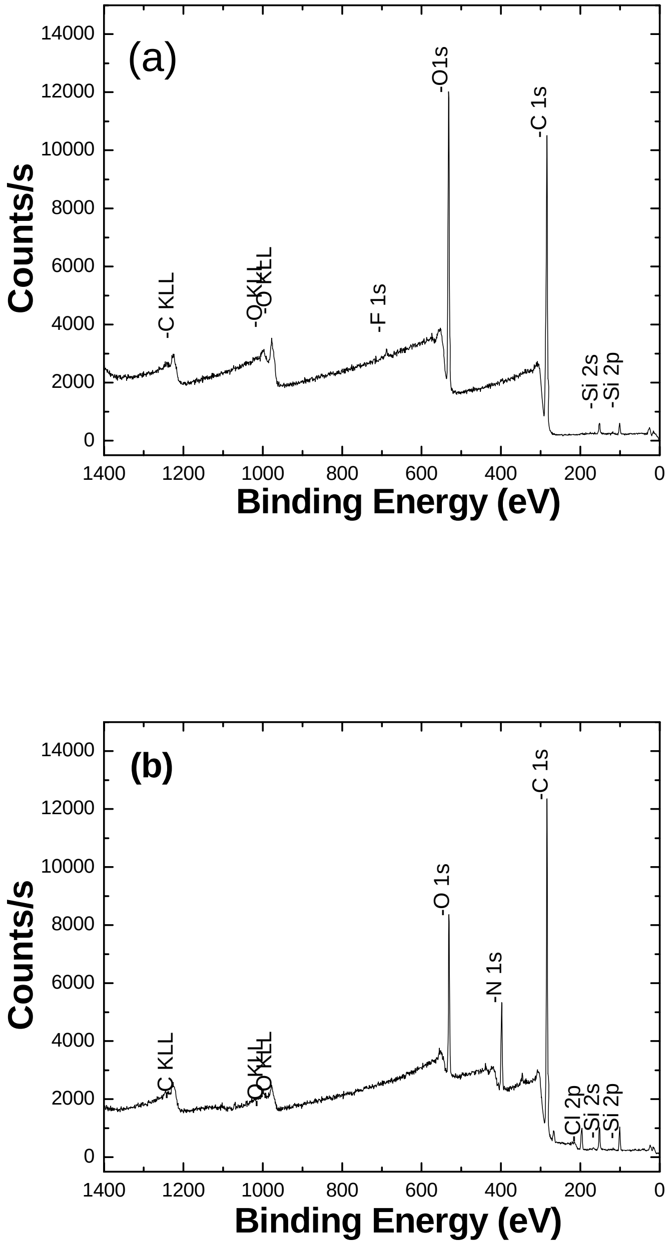

Figure 3.5 XPS survey spectra of hollow particles in (a) dichloromethane, and (b) water.

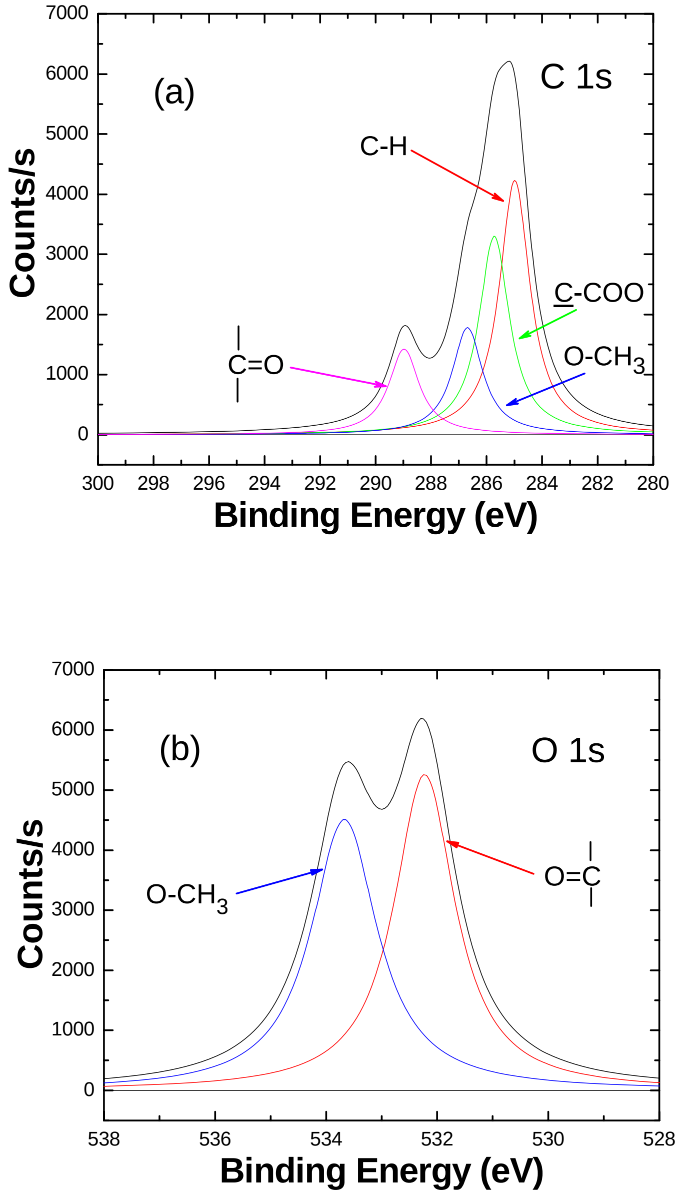

Figure 3.6 XPS spectra of peak-fitted and deconvoluted (a) C1s and (b) O 1s of hollow particles treated in dichloromethane.

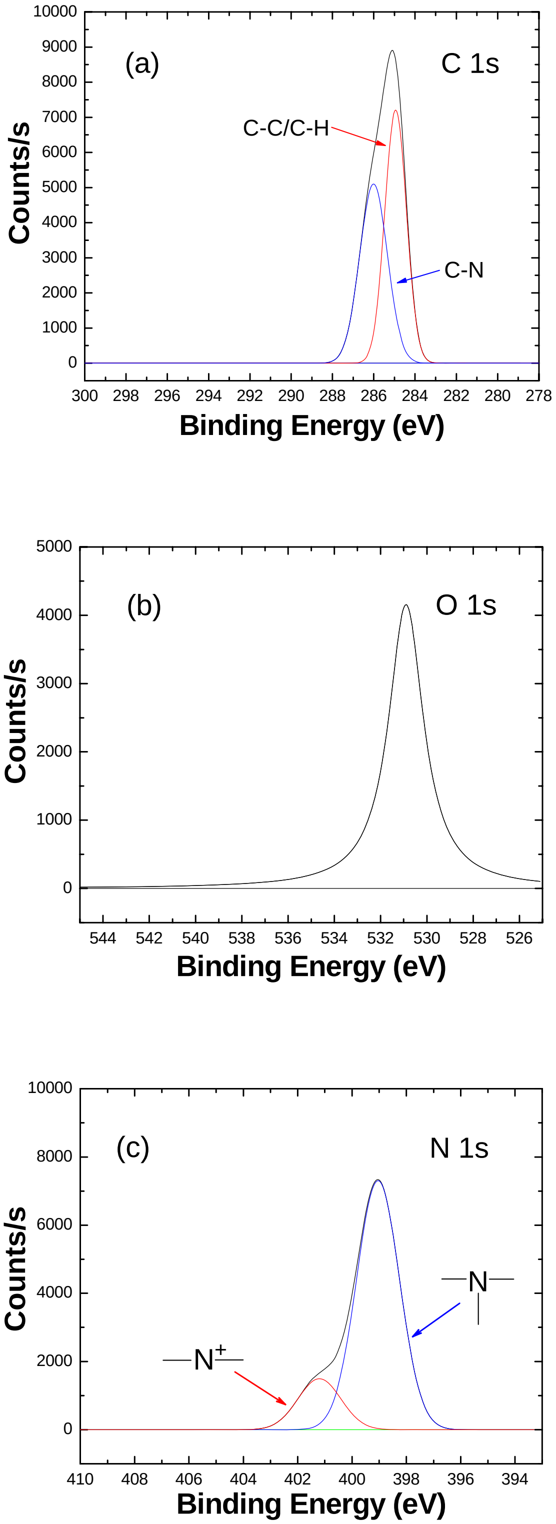

Figure 3.7 XPS spectra of peak-fitted and deconvoluted (a) C 1s, (b) O 1s and (c) N 1s of hollow particles treated in aqueous solution.

To identify the morphology of the particle and verify the placement of the hydrophilic PEI moiety in both DCM and water, the solvent pretreated particle was dried and subsequently treated with 2 wt. % phosphotungstic acid (PTA) to stain the amino group of PEI. The resulting PTA stained areas should have higher atomic weight species that provide the darker contrast. Figure 3.8a, shows TEM image of water-dispersible hollow particles. The presence of a dark ring around the particle in the corona relative to the cavity is observed. In the case of the hollow particles in DCM, the darker areas appear in the particle cores, indicating the presence of positive charged hydrophilic PEI (Figure 3.8b). The TEM observation confirms that the hydrophilic PEI unit and the hydrophobic PMMA can switch in response to solvents of different polarity.

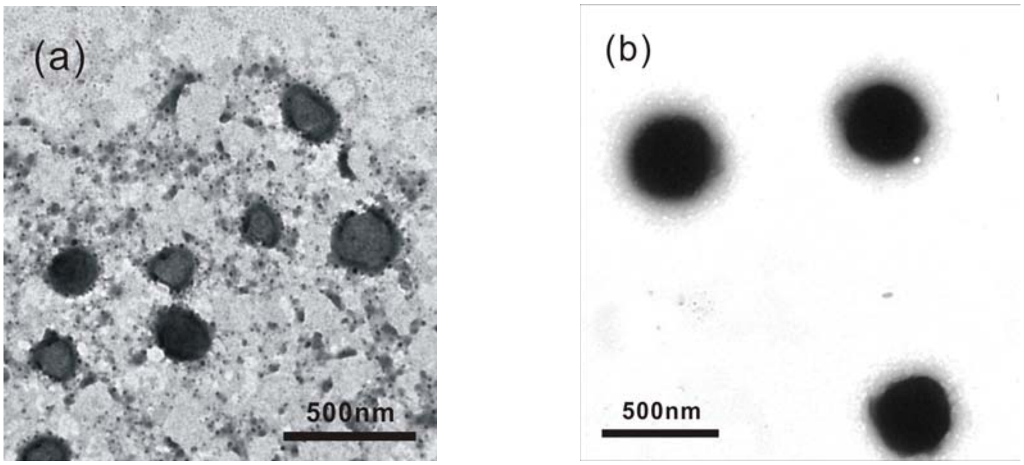

Figure 3.8 Transmission Electron Micrograph of PEI-g-PMMA hollow particles in (a) water and (b) dichloromethane.

For hollow particle assembly, three key factors are expected to strongly affect the assembly process: 1) The shape of the hollow particles; 2) The surface tension between the inner grafted PMMA and the solvent; and 3) The interactions among the grafted PMMA chains.

Since water is a good solvent only for PEI chains, but not for PMMA chains, the solvent environment becomes progressively worse for the PMMA chains as water is added slowly to the particle dispersion in DCM. At first, the PMMA graft chains are swollen by the solvent of dichloromethane. However, the average degree of stretching of the PMMA chains decreases with an increase of water volume. At appropriate ratios of water to DCM, the PMMA chains start to associate with each other in order to minimize their surface energy in water. The resulting morphology is a delicate balance of various forces and factors, i.e. the lengths of both hydrophobic grafted PMMA and hydrophilic PEI chains, the graft copolymer concentration, solvent composition, and other variables.

3.4 Shear-induced elongation of hollow particles

3.4.1 Background

Flow can induce both microscopic and macroscopic changes of the structure, with simultaneous changes in rheological behavior in various complex fluids. These phenomena have been reported for various systems such as polymer solutions, liquid crystalline polymers, polymer blends, colloidal suspensions, and wormlike micelles.[25-27]. For example, flow caused by stirring can induce elongation or thinning of soft or hollow nanoparticles with simultaneous changes in rheological behavior. Scheme 3.1 illustrates the shape deformation of hollow particle as a function of stirring rate. Spherical shaped hollow particles can elongate along $\hat{\mathbf{x}}$ into elliptical shapes in the equatorial plane at high stirring rate. Further increasing stirring rate can elongate the resulting ellipsoidal particles into thin filaments along $\hat{\mathbf{x}}$, thus exhibiting a transition to highly anisotropic shapes extended along $\hat{\mathbf{z}}$.

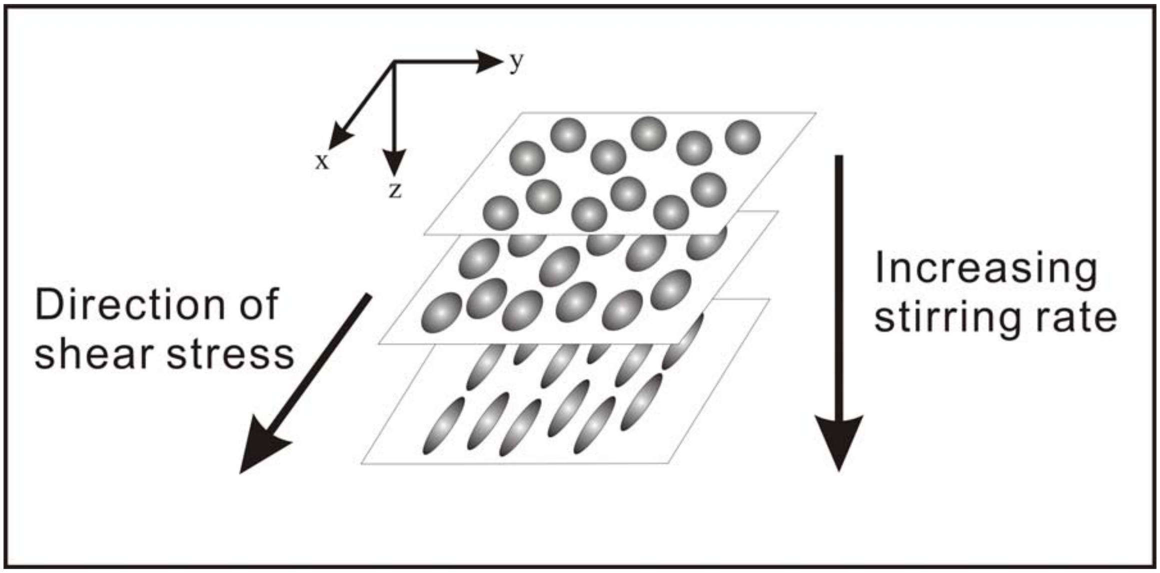

Scheme 3.1 Geometry of the shear induced elongation where the fluid flow, gradient, and stirring rate are along $\hat{\mathbf{x}}$, $\hat{\mathbf{y}}$, and $\hat{\mathbf{z}}$, respectively. For a steady flow, the aspect ratio of local hollow particle morphology is a function of z and the effective shear rate applied on the hollow particle is a function of y.

In our system, the nanotubular formation is induced by the shear force on hollow particles in an organic solvent/water mixture. Several concurrent transformations may take place during the assembling process, including intrinsic particle deformation upon core extraction, viscous shear and breakup of the particle shell. Here we focus on the ellipsoidal formation caused by the shear flow.

3.4.2 Characterization Methods

The field-emission scanning electron micrographs were obtained using a JEOL-JSM 6335F field-emission scanning electron microscope (FE-SEM) at an accelerating voltage of 5 kV and emission current of 10.5 μA. A small drop of a diluted hollow particle sample which has been stirred at a specific rate (between 250 and 350 rpm), was placed on a glass substrate, followed by drying it at room temperature for 24 hrs. The dried samples were subsequently sputtered with a thin layer of gold under vacuum to a depth of approximately 1-2 nm.

Transmission electron micrographs were obtained using a JEOL 100 CXII TEM at an accelerating voltage of 100 kV. Sample was prepared by wetting a carbon-coated copper grid with a small drop of dilute nanotube dispersion in water (10 μL, 500 ppm). Upon drying, the nanotubes were stained with 2 wt. % phosphotungstic acid (PTA) solution for 1-2 min. The samples were then dried at room temperature before microscopic analysis. All TEM images were taken in bright field mode.

Images of self-assembled nanotubes from elongated hollow nanoparticles were investigated using a Nanoscope IV Atomic Force Microscope (AFM, Digital Instruments) with a NSIV controller in a fluid tapping mode using a V-shaped silicon nitride ($Si3N_4$) cantilever (NP-S, 200W, Veeco Probes, CA) at a frequency of 8 ± 0.5 kHz. Images were acquired after 5 min. of sample injection, and continued for several hours. Aqueous sample (100-200 μL, 2 mg mL^{-1}) was thermally equilibrated to the temperature of fluid cell, and then injected into the cell at a rate of 10 μL s^{-1}. The scan sizes of AFM images were 0.7 and 1 μm, respectively, and the scan data were acquired at 0.5 Hz scan rate with a resolution of 512 × 512 lines.

3.4.3 Results and discussion

The assembly mechanism of the hollow particles in a mixture of DCM/water was studied by capturing the morphological changes at a lower reaction temperature (15°C). In this process, DCM was allowed to evaporate slowly from a mixture of DCM/water, and finally all DCM molecules were removed after 24 hrs, giving an aqueous solution containing resulting elongated nanoparticles and suspended PMMA homopolymer. Under these conditions, the fluid shear (stirring rate) plays a critical role in the assembly process. When the DCM/water mixture was not stirred or stirred at low speeds (< 100 rpm), the hollow particles remained as spherical morphology as indicated from TEM micrograph in Figure 3.9. However, when the stirring speed was increased to 250 rpm, the spheres began to assemble into short nanotubes (< 1μm) as illustrated in Figure 3.10a. Further increasing the stirring speed to 350 rpm resulted in complete conversion of spherical particles to nanotubes (Figure 3.10b). In order to capture the morphological transition of the hollow particles before the formation of nanotubes, a sample was withdrawn after the mixture was stirred at 350 rpm for 1 hr, and observed the morphology by TEM. Figure 3.11 revealed that hollow particles which had not yet assembled into short nanotubes were deformed to ellipsoidal hollow particles. This suggests that the shape of the hollow particle is one of the key factors which induce the assembly of amphiphilic hollow particles. This effect may be due to the fact that spherical hollow particles are stable in solution because they possess minimum overall Gibbs free energy at equilibrium, which is attributed to the free energies of core, interface and corona of the particles. On the other hand, the ellipsoidal particles possess higher Gibbs free energies,[28] resulting in stronger tendency to self-assemble into aggregates in order to minimize their overall Gibbs free energy in water.

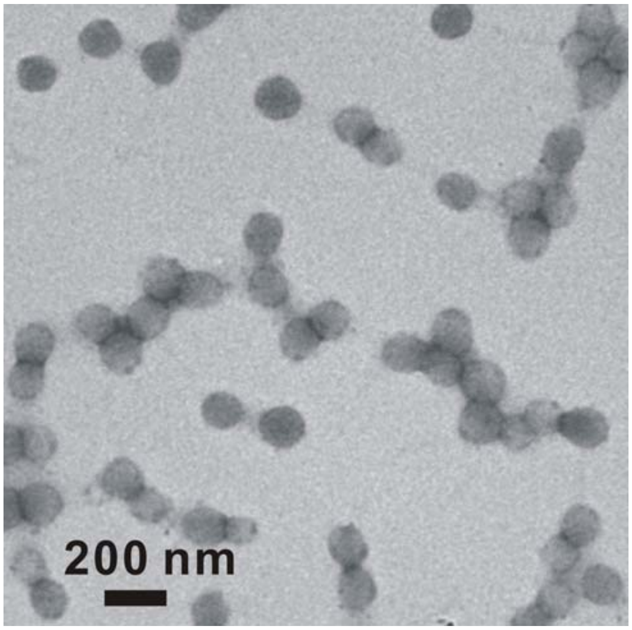

Figure 3.9 TEM micrograph of hollow particles in spherical morphology obtained from aqueous layer of the DCM/water ratio of (3:7 (v/v)) without stirring.

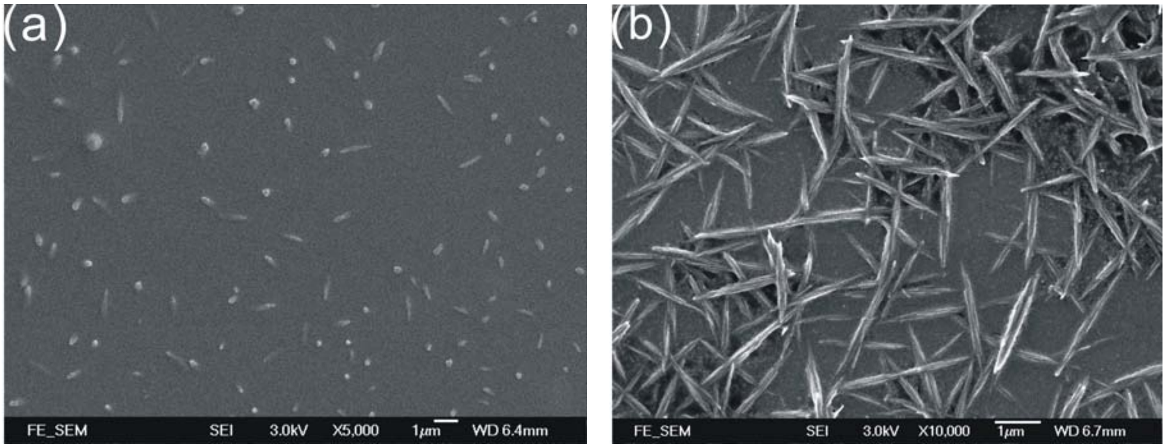

Figure 3.10 FE-SEM micrograph of ellipsoidal particles obtained from the aqueous layer of the DCM/water ratio of 3:7 (v/v) at 17°C and stirring rate of (a) 250 rpm and (b)350 rpm.

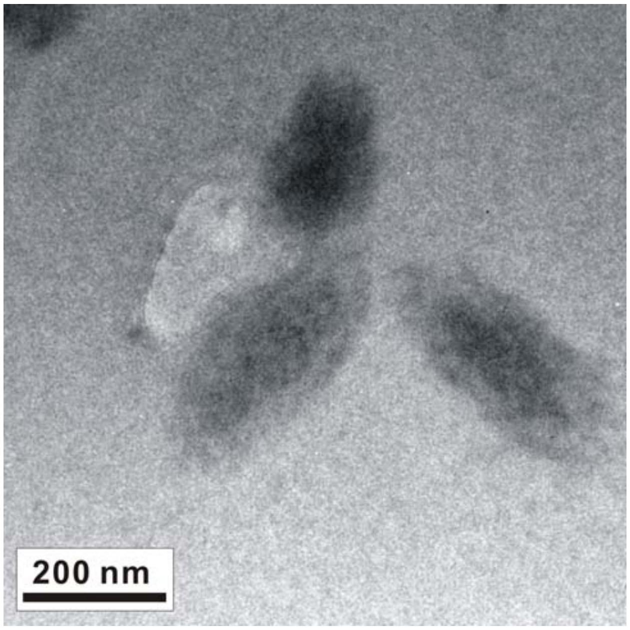

Figure 3.11 Ellipsoidal hollow particles observed after 1 hr stirring.

3.4.4 Aggregation of hollow particles and their assembly mechanism

After understanding the behavior of hollow particles in organic and aqueous media and the effect of stirring rate, the assembly mechanism for the formation of nanotubes was investigated by transmission electron microscopy. Figure 3.12a and 3.12b clearly reveals the aggregation of two short nanotubes having an average aspect ratio (Λ) ~ 3. The darker region in TEM micrograph is attributed to the PEI shell as a result of staining with 0.5 % (w/w) phosphotungstic acid solution. The connecting boundary between two elongated hollow particles, where the shells fuse together, is clearly observed. Figure 3.12c shows a TEM image of a longer nanotube. The marked arrows indicate a connecting junction and a broken boundary. These morphological transitions suggest that the nanotubes are formed via a tip-to-tip assembly of the elongated hollow particles. The connecting junction can open up and fuse with the neighboring connecting part to form linear tubular nanostructure up to the length of micron scale without any lateral aggregation. This preferential connection may be driven by stronger hydrophobic PMMA chains which are more densely packed at the tip region.

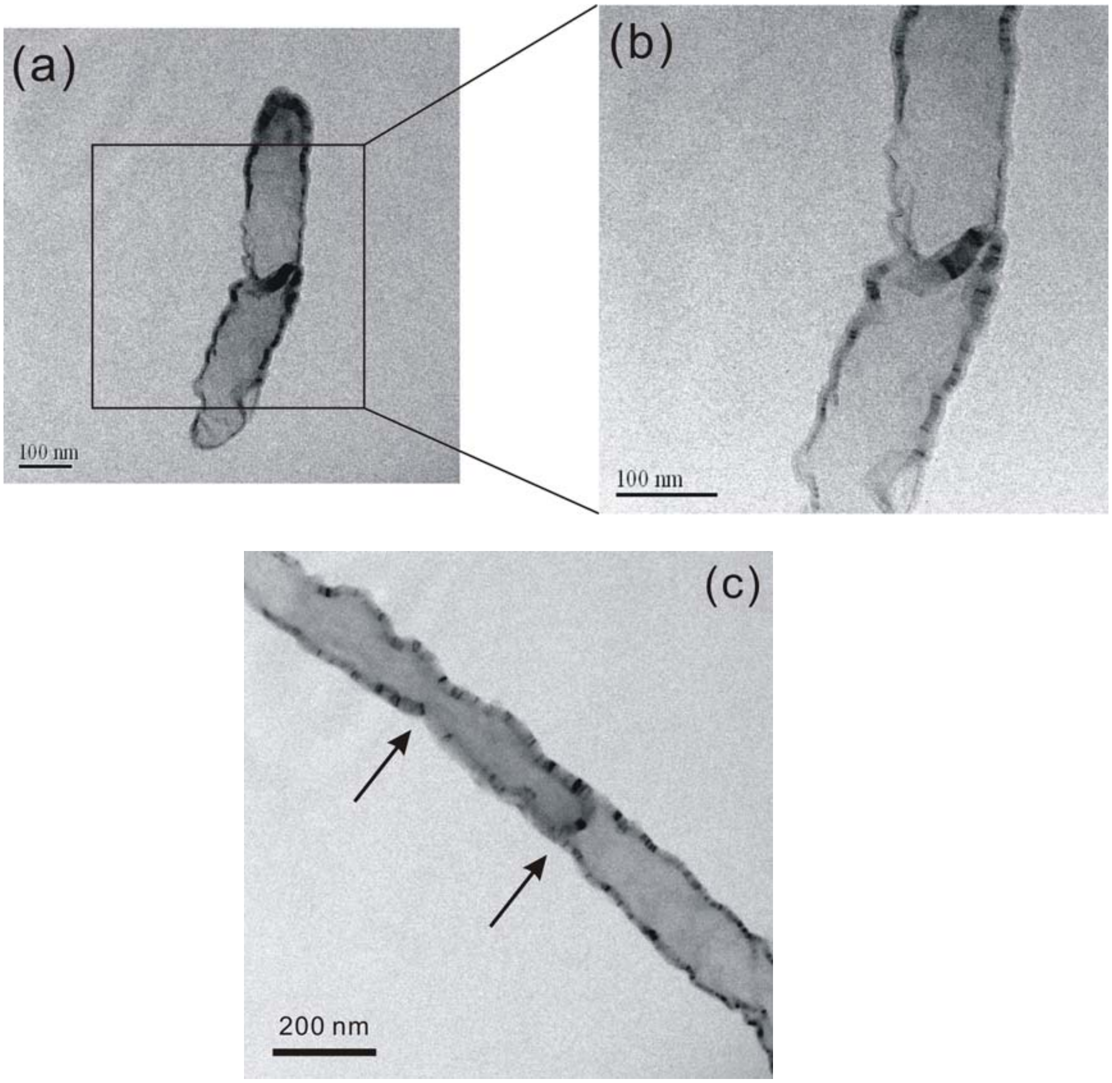

Figure 3.12 TEM images of nanotube formation (assembling conditions: DCM/water = 3:7 v/v, stirring at 350 rpm for 5 hrs at 17 °C). The TEM samples were prepared by immediately treating the aqueous sample with 0.5% w/w PTA solution for 1 min and drying on carbon-coated grids. (a) Aggregation of two short nanotubes. (b) Boundary between two connected nanotubes and (c) Merged tubular structure with opened and closed junctions.

3.5 Effect of elongated (anisotropic) hollow particles in nanotube formation

3.5.1 Background

Significant progress has been made in recent years toward the controlled assembly of nonspherical colloidal particles. A broad array of structures has been achieved with micrometer-scale[29-32] and nanometer scale particles[33,34] via assembly far from equilibrium (e.g., evaporation of solvent from the dispersion). Bibette[35] in 1991 pioneered the use of the geometry dependence of the depletion interactions osmotic-based attractive force between surfaces in the presence of a non-adsorbing solutes to drive phase separation near equilibrium.[36] Over the past decade, others have exploited this phenomenon to generate structure via geometry dependent interactions of colloids with surfaces[37,38] or colloids with colloids.[39,40] This strategy, which is based on near-equilibrium behavior, is amenable to rational design of selective "interactions" on the nanoparticle scale, but its use has been hindered by the lack of colloids with well-defined size and nonspherical shape and by an incomplete accounting of the colloidal interactions at play.

Prior to further discussion on the formation of tubular nanostructure, it is necessary to understand the interactions among elongated nanoparticles or anisotropic particles in liquid-vapor, solid-vapor and solid-liquid interfaces. It is known that shear flows tend to bring hollow particles close to each other more rapidly than Brownian motion does; hence altering particle aggregation kinetics by speeding up the process.[41] Shear-induced association is known as "orthokinetic" aggregation and frequently operates in solutions containing sticky particles at moderate shear rates. But at high shear rate, the aggregates are expected to break up under the action of large shear stresses.

The use of particles of anisotropic shape is of much interest since it allows fabrication of structures with special symmetries and degree of packing and/or anisotropic properties. The entropic effects during the organization of rod-like or tubular-like structures into colloidal liquid crystals have been studied intensively for decades[42,43] but most of the studies theoretically using biological particles such as viruses.[44,45] A few studies utilizing other anisotropic particles have demonstrated the potential of the anisotropic colloids in preparing new liquid-crystalline phases.[46-48] Despite the remarkable recent progress in the synthesis of various nanorods, nanotubes, and nanowires,[49-57] little has been done in the making of tubular-like and fiber-like structure on the sub-micrometer scale with anisotropic particles as major building block in self-assembled process.

Understanding and controlling the collective behavior of nanoparticles (NPs) is a challenging problem of fundamental and practical importance.[58,59] This is particularly true for shear induced elongated particles because their anisotropy implies additional functionality on the scale of individual particles and their assemblies, enabling a variety of applications from cloaking devices[60] to biological sensing[61] and solar energy conversion.[62] There are two basic approaches to nanotube assembly. The first one relies on the Onsager (excluded volume) mechanism, driving the parallel alignment of ellipsoidal hollow particles when their volume fraction Φ and their aspect ratio are high enough.[63,64] The second mechanism utilizes anisotropic attractive forces. Examples include end-to-end assembly of anisotropic particles with covalently bound biotin connected into chains by streptavidin[65] and side-by-side assembly of one-dimensional nanomaterials with an oppositely charged B-DNA,[66] as well as hydrophobic/hydrophilic interactions.[67,68]

3.5.2 Mechanism of selective assembly

When a colloidal particle is located at a planar interface between organic solvent and water, the interface deforms to satisfy the wetting boundary condition and free energy minimization. The relevant free energy is shown by the sum of the surface energies of the liquid-vapor, solid-vapor and solid-liquid interfaces. This free energy is minimized to determine the particle configuration and its interfacial phenomena. The interfaces assume a particle shape with quadrupolar elements. Quadrupolar deflections are known to describe the excess surface area that drives the aggregation in selective conformation.[69] The orientation driven by the curvature depends on the excess surface area created by these interface distortions. For an isolated anisotropic particle with outward pointing vector normal **n** in an interface with non-azimuthal tangent ***t*** is shown in Figure 3.13.

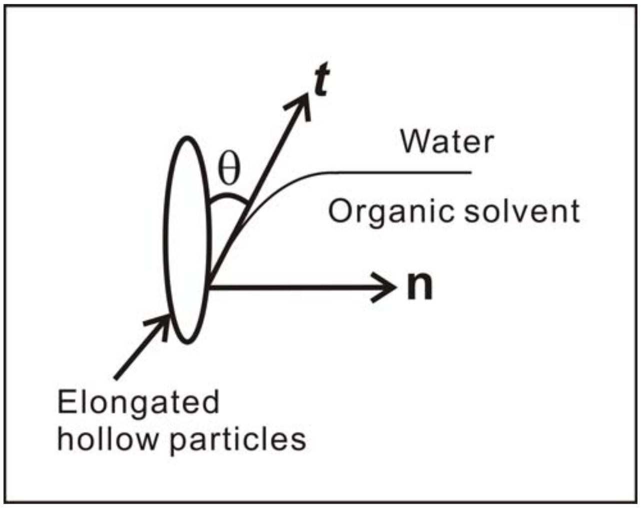

Figure 3.13 Schematic diagram of the tip region of an elongated hollow particle, with outward pointing normal vector **n** in a water-DCM interface which has non-azimuthal slope of tangent ***t*** at the three phase contact line profile.

According to the equilibrium interface topology around an elongated hollow particle with aspect ratio ($\Lambda \sim 3$) in equations 3.1, γ is the surface tension of the water-organic solvent interface, and the integral is taken around the surface contact line. Equation 3.2 describes that the interface intersect the particle with the contact angle θ_c.

$$\gamma \int t ds = 0 \tag{3.1}$$

and

$$\mathrm{n} \bullet t = \sin \theta \tag{3.2}$$

The fluid interface is located at z = $h(r,\theta)$ where r measures the distance from the origin, located at the center of mass of the hollow particle, and θ is measured from the y-axis. The fluid interface pulls upward at the end region of the anisotropic particle; this force is balanced by the downward force exerted by the interface along the lateral surface of the elongated hollow particles. This balance implies that aspect ratio of hollow particle plays a strong role in the local magnitude of surface deformation around the particle. For an anisotropic particle of planar length (L_p) and curved length (L_c), the vertical component of the force balance in Eqn. 3.1 requires that:

$$\left|t_{z1}\right| L_p \approx \left|t_{z2}\right| L_c \tag{3.3}$$

where t_{z1} is the characteristic slope of the interface along the planar (lateral) surface, and t_{z2} is the characteristic slope of the interface along the curved surface. Let z = $h(x,y)$ is defined as the height of the interface relative to the planar height. At each corresponding surface, $|t_z| = |\nabla h|$. Based on the small slope limit, the strong deflections at the particle interface due to fluid shear create excess surface area (A_E) at the highly curved region:

$$A_E \approx \iint_S \frac{\nabla h \cdot \nabla h}{2}\, dx\, dy \tag{3.4}$$

therefore the local excess surface area around the particle is maximum in regions with the steepest slope. Based on the above description suggest that the aspect ratio:

$$\Lambda \approx \sqrt{\frac{A_{E2}}{A_{E1}}} \tag{3.5}$$

where A_{E1} and A_{E2} are the characteristic magnitudes of the excess area along the planar surface (lateral surface) and the highly curved surface of the elongated hollow particles, respectively. Eqn (3.5) suggests that elongated hollow particles ($\Lambda > 1$) should have excess surface area of hydrophobic site concentrated near the tip region of the anisotropic particles. Since the interaction result from the excess surface area, attractions should be greatest at the end point region of the anisotropic hollow particles, which should therefore assemble in tip-to-tip connection. In the case of hollow particle with aspect ratio Λ approaches to 1, there is no preferred surface for assembly because the slopes along the surface around the particle with low anisotropy are similar.

The effect of aspect ratio is clearly significant at the dichloromethane/water interfaces. On the other hand, it is well known that charged spherical particles at the DCM-water interface give rise to a long range order of electrostatic repulsion.[70] The electrostatic interactions are slightly weaker than the capillary interactions. For example, suppose the ellipsoid cross-section area with the interface is modeled as being covered by electric dipoles; the ellipsoids would be expected to repel each other strongly when parallel to each other. This phenomenon may allow us to explain the predominant tip-to-tip assembly pathway.

For elongated particles (ellipsoids), the electrostatic repulsion is not sufficient to overcome the hydrophobic attraction. This effect may be due to the decrease of charge density per unit surface area. When a sphere is stretched to form an ellipsoidal particle, there is an increase in surface area. Using FE-SEM micrograph in Figure 3.14 as examples, the ellipsoidal particle has an aspect ratio (Λ) of around 3 (major axis a = 400 nm, minor axis b = 130 nm and thickness c = 70 nm), starting from a sphere of 150 nm diameter. Thus, there is approximately 5 times increase in surface area. Hence, the number of charges per unit surface area decreases.

Therefore, the preferential tip-to-tip interaction can be explained by the wetting properties of the elongated particles, which in turn are controlled by the hydrophobic interaction. Preferential positioning within the aggregates tends to minimize the interfacial distortions, and thus the overall interfacial energy. In addition, single ellipsoidal particle or assembled ellipsoidal particles could freely move around one another without disassembly. Evidently, these aggregates are kinetically frozen structures with binding energies larger than k_BT.

The observations cannot be explained by attractive van der Waals interactions since they are much smaller than k_BT at distances in micrometers.[71] Electrostatic effects due to positive charged amine groups existed on the particle surfaces are typically repulsive, and repulsion is observed only at particle contact.

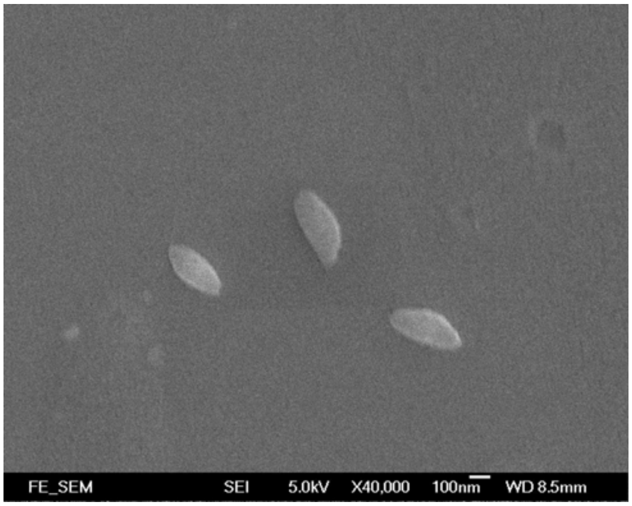

Figure 3.14 FE-SEM image of the ellipsoidal particle with an aspect ratio (Λ) of around 3 (major axis a = 400 nm, minor axis b = 130 nm)

3.5.3 Characterization of the tubular formation

Ellipsoidal particles could assemble into long nanotubes, nanofibers or bundle form in aqueous solution. This important feature is evident from the AFM phase image as shown in Figure 3.15. When the elongated hollow particles were lined up, they tended to display apparent boundary in the assembly. This feature was most pronounced from the intermediate connected nanotubes because the assembly was preferable in tip-to-tip connection. As the assembled structures proceeded up to 24 hrs, short nanotubes had connected themselves together via a tip-to-tip orientation to form longer nanotubes, as shown in Figure 3.15b. At this stage, the gap between each short nanotube was clearly observed. (Figure 3.16) However, when storage of the assembled nanotube for one month, the distinct boundaries or gaps between connected nanostructured materials were almost disappeared (Figure 3.17). These long nanotubes or nanofibers are very stable and the nanotubular length can be extended to several microns with diameter of the PEI-*g*-PMMA nanotubes between 75 and 90 nm.

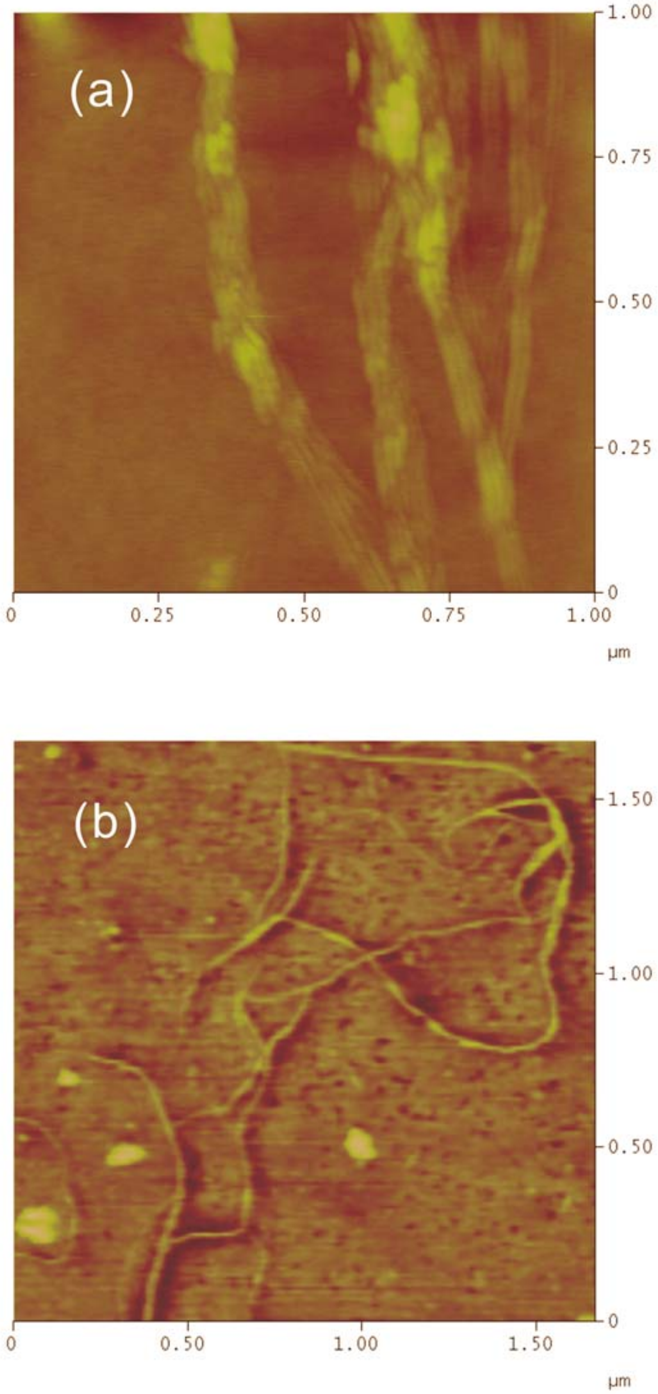

Figure 3.15 AFM images of the self assembled tubular nanomaterials of PEI-*g*-PMMA copolymer with tapping mode in (a) fluid (water) and (b) air.

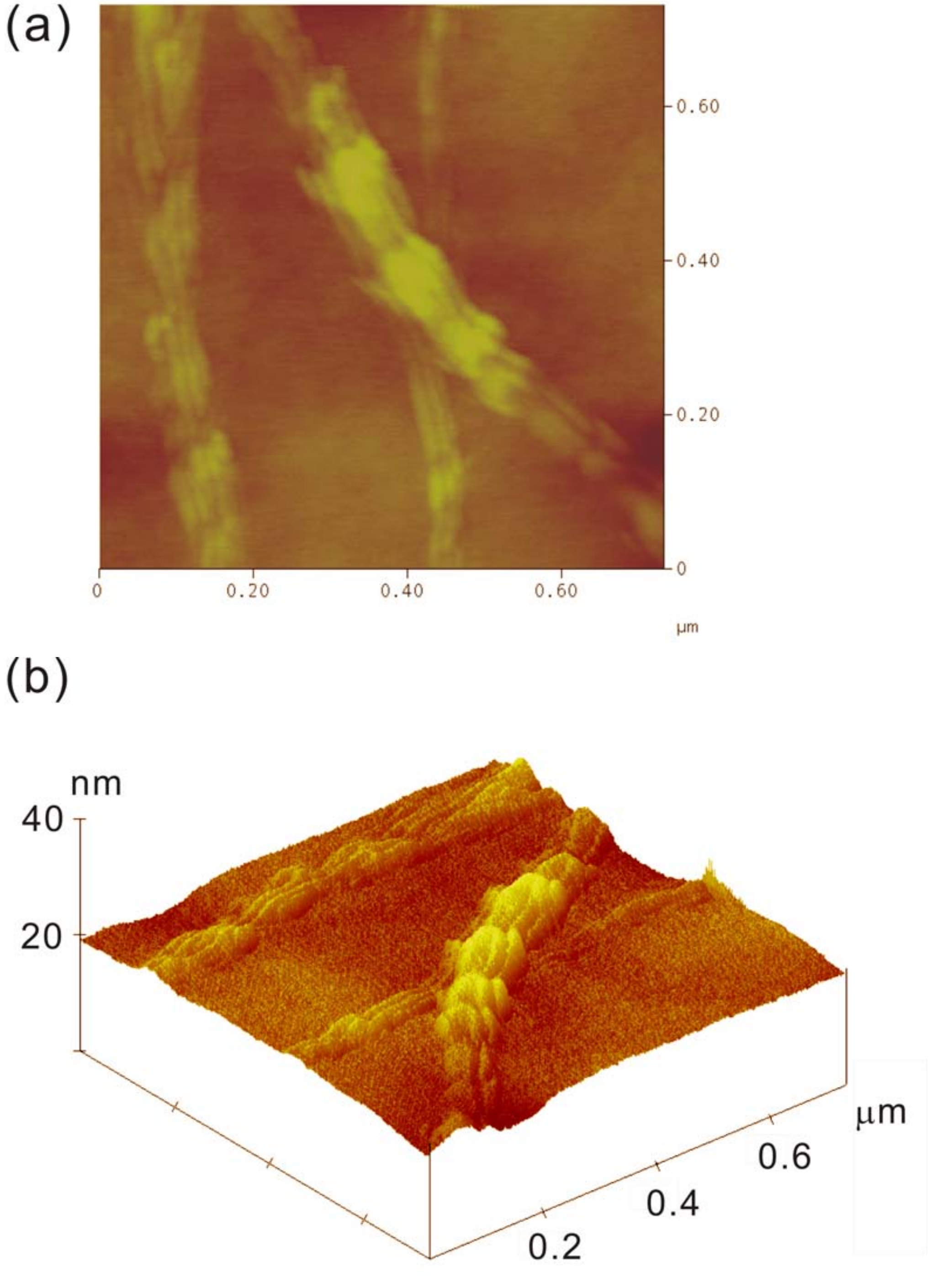

Figure 3.16 AFM images of the self-assembled tubular bundle structure of PEI-*g*-PMMA copolymer with fluid mode in (a) 2D and (b) 3D image profiles.

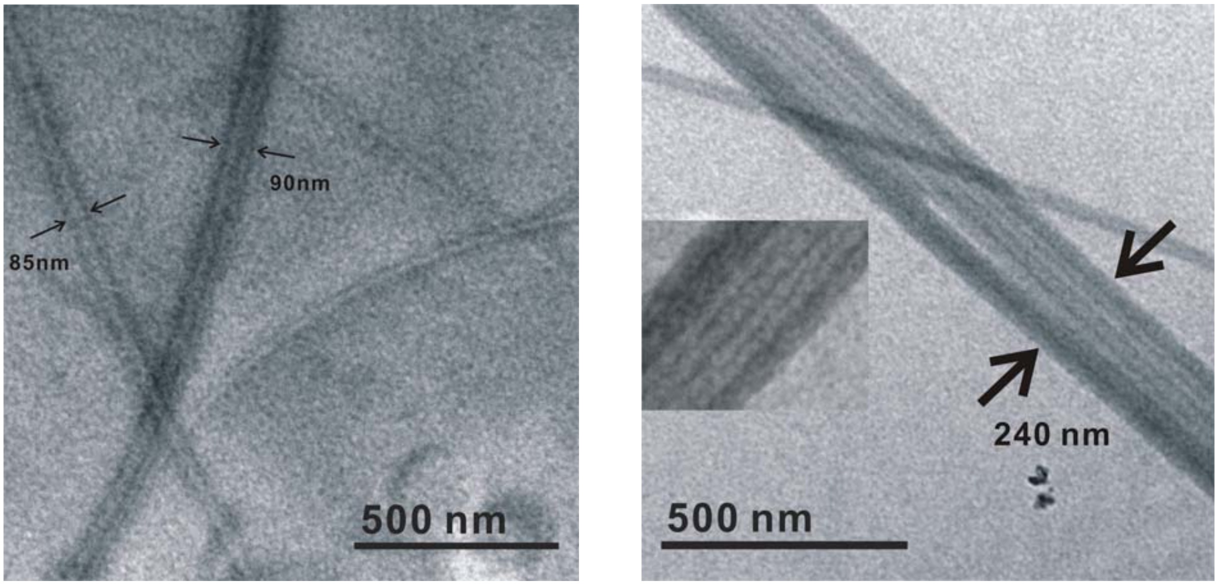

Figure 3.17 TEM images of long PEI-*g*-PMMA copolymer nanotubes.

3.6 Conclusion

This work provides a basis for creating PEI-*g*-PMMA nanotubular structure via directed assembly of elongated hollow particles. It has been found that tip-to-tip connection is a pronounced effect for elongated hollow particles on liquid-vapor interface, driven by high excess area near the highly curved (tip) regions. Curvature on the particle surface can be used to tune the excess area landscape and thereby favor modes of aggregation that are not preferred on lateral interfaces. For anisotropic nanoparticles, interfacial curvature can be used to orient the particles as they aggregate, allowing the tip-to-tip assembly.

The nanotubes assembled by our method are of nanometer scale diameter and up to tens of micrometers in length. It was proposed that there are three key factors governing the self-assembly process of the amphiphilic hollow particles under non-equilibrium conditions: (1) the amphiphilic hollow particles are elongated into ellipsoidal morphology under an appropriate stirring rate; (2) These elongated hollow particles direct the assembly preferentially via tip-to-tip connection under appropriate assembling conditions; (3) The aggregated ellipsoidal hollow particles coalesce into nanotubes through shear induced thinning process. This facile assembly approach is feasible in a large scale production of polymer nanotubular materials.

References

1. Andrade, J. D. *Polymer Surface Dynamics*, Andrade, J. D., Ed., Plenum Press: New York, **1988**.
2. Hou, Y.; Tulevski, G. S.; Valint, Jr P. L.; J. A. Gardella, Jr J. A.. *Macromolecules* **2002**, *35*, 5953.
3. Tingey, K. G.; Andrade, J. D. *Langmuir*, **1991**, *7*, 2471.
4. Tezuka, Y.; Ono, T. and Imai, K. *J. Coll. Interface Sci*. **1990**, *136(2)*, 408.
5. Takahara, A.; Jo, J.; Takamori, K.; Kajiyama, T. *Progress in Biomedical Polymers*, Gebelein, C. G.; Dunn, R., Eds., Plenum: New York, **1989**.
6. Ratner, B. D.; Weathersby, P. K.; Hoffman, A. S.; Kelly, M. A. ; Scharpen, L. H. *J. Appl. Polym. Sci*., **1978**, *22*, 643.
7. Lewis, K. B.; Ratner, B. D. *J. Coll. Interface Sci.* **1993**, *159*, 77.
8. Lukas, J.; Sodhi, R. N. S.; Sefton, M. V. *J. Coll. Interface Sci.* **1995**, *14*, 421.
9. Russell, T. P. *Science*, **2002**, *297*, 964.
10. Senshu, K.; Kobayashi, M.; Ikawa, N.; Yamashita, S.; Hirao, A.; Nakahams, S. *Langmuir*, **1999**, *15*, 1763.
11. Senshu, K.; Yamashita, S.; Ito, M.; Hirao, A.; Nakahams, S. *Langmuir*, **1995**, *11*, 2293.

12. Senshu, K.; Yamashita, S.; Mori, H.; Ito, M.; Hirao, A. and Nakahams, S. *Langmuir*, **1999**, *15*, 1754.
13. Mori, H.; Kirao, A.; Nakahama, S. *Macromolecules*, **1994**, *27*, 4093.
14. Ratner, B. D.; Castner, D. G., *Colloids and Surfaces B: Biointerfaces*, **1994**, *2*, 333.
15. Larson, R. G. *Rheol. Acta* **1992**, *31*, 497.
16. Polzonetti, G.; Russo, M. V.; Furlani, A.; Iucci, G. *Chem. Phys. Lett.* **1991**, *185*, 105.
17. Ratner, B. D.; Weathersby, P. K.; Hoffman, A. S.; Kelly, M. A. and Scharpen, L. H. *J. Appl. Polym. Sci*., **1978**, 22, 643.
18. Grymayer, W. F., *J. Polym. Sci. Symp*. **1974**, 44, 25.
19. Linner, J. G.; Liversay, S. A.; Harrison, D. S. and Steiner, A. T., *J. Hist. Cytochem.*, **1986**, 34, 1123.
20. Mackenzie, A. P., *Philos. Trans. R. Soc. London, B*, **1977**, 278, 167.
21. Lewis, K. B.; Ratner, B. D. *J. Coll. Interface Sci.* **1993**, 159, 77.
22. Lukas, J.; Sodhi, R. N. S.; Sefton, M. V. *J. Coll. Interface Sci.* **1995**, 14, 421.
23. Ratner, B. D. and Castner, D. G. Colloids and Surfaces B: *Biointerface*, **1994**, 2, 333.
24. Gilding, D. K.; Paynter, R. W. and Castle, J. E. *Biomaterials*, **1980**, 1, 163.
25. Larson, R. G. *Rheol. Acta* **1992**, *31*, 497.
26. Larson, R. G., "The Structure and Rheology of Complex Fluids," Oxford Univ. Press, New York, **1999**.
27. Wagner, N. J. *Curr. Opin. Colloid Interface Sci.* **1998**, *3*, 391.
28. Wallqvist, A.; Berne, B. J. *J. Phys. Chem.* **1995**, *99*, 2885.
29. Tetreault, N.; Miguez, H.; Ozin, G. A. *Adv. Mater.* **2004**, *16*, 1471.
30. Manoharan, V. N.; Elsesser, M. T.; Pine, D. J. *Science* **2003**, *301*, 483.
31. Yin, Y. D.; Lu, Y.; Xia, Y. N. *J. Am. Chem. Soc.* **2001**, *123*, 771.

32. Velikov, K. P.; Christova, C. G.; Dullens, R. P. A.; van Blaaderen, A. *Science* **2002**, *296*, 106.
33. Shevchenko, E. V.; Talapin, D. V.; Kotov, N. A.; O'Brien, S.; Murray, C. B. *Nature* **2006**, *439*, 55.
34. Kalsin, A. M.; Fialkowski, M.; Paszewski, M.; Smoukov, S. K.; Bishop, K. J. M.; Grzybowski, B. A. *Science* **2006**, *312*, 420.
35. Bibette, J. *J. Colloid Interface Sci.* **1991**, *147*, 474.
36. Hunter, R. J. *Foundations of Colloid Science*, 2nd ed.; Oxford University Press: Oxford, **2001**.
37. Dinsmore, A. D.; Yodh, A. G.; Pine, D. J. *Nature* **1996**, *383*, 239.
38. Lin, K.; Crocker, J. C.; Prasad, V.; Schofield, A.; Weitz, D. A.; Lubensky, T. C.; Yodh, A. G. *Phys. Rev. Lett.* **2000**, *85*, 1770.
39. Adams, M.; Dogic, Z.; Keller, S. L.; Fraden, S. *Nature* **1998**, *393*, 349.
40. Mason, T. G. *Phys. Rev. E* **2002**, *66*, 060402.
41. Phung, T. N.; Brady, J. F.; Bossis, G. *J. Fluid. Mech.* **1995**, *313***,** 181.
42. Forsyth, P. A.; Marcelja, S., Jr.; Mitchell, D. J.; Ninham, B. W. *Adv. Colloid Interface Sci.* **1978**, *9*, 37.
43. Vroege, G. J.; Lekkerkerker, H. N. W. *Rep. Prog. Phys.* **1992**, *55*, 1241.
44. Dogic, Z.; Fraden, S. *Phys. Rev. Lett.* **1997**, *78*, 2417.
45. Adams, M.; Dogic, Z.; Keller, S. L.; Fraden, S. *Nature* **1998**, *393*, 349.
46. van Bruggen, M. P. B.; van der Kooij, F. M.; Lekkerkerker, H. N. W. *J. Phys.: Condens. Matter* **1996**, *8*, 9451.

47. Vliegenthart, G. A.; van Blaaderen, A.; Lekkerkerker, H. N. W. *Faraday Discuss.* **1999**, *112*, 173.
48. van der Kooij, F. M.; Lekkerkerker, H. N. W. *Phys. Rev. Lett.* **2000**, *84*, 781.
49. Dresselhaus, M. S.; Dresselhaus, G.; Eklund, P. C. *Science of Fullerenes and Carbon Nanotubes*; Academic Press: San Diego, CA, **1996**.
50. Lieber, C. M. *Solid State Commun.* **1998**, *107*, 607.
51. Hu, J.; Odom, T. W.; Lieber, C. M. *Acc. Chem. Res.* **1999**, *32*, 435.
52. Agrait, N.; Yeyati, A. L.; Ruitenbeek, J. M. *Phys. Rep.* **2003**, *377*, 81.
53. Ding, J.; Liu, G.; Yang, M. *Polymer* **1997**, *38*, 5497.
54. Yu, Y.; Eisenberg, A. *J. Am. Chem. Soc.* **1997**, *119*, 8383.
55. Liu, G.; Yan, X.; Duncan, S. *Macromolecules* **2002**, *35*, 9788.
56. Raez, J.; Tomba, J. P.; Manners, I.; Winnik, M. A. *J. Am. Chem. Soc.* **2003**, *125*, 9546.
57. Kim, C. U.; Lee, J. M.; Ihm, S. K. *J. Fluorine Chem.* **1999**, *96*, 11.
58. Roco, M. C.; Williams, R. S.; Alivisatos, P. *Nanotechnology Research Directions*; Kluwer Academic: Dordrecht, The Netherlands, **2001**.
59. Tang, Z.; Kotov, N. A. *Adv. Mater.* **2005**, *17*, 951.
60. Cai, W. S.; Chettiar, U. K.; Kildishev, A. V.; Shalaev, V. M. *Nat. Photon.* **2007**, *1*, 224.
61. Tang, Z.; Kotov, N. A.; Giersig, M. *Science* **2002**, *297*, 237.
62. Tang, Z.; Kotov, N. A.; Magonov, S.; Ozturk, B. *Nat. Mater.* **2003**, *2*, 413.
63. Nikoobakht, B.; Wang, Z. L.; El-Sayed, M. A. *J. Phys. Chem. B* **2000**, *104*, 8635.
64. Jana, N. R. *Angew. Chem., Int. Ed.* **2004**, *43*, 1536.
65. Caswell, K. K.; Wilson, J. N.; Bunz, U. H. F.; Murphy, C. J. *J. Am. Chem. Soc.* **2003**, *125*, 13914.

66. Dujardin, E.; Hsin, L. -B.; Wang, C. R. C.; Mann, S. *Chem. Commun.* **2001**, 1264.

67. Nie, Z.; Fava, D.; Kumacheva, E.; Zou, S.; Walker, G. C.; Rubinstein, M. *Nat. Mater.* **2007**, *6*, 609.

68. Khanal, B. P.; Zubarev, E. R. *Angew. Chem., Int. Ed.* **2007**, *46*, 2195.

69. Würger, A. *Phys. Rev. E* **2006**, *74*, 041402.

70. Aveyard, R. *et al. Phys. Rev. Lett.* **2002**, *88*, 246102.

71. Israelachvili, J. N. in *Intermolecular and Surface Forces* 2nd ed.; Academic, London, **1992.**

Chapter 4

Effect of Solvent Composition in Morphological Changes

4.1 Introduction

The effect of solvent on polymer assembly is usually studied in a mixture of two types of solvents in three aspects: (1) The effect of co-solvent volume ratio or the solvent composition; (2) The nature of the common solvent; and (3) The effect of selective solvent. Varying the solvent composition changes polymer solvent interaction parameter (χ), thus affects the interfacial free energy and the resulting assembled morphology. In this study, the effect of solvent composition has been investigated in different water contents in DCM/water mixture. The resulting morphologies with the use of different solvent compositions were captured and visualized by SEM and TEM microscopies.

4.2 Experimentals

4.2.1 Materials and Methods

Amphiphilic particles that consist of poly(methyl methacrylate) cores and branched poly(ethyleneimine) shells have been synthesized according to procedures described in the Section 2.2 in Chapter 2. The assembling process was carried out in a 20 mL jacketed flask covered with a Whatman filter paper (Whatman 2). Freeze-dried PMMA/PEI particles (0.05 g) were first mixed with 5 mL of dichloromethane. The suspension was gently stirred at 150 rpm at room temperature for 3 hrs to extract the PMMA homopolymer from the particle cores. Deionized water was then added dropwise (4.8 mL/min) to the DCM solution containing both the hollow particles and homopolymer to various DCM/water volume ratios (8/2; 7/3; 5/5; 4/6; 3/7; 2/8; 1/9), respectively. The resulting DCM/water mixture was subsequently stirred at 350 rpm with a magnetic stirrer. During this process, the solution temperature was thermostated by a water circulation using a temperature controlled circulator (IMT InMedtec Co.) at 25°C. To study morphological transitions, samples were withdrawn from the top aqueous layer for microscopic analysis. After 24 hours, the DCM had been completely removed through evaporation, some PMMA homopolymer (white solids) were suspended in water. They were simply removed by filtration, followed by drying in a vacuum oven for 24 hrs.

4.2.2 Turbidity measurements

Turbidity was measured by a Hewlett Packard HP 8453 Photo-diode Array UV-Visible spectrometer with an UV-Visible ChemStation software. The measurements were carried out at a wavelength of 700 nm where the absorption of the aggregates was minimized. The sample vials were sealed with Teflon tape and placed in a temperature cell in which the temperature was controlled by a temperature controller. Deionized water was used as the reference for all the measurements.

4.2.3 Characterization using electron microscopy

To study morphological transformation under different co-solvent volume ratios, the scanning electron microscopy images were obtained using a JEOL-JSM 6335F field-emission scanning electron microscopy (FE-SEM) at an accelerating voltage of 5 kV. All SEM samples were prepared by placing a small drop of dilute particle dispersion (~ 500 ppm) on a mica substrate, and allowed drying for 24 hrs at room temperature. The completely dried sample was then sputtered with a thin layer of gold under vacuum to a depth of approximately 1-2 nm.

Transmission electron microscopy micrographs were obtained using a JEOL 100 CXII TEM at an accelerating voltage of 100 kV. Sample was prepared by wetting a carbon-coated copper grid with a small drop of dilute particle dispersion in water (10μL, 500 ppm). Upon drying, the particles were stained with a tiny drop of 0.5% w/w phosphotungstic acid solution (PTA) for 30 seconds, and then dried at room temperature before analysis.

4.3 Results and discussion

The self-assembly behavior of amphiphilic hollow particles of PEI-*g*-PMMA in different dichloromethane/water mixture has been studied systematically. Water is a selective solvent for the PEI segment, thus variation of water content may lead to generation of different particle assemblies. Figure 4.1 shows a set of SEM images of the morphologies of the assemblies under different water to DCM ratios. The concentration of the hollow particles was 5 mg/mL. At 10 vol. % water, the particles remained spherical (Figure 4.1a), but they started to change from spheres and short tubular aggregates at 30 vol. % water (Figure 4.1c). At 40 vol. % water as shown in Figure 4.1d, the tubular network formed which consisted of self-assembled tubular-like cylinders interconnected by both “Y-” and “T-”shaped junctions. The tubular-like network structure was highly entangled with a macroscopic size and multiple junctions. Such a network structure could be considered as counterpart of the bicontinuous structures formed in the bulk.[1] The network structure was stable, and did not change for several months if no additional water was added into the system. (Figure 4.2)

It is known that both the interfacial area occupied per chain and degree of stretching of the PMMA graft chains within the core are lower for the spherical geometry than those in the tubular geometry.[2] Therefore, existence of the spherical end caps of the short nanotube is thermodynamically unfavorable. The end capping energy has been found to be curvature-dependent, and it decreases as the spontaneous curvature decreases when junctions were formed.[6] In order to reduce the end caps, the tubular-like morphology may also form toroids or dongnut-like structures which was observed in our copolymer nanotubular system (Figure 4.13 and 4.14). Yet the toroid formation requires that the tubular-like structures should be flexible enough in order to bend (with a relatively lower bending energy).[7]

In a DCM/water system, the tubular-like cylinders with PMMA grafts may not be sufficiently flexible at room temperature due to the high glass transition temperature of the PMMA chains. One of the driving forces to form the network may be attributed to the reduction of the free energy by decreasing the number of end caps to form the interconnections if the length of the tubular-like structures is not too long. Therefore, formation of the network is a result of interplay among the bending energy (curvature), the end capping energy, and the network configurational entropy. One factor which influences the bending energy and the network entropy is the number density of the junctions. All these factors contribute to the free energy of the network which can be expected to attain a configuration, thus minimizing the free energy. This would decide the relative appearance of end caps and junctions. In the case of graft copolymers, the PMMA chain stretching and steric interactions at the junctions are also need to be considered.

However, the length of the tubular aggregates becomes increasingly long (several μms) with a decreased population of spherical structures. At a water concentration of 70 (vol.) %, a morphological change occurs to form exclusively long nanotubes without bumps (Figure 4.1f). Further increasing the water concentration to 80 and 90 (vol.)%, only nanofiber morphology with average diameter of 120 nm appeared (Figure 4.1g and 4.1h). Thus, morphology changes to exclusively nanotubes occurred at water contents between 70 and 90 (vol.)%. The morphologies were frozen because the observed morphology did not change further.

In the case of amphiphilic graft copolymers, the formation of “Y” junctions results in saddle points with negative curvature, and thus the net curvature of the tubular network is reduced.[2] A drawing of the “Y” junction is shown in Figure 4.3 where C is the negative curvature. Therefore, as the “Y” junctions populate, the net curvature would decrease and finally, lead to formation of a network. The network is also considered to have favorable configurational entropy due to the existence of several possible configurations of the network.[3] These different configurations can be varied in terms of different PMMA graft length distributions of the network. However, there is also a loss in entropy as the free ends of the tubular-like structures are constrained to meet at a junction. In the tubular-like cylinder network, free ends of the nanotubes[4,5] are strongly eliminated due to the formation of interconnections.

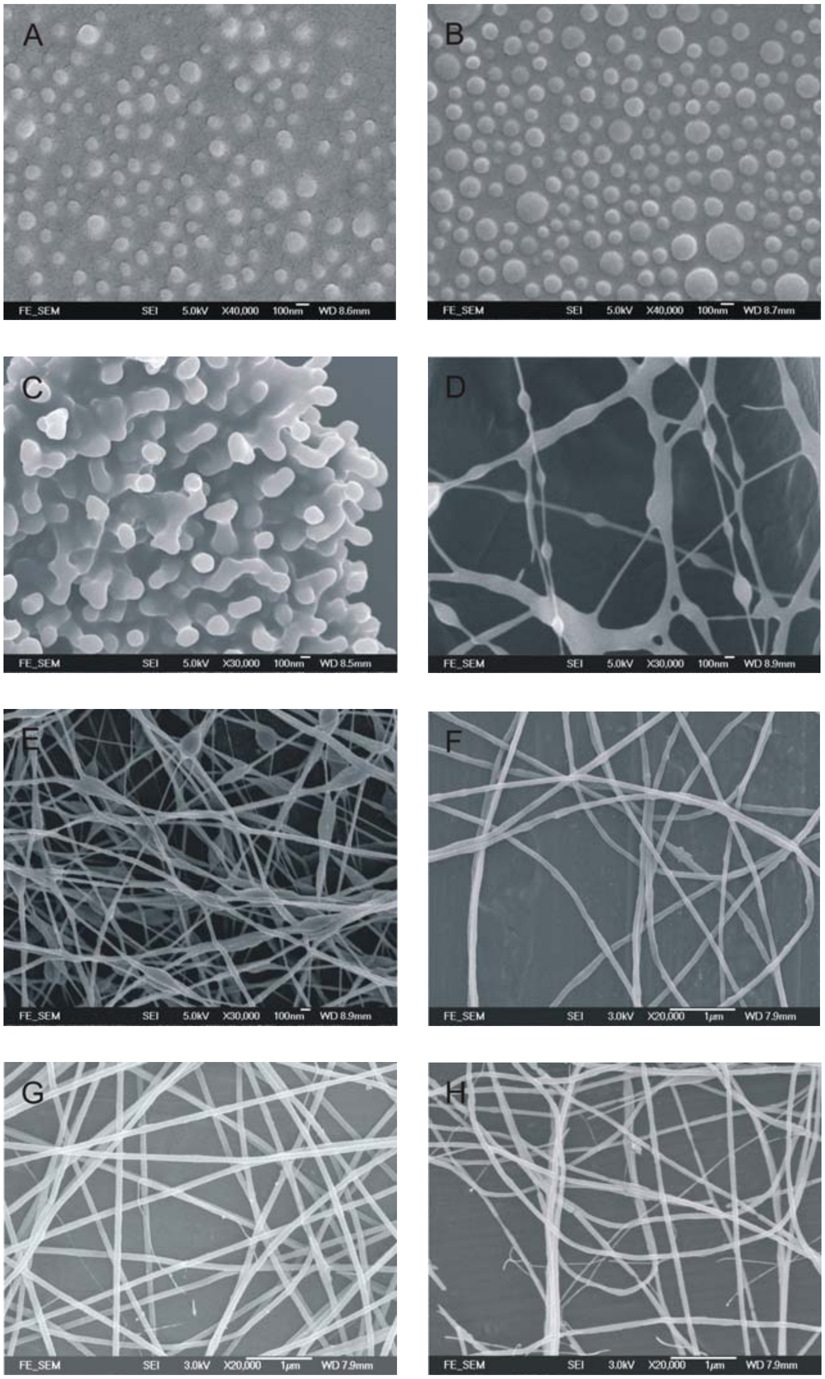

Figure 4.1 Morphological transitions of various water contents in the DCM/water system (initial particle concentration was 5 mg/mL). (a) vesicle-like morphology at 10 vol.% water; (b) a larger vesicle-like morphology at 20 vol.% of water; (c) aggregated short tubular morphology at 30 vol.% water; (d) nanotubular network morphology at 40 vol.% water (e) nanotubular morphology with ellipsoidal bumps at 50 vol.% water; (f) nanofiber-like morphology at 70 vol.% water; (g) nanofiber-like morphology at 80 vol. % water; (h) nanofiber-like morphology at 90 vol.% water.

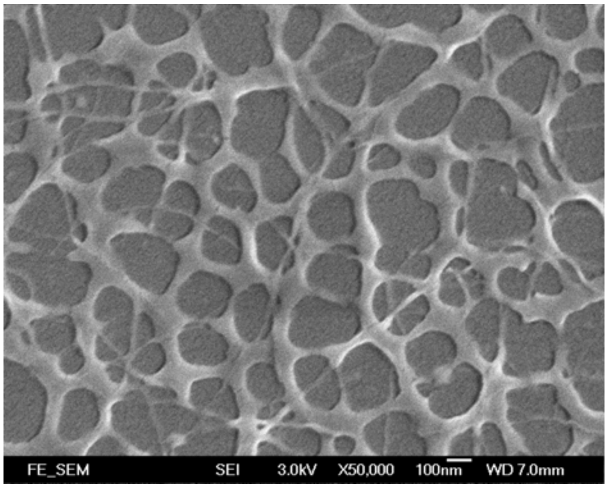

Figure 4.2 FE-SEM micrograph of nanotubular network morphology at 40 vol. % water after storage for 6 months.

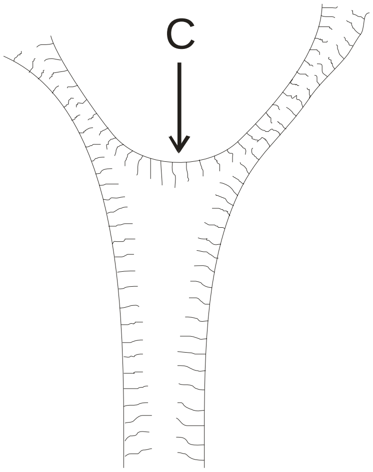

Figure 4.3 Schematic diagram of tubular-like network with “Y” junction.

Figure 4.4(a-d) showed a set of TEM images of the hollow particle morphologies in DCM/water system with a 5 mg/mL initial particle concentration. At low water volume ratios (10-20 vol. %), the hollow particles appeared to be spherical-like vesicle (Figure 4.4a and b).

They changed to short tubular structures (tube diameter: 200- 250 nm) at water volume ratio of 30 vol. % (Figure 4.4c). At water content of 40 vol. % as shown in Figure 4.4d, the tubular network with ellipsoidal bumps could be observed. However, the length of the tubes became longer (up to several μms) with a decreased population of spheres. At water volume ratio of 50 vol. %, a morphological change occurred to form exclusively long nanotubes without network junction, but the ellipsoidal bumps along the tubes are still exist. On further increasing the water volume to 70 vol.%, only nanotubular morphology appeared (Figure 4.5). Similar morphologies in stable tubular form were obtained with further increase of water content up to 90 vol. %.

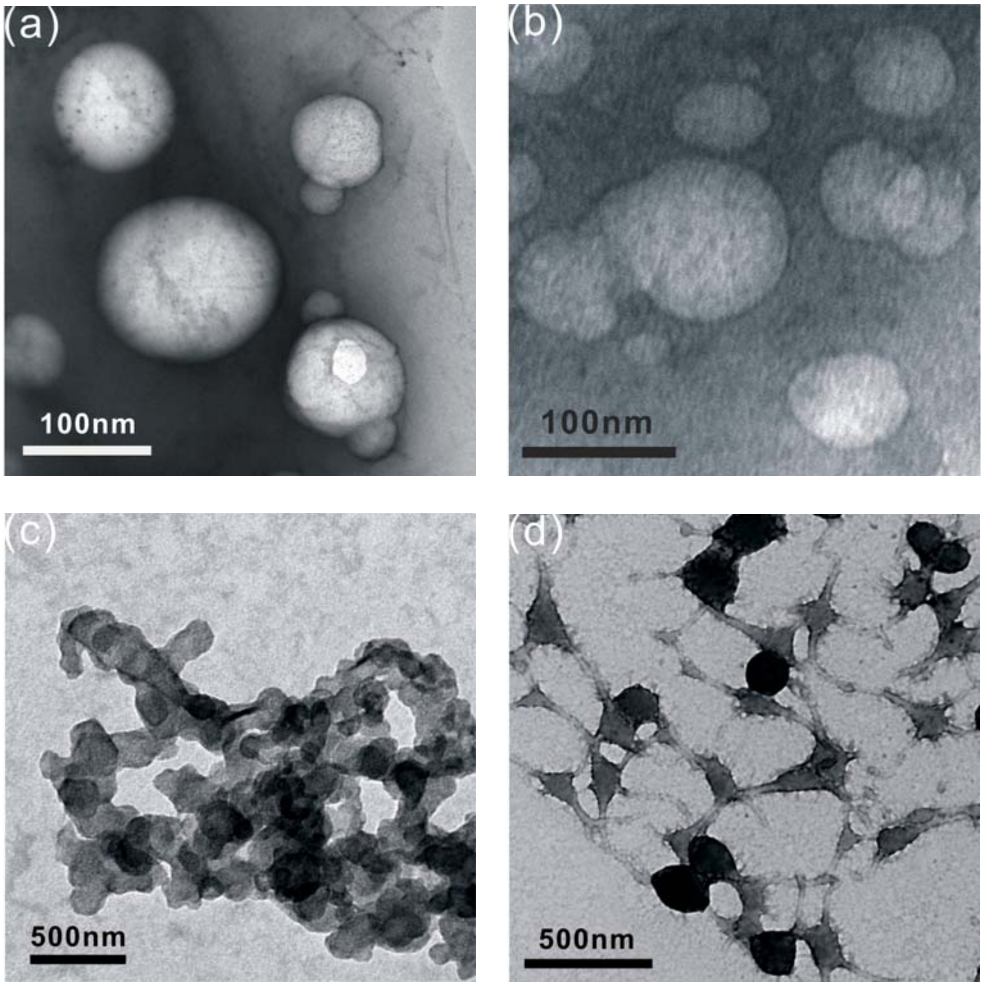

Figure 4.4 TEM micrographs of morphologies of various assemblies formed after mixing PEI-*g*-PMMA hollow particles in different DCM/water volume ratios (particle concentration = 5 mg/L. (a) 10 vol. % water, (b) 20 vol.%.water; (c) 30 vol.% water; (d) 40 vol.% water

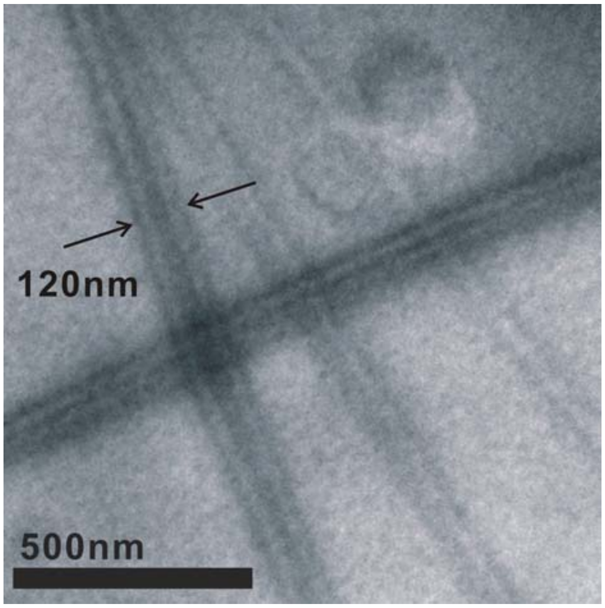

Figure 4.5 TEM micrograph of nanotubular morphologies with diameter ranged from 60 to 120 nm were observed at water content of 70 vol.%.

Turbidity experiments using two different hollow particle concentrations (5 and 50 mg/mL), have also revealed the effect of water contents on the morphological changes. Figure 4.6 shows that at low particle concentration (5 mg/mL), the turbidity started to increase at 20 vol.% water, but the changes were not very obvious. When increasing the particle concentration up to 50 mg/mL, the turbidity changes became significant. It increased gradually with increasing the water contents from 10 to 30 vol.%. But a considerable turbidity increase occurred when 40 vol.% water was used. Further increasing water contents from 50 to 70 vol. % only slightly increased the turbidities. There was almost no change at water contents of 70, 80 and 90 vol.%., indicating the formation of similar nanotubular assemblies at these ratios. These results indicated that network formation started to occur at 40 vol % water content, and complete nanotube formation at 70 vol. % water. These findings are consistent with SEM and TEM observations.

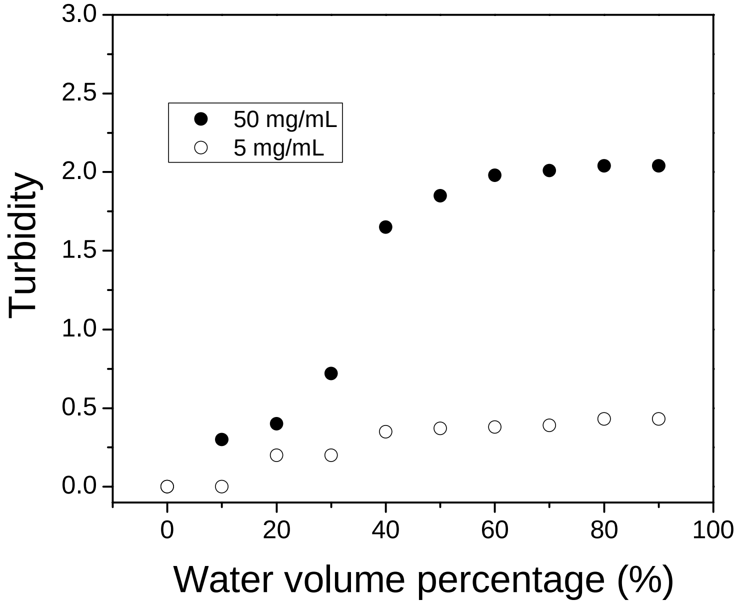

Figure 4.6 Turbidity measurements as a function of water volume percentage.

The water effect on the morphological transformation of hollow particles to tubular nanostructures may be explained on the basis of polymer-solvent interactions. As water is added, the solvent becomes progressively poorer for the PMMA graft chains. In fact, the polymer-solvent interaction property can be estimated through calculation using the van Laar-Hildebrand equation[9] as expressed in Eq. (4.1)

$$\chi_{P-S} = \frac{V_s}{RT}\left(\delta_P - \delta_S\right)^2 \tag{4.1}$$

where V_s represents the molar volume of the single solvent, δp and δs are the solubility parameters of the polymer and selective single solvent, respectively.

The dichloromethane has a solubility parameter, δ_{DCM}, of 20.2 $(MPa)^{1/2}$, while PMMA is equal to $19(MPa)^{1/2}$.[25] Thus DCM is a selective solvent for the PMMA chains. On the other hand, the solubility parameter of PEI is 45 $(MPa)^{1/2}$, while water is 48 $(MPa)^{1/2}$. Thus water is a selective solvent for the PEI chain. The polymer-solution interaction parameter values ($\chi_{P\text{-}S}$) for both systems can be calculated as $\chi_{PEI\text{-}water} = 0.065$ and $\chi_{PEI\text{-}DCM} = 15.862$. The $\chi_{PEI\text{-}DCM}$ value is approx. 244 times higher than that of the $\chi_{PEI\text{-}water}$, indicating that dichloromethane is a much poorer solvent for PEI as compared to water. Therefore, adding a controlled amount of water can result in a substantial increase in the interfacial free energy, thus leading to the increase of PMMA chain aggregation in order to minimum the surface energy. At the same time, graft PMMA chains exhibited in highly packed state to minimize the surface area contact with water.

4.4. Mechanism of morphological transformation

Based on the results from SEM and TEM observations, turbidity study and polymer-solvent interaction theory, a plausible assembly mechanism for the observed morphological changes are proposed. Figure 4.7a shows a drawing of spherical-like morphology formed at low water volume ratio. On increasing water concentration, short tubular-like structures are formed. The interacting spheres under shear-induced elongation and aggregation can lead to the formation of short tubes (Figure 4.7b). As more water is added, more elongated hollow particles can assemble into short tubular structures, thus increasing the length of the tubes and decreasing the relative population of the spheres. At 40 vol. % water, tubular-like materials aggregate into network morphology with ellipsoidal bumps along the nanotubes as shown in Figure 4.8. (Actual diameter of ellipsoidal bump would be somehow larger than the resulting nanotube diameter). Adding more than 40 vol. % water leads to the formation of extended tubular structures with ellipsoidal bumps. These bumps eventually disappear when water contents are above 70 vol. %. The shrinkage of ellipsoidal bumps can be attributed to both the shear induced thinning and hydrophobic interaction among the PMMA graft chains. The well-defined nanotubular morphology is maintained and uniformly distributed in diameter as the water volume ratio greater than 70 % (Figure 4.9).

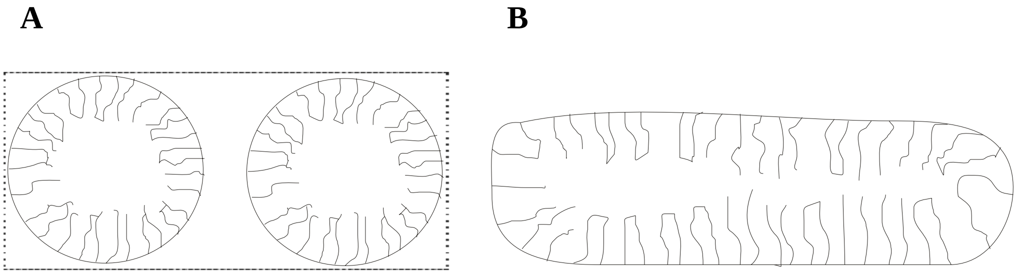

Figure 4.7 Schematic diagram of (A) spherical and (B) short tubular morphologies of the PEI-g-PMMA hollow particles observed at low water volume ratio.

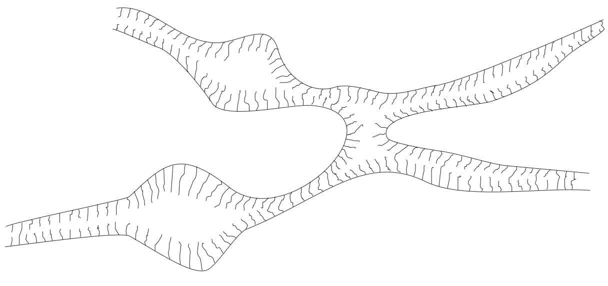

Figure 4.8 Schematic diagram of tubular network morphology with ellipsoidal bumps.

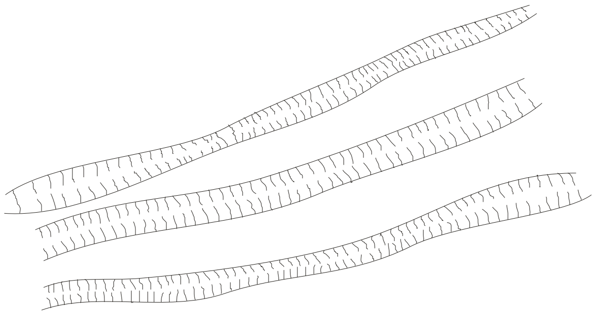

Figure 4.9 Schematic diagram of tubular structures with uniformly distributed diameter.

4.5 Thermodynamic and Kinetic Aspects of the Morphological Changes

The criteria for achieving stable morphologies are that the obtained morphologies must be stable over a long period of time and the morphological changes due to varying the selective solvent volume should be reversible.[7] A question is whether the morphological changes in various DCM/water volume ratio is the thermodynamically driven process or kinetically driven process. In other words, does the rapid rate of adding water affect the morphological changes? It is assumed that the evolution towards equilibrium morphologies depends upon the mobility of the PMMA graft chains, which are associated with the solubility of the amphiphilic graft copolymer in the solvent. Our experience suggests that the rate of adding water into the system must be slow enough and the amount of water added each time must be drop-wise in order to obtain the stable morphologies. The nanotubular morphologies observed in Figures 4.5 is still quite stable after 6 months. In order to prove that the self-assembled morphologies obtained are really in thermodynamic driving process, the water was added in a sufficiently fast rate (1 mL/sec) to generate kinetically "quenched" morphologies. We then carried out annealing experiments to monitor whether these kinetically generated morphologies could return to the thermodynamically stable morphology. We started with a system which contained 5 mg/mL PEI-*g*-PMMA hollow particle in DCM, the water was added at a fast rate (1 mL/min) to reach a water volume ratio of 30 and 70 vol.%, respectively. Figure 4.10 shows "quenched" morphology in 70 vol.% water. After annealing these assemblies at room temperature for 1 month, the morphology changed to tubular-like structures with diameter ranged from 50 to 70 nm as shown in Figure 4.11. Therefore, the tubular-like structure should be the thermodynamically stable morphology.

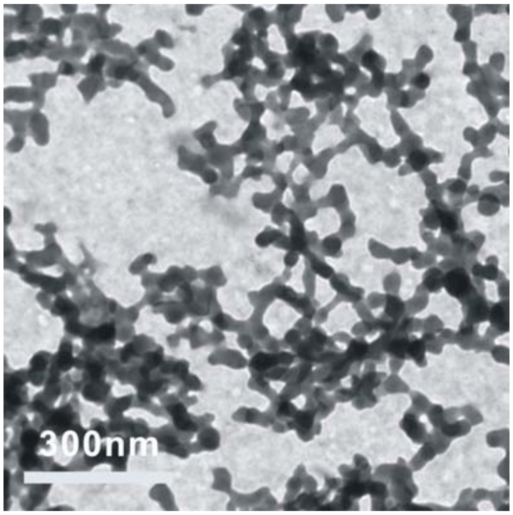

Figure 4.10 Kinetically trapped morphologies formed by a fast rate of water addition (1 mL/min) to a DCM containing 5 mg/mL hollow particles. Water was added to 70 vol. %.

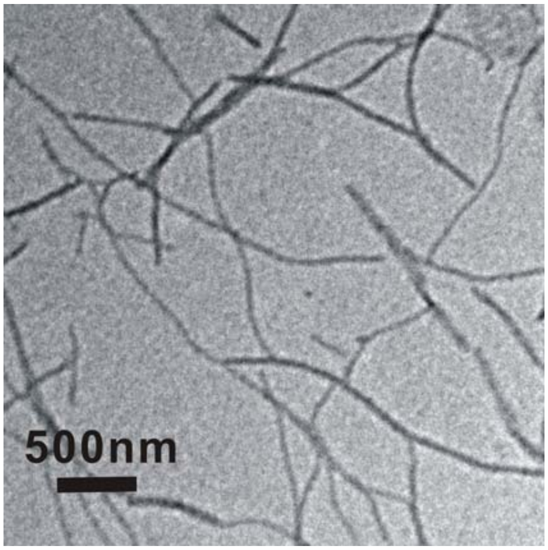

Figure 4.11 Kinetically trapped morphologies formed by a fast rate of water addition (1 mL/min.) to a DCM solution containing 5 mg/mL hollow particles up to 70 vol. % water, then stored the resulting solution at room temperature for 1 month.

A fast rate of water addition may form kinetically trapped morphologies and no distinct morphological transitions can be induced if the rate of water addition is too fast. Figure 4.12 shows raspberry–like submicron sized particles which are formed in large aggregates when water addition is 10 times faster (0.17 mL/sec). The formation of raspberry-like shaped aggregates with thread-like connected structure may be due to the non-uniform aggregation of PMMA chains with rapid change in solvent composition. Since the stretching degree of PMMA chain is highly restricted when the solvent quality becomes immediately poor, the rapid addition of water can vitrify the extension of PMMA chains in thread-like morphologies at the aggregate surface as indicated in Figure 4.12. The diameter of raspberry-like aggregates was ranged from 70 nm to 300 nm. Although kinetically "quenched" morphologies can be achieved through a fast rate of adding water, the thermodynamically stable morphology can always be recovered as long as the system is annealed for sufficient time. The equilibrium time required to recover the thermodynamically stable morphologies depends on the PMMA chain dynamics, which is in turn dependent on the solvent composition.[7] At high water content, the chain dynamics would be slow as compared to low water content because water is a poor solvent for PMMA and the chain interaction forces would also increase as the inner core becomes shrinked.[8] Thus, the annealing time required to recover the thermodynamically stable morphologies is strongly relied on the composition of DCM/water mixture in our system.

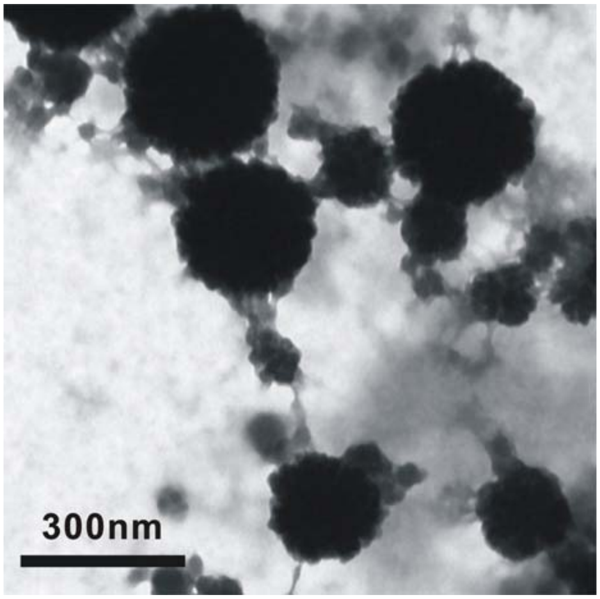

Figure 4.12 Kinetically trapped morphologies formed by a fast rate of water addition (0.17mL/sec) to a 5 mg/mL initial hollow particle solution in DCM, water was added up to 70 vol. %.

In an extreme case, if water is added rapidly (1 mL/sec) to a DCM solution up to 70 vol.%, spherical-like vesicles (toroid morphology) are obtained as kinetically trapped morphologies (Figure 4.13a). This is because, in case of rapid change in solvent environment, the $\chi_{\text{polymer-solvent}}$ is small and the expected morphologies may not be thermodynamically accessible.

The self assembled vesicles are expected to be three dimensional. In order to confirm this, the carbon-coated Cu grid was tilted to 45° for TEM observation. Figure 4.13b shows the TEM images of toroid-like structures and clearly indicates that these aggregates are three-dimensional and the size distribution of the toroid structures was very wide (50 to 300 nm).

The aggregates were found not to change after 6 months in the solution as illustrated from FE-SEM micrograph in Figure 4.14a but exhibited slightly distortion at vesicular surface after 1 year storage as shown in Figure 4.14b.

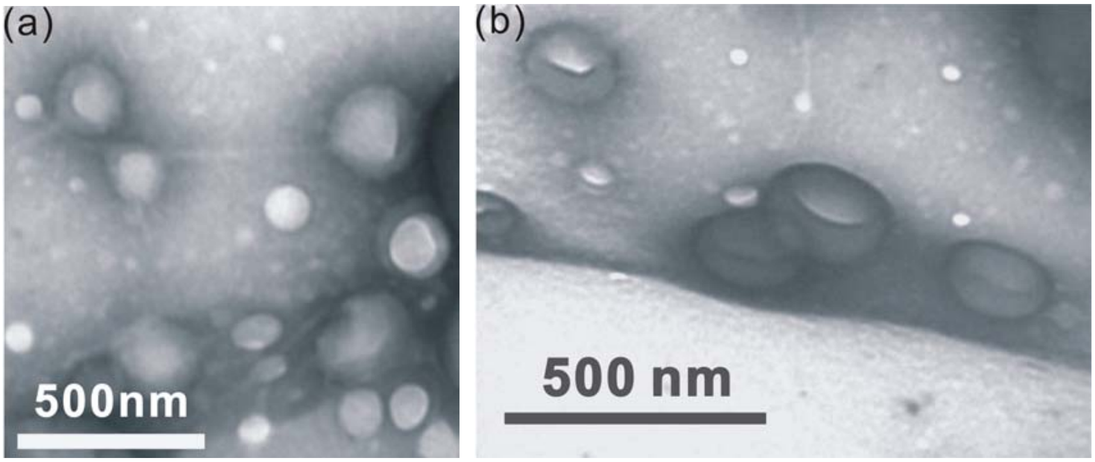

Figure 4.13 Kinetically trapped toroid morphologies formed by a fast rate of water addition (1 mL/sec) to a DCM solution containing 5mg/mL hollow particle up to 70 vol. % water. (a) Planar view; (b) Tilting the carbon-coated Cu grid to 45^{o}.

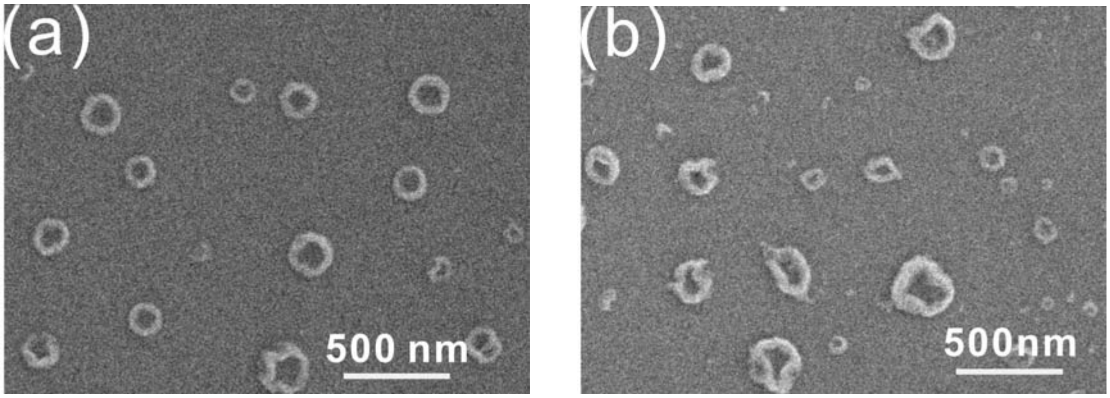

Figure 4.14 Kinetically trapped toroid morphologies formed by an extremely fast rate of water addition (1mL/sec) to a DCM solution containing 5mg/mL particle up to 70 vol.% water. The sample was stored for (a) 6 months and (b) 12 months, respectively.

4.6 Conclusion

In this study, the effect of DCM to water ratio on the morphological transition of the assembled hollow particles under fixed stirring rate (350 rpm) was examined. Increasing water content in the DCM/water mixture leads to transforming the spherical hollow particles to tubular nanostructure via network morphology intermediate. This transformation process was monitored by capturing the intermediate morphologies and observing them with SEM and TEM. In addition, the morphological changes in different water to DCM contents were confirmed by the turbidity study. The formation of the network or tubular nanostructures at different water to DCM ratios are governed by interplay between end capping energy, bending energy (curvature) and the network configurational entropy. The final configuration of the morphology should be one which minimizes the free energy. Rate of water addition was also investigated to gain insight into the the driving force for these morphological changes. Results suggest that the nanotubes generated are thermodynamically stable structures. In addition, fast addition of water could also generate other interesting nanostructures such as spherical-like vesicles.

References

1. Hasegawa, H.; Tanaka, H.; Yamasaki, K.; Hashimoto, T. *Macromolecules* **1987**, *20*, 1651.
2. Choucair, A.; Eisenberg, A. *Eur. Phys. J.* E **2003**, *10*, 37.
3. Tlusty, T.; Safran, S. A. *Journal of Phys.: Condens. Matter* **2000**, *12*, A 253.
4. Jain, S.; Bates, F. S. *Science* **2003**, *300*, 460.
5. Bernheim-Groswasser, A.; Wachtel, E.; Talmon, Y. *Langmuir* **2000**, *16*, 4131.
6. Vab dee Schoot, P.; Wittmer, J. P. *Macromol. Theor. Simul*. **1999,** *8*, 428.
7. Shen, H.; Eisenberg, A. *J. Phys. Chem. B* **1999**, *103*, 9473.
8. Tian, M.; Qin, A.; Ramireddy, C.;Webber, S. E.; Munk, P.; Tuzar, Z.; Prochazka, K. *Langmuir* **1993**, *9*, 1741.
9. Barton, A. F. M. *Handbook of Polymer-Liquid Interaction Parameters and solubility parameters*; CRC Press: Boston, MA, **1990**, p. 12.

Chapter 5

Effect of Reaction Temperature on Structural Transitions of Hollow Particles and Nanotubes

5.1 Introduction

Since the theory of self-assembly of amphiphiles to micelles have been well established, the fundamental understanding in their micellization may provide some insights into our system using the amphiphilic hollow particles as building block. Equation 5.1 shows the standard free energy change for transferring 1 mol of amphiphile from the solution to the micellar phase. ΔG_m^0 is given in terms of the dominant standard enthalpy ΔH_m^0, and the negative standard entropy ΔS_m^0 of micellization per mol of amphiphile. The entropy contribution usually dominates the micellization process in aqueous solutions, with the enthalpy playing a minor role.

$$\Delta G_m{}^0 = \Delta H_m{}^0 - T\Delta S_m{}^0 \qquad (5.1)$$

The micellization free energy values are negative since thermodynamically stable micelles are formed spontaneously. Since the hydrophobic polymer in water disrupts intermolecular hydrogen bonding of water molecules and creates a cavity which is devoid of the water molecules, the presence of the hydrophobic moieties significantly decreases water entropy owing to the cavity formation. At the surface of the cavity, water molecules rearrange in an orderly manner. This results in a thermodynamically unfavorable decrease in entropy. To compensate for the loss of entropy, water molecules force the hydrophobic molecules to cluster and thus occupy the minimum space.

However, when hydrophobic groups aggregate in the aqueous solution in a closely packed domain, the random hydrogen-bonding structure in the water is restored at a large extent, and the water entropy increases. This overcomes the loss of entropy due to localization of the hydrophobic segments.

Assuming an equilibrium between unimer and micelle is given by [4,5]

$$\Delta G^0 = RT\ln(X_{CMC}) \tag{5.2}$$

where *R* is gas law constant, T is the absolute temperature, and X_{CMC} is the critical micelle concentration (CMC) expressed in mole fraction units at temperature T**.** The micellization free energy values, ΔG^o, are negative. Since thermodynamically stable micelles are formed spontaneously; the ΔG^o becomes more negative at a higher temperature, resulting in a stronger driving force for micellization. Thus it is anticipated that a positive entropy contribution may be the driving force for aggregation of the PEI-*g*-PMMA hollow particles due to an increase in solution entropy.

The aggregation behaviors of hollow particles under various temperatures have been investigated in order to gain insights into the temperature-induced clustering-collapse transition of these amphiphilic graft copolymers. The PMMA-*g*-PEI hollow particles are comprised of hydrophobic PMMA chains located at inner shell with hydrophilic PEI chains at the outer shell. The morphological changes of the hollow particles and nanotubes under various temperature annealing conditions were observed by transmission electron microscopy. Turbidity of particle dispersion as a function of temperature was also investigated using a UV-vis spectrometer.

5.2 Materials, Methods and Characterization

Amphiphilic core-shell nanoparticles that consist of poly(methyl methacrylate) cores and branched poly(ethyleneimine) shells have been synthesized according to method described in Section 3.1 of Chapter 3. The assembling process was carried out in a 20 mL jacketed-flask covered with a Whatman filter paper (Whatman 2). Freeze-dried PMMA/PEI particles (0.05 g) were first mixed with 8 mL of dichloromethane. The suspension was gently stirred at 150 rpm with a magnetic stirrer at room temperature for 3 hrs to extract the PMMA homopolymer from the cores. Deionized water was then added dropwise (4.8 mL/min) to the DCM solution containing both the hollow particles and homopolymer to a DCM to water volume ratio of 3:7 (v/v). The resulting DCM/water mixture was subsequently stirred in a flask at 150 rpm with magnetic stirrer. During the process, the solution temperature was thermostated by a water circulation using a temperature-controlled circulator (IMT InMedtec Co.) at various solution temperatures (15°C, 25^{o}C, 35^{o}C and 45^{o}C). After completely evaporating the DCM from the solution (the complete DCM evaporation times are 48 hrs for 15^{o}C; 24 hrs for 25^{o}C; 18 hrs for 35^{o}C; 10 hrs for 45^{o}C, respectively), the insoluble PMMA homopolymer (white solids) suspended in water was simply removed by filtration, followed by drying it in a vacuum oven. The aqueous solution containing hollow particles was annealed at the corresponding temperature for 1hr before sample collection for TEM observation.

To study the effect of annealing temperature on the morphological changes of the preformed nanotubes, the nanotubes were first prepared according to the following procedure: After extraction of PMMA homopolymer in dichloromethane as described above, deionized water was added dropwise (4.8 mL min^{-1}) to the DCM solution containing both the hollow particles and homopolymer to a DCM to water vol. ratio of 3:7. The resulting DCM–water mixture was subsequently stirred at 350 rpm with a magnetic stirrer. During this process, the solution temperature was thermostated at 15°C by a water circulation using a temperature-controlled circulator (IMT InMedtec Co.). After 48 hours, the DCM was completely evaporated. The PMMA homopolymer (white solids) suspended in water was then removed by a simple filtration. The morphology of the assembled nanotubes was observed by transmission electron microcopy. The nanotube solution was subsequently transferred into a preheated jacketed-flask, and annealed at 25, 35, 40 and 45°C for 1 hr.

5.2.1 Turbidity measurements

Turbidity was measured by a Hewlett Packard HP 8453 Photo-diode Array UV-Visible spectrometer with UV-Visible ChemStation software. The measurements were carried out at a wavelength of 700 nm where the absorption of the aggregates was minimized. The sample vial was sealed with a Teflon tape and placed in a temperature cell in which the temperature was controlled by a temperature controller. Deionized water was used as the reference for all measurements.

5.2.2 Morphological investigation by Transmission Electron Microscopy

The size and morphology of hollow particles were observed using a JEOL JEM 100 CX TEM at an accelerating voltage of 100 kV. The sample was prepared by wetting either a Formvar-coated or a carbon-coated Cu grid with a small drop (5μL) of the diluted particle solution (300 rpm). Upon drying, it was stained with a small drop of 2 wt.% phosphotungstic acid (PTA) for 10 min. The excess solution was blotted away with filter paper. The Cu grid was then dried at room temperature and under atmospheric pressure for 24 hrs before TEM observation.

5.3 Results and discussion

5.3.1 Effect of temperature treatment on size of the hollow particles

TEM micrographs in Figure 5.1 illustrate that diameters of the hollow particles decrease significantly with temperature treatments from 15^{o}C to 45^{o}C. Table 5.1 lists the average diameters of the particles obtained from DCM/H_2O evaporation process at different temperatures. The results show that the hollow particles shrunk significantly from an average diameter of 225 to 38 nm with temperature increase from 15^{o}C to 35^{o}C. The resulting nanoparticles showed good colloidal stability. Careful observation of the particle morphologies reveal that the hollow particles have shrunk isotropically and their cavities almost disappear at temperature higher than 35°C. Further increase solution temperature up to 45^{o}C only slightly decreased the average size to 28 nm in diameter. These results suggest that increasing the solution temperature could reduce the hydrogen bonding between PMMA graft and water, concurrently increase the hydrophobic interaction between the PMMA grafts. As a result, the PMMA graft chains tend to segregate together to form a densely packed solid PMMA cores with hairy PEI shells at a higher temperature. This transformation phenomenon of hollow particles to closely packed nanoparticles via temperature manipulation is a very interesting discovery because it may open up a new route to the encapsulation of water-insoluble molecules.

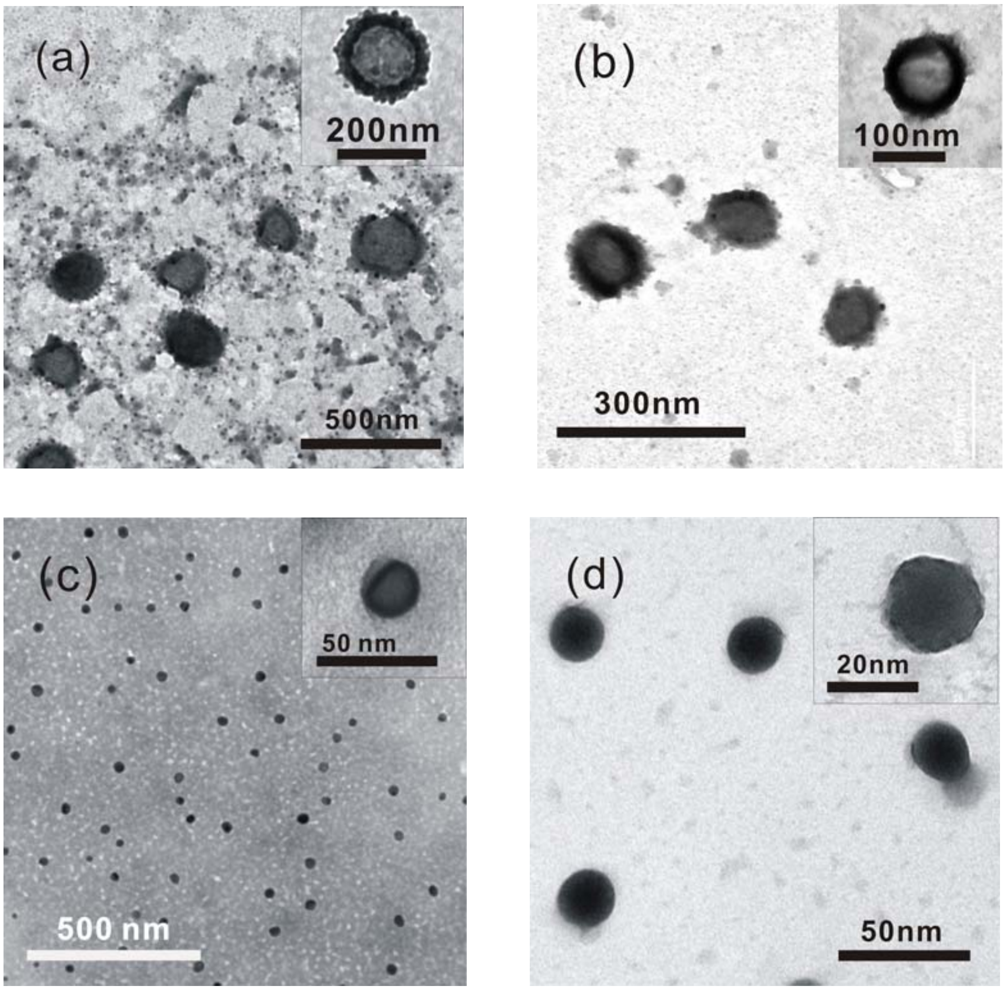

Figure 5.1 TEM images of hollow particles after being treated at various temperatures (a)15°C; (b) 25°C; (c) 35°C and (d) 45°C.

The significance reduction in hollow particle size with the increase of solution temperature may be attributed to either less PEI hydration in water or an increase in hydrophobic interaction of the PMMA grafts, or both. From the thermodynamic point of view, increasing the solution temperature will shift the equilibrium towards the less ordered "free" water, which means that the difference in entropy between bulk water and the shell of ordered water at the hydrophobic surface is increasing. Thus the disruption of the cohesive forces in water produces a positive contribution to the free energy of interface. At the same time, the increase in temperature can weaken the hydrogen bonding between water and the PMMA graft chains.

Table 5.1 Effect of evaporation temperature on average diameters of hollow particles in a DCM/water system.

DCM/water volume ratio (v/v)	Evaporation temperature (^{o}C)	Average diameter based on TEM micrograph (nm)	Observed morphology
3 : 7	15	225 ± 11.25 nm	Spherical hollow particle
3 : 7	25	146 ± 7.3 nm	Spherical hollow particle
3 : 7	35	39 ± 1.95 nm	Spherical and highly packed particle
3 : 7	45	28 ± 1.6 nm	Spherical and highly packed particle

For amphiphilic copolymers in a selective solvent (e.g., water), a microphase separation can occur, in which the association of hydrophobic segments leads to intrachain contraction and interchain aggregation, but hydrophilic segments tend to stay on the periphery. Under proper conditions, the gain of $T\Delta S$ can offset that of ΔH, hence $\Delta G = \Delta H - T\Delta S < 0$, so that further interchain aggregation stops. In our case, the hydrophobic interaction between the PMMA graft chains increases with rising solution temperature to 35ºC, leading to a reduction of the cavity of the hollow particle, and the formation of compact PMMA core. The presence of hydrophilic PEI shell provides both steric and static stabilizations, thus preventing microphase separation of the shrunk nanoparticles precipitating out from water. In addition, the intrachain contraction of the PMMA grafts located in the inner shell leads to significant reduction of the particle size.

5.3.2 Driving Force for the hollow particle size and morphological change

The morphological changes are based on the free energy of the hollow particle which consists of the free energy of the hydrophobic PMMA graft, free energy of the PEI chain and the free energy of the interface. To better understand these changes under different temperature, it is necessary to examine the PEI and PMMA interactions with the solvents and how they are affected by changing the solution temperature. Two major factors have been considered in different solvent compositions and temperatures: 1) Polymer-solvent interaction; and 2) Hydrophobic interaction. The compatibility between polymer and solvent can be estimated based on the polymer-solvent interaction parameters using the widely used van Laar-Hildebrand equation[8] of

$$\chi_{P-S} = \frac{V_s}{RT} \times \left(\delta_P - \delta_S\right)^2 \tag{5.1}$$

where V_s is the molar volume of solvent, δ_P and δ_S are solubility parameters of polymer and solvent, respectively, R is the molar gas constant and T is the absolute temperature. The temperature dependence of δ_P, δ_S (they are slightly temperature dependent[6]) and V_s will be used in our calculations.

For a two-solvent mixture system, the solubility parameter of the solvent can be expressed as

$$\delta_s = \phi_1\delta_1 + \phi_2\delta_2 \tag{5.2}$$

where δ_1 and δ_2 are the solubility parameters of solvent 1 and solvent 2, respectively ϕ_1 and ϕ_2 are the volume percentage of solvent 1 and solvent 2, respectively. Thus, the molar volume of two-solvent mixture V_s can be calculated as

$$V_s = \frac{V_1 V_2}{\phi_1 V_2 + \phi_2 V_1} \tag{5.3}$$

For example, the δ_S and Vs can be calculated as following:

Assume the total volume of the solvent mixture = 10 mL

Volume of DCM = 3 mL (30 vol. %) Molar volume of DCM = 63.9 cm^3/mole

Volume of water = 7mL (70 vol. %) Molar volume of water = 18 cm^3/mole (from Ref.[6])

According to equation 5.2

$$\delta_s = \phi_1\delta_1 + \phi_2\delta_2$$

Solvent parameters obtained from reference [6]

$\delta_{DCM} = 20.2$ $\delta_{H2O} = 48$

Thus the solubility parameter for DCM/water mixture is calculated as:

$\delta_s = \phi_{DCM}\delta_{DCM} + \phi_{H2O}\,\delta_{H2O}$

$= 0.3 \times 20.2 + 0.7 \times 48$

$= 39.66$

Molar volume of two-solvent mixture V_s is calculated according to Equation 5.3

$$V_s = \frac{V_1V_2}{\phi_1V_2 + \phi_2V_1}$$

$Vs = (V_{H2O} \times V_{DCM})/(\phi_{DCM}V_{H2O} + \phi_{H2O}V_{DCM})$

$= (18 \times 63.9)/(0.3 \times 18 + 0.7 \times 63.9)$

$= 22.944$

To determine the PMMA graft to solvent mixture interaction parameter as a function of temperature, we use the equation

$$\chi_{PMMA-S} = \frac{Vs}{RT}(\delta_{PMMA} - \delta_S)^2$$

where $R = 8.314\ cm^3\ MPa\ K^{-1}$ and T is the temperature expressed in Kelvin (^oK), where δ_1 and δ_2 are the solubility parameters of dichloromethane (DCM) and water

Solubility parameter of PMMA, $\delta_{\mathrm{PMMA}} = 19.0$

Solubility parameter of DCM/water solvent mixture (30/70 v/v) (δ_S) = 39.66

Thus the interaction parameter value of PMMA to the solvent mixture can be calculated as following:

For example, at 15°C,

$$\begin{aligned}\chi_{PMMA-S} &= \frac{Vs}{RT}(\delta_{PMMA} - \delta_S)^2 \\ &= \frac{22.944}{8.314 \times 288^o K}(19 - 39.66)^2 \\ &= 4.090\end{aligned}$$

Since DCM is being removed from the solvent mixture through an evaporation, the water content of the solvent system is increased continuously. Based on above calculations, relationships between polymer-solvent interaction parameter as functions of water content and temperature are established in Figure 5.2

When dichloromethane was evaporated during the process, the water percentage increases, the hydrophilic effect of the solvent mixture becomes stronger, while the interaction between PMMA and the solvent environment becomes weaker. In another aspect, we can consider the mobility of PMMA graft chains getting more restricted due to its hydrophobic nature as indicated from the change in $\chi_{\text{PMMA-solvent}}$ value. The solvent composition change (as water percentage increase due to DCM evaporation) enhances the minimization of surface contact area of PMMA graft with the solvent, which is the necessary condition for the determination of the particle size change. With increasing the water percentage, the corresponding increase in PMMA-solvent mixture interaction parameter reflects an unfavorable interaction between PMMA graft and the solvent.

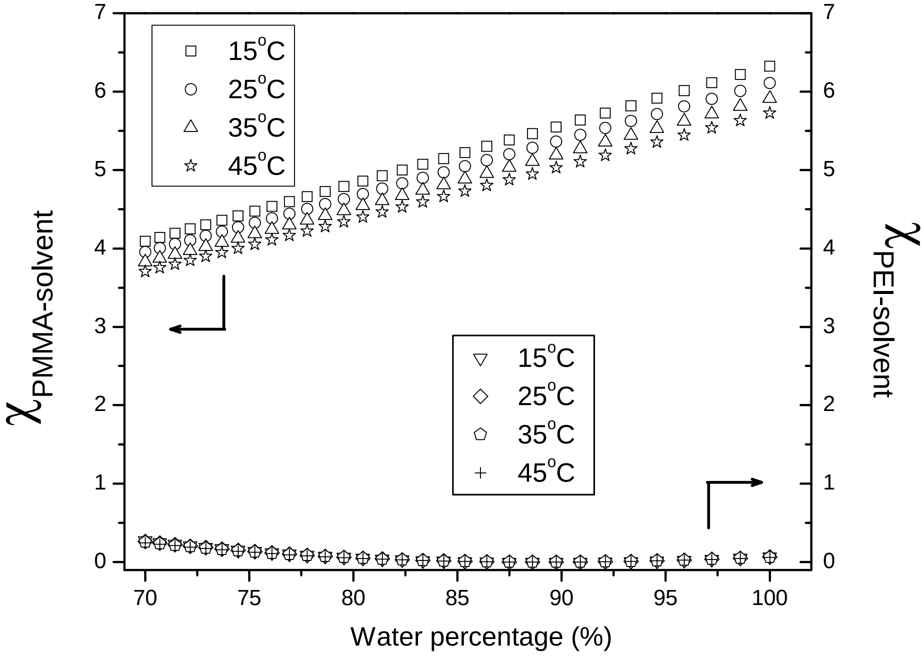

Figure 5.2 Changes in PMMA/DCM-water mixture interaction parameters ($\chi_{\text{PMMA-solvent}}$) and PEI/DCM-water mixture ($\chi_{\text{PEI-solvent}}$) versus water content from 70 vol. % water with DCM evaporation under various temperatures.

From the plot of PEI-segment-solvent interaction parameters ($\chi_{\text{PEI-solvent}}$) vs. water percentage under various temperatures, it is evident that the value of $\chi_{\text{PEI-solvent}}$ is much lower than $\chi_{\text{PMMA-solvent}}$, indicating the solvent mixture from 70 to 100 vol. % water is good for PEI segment and poor for PMMA graft chains. From the plot of PEI segment-solvent interaction parameters versus temperature, the overall trend of $\chi_{\text{PEI-solvent}}$ as a function of temperature changes very little. Thus, the overall PEI-solvent mixture ($\chi_{\text{PEI-solvent}}$) remains almost constant at different water contents and temperatures. In the case of PMMA-solvent interaction parameter versus temperature, $\chi_{\text{PMMA-solvent}}$ does change obviously at elevated temperature. All temperatures exhibit increase in the $\chi_{\text{PMMA-solvent}}$ from initial 70 vol. % (30 vol % DCM) to fully 100 vol. % (complete evaporation of DCM). The overall trend of $\chi_{\text{PMMA-solvent}}$ increases during the evaporation of DCM, thus increasing in water content is somewhat less favorable for PMMA graft chains in terms of polymer-solvent interaction parameter. Furthermore, $\chi_{\text{PMMA-solvent}}$ with respect to water percentage at 15°C is higher than 45°C. The faster change in $\chi_{\text{PMMA-solvent}}$ at lower temperature with the increasing water percentage in the solvent mixture implied that the interfacial free energy between PMMA graft chains and solvent increases.

As is evident from Appendix A, equation 5.2 and 5.3 predicts the changes in the polymer-solvent mixture interaction parameter ($\chi_{\text{P-S}}$) value as the temperature increases. For a 70 vol. % water concentration in the DCM/water system with an assumption that the system obeys the ideal solution behavior (the solubility parameters in the mixture fulfill a linear addition scheme), Figure 5.2 shows the change in $\chi_{\text{PEI-solvent}}$ and $\chi_{\text{PMMA-solvent}}$ with temperature. It is evident that at room temperature the value of $\chi_{\text{PEI-solvent}}$ is much lower than $\chi_{\text{PMMA-solvent}}$, suggesting that from 70 to 100 vol. % water, the DCM/water mixture is poor for PMMA chains and good for PEI chains. As the temperature increases, the $\chi_{\text{PEI-solvent}}$ decreases only slightly, the mixed solvent thus becomes highly favorable for PEI chains. Since the $\chi_{\text{PEI-water}}$ does not change and $\chi_{\text{PEI-DCM}}$ slightly decreases with increasing temperature. Thus, the overall solvent mixture $\chi_{\text{PEI-solvent}}$ remains almost constant.

It is expected that even though there is an increase in the $\chi_{\text{PMMA-solvent}}$ as water volume percentage increase from 70 to 100 % and a corresponding increase in the interfacial tension (γ) between PMMA graft chains and water, the calculated free energy of the interface ($F_{\text{interface}}$) for hollow particles formed at different temperatures can be estimated. This is because the interfacial area (Ai) per PMMA chain occupied in water strongly decreases as reaction temperature is increased. Under this situation, γ increases but the area each chain occupies, Ai, decreases during the particle shrinkage, and $F_{\text{interface}} = \gamma\ Ai$ possesses insignificant change. It can be concluded that the interfacial free energy change due to PMMA-solvent and PMMA-PMMA interactions should not be the main driving force for the change in particle size (particle diameter).

On the other hand, $\chi_{\text{PEI-solvent}}$ maintains a high value (from 4 to 10) for low water volume percentage (10 – 30 vol. %) upon temperature increase, indicating the free energy of the interface $F_{\text{interface}}$ should be in similar profiles in low water volume percentage (10 - 30 %). This trend indicated as temperature increases the interaction between PEI chains and mixed solvents (even at high DCM volume ratios) is still significant since PEI chains have certain degree of interaction with pure DCM.

In another view of particle contraction, we can consider that the mobility of the graft PMMA chains could be strongly restricted due to its strong hydrophobic nature even though the temperature is increased. The good solvent DCM greatly enhances the mobility of the graft PMMA chains, which is the necessary condition for the observation of the change in particle size, it can, however, only take place at low water volume ratios. With increasing the water volume, the morphological change of hollow particle may be very slow due to the restriction of PMMA chain mobility, and no morphological changes could be observed with changing temperatures during DCM evaporation.

5.3.3 Structural Change of Hollow Particles in Isothermal Experiments

In order to investigate whether the morphological changes through heating-isothermal-cooling cycles are identical to initial hollow particle morphology and the effect of annealing time under isothermal condition in the structural stability of hollow particle, two experimental approaches have been performed. First, we monitor the structural changes after heating from low temperature (15^{o}C) to high temperature (45^{o}C), thermal annealing under isothermal condition (45^{o}C) for 3 hrs, cooling from a high temperature (45^{o}C) to 15^{o}C and subsequent equilibrated for 3hrs at 15^{o}C. Second, the same hollow particle solution system is initially transferred to reactor with preheated water-circulated temperature of 45^{o}C and study the morphological change (stability) of the hollow particle versus annealing time under isothermal condition (45^{o}C). The structural morphology at a particular temperature is dependent upon the initial phases and the thermal histories of the systems. Therefore, the particle structural morphologies obtained are not thermodynamically stable.

Different from the first experiment, snowflake morphologies with various structural change in terms of degree of packing are formed from original hollow particles and the solution system is pre-heated to 45°C under different isothermal time. Therefore, with respect to the initial morphology (spherical) and the initial temperature (15ºC) of the system from which the morphology at 45ºC is accessed.

An aqueous solution containing hollow particles (5 mg/mL) was first prepared at 15°C according to the procedure described in Section 3.2.1. The initial morphology is hollow particle in spherical. The hollow particle dispersion was then heated from 15 to 45°C at a heating rate of 2°C/min. After reaching at 45°C, the solution temperature was remained at 45°C for additional 3 hrs. The thermally treated solution was then quenched to 15°C at a cooling rate of 2°C/min., and further equilibrated for another 3 hrs. Samples were withdrawn from the solution at each stage and immediately stained with 2 wt. % PTA solution for 10 minutes on a carbon-coated copper grid, followed by drying in air.

Figure 5.3a illustrates the morphology of the initial hollow particles at 15°C which appear to be spherical with some flexibility. The average particle size observed by TEM is 233 ± 17 nm. After treating the hollow particles from 15 to 45°C, a core-shell structure with a distinct boundary is clearly observed (Figure 5.3b). In addition, the average size of the particles at 45°C (Figure 5.4b) was slightly smaller than the original hollow particles (~ 160 nm in particle diameter) as shown in Figure 5.4a. The inner cavity (darker region where may contain PTA solution) is also considerably reduced. Interestingly, some lighter regions which believe to be the PMMA chains are clearly observed in the core (see enlarged particle in Figure 5.4c). The structural change indicates that the PMMA graft chains may have been stretched during the thermal treatment. The stretched PMMA chains tend to segregate themselves in order to minimizing their surface free energy in water. When continuously annealing the particles at 45 °C for 3 hrs, the segregation of PMMA graft chains becomes even more significant, resulting in a phase separation between the PEI shell and the PMMA core as shown in Figure 5.5.

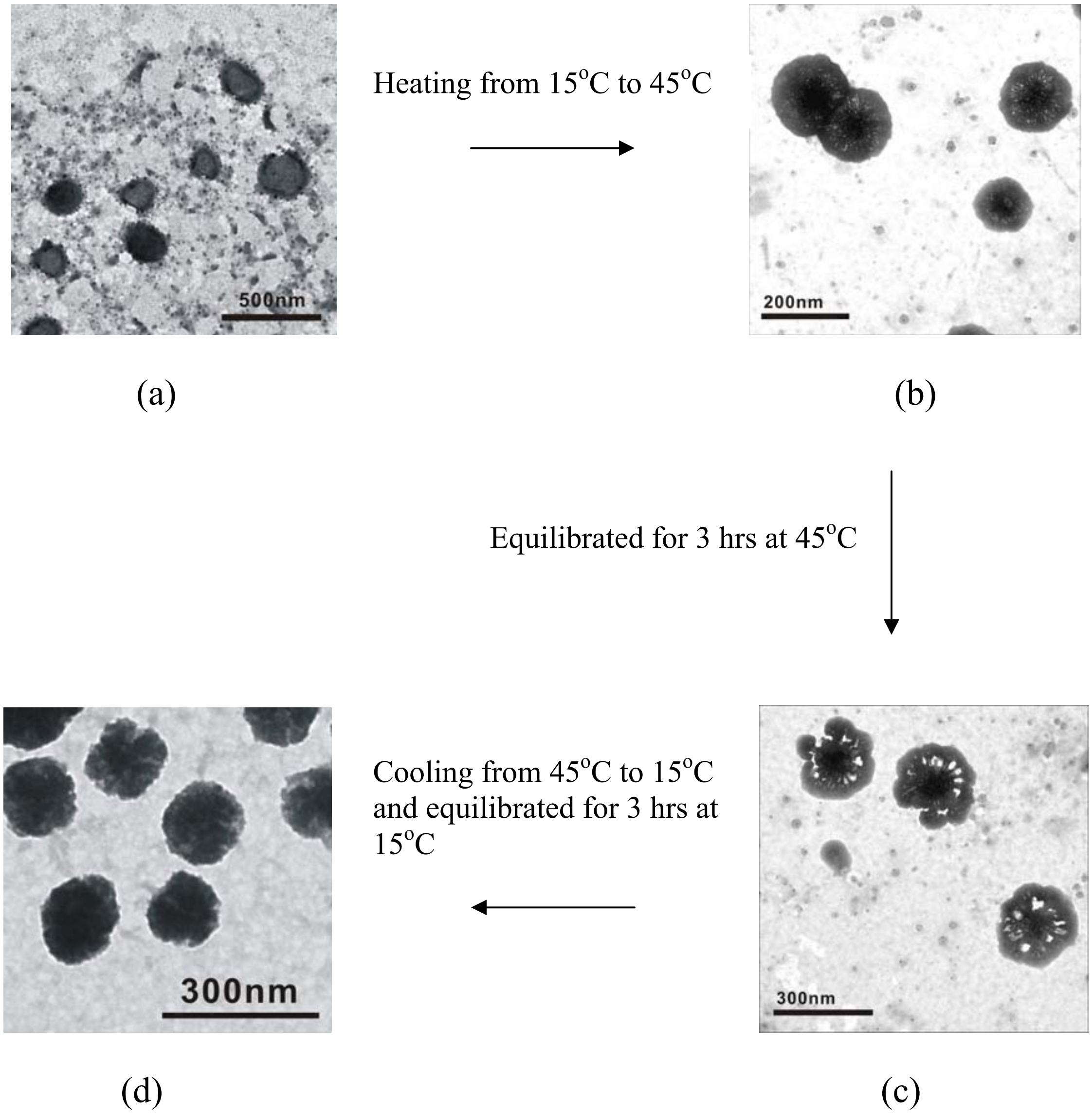

Figure 5.3 After heating a system with 5 mg/mL hollow particle concentration at 70 vol. % of water in DCM/water in which the original morphology was hollow particles morphology as temperature rise from15^{o}C to 45ºC, equilibrating for 3h, then quenching to 15ºC, following by 3h equilibration. (The heating rate is 2^{o}C/min.)

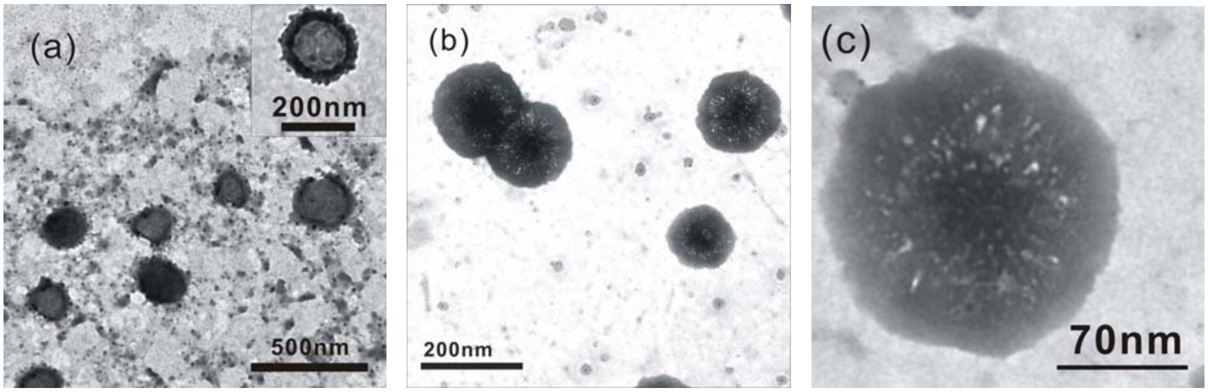

Figure 5.4 TEM micrographs of hollow particles (a) at 15°C ; (b) heating from 15°C to 45°C (c) Hollow particle in (b) with a magnification of ×100,000.The heating rate is 2°C/min.

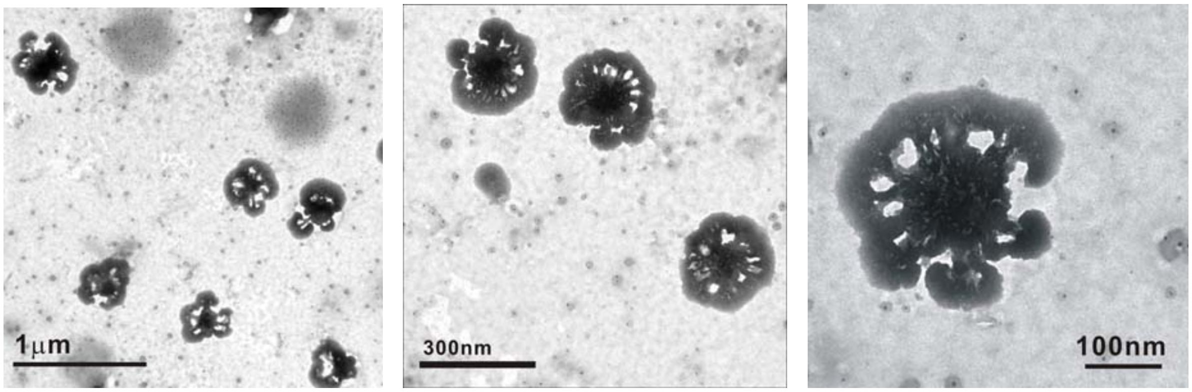

Figure 5.5 TEM micrographs of hollow particles under thermal treatment at 45°C for 3 hrs.

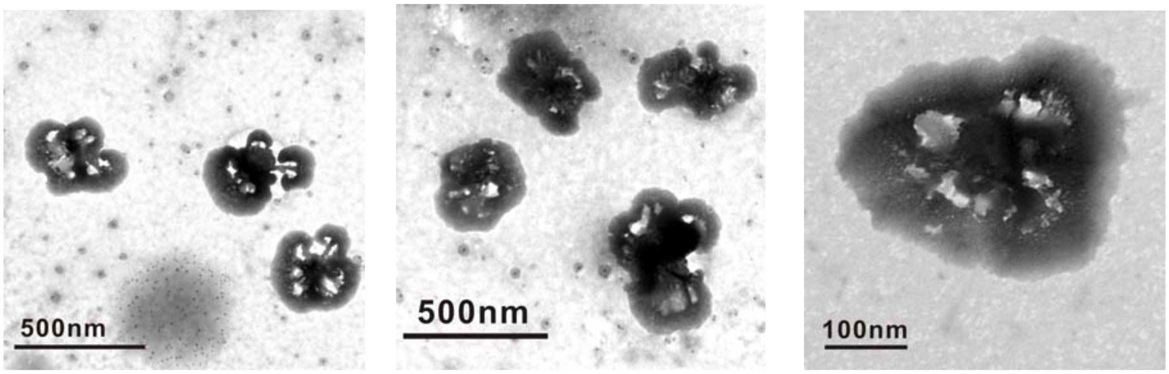

Figure 5.6 TEM micrographs of hollow particles under thermal treatment at 45°C for 4 hrs.

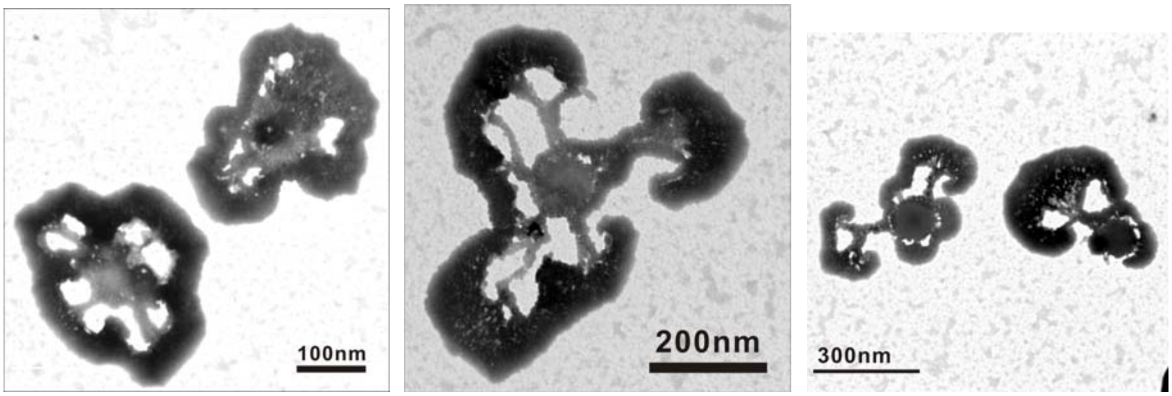

Figure 5.7 TEM micrographs of hollow particles under thermal treatment at 45^{o}C for 5 hrs.

If phase separation within the particle takes place, the driving force for deformation must overcome the accompanying reduction in interfacial free energy, which equals to the product of the surface tension and the total interfacial area associated with the phase separation. Based on the definition the interfacial free energy, $F_{interface} = \gamma Ai$, where γ is surface tension and Ai is the interfacial area each chain occupies. As temperature rises from 15^{o}C to 45^{o}C, surface tension of water reduces and the interfacial area contact between each PMMA chain and the solvent decreases substantially due to the close packing of the PMMA chains, thus resulting in reduction in $F_{interface}$. It can be concluded that the interfacial free energy should be the major driving force for the structural transition of the hollow particle upon temperature change.

Thus it is quite possible that the structural transition under isothermal condition is the result of a dynamic balance between hydrophobic interaction and polymer-solvent interaction. Assuming PEI-*g*-PMMA hollow particle is initially in spherical shape, the interaction between grafted PMMA chains and the solvent at the interface would be extremely weak because the interfacial area each PMMA chain occupied will be less, as compared to the highly packed

PMMA core at 45^{o}C. The segregation of the PMMA chains also pulls some PEI molecules inward, creating connecting bridges between PMMA core and PEI shell. Prolonging the thermal treatment to 4 hrs resulted in the deformation of the phase separated particles as exhibited in Figure 5.6. Further thermal treatment up to 5 hrs leaded to the disintegration of the particles (Figure 5.7). These morphological changes evidently suggest that thermal annealing of the hollow particles induces strong hydrophobic interaction of PMMA chains in aqueous solution, resulting in the formation of highly packed hydrophobic core.

Since the aggregates are not thermodynamically stable, the particle would spread into an extended structure, like snowflake-like morphology. Thus it was of interest to understand if the snowflake-like morphology could be relaxed back to spherical particle when lowering the solution temperature. Thus, the hollow particles system was cooled from isothermal temperature (45^{o}C) to 15ºC with a cooling rate of 2^{o}C/min followed by further treatment at 15^{o}C for 3 hrs.

Figure 5.8 shows the particle morphological changes when cooling the thermally treated particles from 45^{o}C back to 15^{o}C. For particles which had been treated at 45^{o}C for 3 and 4 hrs, their morphology changed from snowflake-like to packed spore morphology. Most particles returned to spherical shape with diameter in the range of 90 to 160 nm. In the case of hollow particles which were treated at 45^{o}C for 5hrs, followed by 15^{o}C quenching process with 3 hrs equilibration, large raspberry morphology (particle diameter range: 200-400 nm) with surface roughness were observed. The morphological changes discovered from the annealing experiment indicate a strong dependence of the annealing time and the thermal histories of the hollow particle system. Cooling the snowflake-like particles at 15^{o}C resulted in the formation of compacted structures, rather than returning to the original hollow spheres. These results suggest that the morphological changes are irreversible and the system is not in a thermodynamic equilibrium. Therefore, the morphology after heating-cooling cycle is at the best a thermodynamically metastable morphology if it is not unstable. This also indicates that the pathways of the morphological changes can be manipulated by both isothermal annealing time and heating cooling cycle.

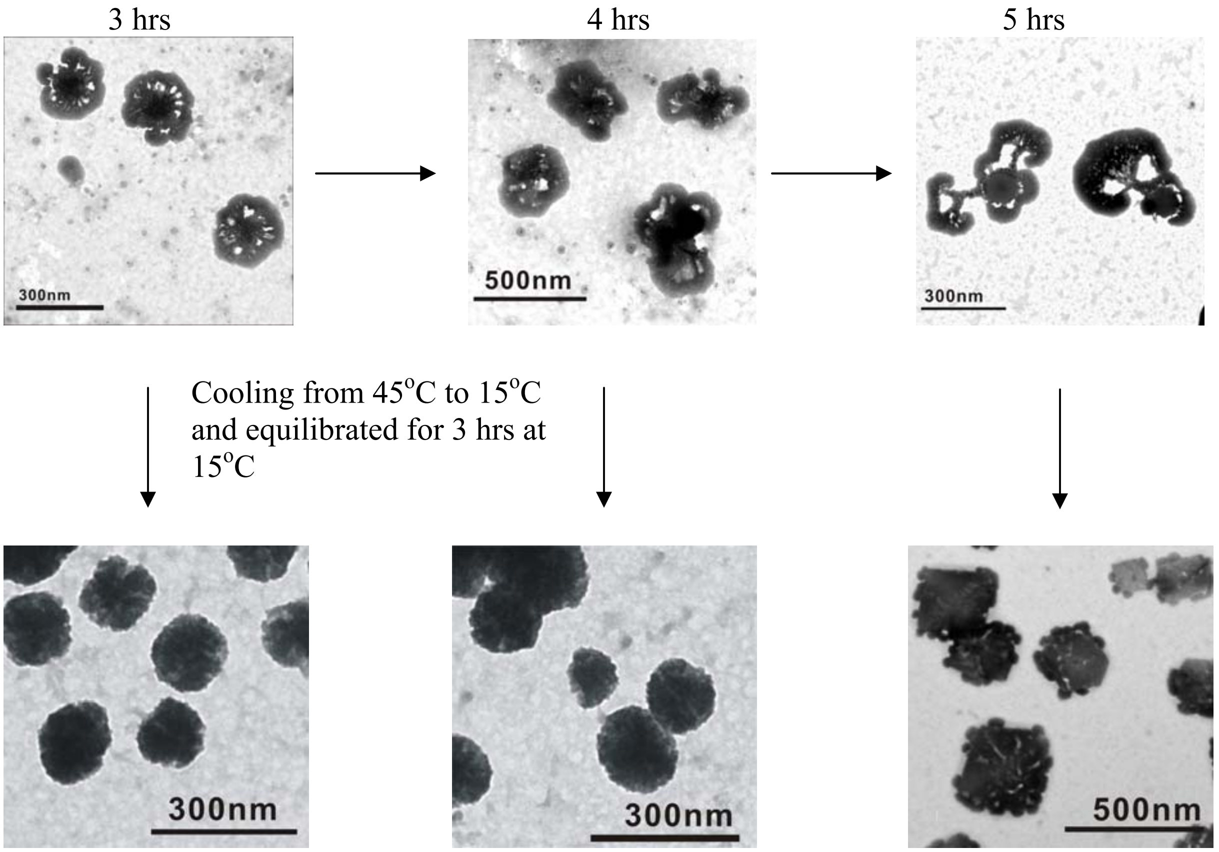

130-150 nm in diameter

90-160 nm in diameter

200-450 nm in diameter

Figure 5.8 Morphological changes of hollow particles from various isothermal annealing time and further cooled down to 15°C , following by 3 hrs equilibration.

5.3.4 Effect of Temperature Treatment on the Diameter of Preformed Nanotube

In order to investigate whether the shrinkage behavior of the preformed nanotubes are similar to the spherical hollow particles, morphological changes of the preformed nanotubes have been monitored at different storage time and thermal treatment. The nanotubes were first obtained from a DCM/water mixture (3/7 v/v) at 15°C according to the procedure described in the experimental section. SEM analysis of polymer in the aqueous solution showed that long and flexible tubular nanomaterials with diameters ranging from 60 to 120 nm were generated (Figure 5.9a). The TEM image of this sample revealed the cavity of nanotubes which appeared to be lighter than the outer PEI layer (Figure 5.9 b and c). After storage this sample at room temperature for 87 days, the tubular nanostructured materials were barely observed by TEM. Instead, they looked like nanofibers with diameters around 50 nm in diameter. (Figure 5.9d)

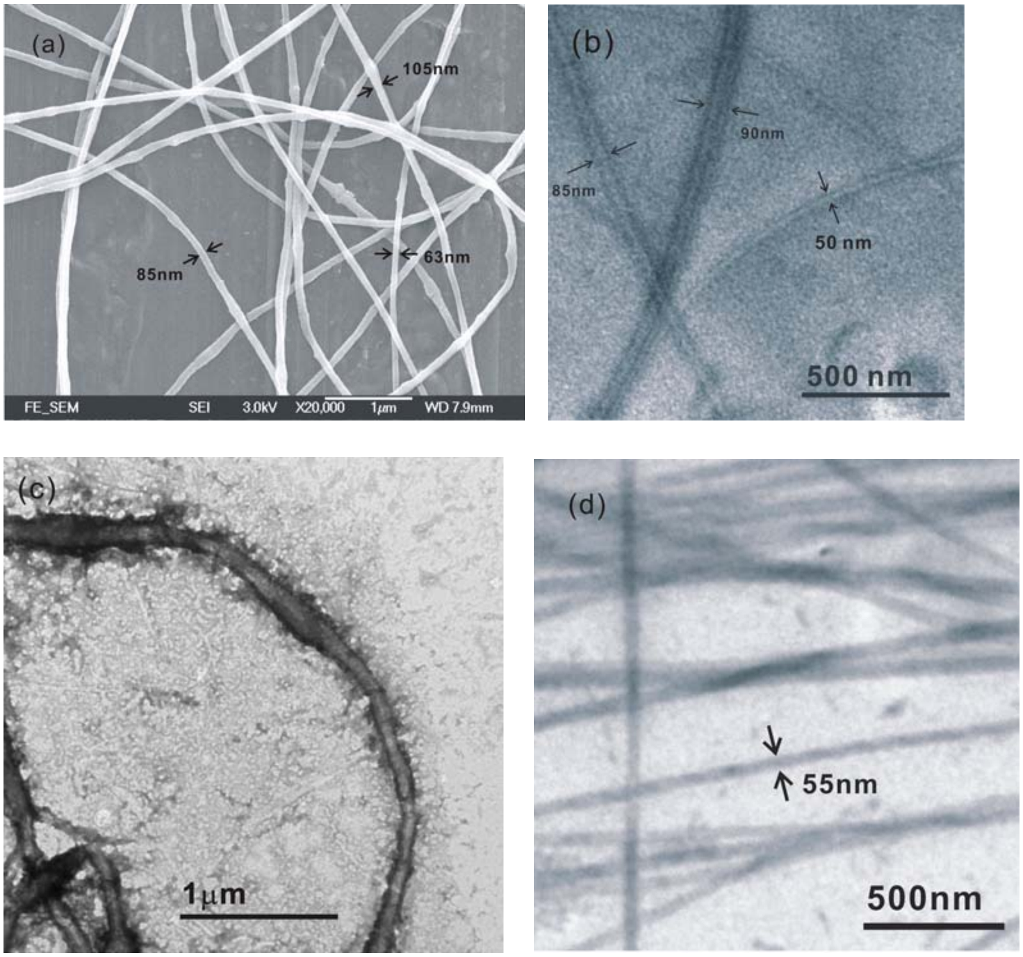

Figure 5.9 Nanotube formation after stirring the hollow particles at 350 rpm in a DCM/water mixture (3:7 v/v) for 24 hrs at 15°C and storage at different periods. (a) FE-SEM image of tubular nanomaterials (sample was stored at room temperature for 10 days before observation). (b) TEM image of nanotubes (sample was stored at room temperature for 28 days before observation). (c) TEM image of nanotubes (sample was stored at room temperature for 1 day before observation) (d) TEM image of fibrous-like nanomaterials (sample was stored at room temperature for 87 days. All TEM samples were stained with 2% w/w PTA solution before observation).

To accelerate the transformation from nanotubes to nanofibers, the preformed nanotubes were treated at 25, 35 and 45°C for 1 hour annealing time. Figure 5.10(a) shows that the nanotubes with diameter around 100 nm still remain after treating them at 25^{o}C. When increasing the solution temperature to 35°C, tubular morphology became less obvious. Instead, fiber-like morphology is appeared as shown in Figure 5.10(b). Further increasing the solution temperatue to 40°C resulted in the formation of almost fibrous morphology with mean diameter of 40 nm (Figure 5.10c). When heating the preformed nanotube dispersion at 45^{o}C, the diameters of nanofibers were further reduced to around 20 nm in diameter as illustrated in Figure 5.10(d). In addition, some short nanofibers (less than 1 micrometer in length) were observed, indicating that the fibrous-like nanostructured materials may start to break up under this temperature treatment. The correlation between mean diameters of tubular nanostructures as a function of annealing temperature is shown in Table 5.2.

These results suggest that the transformation from nanotubes to nanofibers can be accelerated via the solution temperature treatment. These one-dimensional amphiphilic nanostructures with high aspect ratio may find potential applications in fillers for nanocomposites, as precursor materials for fabrication of other 2D nanostructures, Moreover, they are appropriate for studying size-dependent properties, such as encapsulation of materials or other processes with length scales comparable to some of the sizes of the nanostructure, such as phase separation in amphiphilic copolymers.

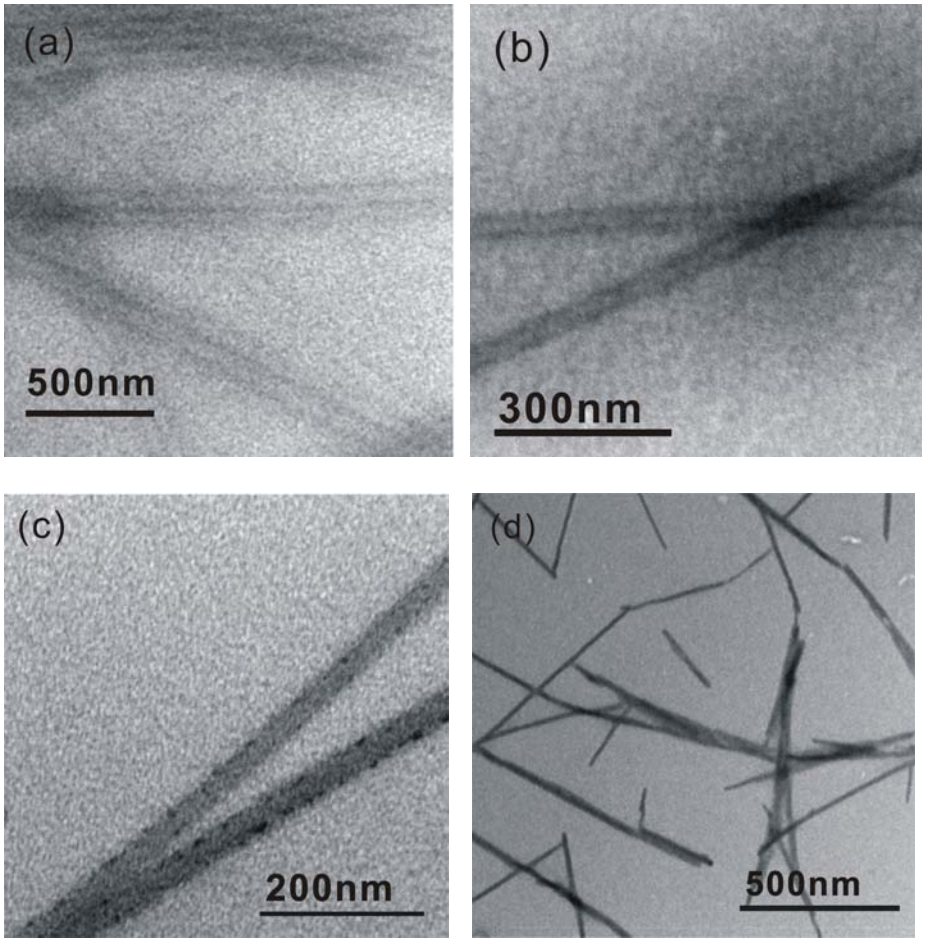

Figure 5.10 TEM micrographs of preformed PEI-g-PMMA copolymer nanotubes treated at (a) 25°C, (b) 35°C; (c) 40°C and (d) 45°C, respectively.

Table 5.2 Mean diameters of preformed nanotube vs. thermal treatment

Treatment temperature (°C)	Mean tubular diameter (nm) based on TEM micrograph
15	136.8 ± 27.4 nm
25	85.3 ± 17 nm
35	43.5 ± 8.7 nm
40	34.2 ± 6.8 nm
45	16.9 ± 3.4 nm

5.4 Conclusion

The particle size of PEI-g-PMMA hollow particles can be induced by solely changing the solution temperature under fixed copolymer concentration and solvent composition in a DCM/water volume ratio of (3:7). The rising temperature induces the contraction of PMMA graft chains, leading into a highly packed particle and reducing hollow particle size and nanotube diameter. The contraction of PMMA graft chains seems to be reinforced by hydrophobic interaction and the cleavage of hydrogen bonding between PMMA and water molecules.

Further insight into the thermodynamic nature of size dependent changes was achieved under various temperature treatments in DCM/water mixtures. With increasing the temperature, changes in the size from hollow particles to highly packed solid particles were observed. Metastable aggregate morphology is also found in the pathway from one morphology to another during isothermal experiments. These observations provide useful insights into the mechanism of these phase separation and the formation of these non-equilibrium structures.

References

1. Tanford C. *J. Phys. Chem.* **1974**, *78*, 2469.
2. Tanford C., "*The Hydrophobic Effect: Formation of Micelles and Biological Membranes*", 2nd ed.; J. Wiley & Sons, New York, **1980**.
3. Hamad E. *Macromolecules* **1990**, *23*, 4185.
4. Alexandridis, P.; Holzwarth, J. F.; Hatton, T. A**.** *Macromolecules* **1994**, *27***,** 2414.
5. Hunter, R. J. *Foundations of Colloid Science;* Oxford University Press: New York**,** **1987**; Vol. 1.
6. Barton, A. F. M. *Handbook of Solubility Parameters and Other Cohesion Parameters,* CRC Press:Boston, MA, **1983**, p. 12.
7. Baldwin, R. L. *Proc. Natl. Acad. Sci. USA* **1986**, *83*, 8069.
8. Barton, A. F. M. *Handbook of Polymer-Liquid Interaction Parameters and solubility parameters*; CRC Press:Boston, MA, **1990**.

Chapter 6

Effect of pH on the Formation of Hierarchical Structures

6.1 Introduction

Self-organization using preformed discrete nanostructures as building blocks into microscopic or macroscopic higher-ordered superstructures through manipulation of various intra and/or intermolecular interactions, such as hydrophobic interactions, H-bonding, electrostatic interactions, etc is of much interest in both fundamental research and practical applications. In fact, there are numerous examples of hierarchical self-assemblies in nature. In principle, The creation of well-defined hierarchical structures through self-assembly of preformed building blocks strongly depends on the molecular interactions between the building block,[1-2] as well as the size distribution[3] and the shape.[4,5] Nowadays, the prevalent self-assembly approaches to prepare various hierarchical structures starting from the preformed nanostructured materials include droplet evaporation,[6-9] mixing non-solvent,[10,11] Langmuir-Blodgettry technique,[12-14] and small-molecule or polymer mediator-induced assembly.[15-18] In addition to these approaches, the surface template-assisted self-assembly approach based on the lithographically defined physical template[19] or self-organized chemical template[20] have been extensively investigated because they can directly achieve assembled pattern of the building blocks on substrates. Although above mentioned methods have been used to successfully fabricate various interesting hierarchical structures such as microporous, triangular shaped and phase separated laminar structures,[21,22] they still suffer from some drawbacks including the need to pre-fabricate tailor-made building blocks with uniform shape and size by means of specific synthetic routes or tedious size selection processes before the self-assembly.

In this part of work, we have studied the effect of solution pH on the assembly of preformed PEI-*g*-PMMA nanotubes. The assembled hierarchical structures were carefully examined using various microscopic techniques (SEM, TEM and AFM). Since the outer shells of the nanotubes contain polyethyleneimine which is comprised of primary, secondary and tertiary amines, modification of surface charge density of the nanotubes could simply achieve through varying the solution pH, thus affecting their electrostatic repulsive force and hydrogen bonding. The manipulation of these molecular interactions thus result in the formation of different hierarchical structures.

6.2 Experimentals

6.2.1 Formation of PEI-*g*-PMMA hollow particles

Freeze-dried PMMA/PEI particles (0.05g) were first mixed with 8 mL of dichloromethane (DCM) in a jacketed-flask. The suspension was gently stirred at 150 rpm at 25^{o}C for 4 hrs in order to extract the PMMA homopolymer from the cores. Viscosity of the solution increased considerably due to the dissolution of the PMMA homopolymer. Water was then added in dropwise at a rate of 1 drop per second, and the heterogeneous mixture was stirred at a rate of 150 rpm for 3 hrs. The aqueous phase was then isolated, diluted with water and stored at room temperature for characterization.

6.2.2 Formation of preformed tubular nanostructured materials

The nanotubes were first generated by stirring the PMMA/PEI hollow particles in a DCM/water (3:7 v/v) mixture at 350 rpm for 24 hrs at 15°C, according to the method described in Section 3.2.1. DCM should have all evaporated at the end, resulting in a clear aqueous solution. The PMMA homopolymers initially dissolved in DCM became insoluble in aqueous phase, giving small pieces of transparent thin film. They were then removed from the aqueous solution by a simple filtration.

6.2.3 Formation of various hierarchical structures under different solution pHs

To study the effect of solution pH on the assembly of preformed PEI-*g*-PMMA nanotubes, the pH of aqueous solution containing PEI-*g*-PMMA nanotubes (5mg/mL, pH = 6.5) was adjusted by a dropwise addition of either 0.01 M HCl or 0.01 M NaOH solution under gentle stirring (50 rpm). The final pH values of the solutions (3.0, 5.0, 7.0, 9.0, 11.0 and 13.0) were measured by an Orion 555A pH meter. Each solution containing preformed nanotubes was subsequently stirred at 50 rpm for 24 hrs at 25^{o}C. Depending on the solution pH, the initial clear solution could turn into cloudy after several hours. The appearance of cloudiness indicated the formation of newly assembled materials.

6.2.4 Zeta-potential measurement

ζ-Potential measurements were conducted on a Malvern Zetasizer 3000 HSA (Malvern, UK) with a 30 mW solid-state laser operated at a laser wavelength of 635 nm He-Ne laser. The measurements of electrophoresis mobility (EPM) were performed at 25°C. The ζ-potential was determined from the measured electrophoretic mobility, m, using the Smoluchowski approximation even though it is rigorously valid only for spherical shaped particles. The Smoluchowski approximation also assumes that the particle permittivity is much less than dielectric constant of the medium (ε_m), which is true for nanotubes. O'Brien *et al.* have extended this model to higher aspect ratio structures, taking into account the change in the ion density induced by the applied electric field.[24]

6.2.5 Characterization by electron microscopies

Scanning electron microscopy images were obtained using a JEOL-JSM 6335F field-emission scanning electron microscopy (FE-SEM) at an accelerating voltage of 5kV. Sample was prepared by placing a small drop of dilute dispersion (~ 500 ppm) on a mica substrate, and allowed it to dry at room temperature for 24 hrs. The air-dried sample was subsequently sputtered with a thin layer of gold under vacuum to a depth of approximately 1-2 nm.

Transmission electron micrographs were obtained using a JEOL 100 CX II TEM at an accelerating voltage of 100 kV. Sample was prepared by wetting a carbon-coated copper grid with a small drop of dispersion (10 μL, 300 ppm). To enhance the contrast between PEI and PMMA components, the assembled materials were stained with appropriate concentration of phosphotungstic acid solution (PTA) solution and time after drying. For the preformed nanotubes, they were stained with 0.5 wt.% PTA solution for 1 minute. In the case of hierarchical structures, they were stained with 2 wt. % (w/w) PTA solution for 3 minutes. All stained samples were then dried at room temperature before analysis.

6.2.6 Characterization by atomic force microscopy

Images of hierarchical structures generated from the controlled aggregation of the nanotubes were also investigated using a Nanoscope IV Atomic Force Microscopy (AFM, Digital Instruments) with a NSIV controller in a tapping mode under an ambient condition. Cantilever with a spring constant of 40 N/m resonating at 300 kHz was used in all measurements. Images with scan sizes of 3 and 5μm were acquired at a 0.5 Hz scan rate with a resolution of 512 × 512 pixels. Each sample (200 μL, 2 mg/mL) was thermally equilibrated to the temperature of fluid cell, and then injected into the cell at a rate of 5 μL s^{-1}. Imaging was also obtained in a fluid tapping mode using a V-shaped silicon nitride (Si_3N_4) cantilever (NP-S, 200W, Veeco Probes, CA) at a frequency of 30±0.5 kHz. The images were acquired after 5 min of injection, and continued for 2 hours. Topographical height mode was acquired at a scan range of 1 μm. The images were presented after first-order flattening.

6.3 Results and Discussion

Nanotubes were first generated by stirring the PEI-*g*-PMMA hollow particles in a mixture of DCM/water (3/7 v/v) at 350 rpm for 24 hrs at 25 °C. At the end of the assembly process, the DCM was completely evaporated, resulting in a clear aqueous solution. The PMMA homopolymers initially dissolved in DCM became insoluble in water, and formed small pieces of thin film suspending in the aqueous solution. They were then removed from the aqueous solution by a simple filtration. Figure 6.1 shows the FE-SEM image of the preformed nanotubes which seem to be aggregated in a buddle form. The individual tubular diameters are in the range of 100 to 150 nm and unit length from 5 to 8 μm. The pH of the obtained nanotube aqueous solution was approx. 6.5.

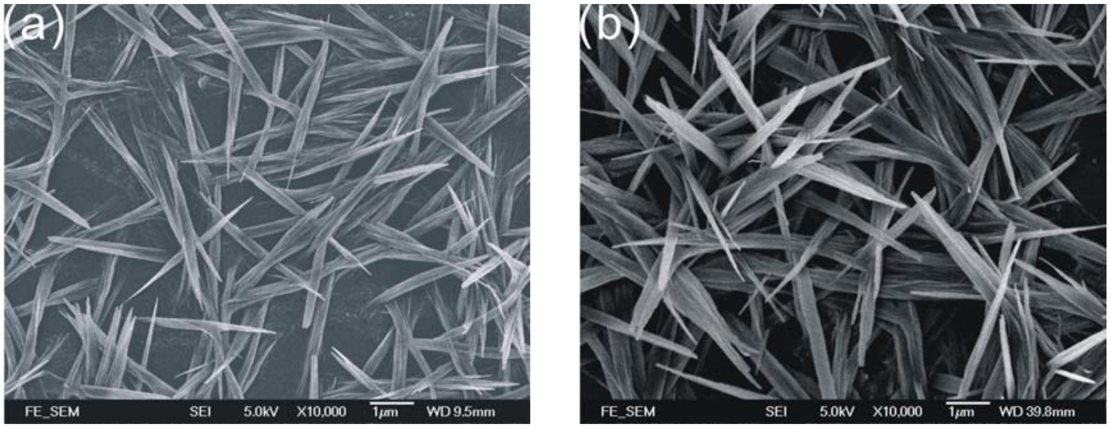

Figure 6.1 FE-SEM micrographs of preformed PEI-*g*-PMMA based nanotubes obtained from aqueous solution (pH 6.5). Magnifications of the FE-SEM images are of (a) × 5,000; and (b) × 10,000.

6.3.1 Zeta-Potential of hollow nanoparticles and preformed nanotubes at various solution pHs

As discussed in previous chapters, the assembled nanotubes are comprised of PEI shells with graft PMMA chains located in the inner tubes. Since the branched PEI contains 25% primary, 50% secondary and 25% tertiary amino groups, the degree of protonation is strongly pH-dependent. Figure 6.2 shows the degree of protonation as a function of solution pH based on a literature result.[25] The percentage of protonated amines at pH 3, 5, 7, 9, 12 are 73, 52, 27, 8, 0 %, respectively. To confirm the correlation between the surface charge density of the hollow particles and nanotubes as a function of pH, the *zeta*-potential of both hollow particles and nanotubes were measured using a *zeta*-potentiometer. Results shown in Figure 6.3 suggest that *zeta*-potential changes for both hollow particles and nanotubes are very similar. Increasing solution pH from 3 to 8 gradually reduces *zeta*-potential of the nanotubes. At near pH 9, the *zeta*-potential value is almost approaching to zero, indicating almost neutral surface. These results are consistent with the fact that there is very low percentage of PEI protonation at pH 9. Thus it is expected that increasing solution pH may lead to higher degree of aggregation of the hollow particles and nanotubes due to the decrease of surface charge density.

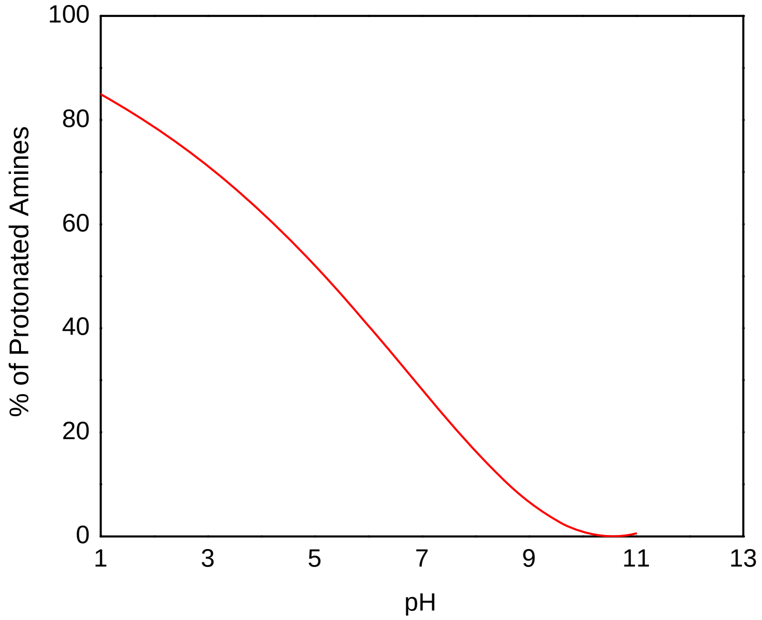

Figure 6.2 Fractions of protonated amines for PEI at various pH values and 25°C.[25]

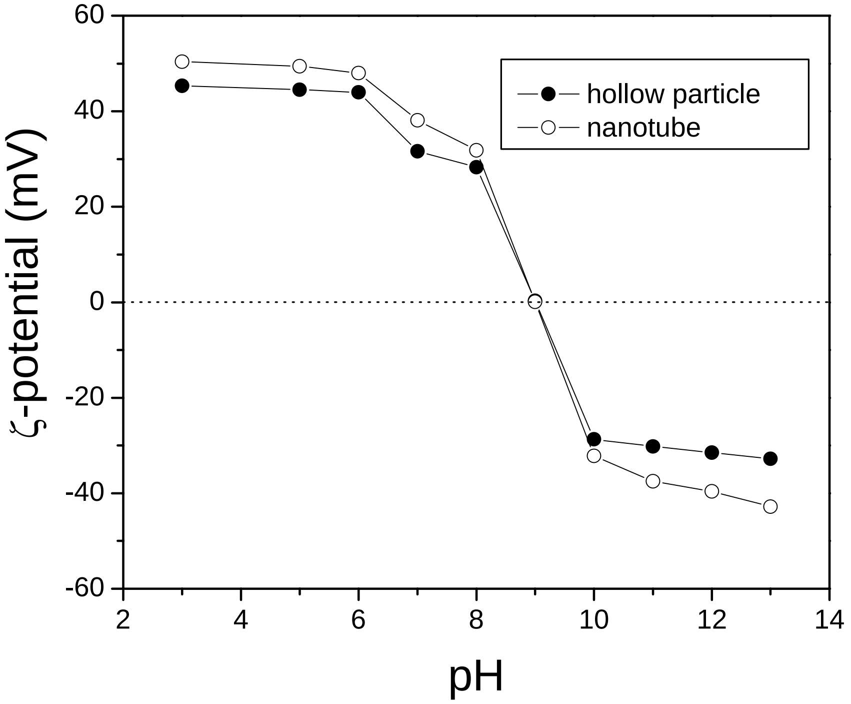

Figure 6.3 ζ-potential of PEI-*g*-PMMA based hollow particles and nanotubes at various pHs. Particles and nanotubes were dispersed in 1 mM NaCl solution at 25^{o}C, respectively.

6.3.2 Electron microscopic observation of hollow particle aggregation

Figure 6.4 presents TEM micrographs of spherical hollow particles obtained at various solution pHs. The surface charges of the hollow nanoparticles can be controlled by the solution pH. At a pH below the isoelectric point (IEP, pH < 9), particles carry a net positive charge; while particle charges are almost zero at IEP pH (pH 9). Further increase of the solution pH through addition of NaOH solution results in the absorption of excess amount of OH^- ions, thus creating negative charges on the particle surface. TEM images of particles at pH 5, 7, 9, 11 and 13 as shown in Figure 6.4 reflect this effect: particles are well separated at pH 5 and 7 due to their high surface charges. But particles are seriously aggregated near IEP (pH 9). A further increase in pH to 11 and 13 leads to charge reversal to re-disperse the flocculated material as negatively charged particles. The negative surface charge is attributed to the adsorption of hydroxide ions at the particle surface.

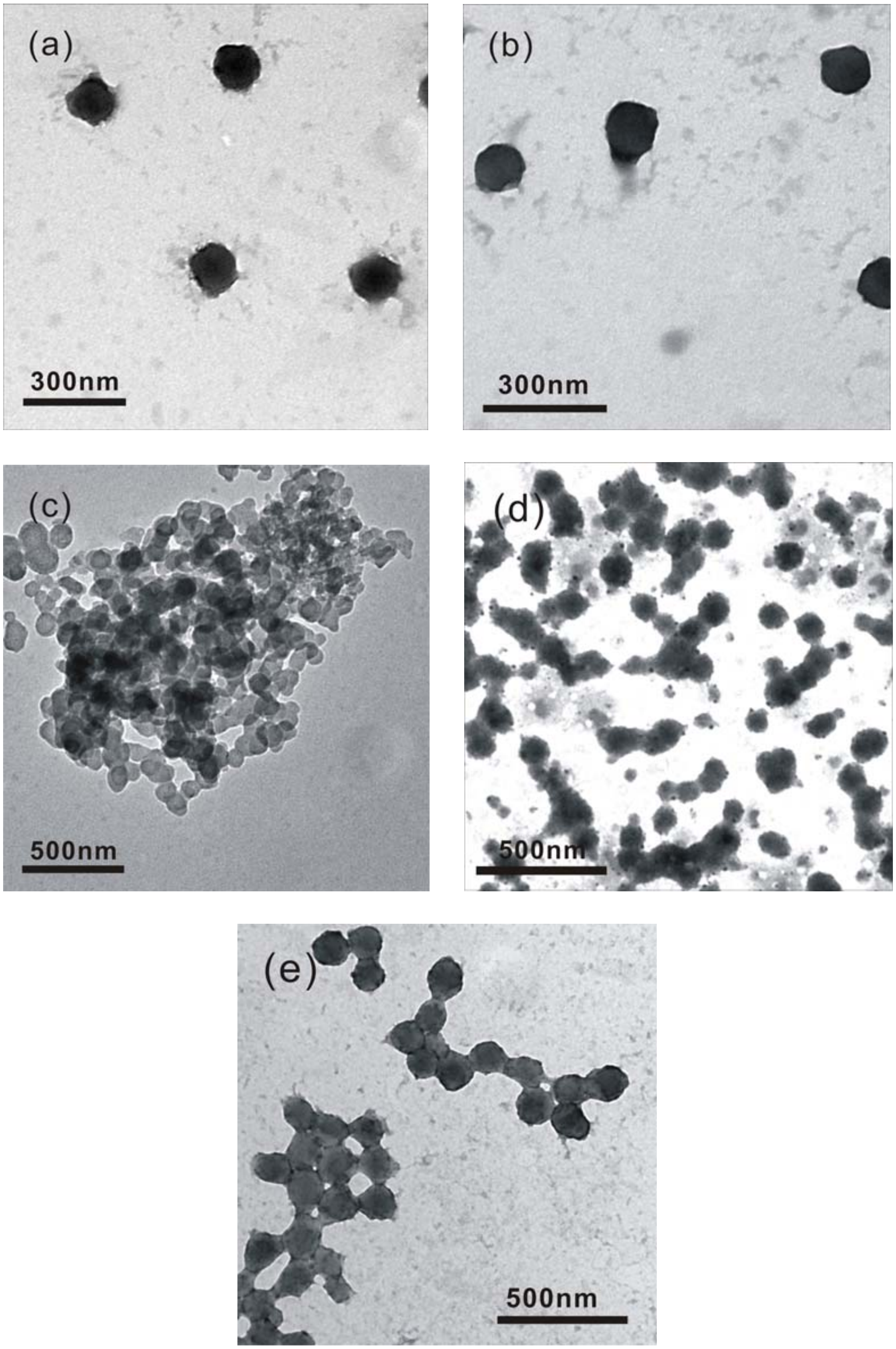

Figure 6.4 TEM micrographs of PEI-*g*-PMMA based hollow particles in solution with (a) pH 5; (b) pH 7; (c) pH 9; (d) pH 11 and (e) pH 13, respectively.

6.3.3 pH-dependent hierarchical structure assembly using PEI-*g*-PMMA nanotubes as the building block

Hierarchical structures are assemblies of molecular or nanostructured units into organized patterns in multiple length scales. In fact, hierarchical self-assembly of a wide spectrum of biomolecules such as proteins, peptides, DNA and lipids are well known phenomenon.[26-35] In our system, since the preformed nanotube is semi-flexible due to the presence of rigid PMMA graft chains and flexible PEI chains, and contains PEI shell that is pH-sensitive, it was anticipated that variation of solution pH might induce different degree of nanotube aggregation, thus possibly generating some intriguing hierarchical structures. Therefore it was of much interest to investigate the pH-induced self-assembly of nanotubes through treating the preformed PEI-*g*-PMMA nanotubes under different solution pHs. Several molecular interactions are expected to interplay for the nanotube assembly: 1) Electrostatic repulsion due to the presence of surface charges; 2) Hydrogen bonding between PEI chains 3) Van der Waals forces between interchain and intrachain attractive forces; 4) Dispersion and dipole-dipole forces. Therefore, the formed nanostructures are a result of delicate balance between these repulsive and attractive forces.

When reducing the original pH of the preformed nanotube dispersion from 6.5 to 5.0, the nanotube bundles became loose where individual nanotube could be clearly identified (Figure 6.6). While the bundle diameters increased from 300 nm to 3 µm, their lengths remained almost the same. When further reducing the solution pH of the nanotube dispersion from 6.5 to 3, the tightly packed nanotube bundles were almost all freed. Well-separated individual nanotubes with diameter ranging from 80 to 150 nm were clearly identified by the SEM image (Figure 6.5). In addition, the lengths of the nanotubes became broader, and many short nanotubes (less than 1 μm) were also found. The resulting assemblies may be a result of a balance of three key molecular interactions of the PEI located on the outer shell of the nanotube: i) electrostatic repulsion; ii) attractive binding (hydrogen bonding, dipole-dipole interaction, Van der Waals forces); and iii) chain diffusion and entanglement. At pH 5, the protonation degree of the branched PEI is approximately 50%.[25] The higher charge density of the PEI increases the electrostatic repulsion of the nanotube, thus reducing the packing density of the nanotube bundle. At pH 3, the protonation degree of branched PEI reaches nearly 75%.[25] The stronger electrostatic repulsion of the nanotubes resulted in complete dissociation of the nanotube bundle to individual nanotubes. Moreover, the strong electrostatic repulsion could even break down the nanotube into shorter segments since some PEI junctions of the nanotube were still present within the nanotube.[23]

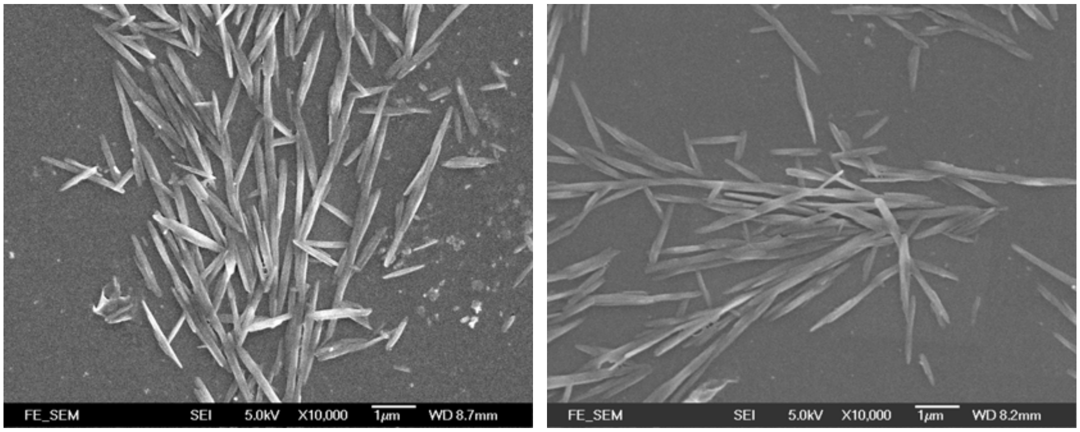

Figure 6.5 Morphologies of nanostructured materials obtained at pH 3.

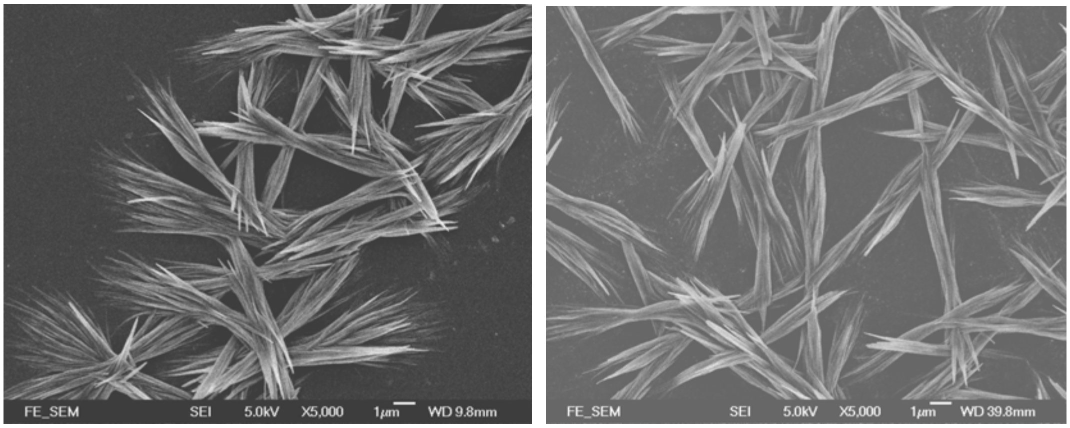

Figure 6.6 Straw-sheaf like morphologies of nanotube aggregates formed at pH 5.

When the preformed nanotube bundles were treated at pH 7, they assembled into fractal pattern with a straw-sheaf-like centre as shown in Figure 6.7a and 6.7b. A close look of the centre part reveals many fused nanotube bundles (Figure 6.7c). The branches are also built up from many nanotubes (Figure 6.7d). The TEM image under higher magnification also reveals individual preformed nanotube with very narrow cavity in the range of 15-20 nm in diameter. (Figure 6.7e inset)

At pH 7, the protonation degree of PEI dropped to approximately 25%,[35] thus the electrostatic repulsion is significantly reduced. As a result, the attractive binding and chain diffusion and entanglement of the PEI become dominant forces, leading to tightly packed bundle. At this pH, the solubility of the PEI is also much lower due to the lower degree of amine protonation. Therefore, the bundles would undergo further self-assembly to fractal structure in order to reduce their surface energy. In fact, Chau *et al*. has reported a similar fractal formation when using peptide nanorods as building blocks.[36] They have pointed out that the diffusion units should be short. In fact, our nanotube bundles are in the length scale from 5 to 8 μm and sufficiently rigid to form fractal patterns. In addition, slow removal of solvent is necessary for hierarchical assembly based on the conventional diffusion-limited aggregation model. In our system, the nanotube bundles have appropriate length scale (1-5 μm), and contain rigid PMMA graft chains. Thus we believe that our system may undergo a similar fractal assembly mechanism. Once the nucleation site is formed from the side-by-side aggregation of the nanotube bundles, the free bundles could undergo random diffusion to attach and become a part of the assembly based on a diffusion-limited aggregation mechanism.[37-39]

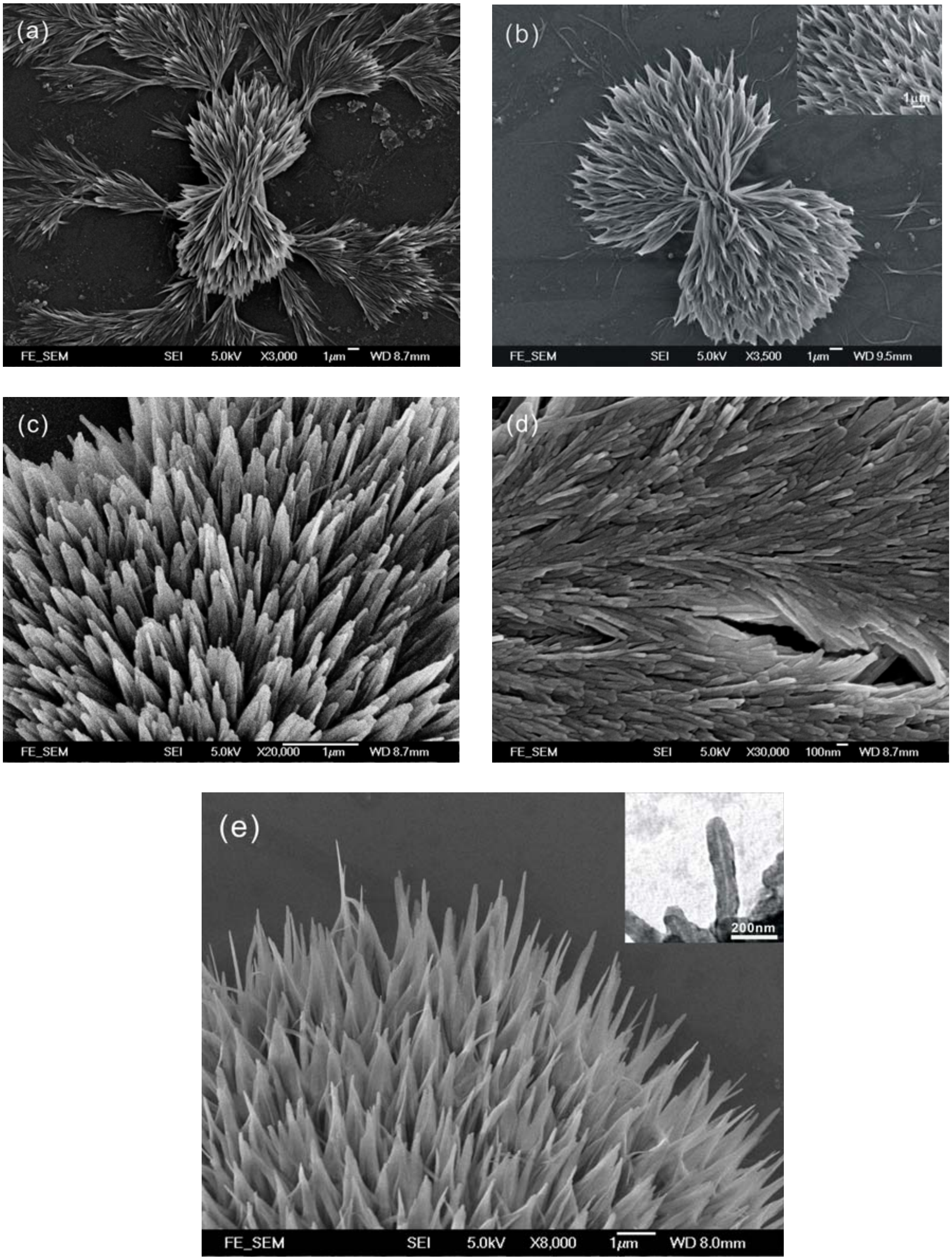

Figure 6.7 Morphologies of fractal patterns assembled at pH 7.

When the preformed nanotube bundles were treated at pH 9, most of them assembled into 3-D single columnar bundles as shown in Figure 6.8a and 6.8b. The columnar length is in the range of 10-18 μm with diameter between 5 and 8 μm. Each micro-column contains many fused nanotubes (Figure 6.8c and 6.8d) which were clearly revealed by the atomic force microscopy (Figure 6.9a and 6.9b). The cavity of the nanotube was also observed by the TEM image (Figure 6.8d inset). The formation of columnar structure may be attributed to the aggregation of high number of bundles as illustrated in Figure 6.8e. At pH 9, the protonation degree of PEI is only 8%.[25] Thus, there was a minimal electrostatic repulsion between the nanotubes. At this pH, the solubility of the PEI is also reduced, thus the smaller bundles would undergo further aggregation to a larger columnar structure in order to reduce their surface energy through minimization of the surface area.

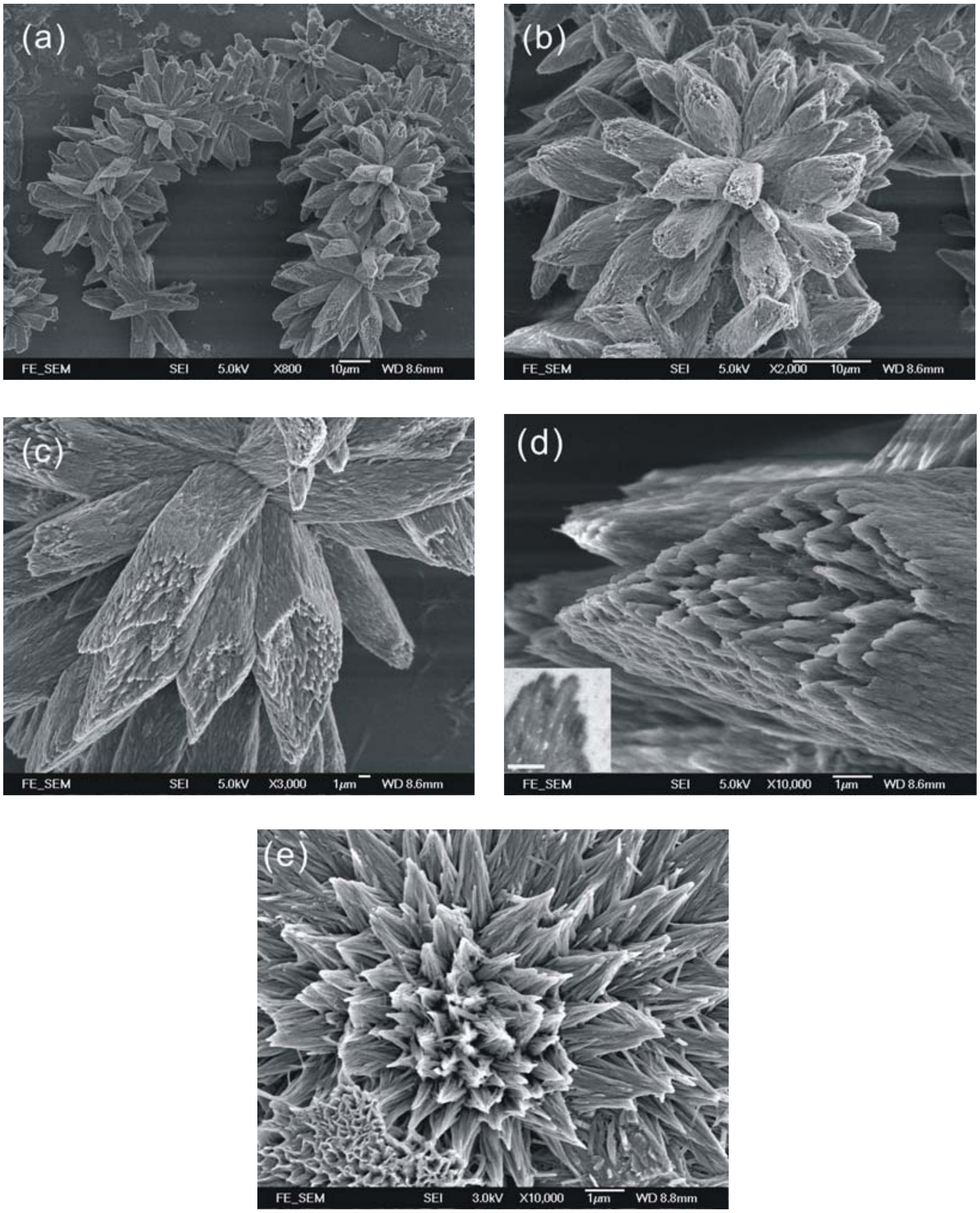

Figure 6.8 FE-SEM images of flower-like patterns assembled from micro-columns of preformed nanotubes at pH 9: (a) Flower-chain like structures; (b) and (c) Micro-columns assembled into flower-like pattern. (d) Micro-column that is formed through assembly of pre-formed nanotubes. (Inset: TEM image of nanotube bundle. Scale bar: 200 nm) (e) Aggregation of nanotube bundles towards the formation of columnar structure.

To further verify if the micro-columns were actually formed in the pH 9 solution, not during the drying process on a substrate, morphology of the micro-columns were observed with AFM in fluid mode. Figure 6.9 shows two- and three-dimensional images of the assemblies in water. Individual nanotubes with diameters in the range of 90 to 120 nm are aligned in bundles. These results support that the micro-columns are first formed in the pH 9 aqueous solution through formation of orderly packed nanotubes via the side-by-side assembly. The resulting nanostructure may be formed due to the increase of hydrogen bonds and hydrophobic interaction near isoelectric point of the nanotube, thus resulting in the increase of nanotube aggregation in order to minimize their interfacial energy.

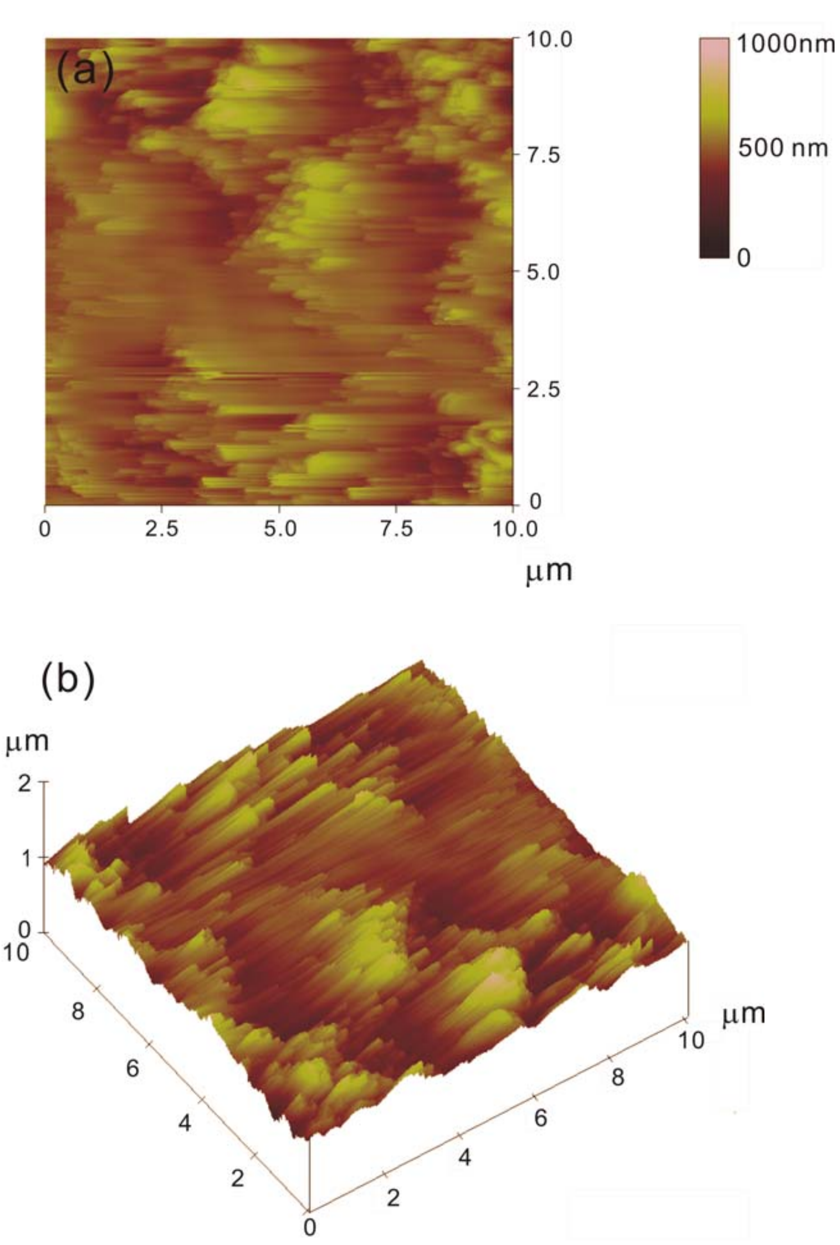

Figure 6.9 AFM image (fluid mode) of columnar structures in (a) 2D and (b) 3D profiles. The hierarchical structure was assembled with preformed nanotubes in aqueous solution of pH 9.

When treating the nanotube bundles at pH 11, reticular disk-like structure with rectangular shape were formed as illustrated in Figure 6.10a and 6.10b. A close observation of the detailed architecture reveals that the hierarchical disk-like structure is assembled from individual nanotubes perpendicular to one another (Figure 6.10c and 6.10d). TEM image confirms this kind of architecture as shown in the inset of Figure 6.10c. Under this strong alkaline condition, the water-solubility of the PEI molecule is decreased due to the lack of amine protonation. As a result, the PEI chains tend to compact on the nanotube surface, instead of highly extended in water in the case of acidic conditions. Therefore, the nanotube is dispersed as individual unit instead of aggregating into bundle because of low chain diffusion and entanglement. In addition, the hydroxyl ions (OH^-) tend to adsorb on the nanotube surface, providing a negative surface charge as shown in Figure 6.3 (*zeta*-potential of nanotubes was approximately -40 mV). The presence of strong negative electrostatic repulsion causes the nanotubes to arrange themselves in a perpendicular fashion in order to minimize their charge repulsion.

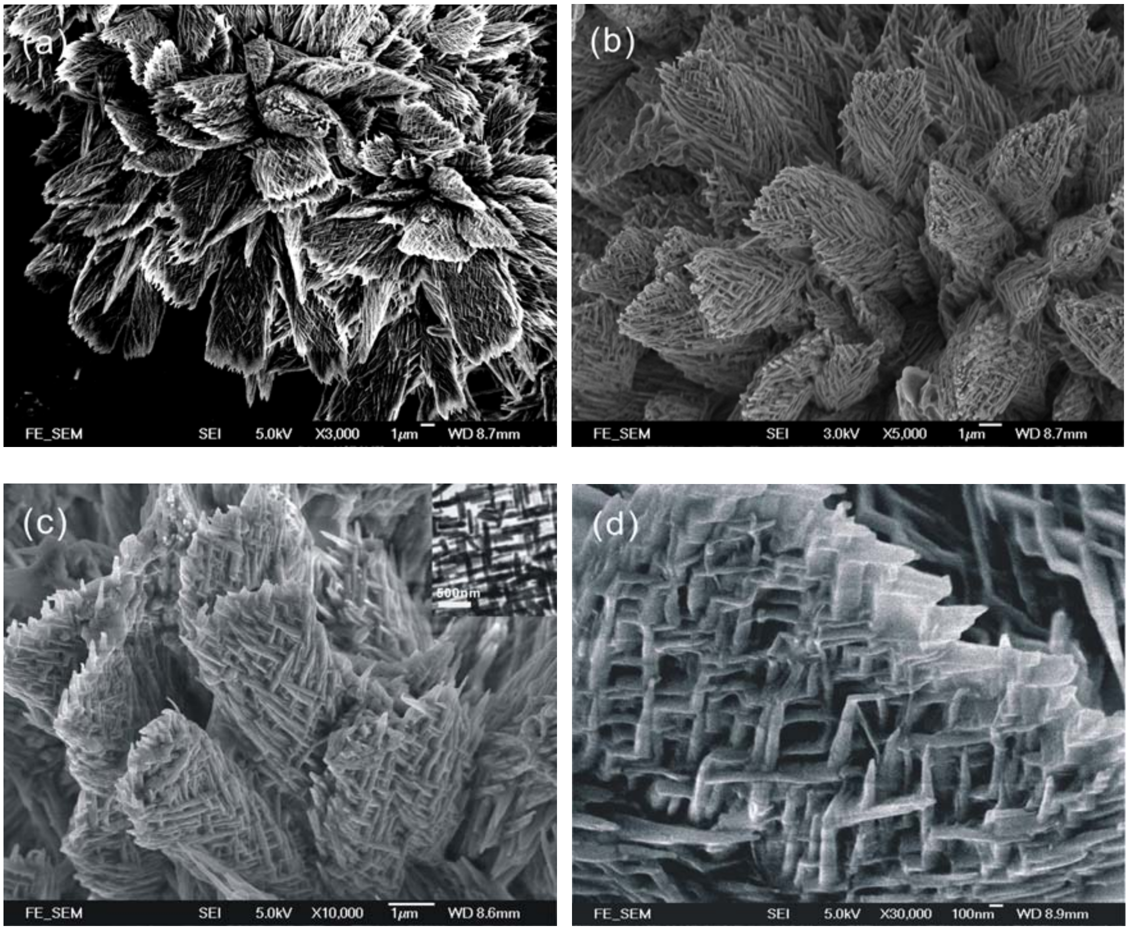

Figure 6.10 FE-SEM image of the crossed reticular-like structure with rectangular shape prepared at pH 11. Magnifications of the FE-SEM images are of (a) × 3,000 ; (b) × 5,000; (c) × 10,000, Inset : TEM image of the nanotubes having interwoven hierarchical structure (scale bar: 500 nm) and (d) × 30,000.

When treating the nanotubes dispersion at pH 13, similar interwoven disk-like materials were obtained except that the interwoven structure became much tighter, as illustrated in Figure 6.11. The nanotubes interweave to one another at an angle of approximately 45^{o}.

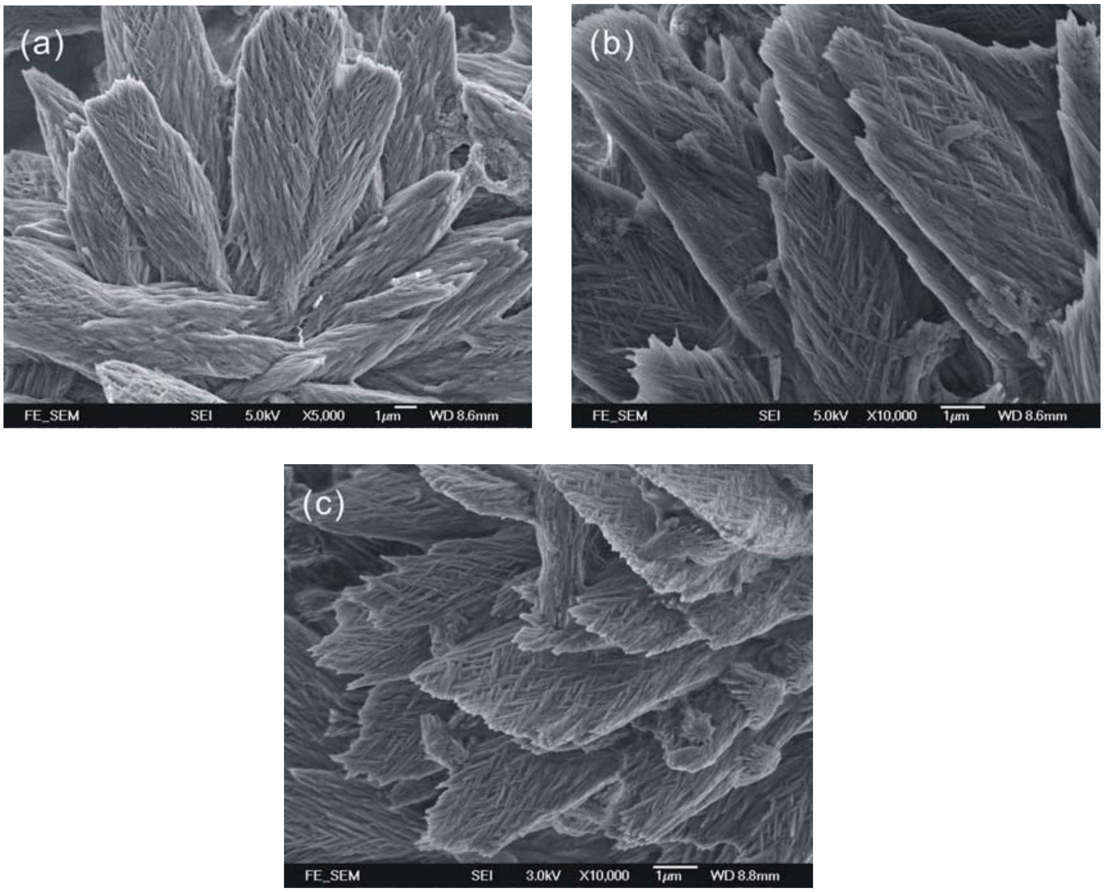

Figure 6.11 Morphologies of nanostructured materials obtained at pH 13.

We have attempted to understand the formation of this structure through capturing intermediate assemblies at different assembly time. The preformed PEI-*g*-PMMA nanotubes were treated at pH 13 up to 6 hours at room temperature. Sample was withdrawn at each hour interval and immediately air-dried for SEM observation At the first hour, the nanotubes with average length scale of 3-6 µm had already assembled into sheaf-like structure (Figure 6.12a). Similar morphologies were obtained after 2 and 3 hours with higher density. After the fourth hour, vertical straw sheaf-like nanostructure started to appear as illustrated in Figure 6.12d. The vertical growth of nanotubular assembly is an indication on how the three-dimensional interwoven disk-like structure is formed. On the basis of these morphological observations, a plausible formation mechanism of the interwoven reticular architectures at pH 13 is proposed as follows: The preformed nanotubes act as the primary template which first self-assembles into straw sheaf-like bundles with fantail shape. In this process, the preformed nanotubes self-organize via a side-by-side orientation in order to minimum their high free energy surfaces. The primary assembled bundle structures could serve as the template for secondary assembly which grows from vertical direction. The vertical nanotubes could preferentially form an interwoven nanostructure in order to increase their structural stability. On the basis of these observations, we can reasonably assume that the extension of fanlike patterns may play an important role in the formation of hierarchical structures from parallel bundles to interwoven reticular architectures.

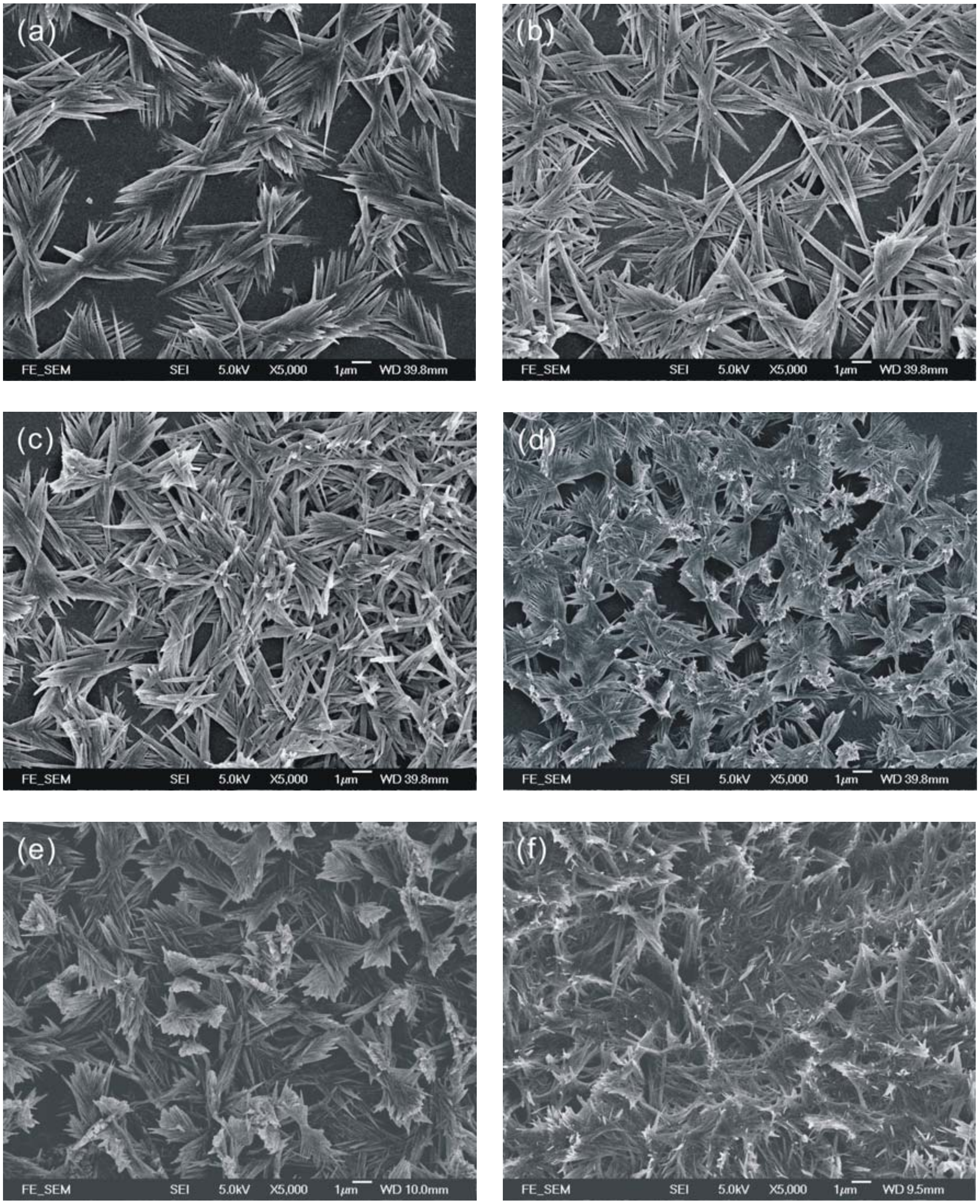

Figure 6.12 FE-SEM image of hierarchical structures formation at solution pH 13 with reaction time of (a) 1 hr; (b) 2 hrs; (c) 3 hrs; (d) 4 hrs and (e) 5hrs and (f) 6 hrs.

These results demonstrate that control of solution pH enables us to generate various intriguing 2D and 3D hierarchiical structures using preformed PEI-*g*-PMMA nanotubes as the building block. Table 6.1 summarize our findings on the correlations between solution pHs and their resulting nanostructures and scales. Figure 6.13 shows representative morphologies under different pH treatments. These results suggest that the change of solution pH notably alters the electrostatic interaction of the building blocks, thus strongly influence the stacking process of precursor from parallel bundle to dual fantail shaped bundle, then to interwoven structure.

Table 6.1 Summary of correlation between the solution pH and the corresponding morphologies of the assembled hierarchical structures

Solution pH	Morphology	Length of hierarchical structure (μm)
3	nanotube	3-5
5	2D nanotube bundle	7-9
7	Fractal-like bundle	13-15
9	Columnar-like bundle	15-20
11	Interwoven nanotubular disk with loose packing	3-5[a]
13	Highly packed interwoven nanotubular disk	10-15[a]

a: Observable length from FE-SEM micrograph. The actual length of the hierarchical structure is longer than the observed length from FE-SEM image. The length cannot be measured accurately because the nucleation sites have not been identified from the SEM micrographs.

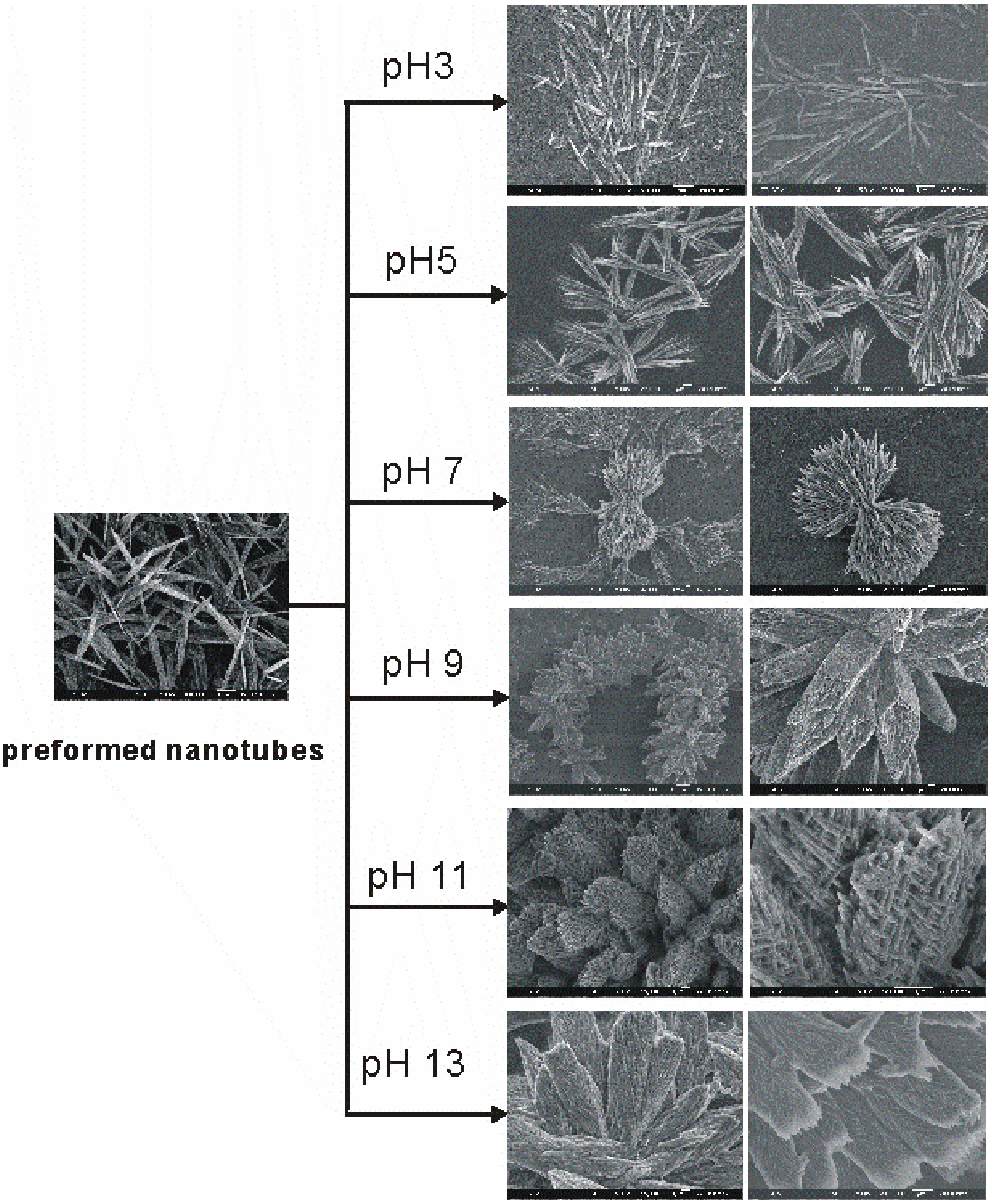

Figure 6.13 Summary of resulting assembled nanostructures at different solution pH.

Scheme 6.1 summarizes the effect of pH on the assembly of PEI-*g*-PMMA nanotubes into various nanostructured patterns. The preformed nanotubes were primarily assembled from elongated hollow particles at controlled stirring rate and solvent composition. Under acidic condition (pH 3), the PEI-*g*-PMMA nanotubes with high positive surface charges are well dispersed owing to the electrostatic repulsive force exceeding attractive hydrophobic interaction between the nanotubular building blocks. These free-standing PEI-*g*-PMMA nanotubes can first form the nanotubular assemblies in parallel and crossed bundles depending on solution pH in secondary self-assembly stage. The assembly of bundles in parallel or X-shaped (straw sheaf-like structure) arrangement in side-by-side assembling mode is energetically more favorable than the end-to-end assembling mode. To further reduce the surface free energy, the precursors will continuously attract those nearby nanotube bundles and assemble into the columnar packing. With the increase of the solution pH to nearly isoelectric point (pH 9 in our experiment), the electrostatic repulsive force between assemblies is negligible. Thus some adjacent nanotubular bundles tend to nucleate with each other and form a 3D architecture under the attractive van der Waals force at tertiary self-assembly stage. From the above presented mechanism, the competition between the tubular interactions (i.e., the electrostatic repulsive forces and attractive forces in the building blocks) is the key driving forces for self-assembly of the 3D hierarchical structures.

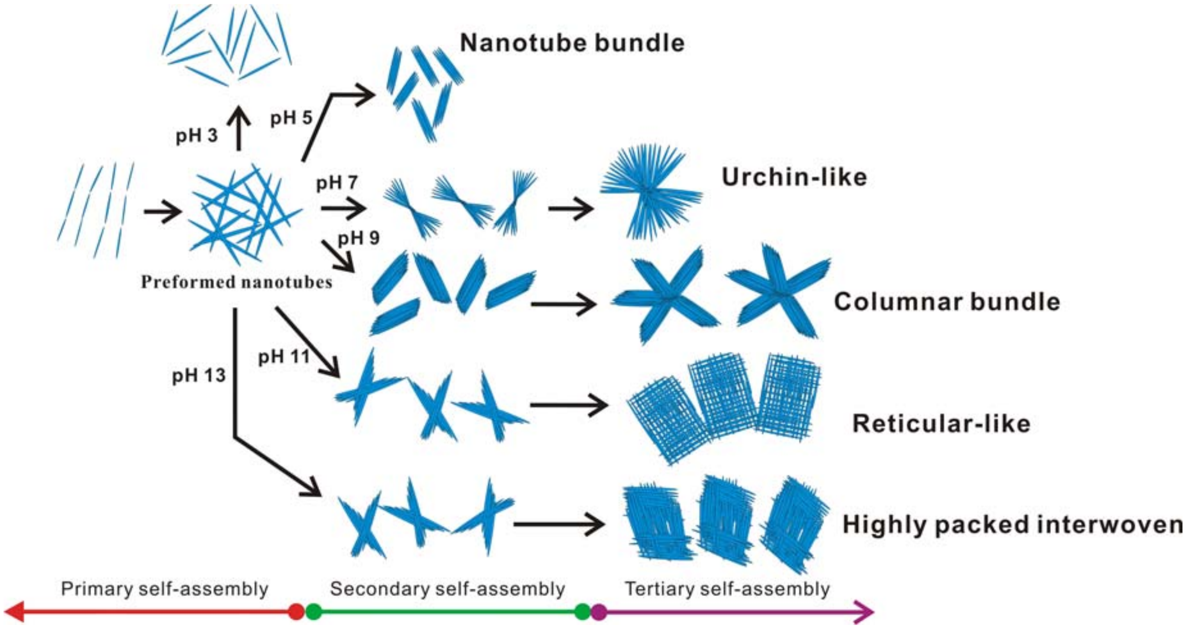

Scheme 6.1 pH effect in the hierarchical assembly from preformed nanotubes as building blocks.

6.4 Conclusion

A novel one-step solution self-assembly route for the selective preparation of straw-sheaf-like nanotube bundles, columnar bundles, interwoven disk-like assemblies have been achieved via a simple solution pH tuning strategy of the preformed PEI-*g*-PMMA nanotubes. The formation mechanism of these hierarchical structures has been partially elucidated. The preformed nanotube building block can initially aggregate into well-defined bundles, which can act as template for subsequent assemblies to straw sheaf-like structures, columnar bundles and interwoven disk-like nanostructures. We believe that these studies are not only important for us to fundamentally understand the assembly mechanism of the amphiphilic nanotubes, but also open up a new revenue for the creation of various kinds of interesting soft nanostructured materials.

References

1. Pileni, M. P. *J. Phys. Chem. B* **2001**, *105*, 3358.
2. Percec, V.; Ungar, G.; Peterca, M. *Science* **2006**, *313*, 55.
3. Kol, N. et al. *Nano Lett.* **2005**, *5*, 1343.
4. Zhang, S. *Nature Biotechnol*. **2003**, *21*, 1171.
5. Rothemund, P. W. K. *Nature* **2006**, *440*, 297.
6. Xu, J.; Xia, J. F.; Lin, Z. Q. *Angew. Chem., Int. Ed.* **2007**, *46*, 1860.
7. Bigioni, T. P.; Lin, X. M.; Nguyen, T. T.; Corwin, E. I.; Witten, T. A.; Jaeger, H. M. *Nat. Mater.* **2006**, *5*, 265.
8. Querner, C.; Fischbein,M. D.; Heiney, P. A.; Drndió, M. *Adv. Mater.* **2008**, *20*, 2308.
9. Ming, T.; Kou, X. S.; Chen, H. J.; Wang, T.; Tam, H. L.; Cheah, K. W.; Chen, J. Y.; Wang, J. F. *Angew. Chem., Int. Ed.* **2008**, *47*, 9685.
10. Shevchenko, E. V.; Talapin, D. V.; Rogach, A. L.; Kornowski, A.; Haase, M.; Weller, H. *J. Am. Chem. Soc.* **2002**, *124*, 11480.
11. Shevchenko, E.; Talapin, D.; Kornowski, A.; K∈otzler, J.; Haase, M.; Rogach, A. L.; Weller, H. *Adv. Mater.* **2002**, *14*, 287.
12. Huang, J. X.; Kim, F.; Tao, A. R.; Connor, S.; Yang, P. D. *Nat. Mater.* **2005**, *4*, 896.
13. Tao, A. R.; Sinsermsuksakul, P.; Yang, P. D. *Nat. Nanotechnol.* **2007**, *2*, 435.
14. Tao, A. R.; Huang, J. X.; Yang, P. D. *Acc. Chem. Res.* **2008**, *41*, 1662.
15. Fan, H. Y.; Leve, E.; Gabaldon, J.; Wright, A.; Haddad, R. E.; Brinker, C. J. *Adv. Mater.* **2005**, *17*, 2587.
16. Bai, F.; Wang, D. S.; Huo, Z. Y.; Chen, W.; Liu, L. P.; Liang, X.; Chen, C.; Wang, X.; Peng, Q.; Li, Y. D. *Angew. Chem., Int. Ed.* **2007**, *46*, 6650.

17. Zhuang, J. Q.; Wu, H. M.; Yang, Y. A.; Cao, Y. C. *Angew. Chem., Int. Ed.* **2008**, *47*, 2208.
18. Park, S. Y.; Lytton-Jean, A. K. R.; Lee, B.; Weigand, S.; Schatz, G. C.; Mirkin, C. A. *Nature* **2008**, *451*, 553.
19. Lee, I.; Zheng, H. P.; Rubner, M. F.; Hammond, P. T. *Adv. Mater.* **2002**, *14*, 572.
20. Choi, J. H.; Adams, S. M.; Ragan, R. *Nanotechnology* **2009**, *20*, 065301.
21. Hammond, P. T. *Adv. Mater.* **2004**, *16*, 1271.
22. Smith, R. K.; Lewis, P. A.; Weiss, P. S. *Prog. Surf. Sci.* **2004**, *75*, 1.
23. Lee, C. H.; Ho, K. M.; Harris, F. W.; Cheng, S. Z. D. and Li, P. Soft Matter **2009**, *5*, 4914.
24. O’Brien, R. W.; Ward, D. N. *J. Colloid Interface Sci.* **1988**, *121*, 402.
25. Suh, J. H.; Lee, S. H.; Kim, S. M.; Hah, S. S. *Bioorg. Chem.* **1997**, *25*, 221.
26. Whitesides, G. M.; Boncheva, M. *Proc. Natl. Acad. Sci. U.S.A.* **2002**, *99*, 4769.
27. Rogach, A. L.; Talapin, D. V.; Shevchenko, E. V.; Kornowski, A.; Haase, M.; Weller, H. *Adv. Funct. Mater.* **2002**, *12*, 653.
28. Jana, N. R. *Angew. Chem., Int. Ed.* **2004**, *43*, 1536.
29. Song, Q.; Ding, Y.; Wang, Z. L.; Zhang, Z. J. *J. Phys. Chem. B* **2006**, *110*, 25547.
30. Zhang, S., Holmes, T., Lockshin, C. & Rich, A. *Proc. Natl Acad. Sci.* USA **1993**, *90*, 3334.
31. Goodman, R. P. et al. *Science* **2005**, *310*, 1661.
32. Hung, A. M.; Stupp, S. I. *Nano Lett.* **2007**, *7*,1165.
33. Ringler, P.; Schulz, G. E. *Science* **2003**, *302*, 106.
34. He, Y.; Ye, T.; Zhang, C.; Ribbe, A. E.; Jiang, W.; Mao, C. *Nature* **2008**, *452*,198.

35. Spector, M. S.; Singh, A.; Messersmith, P. B.; Schnur, J. M. *Nano Lett.* **2001**, *1*, 375.

36. Wang, W. P.; Chau, Y. *Soft Matter*, **2009**, *5*, 4893.

37. Ossadnik, P.; Lam, C. H.; Sander, L. M. *Phys. Rev. E: Stat. Phys., Plasmas, Fluids, Relat. Interdiscip. Top*., **1995**, *51*, R2767.

38. Rothenbuhler, Huang, J. R.; DiDonna, B. A.; Levine, A. J.; Mason, T. G. *Soft Matter* **2009**, *5*, 3639.

39. Giri, K.; Bhattacharyya, N. P.; Basak, S. *Biophys. J.* **2007**, *92*, 293.

Chapter 7

Concluding Remarks and Future Studies

7.1 Introduction

In this chapter, a final conclusion is made. The chapter begins with a summary of the major findings, followed by significance and implications of the study. Finally, the limitations of this research and recommendations for future work are discussed.

7.2 Summary of the Major Findings

A comprehensive characterization of amphiphilic PEI-*g*-PMMA hollow particle performed in the course of this dissertation provides some important insights into the relationships between PEI-*g*-PMMA based hollow particles self-assembly and morphological changes under the effect of various solution parameters. The following results were obtained towards three specific aims:

1) By preparing PEI-*g*-PMMA hollow particles after core extraction of core PMMA homopolymer in organic solvent (dichloromethane), it has been demonstrated that the nanotube formation are mainly determined by the selective assembly of curvature-dependent morphology of elongated hollow particles under controlled fluid shear condition. Relationships between morphological changes and DCM/water volume ratio were established. The morphology was changed from spheres or vesicle at low water content to nanotubular form at high water content via network morphology.

2) The effect of temperature on the hydrophobic interaction of PMMA grafts induces shrinkage of both particle and nanotube diameter. The reduction in both particle and tubular sizes and the aggregated pattern depends on hydrophobic interaction induced by PMMA grafts as a function of solution temperature. The possible mechanism was described in terms of the calculation results of polymer-solution interaction parameters and interfacial free energy prediction of the hollow particles.

3) In summary, we have developed an effectual route to fabricate 3D hierarchical self-assembled PEI-*g*-PMMA nanotubes based on pH-induced strategy. Stock solution prepared in 0.01 M HCl or NaOH were used to adjust the pH of the reaction system, control the intertubular packing arrangement as precursor, and further induce the spontaneous self-assembly of the preformed PEI-*g*-PMMA nanotubes through the force balance between hydrogen bonding and electrostatic repulsion. Despite that it is very simple and straightforward, the proposed simultaneous synthesis and self-assembly method is remarkably effective and reproducible to interwoven reticular-like and 3D columnar structures of nanotubular building blocks in straw sheaf-like morphology and parallel bundles, respectively. We believe that the present strategy will be very useful for the fundamental research and practical application on the self-assembled copolymer-based nanostructures and meanwhile provides an alternative pathway to assemble 3D structural analogues of other functional nanostructures.

This thesis describes a novel dynamic assembly of nanostructured materials with controlled morphologies based on amphiphilic PEI-g-PMMA hollow particles after core extraction of well-defined PMMA/PEI core shell nanoparticles. One-dimensional nanomaterials assembly with elongated hollow particles as basic building block which spontaneously formed with controlled solution parameters.

Amphiphilic copolymer has been widely studied in block copolymer, but rarely in graft copolymer. Our work demonstrates that 1D nanotubular materials can be obtained through tip-to-tip assembly of elongated hollow particles via fluid shear selective coalescence effect and solution condition. Since our method does not depend on any surface chemistry on the building block except the solution condition.

7.3 Significance and Implications of This Study

In this work, the primary motivation was to create desirable core–shell particles with functional shells as well as hollow particles based on the dissolution of core PMMA homopolymer from PEI/PMMA core shell nanoparticles. Although spherical hollow capsules have received considerable attention,[107–109] only limited effort has been paid to non-spherical hollow particles such as elongated hollow particles. Extremely rare attention has concentrated on the interaction of nonspherical hollow particles based on amphiphilic graft copolymer and the relevant morphological change under controlled self assembling process. Herein, well-defined core–shell particles and various ellipsoidal hollow capsules through fluid shear process, especially amphiphilic hollow capsules with both exterior and interior were sensitive with solvent microenvironments, were investigated. These ellipsoidal or elongated hollow particles may also find useful as building blocks to form one-dimensional nanostructured materials (e.g. nanotubes) with properties different from those of conventionally spherical ones. Furthermore, they would be potential unique candidates that could be assembled into hierarchical structure through tuning solution properties.

7.4 Suggestions for Future Work

Our proposed copolymer self-assembled nanostructures using inexpensive amphiphilic graft copolymer based hollow particles by core dissolution of well-defined core shell nanoparticles have a strong potential for the diverse areas of copolymer nanotechnology owing to the extremely simple fabrication procedure for hierarchical structures as well as their notable thermodynamic stability. As a promising application potential of the assembled structures, we can use the preformed hollow nanostructure as building block that direct secondary assembly of higher order structures. In such case, the hierarchical structures can be effectively used as a nanocontainer or directing material for the functional units since it will readily localize them into a specific site if the nanostructure surface is properly functionalized so that it can strongly interact with the functional units. It is notable that the cationic shell surface can be more easily functionalized with various chemicals in comparison to the corresponding graft copolymers. The resulting functionalized copolymer nanopatterns can be used in numerous areas of nanotechnology such as nanostructured networks and membranes for fuel cells, nanotemplates and scaffolds for the fabrication of nanometer scale arrays in the immobilization of bio-molecules, photonic materials for optical applications, and immobilization of metal nanoparticles as metal-colloid in catalytic applications.

Future work aims to investigate the scope of this assembly approach based on the hollow particles of poly(ethyleneimine)-graft-poly(methyl methacrylate) (PEI-*g*-PMMA) copolymers with different chain architectures. New types of nanostructured materials can be created through varying the properties of building blocks and manipulating the assembling conditions. This will allow us to design and tailor the shape, composition, structure, properties and functions of nanostructured materials for specific applications.

Strategies can be proposed including (1) Synthesis and characterization of PEI-g-PMMA hollow particles with different chain architectures (variation of graft chain length and shell thickness). These hollow particles will then be used as new types of building block for self-assembly in solution. (2) Manipulation of solution conditions to create a variety of new nanostructured materials, followed by detailed characterization of potential properties of the assembled materials. (3) Fabrication of novel hierarchical nanostructures or microstructures from pre-assembled nanotubes or other preformed nanostructures as basic building blocks via different solution treatment methods.

Appendix A

Calculation of polymer solvent interaction parameter as function of temperature

Assume the total volume of the solvent mixture = 10 mL

Volume of DCM = 3 mL (30 vol. %) Molar volume of DCM = 63.9 cm^3

Volume of water = 7mL (70 vol. %) Molar volume of water = 18 $cm^{3\ (ref)}$

According to equation 5.2 $\delta_s = \phi_1\delta_1 + \phi_2\delta_2$ (5.2)

Solvent parameters obtained from reference [6] in Chapter 5

$\delta_{DCM} =$ 20.2 δ_{H2O} = 48

Thus the solubility parameter for DCM/water mixture is calculated as:

$\delta_s = \phi_{DCM}\delta_{DCM} + \phi_{H2O}\,\delta_{H2O}$

= 0.3 × 20.2 + 0.7 × 48

= 39.66

Molar volume of two-solvent mixture V_s is calculated according to Eq 5.3

$$V_s = \frac{V_1V_2}{\phi_1V_2 + \phi_2V_1} \qquad (5.3)$$

$Vs = (V_{H2O} \times V_{DCM})/(\phi_{DCM}V_{H2O} + \phi_{H2O}V_{DCM})$

= (18×63.9)/(0.3 × 18 + 0.7 × 63.9)

= 22.944

To determine the PEI to solvent mixture interaction parameter as a function of temperature, we use the equation

$$\chi_{PEI-S} = \frac{Vs}{RT}(\delta_{PEI} - \delta_S)^2$$

where R = 8.314 cm^3 MPa K^{-1} and T is expressed in Kelvin (^oK), where δ_1 and δ_2 are the solubility parameters of solvent 1 and solvent 2

solubility parameter of PEI, $\delta_{PEI} = 45$

solubility parameter of DCM/water (30/70) mixed solvent calculated = 39.66

Thus the interaction parameter value of PEI to the solvent mixture can be calculated as follow:

At 15°C,

$$\chi_{PEI-S} = \frac{Vs}{RT}(\delta_{PEI} - \delta_S)^2$$

$$= \frac{22.944}{8.314 \times 288^o K}(45 - 39.66)^2$$

$$= 0.273$$

Appendix B

Table 1

Poly(methyl methacrylate)-solvent mixture interaction parameter ($\chi_{\text{PMMA-solvent}}$) versus water percentage from 70 to 100 % at various temperatures

Water percentage (%)	$\chi_{\text{PMMA-solvent}}$ (15^{o}C)	$\chi_{\text{PMMA-solvent}}$ (25^{o}C)	$\chi_{\text{PMMA-solvent}}$ (35^{o}C)	$\chi_{\text{PMMA-solvent}}$ (45^{o}C)
70	4.0901	3.95285	3.82451	3.70424
70.70707	4.14149	4.00251	3.87256	3.75078
71.42857	4.194	4.05326	3.92166	3.79834
72.16495	4.24767	4.10513	3.97185	3.84695
72.91667	4.30254	4.15816	4.02316	3.89664
73.68421	4.35865	4.21239	4.07562	3.94746
74.46809	4.41603	4.26784	4.12928	3.99943
75.26882	4.47474	4.32458	4.18417	4.05259
76.08696	4.5348	4.38263	4.24034	4.10699
76.92308	4.59628	4.44204	4.29782	4.16267
77.77778	4.65921	4.50286	4.35667	4.21966
78.65169	4.72365	4.56514	4.41692	4.27802
79.54545	4.78965	4.62892	4.47863	4.3378
80.45977	4.85726	4.69427	4.54186	4.39903
81.39535	4.92655	4.76123	4.60664	4.46178
82.35294	4.99757	4.82986	4.67305	4.5261
83.33333	5.07038	4.90023	4.74114	4.59204
84.33735	5.14505	4.9724	4.81096	4.65967
85.36585	5.22166	5.04644	4.88259	4.72905
86.41975	5.30027	5.12241	4.95609	4.80024
87.5	5.38095	5.20039	5.03154	4.87332
88.60759	5.4638	5.28045	5.10901	4.94835
89.74359	5.54889	5.36269	5.18858	5.02541
90.90909	5.63632	5.44718	5.27032	5.10459
92.10526	5.72617	5.53402	5.35434	5.18597
93.33333	5.81855	5.6233	5.44072	5.26963
94.59459	5.91356	5.71511	5.52956	5.35567
95.89041	6.0113	5.80958	5.62096	5.4442
97.22222	6.1119	5.90681	5.71503	5.53531
98.59155	6.21548	6.00691	5.81188	5.62912
100	6.32217	6.11001	5.91164	5.72574

Table 2

Poly(ethylenimine)-solvent mixture interaction parameter ($\chi_{\text{PEI-solvent}}$) versus water percentage from 70 to 100 % at various temperatures

Water percentage (%)	$\chi_{\text{PEI-solvent}}$ (15^{o}C)	$\chi_{\text{PEI-solvent}}$ (25^{o}C)	$\chi_{\text{PEI-solvent}}$ (35^{o}C)	$\chi_{\text{PEI-solvent}}$ (45^{o}C)
70	0.273247	0.264078	0.255504	0.247469
70.70707	0.25187	0.243418	0.235515	0.228109
71.42857	0.231092	0.223337	0.216086	0.209291
72.16495	0.210943	0.203864	0.197245	0.191043
72.91667	0.191454	0.185029	0.179022	0.173392
73.68421	0.172657	0.166864	0.161446	0.156369
74.46809	0.154588	0.149401	0.14455	0.140004
75.26882	0.137282	0.132676	0.128368	0.124331
76.08696	0.120778	0.116725	0.112935	0.109384
76.92308	0.105114	0.101587	0.098288	0.095198
77.77778	0.090332	0.087301	0.084467	0.08181
78.65169	0.076477	0.073911	0.071511	0.069262
79.54545	0.063594	0.06146	0.059464	0.057594
80.45977	0.05173	0.049994	0.048371	0.04685
81.39535	0.040938	0.039564	0.03828	0.037076
82.35294	0.03127	0.030221	0.02924	0.02832
83.33333	0.022782	0.022018	0.021303	0.020633
84.33735	0.015534	0.015013	0.014525	0.014068
85.36585	0.009587	0.009265	0.008965	0.008683
86.41975	0.005007	0.004839	0.004682	0.004535
87.5	0.001863	0.001801	0.001742	0.001688
88.60759	0.000229	0.000221	0.000214	0.000207
89.74359	0.000179	0.000173	0.000168	0.000163
90.90909	0.001797	0.001737	0.001681	0.001628
92.10526	0.005168	0.004994	0.004832	0.00468
93.33333	0.010381	0.010033	0.009707	0.009402
94.59459	0.017534	0.016946	0.016396	0.01588
95.89041	0.026727	0.025831	0.024992	0.024206
97.22222	0.038069	0.036791	0.035597	0.034477
98.59155	0.051672	0.049938	0.048316	0.046797
100	0.067657	0.065387	0.063264	0.061274